



Publicly Accessible Penn Dissertations

2016

Recreating Bioenergetic Elements In Protein Maquettes

Bryan Andrew Fry

University of Pennsylvania, bryan_fry@yahoo.com

Follow this and additional works at: <https://repository.upenn.edu/edissertations>

 Part of the [Biochemistry Commons](#), and the [Biophysics Commons](#)

Recommended Citation

Fry, Bryan Andrew, "Recreating Bioenergetic Elements In Protein Maquettes" (2016). *Publicly Accessible Penn Dissertations*. 2291.
<https://repository.upenn.edu/edissertations/2291>

This paper is posted at ScholarlyCommons. <https://repository.upenn.edu/edissertations/2291>
For more information, please contact repository@pobox.upenn.edu.

Recreating Bioenergetic Elements In Protein Maquettes

Abstract

In all organisms, protein-mediated electron transfers underlie energy metabolism and countless other critical metabolic pathways. Deciphering the factors governing electron transfers offers enormous practical value, including finding reliable guidelines for metabolic engineering to produce clean solar fuels. Protein maquettes provide simple, flexible scaffolds to study biological electron transfer processes. The maquette approach to protein design builds man-made oxidoreductases from first principles with minimal reference to natural protein sequences. This scheme has produced impressive *in vitro* and *in vivo* results to replicate the functions of natural oxidoreductases using simple, straightforward α -helical bundles. The redox function of maquettes has so far been limited to electron transfers within a single water-soluble molecule. This work extends the maquette project to examine electron transfers A) between diffusing redox partners and B) in amphiphilic proteins. Nature employs complimentary electrostatic surfaces to bring diffusing redox proteins together, and a series of maquettes of varying surface charge demonstrate that the same principles apply to flexible manmade proteins. A heme-binding maquette of complimentary surface charge is shown to reduce natural cytochrome c at physiological rates, while a maquette variant similar in charge to cyt c shows a far weaker interaction. The ionic strength dependence of these interactions is shown to be broadly similar to that in natural proteins. This work also presents the first intra-protein redox function in a *de novo* amphiphilic protein and describes progress toward transmembrane electron transfer analogous to that in the cytochrome bc₁ complex. These functional achievements are remarkable given that the proteins are designed from first principles without atomically resolved structures, and they hold promise for future efforts in applying artificial proteins to new metabolic pathways.

Degree Type

Dissertation

Degree Name

Doctor of Philosophy (PhD)

Graduate Group

Biochemistry & Molecular Biophysics

First Advisor

Peter L. Dutton

Second Advisor

Bohdana M. Discher

Keywords

Electron Transfer, Maquette, Protein Design, Spectroscopy

Subject Categories

Biochemistry | Biophysics

RECREATING BIOENERGETIC ELEMENTS IN PROTEIN MAQUETTES

Bryan A. Fry

A DISSERTATION

in

Biochemistry and Molecular Biophysics

Presented to the Faculties of the University of Pennsylvania

in

Partial Fulfillment of the Requirements for the

Degree of Doctor of Philosophy

2016

Supervisor of Dissertation

Co-Supervisor of Dissertation

P. Leslie Dutton, Ph.D., FRS
Eldridge Reeves Johnson Professor of Biochemistry
and Biophysics, Director of the Johnson Foundation
for Molecular Biophysics

Bohdana M. Discher, Ph.D.
Research Associate Professor
of Biochemistry and Biophysics

Graduate Group Chairperson

Kim A. Sharp, Ph.D.
Associate Professor of Biochemistry and Biophysics

Dissertation Committee:

Ravi Radhakrishnan, Ph.D., Professor of Bioengineering
Tobias Baumgart, Ph.D., Associate Professor of Chemistry
Ivan J. Dmochowski, Ph.D., Professor of Chemistry
Sergei Vinogradov, Ph.D., Associate Professor of Biochemistry and Biophysics
Kim A. Sharp, Ph.D., Associate Professor of Biochemistry and Biophysics
Marilyn R. Gunner, Ph.D., Professor of Physics at City College of New York

RECREATING BIOENERGETIC ELEMENTS IN PROTEIN MAQUETTES

© 2016

Bryan Andrew Fry

ACKNOWLEDGEMENTS

I have many people to thank for their help, support, and friendship during my time at Penn.

Les Dutton, one of my two co-mentors, has been a consistent source of advice, encouragement, and guidance. Les offers a wealth of scientific insight and experience while simultaneously trusting his lab members to largely chart their own paths. I specifically appreciate the leeway to undertake molecular dynamics simulations despite being well outside the typical purview of the lab, and I hope that my initial efforts in this realm will ultimately prove fruitful. The unique scientific culture of Dutton group played in my choice to join the lab and I have no regrets. Moreover, Les enjoys a very well-deserved reputation in the BMB graduate group for unwavering support and loyalty to his students.

Bohdana Discher, my second co-mentor, has been similarly invaluable. Through her wide-ranging collaborations I have been exposed to fascinating science pushing our basic protein developments towards specific technological applications in both physical and biological fields. I very much appreciate Bohdana's consistent optimism and empathetic encouragement in the face of challenges, experimental and otherwise. Bohdana's dedication to the Research Experience for Undergraduates program has been a boon to our laboratory. I enjoyed fun and productive collaborations with Bohdana's REU students and was pleasantly surprised at their contributions to our research.

Chris Moser's support has been essential to all of my progress and learning in the lab. Chris possesses a truly uncanny knack for quickly overcoming seemingly hopeless roadblocks at any step in the scientific process. This applies equally to designing or tweaking an experiment, teasing a valuable insight from apparently useless data, or beating a paragraph in a manuscript into something comprehensible. What's more, while offering his help Chris has never passed up a "teachable moment" while always delivering his insight with infinite patience and good humor.

The past and present students and postdocs in our laboratory have made this a wonderful place to work over these years. Bruce Lichtenstein, now tenaciously implanted in Germany, was very generous with his help during my early time in the lab, particularly in thinking through my prelim and in debugging my initial experiments. I appreciate Tammer Farid's insightful help with writing, as well as his deadpan humor and his deep understanding (passed on the me,

unfortunately) of our lyophilizer vacuum pump. Geetha Goparaju's gentle patience and friendship was always a welcome presence in our outspoken lab. Moreover, her calm and methodical approach towards experimental work was a valuable example to me, proving to be a perfect match for the daunting task of developing methods to express and purifying amphiphilic maquettes. Mike Englander was a good friend, confidante, and unfailing partner for burrito lunches. Goutham Kodali's broad understanding of many overlapping fields and techniques proved very helpful in thinking about how to approach problems, along with his "just try it and see" optimism. Lee Solomon was a huge help in and out of lab, including reliably sponsoring Star Wars viewings and our dubious online trivia team. Molly Sheehan was always ready for an interesting scientific or unscientific discussion, as well as keeping us reliably fed with outstanding cakes and brownies. Nate Ennist's tremendous work and discipline in designing a completely new protein scaffold has been offered valuable ideas for my designs for next-generation amphiphilic proteins. Josh Mancini has been a huge help in navigating the weird voodoo of molecular biology, along with an unfailing source of good cheer. Chris Bialas is a valuable purveyor of general ridiculousness as well as frank critical feedback. Zhenyu Zhao has offered countless valuable discussions on the computational aspects of our work. Importantly, I also have him to thank for reminding me of my latent appreciation for D&D. Dirk Auman and Martin Iwanicki, the newest members in the lab, are great additions to the maquette project and I wish them all the best.

I would also like to thank my dissertation committee: Ravi Radhakrishnan, Tobias Baumgart, Ivan Dmochowski, Sergei Vinogradov, Kim Sharp, and Marilyn Gunner for reading and digesting this dissertation as well as offering their suggestions and expertise as my work progressed.

Finally, the love and support of my family has been essential over the last the several years. I owe so much to my parents, Andy and Sandy Fry. Throughout my life they have consistently supported all of my decisions, not least the choice to leave a perfectly good career to take on a nearly unrelated Ph.D. Many good things have come from my time living in Philadelphia, and undoubtedly the best of these was meeting (and marrying!) Lael. In addition to offering unwavering support, she knows when and how to push me to keep perspective in the face of inevitable frustrations. Thank you so much!

ABSTRACT

RECREATING BIOENERGETIC ELEMENTS IN PROTEIN MAQUETTES

Bryan A. Fry

P. Leslie Dutton

Bohdana M. Discher

In all organisms, protein-mediated electron transfers underlie energy metabolism and countless other critical metabolic pathways. Deciphering the factors governing electron transfers offers enormous practical value, including finding reliable guidelines for metabolic engineering to produce clean solar fuels. Protein maquettes provide simple, flexible scaffolds to study biological electron transfer processes. The maquette approach to protein design builds man-made oxidoreductases from first principles with minimal reference to natural protein sequences. This scheme has produced impressive *in vitro* and *in vivo* results to replicate the functions of natural oxidoreductases using simple, straightforward α -helical bundles. The redox function of maquettes has so far been limited to electron transfers within a single water-soluble molecule. This work extends the maquette project to examine electron transfers **A)** between diffusing redox partners and **B)** in amphiphilic proteins. Nature employs complimentary electrostatic surfaces to bring diffusing redox proteins together, and a series of maquettes of varying surface charge demonstrate that the same principles apply to flexible manmade proteins. A heme-binding maquette of complimentary surface charge is shown to reduce natural cytochrome *c* at physiological rates, while a maquette variant similar in charge to cyt *c* shows a far weaker interaction. The ionic strength dependence of these interactions is shown to be broadly similar to that in natural proteins. This work also presents the first intra-protein redox function in a *de novo* amphiphilic protein and describes progress toward transmembrane electron transfer analogous to that in the cytochrome *bc1* complex. These functional achievements are remarkable given that the proteins are designed from first principles without atomically resolved structures, and they

hold promise for future efforts in applying artificial proteins to new metabolic pathways.

TABLE OF CONTENTS

ACKNOWLEDGEMENTS	III
ABSTRACT	V
LIST OF TABLES	XI
LIST OF FIGURES	XII
CHAPTER 1 INTRODUCTION.....	1
1.1 Biological Electron Transfer	1
1.1.1 Redox Cofactors	2
1.2 Theories of Electron Transfer	4
1.2.1 Marcus Theory	4
1.2.2 Electron tunneling in proteins	6
1.3 Interprotein Electron transfer.....	9
1.3.2 Cytochrome <i>c</i>	12
1.3.3 Interprotein Electron Transfer Experiments	13
1.3.4 Promiscuity in Interprotein Electron Transfer	16
1.4 Approaches to Protein Design	17
1.4.1 Computational Design.....	17
1.4.2 Directed Evolution	19
1.4.3. First Principles Design and the “Maquette Approach”	19
1.5 Dissertation Goals.....	22
1.6 References	23
CHAPTER 2 ELECTRON TRANSFER FROM MAQUETTES TO CYT <i>C</i>	29
2.1 Background and Introduction.....	29
2.2 BT6 and BT6+ Maquettes.....	30
2.3 Methods	32
2.3.1 Protein preparation	32
2.3.2 Degassing and CO binding	33
2.3.3 Stopped-flow ET measurements without CO photolysis	33
2.3.4 CO Photolysis-induced ET experiments	34
2.3.5 Kinetics computations for high-salt photolysis: 110 mM NaCl / 50 mM Na ₂ HPO ₄	35
2.3.6 Kinetics computations for low-salt photolysis: 11 mM NaCl / 5 mM Na ₂ HPO ₄	35

2.3.7 Protein Surface Charge Estimates, Visualization, and ET rate predictions	36
2.4 Results.....	36
2.4.1 Stopped-flow interprotein electron transfer	36
2.4.2 BT6 CO flash photolysis	38
2.4.3 Photolysis-induced inter-protein electron transfer	39
2.4.4. Concentration dependence of ET rates	41
2.4.5 Ionic strength dependence of inter-protein electron transfer	43
2.5 Discussion	45
2.6 References	49
CHAPTER 3 PHOTOLYSIS-INDUCED ELECTRON TRANSFER APPARATUS....	52
3.1 Background	52
3.2 Spectrometer Modifications	53
3.3 Post-Processing Script.....	55
3.4 Validating laser artifact removal	56
3.5 References	58
CHAPTER 4 INTERPROTEIN ELECTRON-TRANSFER WITH PHOTOACTIVATABLE MAQUETTES	59
4.1 Introduction: Motivation and Experimental Considerations.....	59
4.1.1 Zinc Porphyrin and Photoactivated ET	59
4.2 Protein Design, Expression and Purification	62
4.2.1 Design	62
4.2.2 Protein Expression, purification, and solubilization	64
4.3 Biophysical characterization	65
4.3.1 MALDI-TOF	65
4.3.2 Circular dichroism.....	66
4.3.3 Porphyrin binding	66
4.4 Methods: ET Experiments and Analysis.....	68
4.4.1 Transient Absorption Spectroscopy	68
4.4.2 Stretched Exponential Fits	69
4.4.3 Singular Value Decomposition and Kinetics Model Fitting	70
4.4.4 SVD with Log-Normal Reaction Rate Distributions	73
4.5 Electron Transfer Results.....	76
4.5.1 GL-H96 photoreduces cyt <i>c</i>	76
4.5.3 Comparing cyt <i>c</i> photoreduction from among maquette designs	79
4.5.4 Ionic strength dependence of cyt <i>c</i> photoreduction	82

4.5.5 Cyt <i>c</i> photo-oxidation.....	82
4.6 Discussion	85
4.7 Conclusions	89
4.8 References	90
CHAPTER 5 AMPHIPHILIC MAQUETTES DESIGNED FOR TRANSMEMBRANE ELECTRON TRANSFER	92
5.1 Introduction: Cytochrome <i>b</i> and Amphiphilic Maquettes	92
5.2 AP6 Maquette	95
5.2.1 Design, synthesis, and liposome assembly of AP6	95
5.2.2 Biophysical Characterization of AP6	96
5.2.3 Developing an AP6 Proteoliposome System for Transmembrane ET	96
5.2.4 AP6 Transmembrane Electron-Transfer Results	99
5.3 AM1 Maquette	101
5.3.1 Design of Amphiphilic Monomer Maquette AM1	101
5.3.2 Expression, Purification and TEV Cleavage of AM1	102
5.3.3 AM1 Solubilization, Detergent Exchange, and Vesicle Incorporation	102
5.3.4 Biophysical Characterization of AM1	103
5.3.5 Light-Activated Intraprotein ET in AM1	105
5.3.6 Transmembrane ET with AM1	106
5.4 Discussion: Modeling Electron transfer with AP6 and AM1	108
5.5 Design of Next-Generation Amphiphilic Maquettes	111
5.5.1 Design of AM2 Lipophilic Region	113
5.5.2 Design of AM2 Aqueous Region and Loops	116
5.5.3 Moser-Dutton Simulation for Transmembrane ET in AM2	118
5.6 References	120
CHAPTER 6 CONCLUSIONS	124
6.1 References	128
APPENDIX A1 SUPPLEMENTARY EXPERIMENTAL METHODS.....	129
A1.1 O₂ Removal in Stopped-Flow Apparatus	129
A1.2 Circular Dichroism Spectroscopy	130
A1.3 Porphyrin Binding Titrations.....	130
A1.3.1 Binding titrations for soluble maquettes	130
A1.3.2 Binding titrations for amphiphilic maquettes.....	131

A1.4 Redox Potentiometry	131
A1.5 Preparing oxidized or reduced cyt <i>c</i>	132
A1.6 Calibrating Co²⁺ Quenching of Calcein Fluorescence.....	133
A1.7 Transmembrane ET Experiments with AP6 Proteoliposomes.....	133
A1.8 Expression and Purification of AM1	135
A1.8.1 AM1 Expression.....	135
A1.8.2 AM1 Inclusion Body Isolation and Ni-NTA Purification.....	136
A1.8.3 AM1 SDS Solubilization, DDM Exchange, and Liposome Incorporation	138
A1.8 References.....	139
 APPENDIX A2 BIOPHYSICAL CHARACTERIZATION OF AMPHIPHILIC MAQUETTES	 140
A2.1 References.....	142

List of Tables

CHAPTER 3

Table 3.1 OLIS spectrometer configurations	59
--	----

CHAPTER 4

Table 4.1 Porphyrin binding constants	71
Table 4.2 SVD algorithm test results	77
Table 4.3 SVD algorithm test results with distributed rates	80
Table 4.4 Maquette dipole estimates.....	89

CHAPTER 5

Table 5.1 Previous amphiphilic maquette designs	98
Table 5.2 Heme binding in AP6.....	100
Table 5.3 Dynamic light scattering with AP6 proteoliposomes	102
Table 5.4 Cofacotr binding in AM1	107
Table 5.5 Computed half-times for transmembrane ET in AP6 and AM1	114
Table 5.6 MZH3 and AM2 loop sequences	121

List of Figures

CHAPTER 1

Figure 1.1 Protein complexes in electron transport chains	3
Figure 1.2 Porphyrin structures.....	5
Figure 1.3 Marcus energy curves.....	7
Figure 1.4 Electron tunneling pathways	9
Figure 1.5 Moser-Dutton analysis of ET experiments.....	11
Figure 1.6 Static and dynamic docking in <i>cyt b</i> and myoglobin.....	17
Figure 1.7 Dynamic encounter complex in <i>cyt f</i> / plastocyanin	18
Figure 1.8 Redundant electron transport network in <i>P. denitrificans</i>	20
Figure 1.9 Topologies and cofactors in protein maquettes	24

CHAPTER 2

Fig 2.1 BT6 topology	34
Figure 2.2 BT6 and BT6+ sequences.....	35
Figure 2.3 BT6 and <i>cyt c</i> spectra	36
Figure 2.4 Modified OLIS spectrometer.....	39
Figure 2.5 Q-band signature of BT6 → <i>cyt c</i> electron transfer	40
Figure 2.6 Kinetics of <i>cyt c</i> reduction by BT6 and BT6+.....	42
Figure 2.7 BT6 CO photolysis spectra.....	43
Figure 2.8 Difference spectra of BT6 → <i>cyt c</i> electron transfer.....	45
Figure 2.9 Concentration dependence of BT6 → <i>cyt c</i> electron transfer.....	46
Figure 2.10 Multi-phasic ET kinetics	47
Figure 2.11 Product inhibition by reduced <i>cyt c</i>	48
Figure 2.12 Ionic strength dependence of BT6 → <i>cyt c</i> electron transfer	49
Figure 2.13 Electron transfer rate surface calculation for BT6.....	51
Figure 2.13 Hypothetical multi- <i>cyt c</i> / maquette complex.....	52

CHAPTER 3

Figure 3.1 OLIS RSM-1000 spectrometer	57
Figure 3.2 Ionic strength dependence of photolysis-induced data.....	58
Figure 3.3 Post-processing flowchart.....	59
Figure 3.4 Flash removal in photolysis-induced electron transfer.....	60
Figure 3.5 Optical filter impact on flash artifact.....	61
Figure 3.6 Validating post-processing with photoisomerization kinetic standard	62

CHAPTER 4

Figure 4.1 Synthetic zinc porphyrin structure and photophysics.....	65
Figure 4.2 Photoactivated interprotein electron transfer schemes	66
Figure 4.3 Photoactivatable maquette designs	67
Figure 4.4 MALDI-TOF results.....	68
Figure 4.5 Circular dichroism spectroscopy	69
Figure 4.6 Porphyrin binding	70
Figure 4.7 Transient absorption apparatus	72

Figure 4.8 SVD validation with discrete rates	76
Figure 4.9 SVD validation with distributed rates	79
Figure 4.10 Triplet quenching in photoactivated maquette	80
Figure 4.11 Transient spectra of reduced cyt <i>c</i> and zinc cation	81
Figure 4.12 Photoreduction rate [cyt <i>c</i>] dependence.....	82
Figure 4.13 Comparing cyt <i>c</i> photoreduction among maquettes	84
Figure 4.14 Ionic strength dependence of triplet quenching.....	85
Figure 4.15 Photooxidation of cyt <i>c</i>	87
Figure 4.16 Ionic strength predictions for interprotein ET	90
Figure 4.17 Maquette geometry and cyt <i>c</i> interaction	91

CHAPTER 5

Figure 5.1 Bovine cytochrome <i>bcl</i> complex	96
Figure 5.2 Sequence and topology of AP6 maquette.....	99
Figure 5.3 Transmembrane ET mediated by heme methyl ester	101
Figure 5.4 AP6 transmembrane system	102
Figure 5.5 Cobalt vesicle leakage assay.....	103
Figure 5.6 AP6 transmembrane ET results	104
Figure 5.7 AM1 sequence and topology	106
Figure 5.8 Intraprotein ET in AM1	108
Figure 5.9 Am1 heme reduction by FMN.....	110
Figure 5.10 AP6 and AM1 Moser-Dutton ET calculations	114
Figure 5.11 MZH3 crystal structure.....	116
Figure 5.12 Cyt <i>b</i> sequence analysis.....	117
Figure 5.13 AM2 lipophilic sequence selection.....	118
Figure 5.14 AM2 hydrophilic design.....	121
Figure 5.15 AM2 sequence and topology	122
Figure 5.16 AM2 Moser-Dutton calculations	123

APPENDIX A1

Figure A1.1 O ₂ removal from stopped flow apparatus	132
Figure A1.2 Calibration of Co ²⁺ vesicle leakage assay.....	136
Figure A1.3 AM1 expression and purification	139

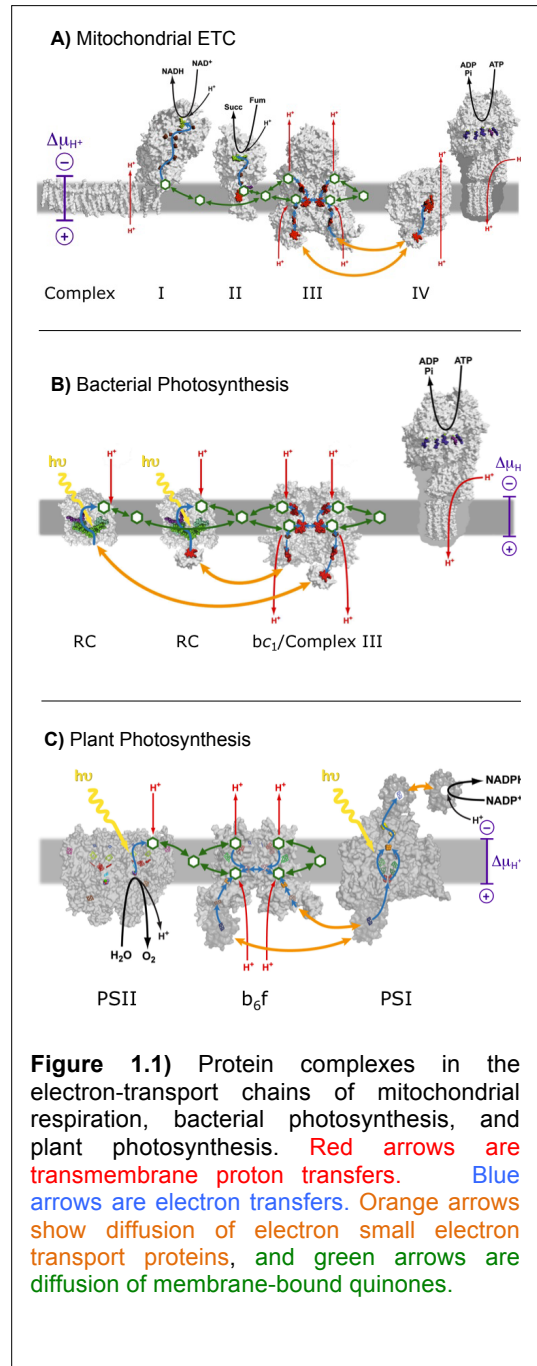
APPENDIX A2

Figure A2.1 AP6 circular dichroism and heme binding	144
Figure A2.2 AM1 MALDI-TOF spectrum	145
Figure A2.3 AM1 porphyrin binding, circular dichroism, and potentiometry	146

Chapter 1 Introduction

1.1 Biological Electron Transfer

Electron transfer (ET) reactions are fundamental to energy metabolism as well as countless other biochemical processes. Conceptually, an electron transfer may be the simplest chemical possible reaction: an electron simply moves between two molecules, or between two moieties in a single molecule. However, Nature has produced very complex molecular structures to direct productive electron transfers, suppress unwanted ones, and to couple ETs to other chemical processes such as making or breaking covalent bonds. **Figure 1.1** shows three basic “electron transport chains” at the root of energy metabolism. In each case an energetically downhill path directs the electrons through several large, membrane-bound protein complexes. Both intra-protein and inter-protein electron transfers are essential to these processes. In respiration (**1.1-A**), the high-energy electrons enter the chain from soluble NADH derived from the breakdown of glucose or other energy-rich nutrients. In photosynthesis (**1.1-B** and **C**) they originate from photo-excited electronic states. In 1961 Peter Mitchell proposed the chemiosmotic hypothesis, stating that the protein complexes couple the energy release of downhill ET to a proton pumping mechanism, storing a portion of the



electronic free energy release as a transmembrane proton gradient [8]. The ET chains of **Figure 1.1** represent a tiny subset of known biological ET processes, and ETs play fundamental roles in many other enzyme systems.

1.1.1 Redox Cofactors

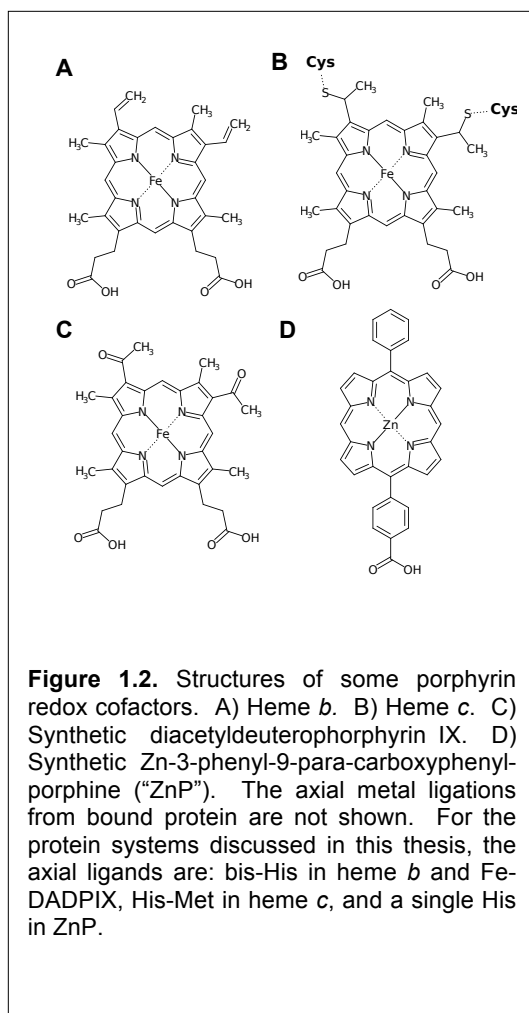
Redox-active “cofactor” groups attached to proteins mediate most biological electron transfers (a smaller number of ETs involve direct oxidation or reduction of protein sidechains). The blue arrows in **Figure 1.1** denote ET between specific cofactors. Nature employs a wide variety of redox cofactors, and all of them are chemically and structurally quite distinct from the amino acid residues comprising the protein. Some, such as quinones, flavins, and pterins, are purely organic groups. Others, such as porphyrins, chlorins, and iron-sulfur clusters, include metal atoms. In some copper proteins the cofactor comprises nothing more than a single metal atom. Transition metals find most of their biological roles in redox cofactors. A range of linkages including covalent side-chain attachment, metal coordination, and hydrogen bonding may attach a cofactor to its protein.

As in redox-active molecules generally, the midpoint potential E_m quantifies the electron affinity of a protein cofactor. Biochemical midpoints are usually expressed in terms of E_{m7} . This is the voltage, relative to a specific hydrogen electrode reference, at which one half the population of a given cofactor will be reduced. An electron transfer from one cofactor to another of higher midpoint potential is exergonic. An electron transfer to a cofactor of lower E_{m7} is endergonic, and physiological uphill ET steps are fairly common.

The ET experiments discussed in this work employ *porphyrin* cofactors as both electron donors and acceptors. The basic porphyrin structure consists of a symmetric, planar, aromatic macrocycle of 20 conjugated carbons and four central nitrogens. The overall structure contains four pyrrole rings and thus is an example of a tetrapyrrole. The nitrogens’ geometry allows them to coordinate a single metal atom at the center of the structure, and both natural and synthetic porphyrins readily accommodate a wide range of transition metals. **Figure 1.2** shows four metal porphyrins employed in this dissertation’s experiments.

Iron porphyrins, or *hemes*, are the most common natural porphyrins. In hemoproteins the iron may exist in the Fe^{2+} , Fe^{3+} , or (transiently) Fe^{4+} oxidation states [11]. The various hemes differ in their arrangement of methyl, vinyl, and other substituents on the macrocycle exterior,

and in C-type hemes these substituents include covalent attachment to the sulfur atoms of cysteine sidechains (**Fig 1.2-B**). In addition to the four nitrogen atoms in the macrocycle, the Fe atom is always bound by one or two additional ligands in protein sidechains: histidine N, cysteine or methionine S, or, less frequently, tyrosine O or lysine N. Pentacoordinate hemes (i.e. only one axial protein ligand) in the Fe^{2+} state may attain hexacoordinate ligation by binding a diatomic gaseous ligand: O_2 , CO , NO . This feature provides the functional basis of the ubiquitous oxygen-transport proteins including hemoglobin and myoglobin. The E_m for the $\text{Fe}^{2+}/\text{Fe}^{3+}$ couple in natural hemoproteins ranges from at least -400 to +400 mV [12]. Many factors influence the heme redox potential including porphyrin substituents, axial ligand identity, solvent exposure, local electrostatic environment, and possibly porphyrin ring distortion [13]. The addition of acetyls or other electron-withdrawing groups in synthetic hemes, for instance,



serves to stabilize the reduced state, raising the redox potential (**Fig. 1.2-C**).

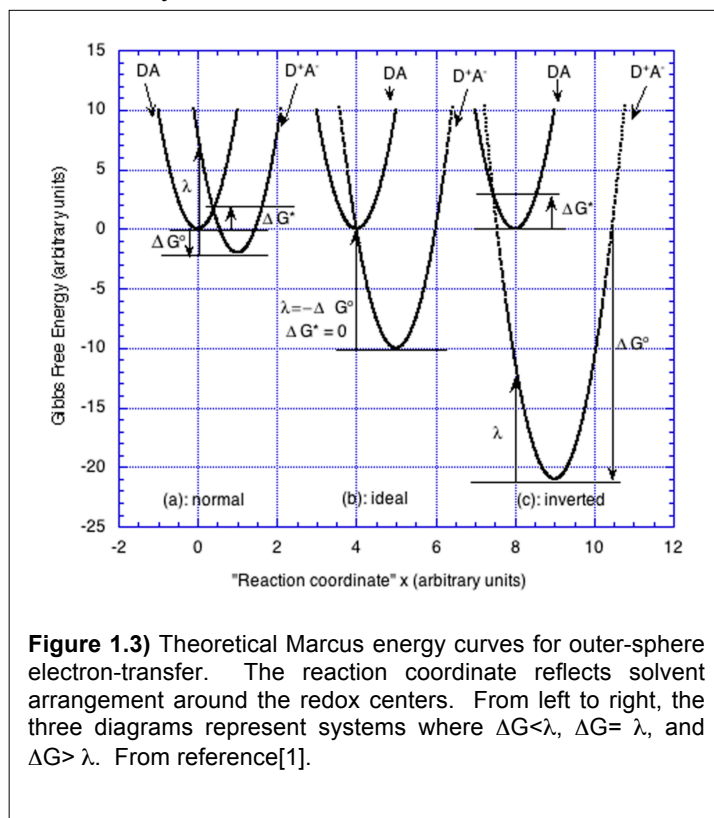
Some metallic and metal-free cofactors are *photoactivatable*, exhibiting long-lived excited electronic states that upon absorbing a photon allow them to donate or abstract an electron from nearby redox partners. Photosynthesis begins with light-induced ET from the magnesium tetrapyrroles chlorophyll or bacteriochlorophyll, and DNA photolyase is driven by a strongly oxidizing photoactivated flavin. Hemes, however, are not photoactivatable. They absorb strongly in the visible spectrum but undergo fast non-radiative decay on a low-ps timescale and so do not exhibit useful photochemistry[14]. However, replacing a tetrapyrrole Fe with Zn yields a photoactivatable group that, like chlorophyll, can reduce many other biological cofactors upon absorbing a photon. **Figure 1.2-D** shows a synthetic zinc porphyrin used for photoactivated electron experiments in **Chapter 4**.

1.2 Theories of Electron Transfer

1.2.1 Marcus Theory

Prior to Marcus, other theoretical approaches had been presented to explain variations in reaction rates, but these did not specifically address electron transfer. Arrhenius introduced the concept of the activation energy, in which a kinetically limited system must obtain some amount thermal energy to overcome an energetic barrier. Eyring and others proposed transition state theory, where reactants were considered to be in dynamic equilibrium with the activated state, and the conversion of that state to the reaction products could be addressed in terms of a molecular vibration[17]. Similarly, Marcus theory assumes the existence of a transition state for ET. Marcus pointed out that in a solvated ET system, the activation energy mainly comes from the repolarization of solvent to accommodate the new charge distribution after the electron moves[15]. This contrasts with the Eyring's description of shorter-range bonded interactions where activation the energy derives from the requirement for reacting nuclei to move to higher energy positions. Viewing the whole arrangement of solvent molecules as a one-dimensional reaction coordinate, Marcus

observed that the energy needed for solvent adjustment after charge transfer between two spheres depends on the square of the charge transfer (as well as on dielectric constants of the solvent). The activation energy is the energy needed to arrange the solvent midway between its optimal configuration for the pre- and post-ET charge distributions. Because the actual electron transfer



is much faster than the solvent motions, the ET must wait until the slow-moving solvent reaches this energetic midpoint; this idea is analogous to the Frank-Condon principle for nuclear vibrations.

Marcus introduced the concept of the “reorganization energy” λ , which is the energy that would be required to completely repolarize the solvent to the post-ET configuration *before* the electron transfer actually happens. The quadratic solvent energy relationships and the reorganization energy are often shown as pairs of intersecting parabolas as in **Figure 1.3**.

If there is no free energy change associated with the electron transfer itself, the activation energy will be $\lambda/4$. In the general case where $\Delta G^0 \neq 0$, the activation energy may be written in terms of the λ and the Gibbs free energy change of ET as:

$$E_{act} = \frac{(\lambda + \Delta G^0)^2}{4\lambda} \quad \text{Eqn. 1.1}$$

The activation energy will be 0, and thus the reaction will proceed at maximal rate, if the ΔG is negative (exergonic) and equal in magnitude to λ . If the ΔG is further decreased to become even more exergonic, Marcus theory actually predicts a drop in the rate; this energy regime is called the “inverted region.” The third parabola pair in **Figure 1.3** illustrates a Marcus-inverted reaction. Physically, this means the solvent rearrangement needed to accommodate ET is so extreme that the reaction is kinetically limited despite being hugely thermodynamically favorable.

The above explanation has been completely classical. However, electron transfer is actually a quantum tunneling process dependent on the overlap of wavefunctions between the donor and acceptor molecules. A semi-classical accommodation of the activation energy in **Eqn. 1.1** gives the following expression for the ET rate:

$$k = \frac{2\pi}{\hbar\sqrt{4\pi\lambda k_B T}} |H_{AB}|^2 \exp\left(-\frac{(\lambda + \Delta G^0)^2}{4\lambda k_B T}\right) \quad \text{Eqn. 1.2}$$

Marcus theory has provided useful descriptions for observed rate trends in many ET systems, including those in the inverted region. The H_{AB} term describes the quantum overlap between donor and acceptor, and is not easy to evaluate, especially in a complex system such as a protein. However, all else being equal, it should show an exponential decay with separation between the donor and acceptor molecules. Thus, assuming constant temperature, free energy change, etc., we may write the distance dependence on the ET rate as:

$$k_{ET} \propto \exp(-\beta R) \quad \text{Eqn. 1.3}$$

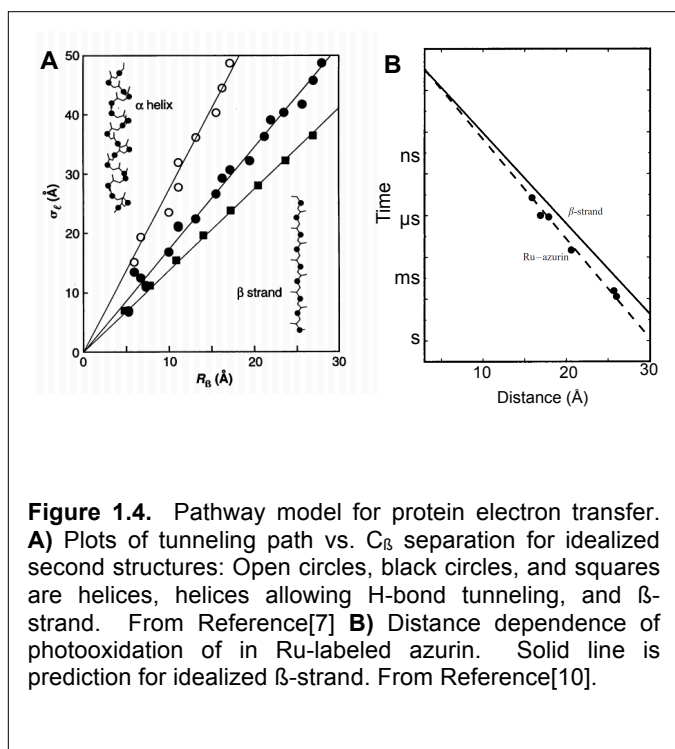
where β describes how quickly the rate falls off with distance. In vacuum, where the electronic coupling is minimal, β lies between 2.8 \AA^{-1} [18] and 3.5 \AA^{-1} [19]. The question of the β -value in proteins is addressed in **Section 1.2.2**.

1.2.2 Electron tunneling in proteins

As the functions of the mitochondrial electron transport complexes emerged, it became clear that electrons were being directed through and between these protein complexes. Chance and Williams suggested that large-scale conformational changes in these proteins brought various cofactors into very close proximity to mediate fast ET [20]. However, early laser-induced ET experiments in bacterial photosynthetic reaction centers by Chance and DeVault in 1967 showed that cytochrome oxidation persisted with a temperature-independent rate below 100 K. This regime was interpreted as quantum tunneling of electrons between redox centers separated by 30 \AA or more[21]. Hopfield later re-analyzed the results of DeVault, incorporating vibronic coupling in the temperature-independent regime. This implied 8-10 \AA tunneling distance, later shown to

be a much more accurate result. [22]

In 1987 Beratan and colleagues proposed that intraprotein ET rates could be predicted by examining the covalent and hydrogen bond networks residing between the cofactors[23]. Essentially, this “pathway model” states that β in **Eqn. 1.3** predictably depends on the features of intervening protein medium. Gray, Beratan, and coworkers tested this model against ET data from a series of Zn-substituted *cyt c* and azurin copper proteins[19],[7] labeled with



ruthenium photo-oxidizing groups covalently attached to several solvent-facing histidine sidechains. The pathways in cyt *c* and azurin are predominantly α -helices and β -strands, respectively, and they show better exponential dependence when plotted against total covalent path distance rather than simple spatial separation of cofactors (**Figure 1.4**). Beratan et. al. later extended this model by employing molecular dynamics simulations to estimate the time-averaged donor-acceptor quantum coupling on a range of new and previously studied Ru-labeled proteins. This work concluded that occasional outliers in the Ru-labeled ET studies could be reconciled by distinguishing between proteins where one ET path was dominant and other proteins that offered multiple competing pathways[24].

Dutton, Moser, and coworkers have proposed an alternative model to explain observed ET rates in proteins, concluding that a simple β value of 1.4 \AA^{-1} is generally appropriate [18, 25]. The empirical “Moser-Dutton Ruler” for exergonic ET is [26]:

$$\log_{10} k_{ET} = 13.0 - (1.2 - 0.8\rho)(R - 3.6) - 3.1 \frac{(\Delta G + \lambda)^2}{\lambda} \quad \text{Eqn. 1.4}$$

Here R is the cofactor separation in \AA and ρ is the “packing fraction”, indicating the fraction of the volume between the cofactors that lies within the Van der Waals radii of the intervening atoms. A PDB survey showed an average packing fraction of ~ 0.75 between cofactors, with no difference in the value between physiological and deleterious “off-pathway” ETs. Fixing $\rho = 0.75$ yields the β value of 1.4 \AA^{-1} , simplifying the expression to:

$$\log_{10} k_{ET} = 13.0 - 0.6(R - 3.6) - 3.1 \frac{(\Delta G + \lambda)^2}{\lambda} \quad \text{Eqn. 1.5}$$

Dutton et. al. pointed out that individual *endergonic* steps are common in multi-cofactor oxidoreductases, and slight modification to **Eqn. 1.5** (not shown) accounts for a Boltzmann activation term in the endergonic case [26, 27]. **Figure 1.5** compares the observed and predicted rates for a variety of electron transfers in natural and Ru-modified systems. Calculated rates are shown both using **Eqn 1.4** with ρ measured from crystal structures as well as fixing ρ at 0.75 (this is equivalent to using **Eqn 1.5**). Overall both models appear to agree equally well with the experimental results, suggesting the simpler expression can be employed without loss of systematic loss of accuracy.

The Gray-Beratan pathway model and the Moser-Dutton approach both predict the typically exponential fall-off in ET rates with cofactor separation. The pathway model appears to better distinguish between secondary structures in some specific Ru-modified proteins. The Moser-Dutton ruler is based on a larger dataset including unmodified reaction centers, and thus may better reflect the overall population of natural proteins. The two approaches differ in their implications for how natural selection impacts ET rates. The pathway model implies that the protein medium evolves to modulate ET rates (while of course also acknowledging the major

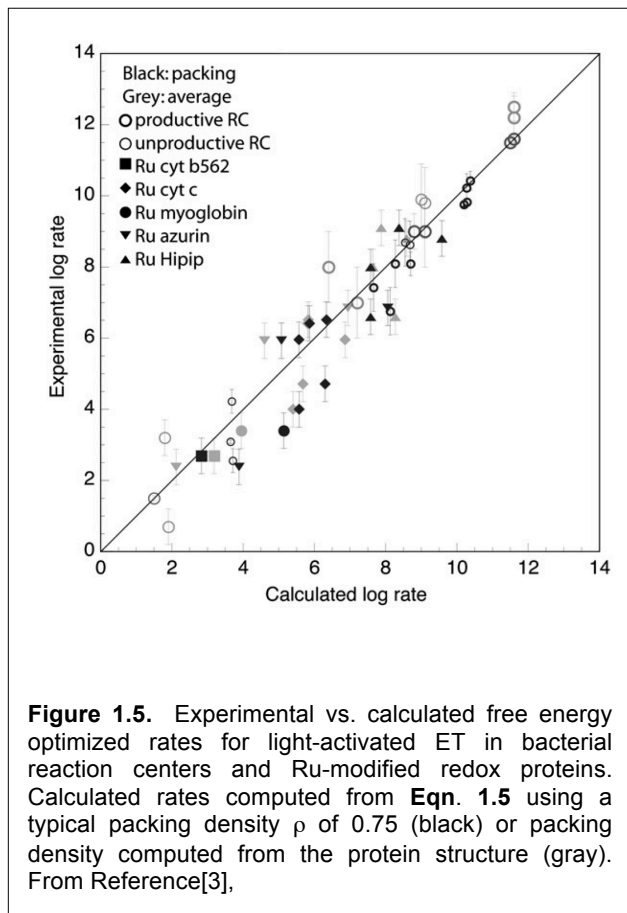


Figure 1.5. Experimental vs. calculated free energy optimized rates for light-activated ET in bacterial reaction centers and Ru-modified redox proteins. Calculated rates computed from **Eqn. 1.5** using a typical packing density ρ of 0.75 (black) or packing density computed from the protein structure (gray). From Reference[3].

roles of driving force, reorganization energy, and especially cofactor separation). In contrast, the Dutton view states that the protein medium is not selected to optimize ET, noting that there seems to be no difference in atomic packing between correct and competing deleterious pathways. Furthermore, the Dutton approach claims that adding details of the protein medium to the list of already-available engineering parameters for ET could actually harm the organism by making oxidoreductases less robust to mutation. [3, 26].

Eqn. 1.5 is used to estimate some electron transfer rates in this dissertation. All of these ETs are discussed in the absence of precise structural data, resulting in significant uncertainties in cofactor separation. It is likely that the rate differences arising from a few Å error in cofactor separation outweigh the differences between the pathway and Moser-Dutton calculations.

1.3 Interprotein Electron transfer

The theoretical ET descriptions presented above do not explicitly distinguish between ET among cofactors in a single protein (*intra*-protein ET) and ET between two distinct redox-active protein molecules (*inter*-protein ET). Interprotein ET is extremely common and is metabolically essential in all organisms. The three electron transport chains in **Figure 1.1** each involve at least one small single-cofactor protein that ferries electrons between larger complexes: cytochrome *c* in respiration, cytochrome *c*₂ in bacterial photosynthesis, and plastocyanin and ferredoxin in plant photosynthesis.

Gray and coworkers co-crystallized natural cytochrome *c* with a photo-activatable zinc-substituted variant and measured photo-induced ET between the two proteins[28]. Importantly, they concluded that the interprotein ET proceeds similarly to ET between cofactors in a single protein, and that the pathway model could be extended to hydrogen-bonded waters at the protein interfaces. This provides strong evidence that whether one chooses to view ET in terms of explicit pathways or the less specific approach of Moser-Dutton, the general principles of ET within a protein can be extended to interprotein ET across a firmly anchored crystal interface. However, physiological interprotein electron transfer is of course complicated by questions of diffusion and protein-protein interaction that do not apply to single-protein systems.

Section 1.3.1 introduces some theoretical descriptions of interprotein ET rates in solution, focusing on the impact of ionic strength. **1.3.2** introduces the well-studied cytochrome *c*, an electron transport protein that has served as a model in understanding interprotein ET and has also been used extensively in the experiments described in this dissertation. **1.3.3** gives a brief overview of some significant experimental studies on interprotein ET.

1.3.1 Theories of Interprotein Electron transfer

Many years of experimental evidence show the importance of electrostatic interactions in interprotein ET. In 1923 Debye and Hückel showed how the interaction of ions in solution leads to an *activity* or “effective concentration” of the ions that differs from the actual concentration[29]. This relation was later combined with the a description of how activities impact the second-order reaction rates between ions, yielding the Brønsted-Debye-Hückel equation:

$$\ln k_I = \ln k_0 - \frac{e^2 \kappa}{8\pi\epsilon k_B T} \left(\frac{z_A^2}{1 + \kappa R_A} + \frac{z_B^2}{1 + \kappa R_B} - \frac{(z_A + z_B)^2}{1 + \kappa R_{AB^*}} \right)$$

where

$$\kappa = \sqrt{\frac{e^2}{\epsilon k_B T} \sum_i n_i z_i^2}$$

Eqn. 1.6

Here k_I and $k_{I=0}$ are bimolecular reaction rates at a given ionic strength I and at 0 ionic strength. z_A and z_B are the integer charges of the two ions, and R_A , R_B , and R_{AB^*} are the radii of the individual ions and their complex. The term κ has units of inverse length, and κ^{-1} is referred to as the “Debye length”. At distance scales beyond the Debye length, an ion is mostly shielded from electrostatic interactions due to its local “cloud” of charges.

In 1976 Wherland and Gray [30] proposed a similar relation that modifies the solvent activation energy of Marcus theory by including a term for the electrostatic work required to bring the reactants together.

$$\ln k_I = \ln k_\infty - 3.576 \left(\frac{\exp(-\kappa R_A)}{1 + \kappa R_B} + \frac{\exp(-\kappa R_B)}{1 + \kappa R_A} \right) \left(\frac{Z_A Z_B}{R_A + R_B} \right)$$

Eqn. 1.7

k_∞ denotes a limiting rate at infinite ionic strength. The authors first applied this expression to ET reactions between cytochrome *c* and several small-molecule reactants. However, Millet et. al. found this model less amenable to describe interprotein ET between cytochrome *c* and cytochrome *b5*[31]. **Eqns. 1.6** and **1.7** treat the reactants as featureless charged spheres, and this major simplifying assumption is likely not generally valid for proteins with dipole moments and other specific charge features. Koppenol and van Leeuwen proposed modified Brønsted-Debye-Hückel solutions accounting for the dipole moments of the individual proteins and the reaction complex, providing a better fit to the cyt *b5* / cyt *c* data of Millet. [32, 33]. Van Leeuwen models two spherical, dipolar proteins that diffuse together to form a complex and “rotate” about one another until they either diffuse apart or align such that a productive ET occurs. In the limit that

the complex will usually dissociate without performing an ET, the ionic strength dependence of this model is:

$$\ln k_l = \ln k_\infty - \left(z_A z_B + [ZP](1 + \kappa R) + [PP](1 + \kappa R)^2 \right) \frac{e^2}{4\pi\epsilon k_B TR} f(\kappa)$$

where:

$$[ZP] = \frac{(z_A P_B \cos\theta_B + z_B P_A \cos\theta_A)}{eR}$$

$$[PP] = \frac{(P_A P_B \cos\theta_A \cos\theta_B)}{(eR)^2}$$

$$f(\kappa) = \frac{(1 - \exp(-2\kappa R_B))}{2\kappa R_B (1 + \kappa R_A)}$$

Eqn. 1.8

Here $R = (R_A + R_B)$ and P_A and P_B are the protein dipole moments. The θ terms represent the alignment between the dipole moment and the protein active site. If the dipole moment is perfectly aligned with the active site to promote docking for productive ET, then $P * \cos\theta = 1$. Some interprotein ET reactions in this dissertation are analyzed against to this model.

Finally, the computational technique known as Brownian dynamics (BD) has been employed to the model interprotein ET processes. In a BD simulation, proteins are modeled as rigid bodies, typically based on known structures, with non-uniform surface charges in a continuum solvent. Sharp and coworkers simulated the diffusion-limited catalysis of superoxide dismutase, showing that the protein's quadrupole field is essential for guiding the substrate to the active site and producing its extremely fast k_{cat} [34]. Shortly thereafter Northrup et. al. reported BD simulations of interprotein ET from cytochrome c to cytochrome c peroxidase[35]. The trajectories showed a range of non-specific, electrostatically-guided conformations capable of ET, paralleling Ubbink's experimental encounter complex observations in a range of electron transport proteins (see **Section 1.3.3**). BD is well-suited to interprotein ET studies because ET can occur over relatively long distances and often does not the require precise spatial alignments that could only be modeled by more detailed, computationally intensive techniques. BD has since been applied to many other interprotein ET systems[5, 36, 37].

1.3.2 Cytochrome *c*

The cytochromes *c* are a well-studied family of small electron transport proteins. Keilin coined the term “cytochrome” to describe the variety of colorful heme-containing proteins, classifying them according to their spectral features[38]. The distinguishing chemical feature of the *c*-type cytochromes was later found to be the presence of covalent thioester bonds between heme vinyl groups and cysteine sulfhydryls. The diverse members of the cytochrome *c* family perform a variety of physiological electron transfers. The specific *c*-cytochrome (hereafter denoted “cyt *c*”) employed in this dissertation’s experiments is the bovine mitochondrial protein responsible for shuttling electrons between electron transfer complexes III (cytochrome *bc1*) and IV (cytochrome *c* oxidase). This 12.3 kDa protein contains a single heme with two cysteine thioester linkages, along with axial Fe ligations from histidine and methionine residues. Independent of the broad literature examining its redox function, cyt *c* has served as an important model in protein genetic[39] and folding[40] studies.

A distinct cleft, surrounded by several surface lysines, sequesters the cyt *c* heme from solvent. The protein has a substantial surface charge of about +7 units at physiological pH. The relatively tight distribution of this charge produces a notable ~320 debye dipole moment, well conserved across vertebrate and invertebrate species [41]. ET studies with cyt *c*’s physiological ET partners indicate that electrostatics play an important role in its interactions, as is typical of small electron transport proteins. For instance, the region surrounding the cyt *c* docking site on Complex III is rich in Glu and Asp residues, complementary to the positive heme patch in cyt *c*. Single point mutations to many (but not all) of these acidic residues in Complex III result in large drops in ET rate[42]. Similarly, a group of acidic residues on the Complex IV binding site provides electrostatic guidance to the specific docking site[43]. The *in vitro* single-ET reaction rates between cyt *c* and both respiratory complexes increase as ionic strength falls, reinforcing the importance of electrostatics in guiding these reactions. Interestingly, the cyclic ET turnover rate between cyt *c* and cyt *c* oxidase shows a maximum around 80 mM ionic strength and then actually *falls* as ionic strength is dropped below this point despite faster rate for a single ET; this is due to the fact that the complex becomes “sticky” with decreasing salt so cyclic turnover is limited by cyt *c* dissociation rather than by initial association and ET. [44].

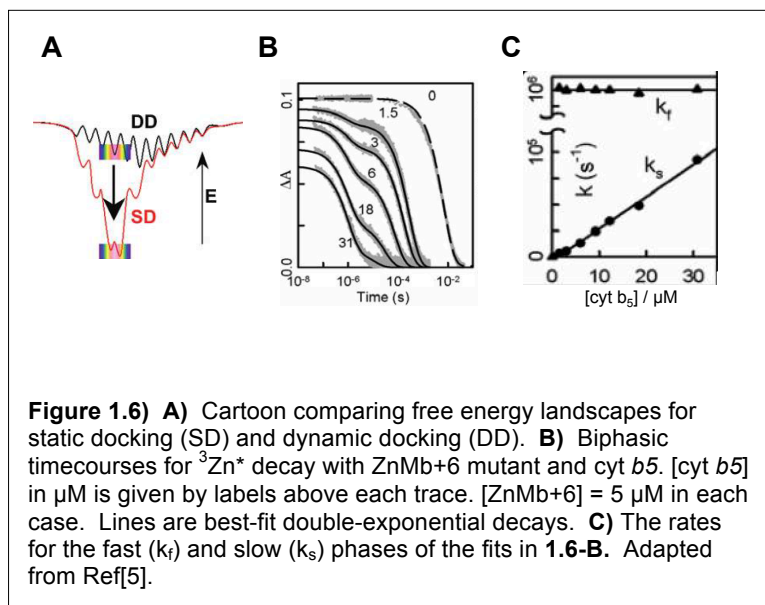
Physiological ET reactions involving mitochondrial cyt *c* extend beyond the protein complexes of the ETC. In yeast, cyt *c* supports peroxide reduction by providing electrons to cytochrome *c* peroxidase. Cyt *c* release from the mitochondria appears to regulate apoptosis, and this pro-apoptotic feature may be modulated by redox interactions with the cytosolic heme protein neuroglobin[45]. Other partners include sulfite oxidase, the sulfhydryl oxidase Erv1, and possibly cyt *b5* [46]. In addition to this notable *in vivo* flexibility and promiscuity, multiple studies have shown that the cyt *c* from one species may be swapped for another while maintaining efficient *in vitro* ET with the original redox partner. Margoliash and Ferguson-Miller showed that bovine complex IV interacts with cyt *c* from horse, *S. cerevisiae*, and *Euglena*, and that at low concentrations their ET kinetics correspond to their binding constants[47]. Likewise, Moser compared the photooxidation of *R. sphaeroides* cyt *c2* and horse cyt *c* by the photosynthetic reaction center of *R. sphaeroides*. The horse cyt *c* was found to bind roughly 4 times more tightly and showed correspondingly faster ET rates[48].

1.3.3 Interprotein Electron Transfer Experiments

This section describes a few specific studies in the board literature examining the kinetics and protein interactions in several interprotein ET systems.

Several basic studies of interprotein ET involve the soluble electron transporter cytochrome *b5*. Cyt *b5* is a small, single bis-His heme protein with a number of physiological roles, including the re-reduction of oxidized globins and the oxidation of some cytochromes P450[49]. Overall cyt *b5* is an acidic protein with a net charge of about -6 at neutral pH. In 1979 Millet and coworkers gave a detailed report of the (possibly non-physiological) electron transfer from cyt *b5* to cyt *c* [46]. Their experiments focused on the ionic strength dependence of this interaction. The reaction remained clearly second order over ionic strengths ranging from 40 mM to 1.6 M. The authors compared their results to the rate predictions of Wherland and Gray (Eqn. 1.7) and found a poor match given the known radii and charges of the reactants. The experimental results fit better using an unrealistic protein complex radius of 2 Å; the authors interpreted this to mean that individual, specific short-range electrostatic effects were more significant in driving the reaction rate than longer-range forces. However, the later theory of van Leeuwen (Eqn. 1.8) highlighting the impact of protein dipoles provided a better fit the these experiments [33].

Hoffman, Beratan, and coworkers carefully examined the role of individual charges in the interaction between the physiological redox partners *cyt b5* and myoglobin. These studies employ zinc-substituted myoglobin that reduces *cyt b5* upon photoexcitation. (The physiological ET proceeds in the opposite direction, but this discrepancy should have little impact on the protein-protein interaction). Initial experiments showed a weak ~ 1 mM K_d binding between *cyt b5* and myoglobin at 18 mM ionic strength, and BD simulations indicated interaction over a large portion of the protein area with little specific binding[50]. Changing the acidic propionates of the Zn-myoglobin to neutral hydrophobic ester or hydrophilic amide groups yielded a ~ 100 -fold increase in the bimolecular rate constant despite showing little change in the binding energy[36]. Similarly, increasing the myoglobin surface charge through mutations near its heme site led to further increases in the rate constant (1.2×10^9 M⁻¹s⁻¹ in one instance), while still maintaining clear second-order behavior and weak binding[37].



Further BD-guided mutations produced a myoglobin mutant where three acidic residues were replaced by lysines for a net charge change of +6. This protein showed a markedly different kinetic behavior: a fast 1st-order component independent of [*cyt b5*] along with a slower [*cyt b5*]-dependent phase[5].

The authors concluded that

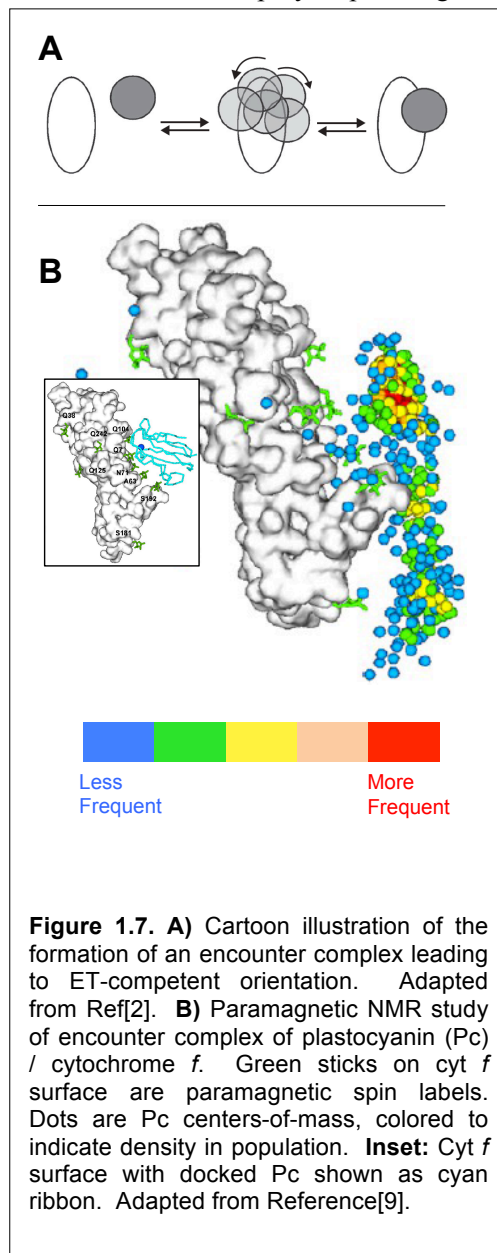
a “pre-bound” population of myoglobin quickly reduces bound *cyt b5* after excitation, while a separate unbound population must diffuse to find reducible *cyt b5*. Moser observed similar biphasic ET, dependent on ionic strength and viscosity, with photosynthetic reaction centers and *cyt c* [48]. **Figure 1.6** shows biphasic myoglobin / *cyt b* results, along with a cartoon comparing the binding energy landscapes for the dynamic and statically docked systems. All of the kinetics measurements until this point had been obtained by measuring the quenching of the Zn triplet excited state. When the same myoglobin +6 / *cyt b5* system was examined on a faster

spectrometer, an additional 400 ps interprotein ET from the Zn *singlet* state was observed, followed by a 23 ps recombination. This is the fastest interprotein ET process reported to date[51].

The Ubbink lab has employed other techniques to examine several interprotein ET interactions. Rather than measuring ET kinetics, Ubbink et. al. have employed paramagnetic NMR to visualize the interaction surfaces of proteins reactants. One partner undergoes several cysteine mutations to attach paramagnetic spin labels at specific surface positions. NMR then measures how each spin label on the first partner impacts the relaxation of nuclei on the second protein. Combining results for the various labeled mutants produces a spatial map over the first partner's surface, estimating how much time second partner spends at each location. **Figure 1.7** shows a result for the small electron transporter plastocyanin with its detergent-solubilized ET partner cytochrome *f* of the *b6f* photosynthetic complex[9]. Although the plastocyanin is most often found at the red and orange locations where it can engage in ET with cyt *f*, it also spends considerable time in other locations, still under the electrostatic influence of cyt *f*.

Paramagnetic NMR experiments show that the time fraction spent in a dynamic encounter complex, as opposed to a specific ET-competent orientation, varies greatly among different redox pairs. In the cyt *f* / plastocyanin system, this value proved difficult to quantify precisely but shows a large variations among plant and cyanobacterial species[52]. In the cytochrome *c* peroxidase / cyt *c*

system, cyt *c* spends 30% of its time in a non-specific encounter complex [53]. However, a single Arg → Ala point mutation in cyt *c* raises the encounter complex fraction to 80%[54]. The



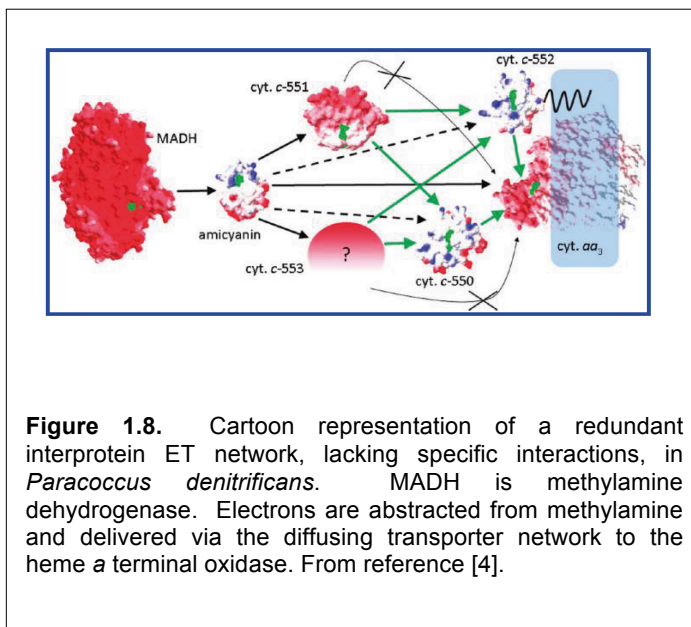
complex between cyt *c* and the small FeS electron transporter adrenodoxin was shown to be 100% dynamic[55]. Cyt *c* and adrenodoxin probably do not interact *in vivo*. However, the physiological couple cyt *b5* and myoglobin, discussed earlier, also seems to lack any specific ET-competent conformation and can be viewed as a “100% encounter complex” [52].

1.3.4 Promiscuity in Interprotein Electron Transfer

These non-specific, largely electrostatic protein-protein interactions are particularly suited to ET processes. If the interprotein ET processes of cyt *c*, plastocyanin, or ferredoxin are insufficiently fast, they will introduce disastrous bottlenecks in the basic electron transport chains of respiration and photosynthesis. In order to maintain acceptable turnover, these transporters must exhibit both fast association (k_a) and dissociation (k_d) from their partners. k_d can be maximized by limiting the number of specific protein contacts in favor of longer-range, less specific electrostatics. As noted previously, some interprotein electron transfers can proceed from a fairly wide range of orientations, a luxury unavailable to enzymes catalyzing covalent chemistry[2, 52].

In addition to promoting agile redox complexes that associate and separate quickly to maximize turnover rates, non-specific electrostatic interaction encourages promiscuity in some electron transport systems. Mammalian cytochrome *b5*, for instance, interacts physiologically with (at least) cyt *b5* reductase, hemoglobin, myoglobin, several cytochromes P450, and several anabolic and catabolic lipid

enzymes[49]. An intriguing example of electron transporter promiscuity is seen in the energy metabolism of the soil bacterium *Paracoccus denitrificans*. This organism can subsist solely by extracting electrons from methylamine (via methylamine dehydrogenase) and transporting them



to a membrane-bound oxidase to ultimately reduce O₂. Ubbink and coworkers showed that *P. denitrificans* uses an overlapping, redundant network of periplasmic cytochromes and copper proteins to shuttle electrons between the dehydrogenase and oxidase[4]. **Figure 1.8** illustrates this network. The authors point out that this diffusing pool of promiscuous transporters may allow the organism to “link in” new catabolic enzymes that it acquires through gene transfer. This built-in robustness could support metabolic flexibility in response to environmental changes impacting available nutrients.

1.4 Approaches to Protein Design

The broad field of protein design tackles the problem of producing unnatural proteins for particular structural and functional goals. Some studies take the approach of *de novo* design, in which the whole sequence is created with minimal direct reference natural examples. More often, researchers make specific, targeted changes in existing proteins without attempting to alter overall structure. By this definition, the medically important field of antibody engineering would be considered an example of non-*de novo* protein design. This section briefly discusses methods that have been employed in protein engineering and places the work of the Dutton and Disher labs in the context of these studies. Importantly, some of the most impactful designs have been the result of combining complimentary approaches.

1.4.1 Computational Design

Computational approaches begin with a desired structure and then employ an iterative algorithm to find a sequence most likely to take on that particular structure. This very complex problem may be viewed as the inverse of the protein folding question (i.e. what is structure for a known sequence?) [56] Problems that have been successfully tackled by computation design include building antibodies to target specific epitopes, creating an unnatural protein fold[57], and producing an enzymes to catalyze a non-biological reactions[58, 59].

Baker and co-workers pioneered the popular structural prediction tool Rosetta[60]. Rosetta works by first dividing a given sequence (of unknown structure) into small fragments several residues in length. It then scans the Protein Data Bank, looking for proteins of known

structure that contain similar sequence fragments. These small structured matches are combined to produce rough structural predictions for the given sequence. These structures are then optimized against an empirical scoring function accounting for physical factors like hydrogen bonding and hydrophobic burial. It is not obvious that purely local sequence patterns might provide a good starting point for structure prediction. β -strands, for example, depend on hydrogen bonding to residues that may be distant in sequence order. Baker came to this local-sequence prediction scheme through an emerging kinetic picture that the initial folding steps were often driven mainly by local sequence patterns rather than by interactions with distant residues[61]. The Rosetta concept was expanded to support protein design by automating the fold-prediction to search for sequences most likely to match a given structural target. Rosetta-Design has produced a number of remarkable *de novo* proteins. The first of these was a specific fold comprising α -helices and β -strands not seen in Nature[57]. The Baker group also used Rosetta to design new enzymes catalyzing Kemp elimination the retro-aldol condensation, both non-biological reactions. [58, 59]. The enzymes were produced through the computational selection of residues to build a pocket stabilizing the reactants' putative transition states.

Saven, DeGrado, and colleagues have pointed out that even if a particular sequence represents an energy minimum for a target structure, the converse need not always be true. Thus, one could imagine the situation where a designed protein readily folds to the target structure, but only as an intermediate on the way to its more stable final conformation. "Negative design" aims to avoid this outcome. This scheme looks for a variety of sequences, each with the possibility to fold to the target structure even if it is not lowest-possible energy for that fold. The design algorithm reports statistical possibilities for residues at each position, rather than a single sequence corresponding to a calculated minimum energy[62]. This approach has produced a wide variety of oligomeric and monomeric 4- α -helical bundle proteins binding a variety of cofactors including di-iron centers[63], synthetic porphyrins[64-66], Iron-sulfur clusters[67], and hemes in water-soluble[68] or membrane-bound[69] scaffolds. Recent efforts based on this approach have yielded a specific transmembrane Zn^{2+} ion transporter[70] and a di-iron bundle stabilizing a semiquinone radical [71].

1.4.2 Directed Evolution

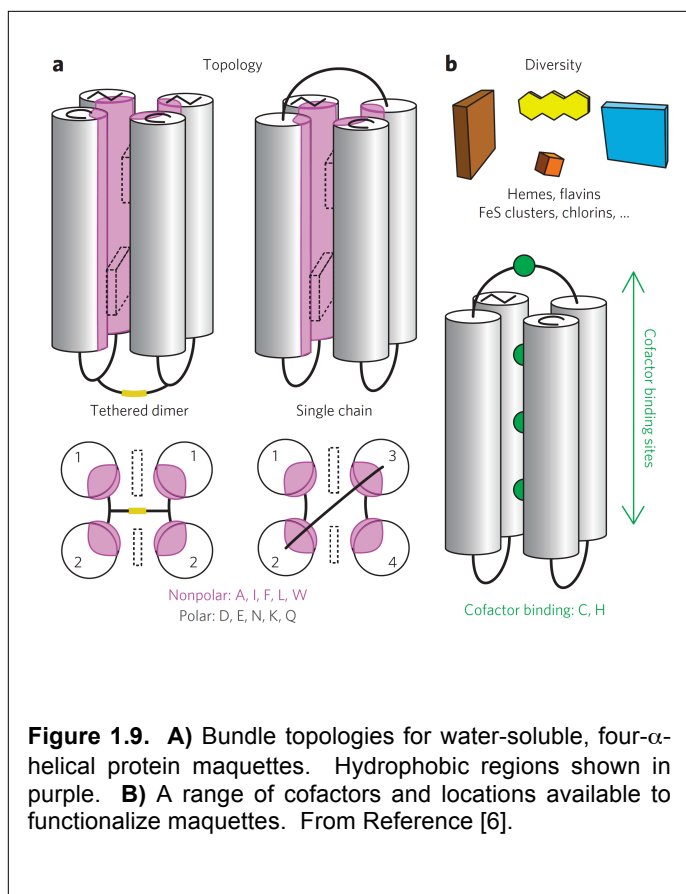
Natural evolution results from random genetic drift in combination with selective environmental pressures. Broadly speaking, directed evolution replaces natural selective pressures with human-imposed ones, aimed toward producing an organism, pathway, or single protein to meet some desired application. The earliest examples are the selection of desirable traits in crops and livestock[72]. In protein engineering, gene libraries containing a variety of mutants for a particular protein are most often produced *in vitro*, often using error-prone PCR. Libraries may be designed to allow randomization at only specific points in the protein sequence, such as a known enzymatic active site or a protein-protein interface. The expression of many protein mutants is then combined with an appropriate assay to screen for the desired function. Fluorescence assays, for instance, are commonly used because they can be easily automated to maximize throughput [72].

Directed evolution has produced impressive functional changes in both natural and *de novo* proteins. Arnold and coworkers evolved a new cytochrome P450 enzyme to perform an unnatural cyclopropanation reaction in lieu of its biological monooxygenase function[73]. The Hecht group produced a library of 4-helical bundle proteins that binds heme *in vivo* and exhibits peroxidase function *in vitro* [74]. In another study, Hecht et. al. showed that evolved, unnatural helical bundle proteins could restore viability in *E. coli* knockouts that otherwise could not survive on minimal media[75]. Intriguingly, these rescue proteins functioned not through directly replacing the function of the gene knockout proteins but rather by modulating the expression of other compensatory genes[76]. Finally, directed evolution has proven to be an excellent complement to other protein design approaches. For instance, focused sequence randomization of Baker's computationally-designed retro-aldase yielded a 4400x improvement in catalytic performance[77].

1.4.3. First Principles Design and the “Maquette Approach”

Sophisticated computational methods and/or intensive screening of many evolved mutants have produced remarkable protein designs, as discussed above. However, other notable functional results have emerged by designing or changing sequences based simply on a high-level

understanding of the properties of the proteinogenic amino acids. This method may be called “first principles design”, referring to first principles not in terms of fundamental physics but rather to biochemical intuition about how amino acid selection drives structure and other properties. Some examples of focused, intuitive sequence updates have yielded remarkable functional changes to natural proteins. One study modified the homodimeric membrane helix glyophorin-A to accommodate a heme cofactor[78]. Aside from adding an iron-ligating histidine, four mutations were added to reduce steric clash with the porphyrin and to electrostatically stabilize its propionates. An additional point mutation produced tighter binding and a -50 mV change in the heme E_m [79]. In another study, a single point mutation conferred Kemp eliminase activity in natural calmodulin. The simple scheme to insert a dehydrated acidic residue in an



already-present dry invagination was based purely on chemical understanding, with only minimal computation directing its placement[80].

In addition to altering natural protein function, first principles design has created completely *de novo* proteins. Most of these have been helical bundle structures. α -helices are particularly amenable to this approach because, unlike some other secondary structures, they hydrogen-bond only with close neighbors in the sequence. These designs employ “binary patterning” in which polar/charged and hydrophobic residues are

systematically alternated to produce distinct inward-facing and solvent-exposed helical faces. Burial of the greasy faces produces a stable structure, as shown in **Figure 1.9-A**. In 1988 Regan and DeGrado produced the first binary-patterned helical bundle using only Leu, Lys, and Glu for the helices with Pro and Arg residues included in inter-helical loops[81]. Another early design

took a different approach, aiming to maximize sequence complexity while still yielding a stable 4-helix structure with unnatural sequence[82]. Others, including the Dutton and Discher groups, have built first-principles proteins in the years since (discussed below.)

Natural proteins evolve through the random drift of mutations, guided by an intricate network of factors defining biological fitness. Such a convoluted process could never be expected to produce proteins optimized for simplicity. Given the countless evolutionary paths that could lead to a protein competent in a particular function, there is no reason why a randomly chosen path would produce the simplest outcome. This does not matter from the organism's point of view, as it needs only to end up with an adequately functioning protein and is unconcerned with that protein's evolutionary history or future. But this evolutionary baggage is certainly concerning to a protein designer. Making seemingly rational changes to a complex natural system is likely to produce unwanted side-effects, including disrupting the overall stability of the molecule[83]. Even computational designs may present ambiguity as to "why" a particular residue is selected, given the convoluted and possibly contradictory components of a scoring function.

In contrast, the logic behind each amino acid selection is completely clear in a first-principles design. This basic understanding enables a designer to make iterative, testable sequence changes with more confidence that they will not have unwanted consequences. When compared to computational design aimed to achieve an atomic-level structure, the first-principles approach may seem quite imprecise. A high level of structural precision is probably necessary for some functions, including building specific catalytic sites. However, long-range ET has less stringent requirements. The Moser-Dutton Ruler (**Eqn 1.5**) is a mathematical expression of the idea that specifics of the inter-cofactor medium are unimportant to ET function; the protein is simply a scaffold to anchor the appropriate cofactors in the correct positions. Extrapolating this idea to *de novo* oxidoreductase design implies that a simple first-principles approach offers the most straightforward approach to building new ET proteins.

When binding redox cofactors, first-principle designs are sometimes called oxidoreductase "maquettes" because they recapitulate natural oxidoreductase functions in a simpler, scaled-down scaffold. The maquette approach is a logical result of extending the Moser-Dutton view of electron transfer to the realm of protein design. In 1994 Robertson and coworkers produced the first cofactor-binding maquette, a dimeric bundle ligating four heme residues[84]. Subsequent designs yielded a maquette crystal structure[85], photoactivated ET between bound

flavin and heme cofactors[86], and redox-driven conformational switching[87]. Further changes produced a heme maquette that, like natural globins, binds O₂[88]. Discher and colleagues have extended maquette development to membrane-bound proteins[89, 90]. A single monomeric scaffold, denoted hereafter as “BT6”, has been shown to support a wide range of oxidoreductase functions with only minimal modification[6]. **Chapter 2** examines ET from BT6 to cyt *c*.

Recently Dutton lab member Nate Ennist has produced the first crystal structure of a porphyrin-binding *de novo* protein, and Zhenyu Zhao has modified this protein to produce a very long-lived light-activated charge separation. Chris Bialas has produced a flavin maquette showing magnetosensitivity analogous to the natural cryptochrome protein family. Josh Mancini has combined first-principles design with directed evolution to optimize inter-cofactor energy transfer in bilin-binding maquettes; this work provides an excellent example of how divergent design techniques may be combined to toward optimizing a particular protein function.

1.5 Dissertation Goals

With this work I aim to extend the substantial body of work on protein maquette function to include a description of maquette interprotein electron transfers. The Moser-Dutton approach to ET views the protein itself largely as an inert structure to anchor well-chosen cofactors in appropriate positions. Nature accepts a stable protein with the right geometry as sufficient to guide intra-protein ET. A protein engineer may likewise follow these same straightforward requirements to produce a first-principles ET protein, taking advantage of the simplicity inherent in this sort of design.

Interprotein ET obviously adds complexity when compared to ET processes confined to a single protein. However, from an engineering standpoint designing for interprotein ET still appears less demanding than producing either an enzyme active site or a specific regulatory protein-protein contact. Two correlated reasons stand out for this greater level of tolerance in interprotein ET design. First, a broad literature supports the view that a given interprotein ET process often proceeds over a range of cofactor separations and protein orientations. This feature follows from the fact that ET is a relatively long-ranged process. Thus a *de novo* design for interprotein ET need only bring cofactors to within several Å with sufficient frequency, and this does not necessarily require atomic-level design. Secondly, the electrostatic forces guiding interprotein ET complex formation are also relatively long-ranged and imprecise. Nature does

provide examples of precise protein electrostatic tuning[34], but these seem to be the exception rather than the rule. The broad promiscuity in some natural interprotein ET systems[4, 47, 49] supports the view that these electrostatic interactions are not intricately designed. Again, maquette designs with well-chosen surface electrostatics should in principle offer a solution.

Easily-modified, uncomplicated artificial proteins offer a valuable tool to study a range of oxidoreductase properties[83], including fundamental interprotein ET processes. Looking forward, the ability to rationally design of new proteins linking to *in vivo* ET pathways would present a major technological boon. Basic work on re-wiring photosynthesis to produce fuels and other industrial products is a very active area of research, and the ability to divert electrons toward new metabolic targets would prove invaluable in this field.

Chapter 2 discusses ground-state ET from the well-characterized BT6 maquette [6] to cyt *c*. Two classes of experiments are examined here: simple stopped-flow mixing, and light-induced ET from the photolysis of CO-bound BT6. **Chapter 3** describes spectrophotometer modifications and software development used for the experiments of **Chapter 2**. **Chapter 4** examines excited-state electron transfer between several maquettes and cyt *c*. A synthetic zinc porphyrin drives these ET reactions. **Chapter 5** largely departs from the theme of interprotein ET to discuss new amphiphilic maquette designs and continuing work toward maquette-mediated transmembrane electron transfer. Finally, the appendices provide additional descriptions of experimental methods and biophysical characterization of the amphiphilic maquettes.

1.6 References

- [1] R.M. Metzger, Unimolecular electronics, *Journal of Materials Chemistry*, 18 (2008) 4364-4396.
- [2] J. Schilder, M. Ubbink, Formation of transient protein complexes, *Current Opinion in Structural Biology*, 23 (2013) 911-918.
- [3] C.C. Moser, J.L.R. Anderson, P.L. Dutton, Guidelines for tunneling in enzymes, *Biochimica Et Biophysica Acta-Bioenergetics*, 1797 (2010) 1573-1586.
- [4] F. Meschi, F. Wiertz, L. Klauss, A. Blok, B. Ludwig, A. Merli, H.A. Heering, G.L. Rossi, M. Ubbink, Efficient Electron Transfer in a Protein Network Lacking Specific Interactions, *Journal of the American Chemical Society*, 133 (2011) 16861-16867.
- [5] P. Xiong, J.M. Nocek, A.K.K. Griffin, J. Wang, B.M. Hoffman, Electrostatic Redesign of the Myoglobin, Cytochrome b(5) Interface To Create a Well-Defined Docked Complex with Rapid Interprotein Electron Transfer, *Journal of the American Chemical Society*, 131 (2009) 6938-+.

- [6] T.A. Farid, G. Kodali, L.A. Solomon, B.R. Lichtenstein, M.M. Sheehan, B.A. Fry, C. Bialas, N.M. Ennist, J.A. Siedlecki, Z. Zhao, M.A. Stetz, K.G. Valentine, J.L.R. Anderson, A.J. Wand, B.M. Discher, C.C. Moser, P.L. Dutton, Elementary tetrahelical protein design for diverse oxidoreductase functions, *Nature Chemical Biology*, 9 (2013) 826-+.
- [7] R. Langen, I.J. Chang, J.P. Germanas, J.H. Richards, J.R. Winkler, H.B. Gray, Electron-Tunneling In Proteins - Coupling Through A Beta-Strand, *Science*, 268 (1995) 1733-1735.
- [8] P. Mitchell, Coupling Of Phosphorylation To Electron And Hydrogen Transfer By A Chemi-Osmotic Type Of Mechanism, *Nature*, 191 (1961) 144-&.
- [9] S. Scanu, J.M. Foerster, G.M. Ullmann, M. Ubbink, Role of Hydrophobic Interactions in the Encounter Complex Formation of the Plastocyanin and Cytochrome f Complex Revealed by Paramagnetic NMR Spectroscopy, *Journal of the American Chemical Society*, 135 (2013) 7681-7692.
- [10] H.B. Gray, J.R. Winkler, Electron tunneling through proteins, *Quarterly Reviews of Biophysics*, 36 (2003) 341-372.
- [11] J. Rittle, M.T. Green, Cytochrome P450 Compound I: Capture, Characterization, and C-H Bond Activation Kinetics, *Science*, 330 (2010) 933-937.
- [12] J.M. Shifman, B.R. Gibney, R.E. Sharp, P.L. Dutton, Heme redox potential control in de novo designed four-alpha-helix bundle proteins, *Biochemistry*, 39 (2000) 14813-14821.
- [13] C. Olea, J. Kuriyan, M.A. Marletta, Modulating Heme Redox Potential through Protein-Induced Porphyrin Distortion, *Journal of the American Chemical Society*, 132 (2010) 12794-12795.
- [14] S. Franzen, L. Kiger, C. Poyart, J.L. Martin, Heme photolysis occurs by ultrafast excited state metal-to-ring charge transfer, *Biophysical Journal*, 80 (2001) 2372-2385.
- [15] R.A. Marcus, On The Theory Of Oxidation-Reduction Reactions Involving Electron Transfer .1, *Journal of Chemical Physics*, 24 (1956) 966-978.
- [16] R.A. Marcus, N. Sutin, ELECTRON TRANSFERS IN CHEMISTRY AND BIOLOGY, *Biochimica et biophysica acta*, 811 (1985) 265-322.
- [17] H. Eyring, The activated complex in chemical reactions, *Journal of chemical Physics*, 3 (1935) 107-115.
- [18] C.C. Moser, J.M. Keske, K. Warncke, R.S. Farid, P.L. Dutton, Nature Of Biological Electron-Transfer, *Nature*, 355 (1992) 796-802.
- [19] D.N. Beratan, J.N. Onuchic, J.R. Winkler, H.B. Gray, Electron-Tunneling Pathways In Proteins, *Science*, 258 (1992) 1740-1741.
- [20] B. Chance, G.R. Williams, THE RESPIRATORY CHAIN AND OXIDATIVE PHOSPHORYLATION, *Advances in Enzymology and Related Subjects of Biochemistry*, 17 (1956) 65-134.
- [21] D. Devault, J.H. Parkes, B. Chance, Electron Tunnelling In Cytochromes, *Nature*, 215 (1967) 642-&.
- [22] J.J. Hopfield, Electron-Transfer Between Biological Molecules By Thermally Activated Tunneling, *Proceedings of the National Academy of Sciences of the United States of America*, 71 (1974) 3640-3644.
- [23] D.N. Beratan, J.N. Onuchic, J.J. Hopfield, Electron-Tunneling Through Covalent And Noncovalent Pathways In Proteins, *Journal of Chemical Physics*, 86 (1987) 4488-4498.
- [24] T.R. Prytkova, I.V. Kurnikov, D.N. Beratan, Coupling coherence distinguishes structure sensitivity in protein electron transfer, *Science*, 315 (2007) 622-625.
- [25] C.C. Moser, C.C. Page, X. Chen, P.L. Dutton, Biological electron tunneling through native protein media, *Journal of Biological Inorganic Chemistry*, 2 (1997) 393-398.

- [26] C.C. Page, C.C. Moser, X.X. Chen, P.L. Dutton, Natural engineering principles of electron tunnelling in biological oxidation-reduction, *Nature*, 402 (1999) 47-52.
- [27] C.C. Page, C.C. Moser, P.L. Dutton, Mechanism for electron transfer within and between proteins, *Curr. Opin. Chem. Biol.*, 7 (2003) 551-556.
- [28] F.A. Tezcan, B.R. Crane, J.R. Winkler, H.B. Gray, Electron tunneling in protein crystals, *Proc Natl Acad Sci U S A*, 98 (2001) 5002-5006.
- [29] P.H. Debye, E., The theory of electrolytes. I. The lowering of freezing points and other phenomena., *Physikalische Zeitschrift*, 24 (1923) 185-206.
- [30] S. Wherland, H.B. Gray, Metalloprotein Electron-Transfer Reactions - Analysis Of Reactivity Of Horse Heart Cytochrome-C With Inorganic Complexes, *Proceedings of the National Academy of Sciences of the United States of America*, 73 (1976) 2950-2954.
- [31] J. Stonehuerner, J.B. Williams, F. Millett, Interaction Between Cytochrome-C And Cytochrome-B5, *Biochemistry*, 18 (1979) 5422-5427.
- [32] W.H. Koppenol, C.A.J. Vroonland, R. Braams, Electric-Potential Field Around Cytochrome-C And Effect Of Ionic-Strength On Reaction-Rates Of Horse Cytochrome-C, *Biochimica et biophysica acta*, 503 (1978) 499-508.
- [33] J.W. Vanleeuwen, The Ionic-Strength Dependence Of The Rate Of A Reaction Between 2 Large Proteins With A Dipole-Moment, *Biochimica et biophysica acta*, 743 (1983) 408-421.
- [34] K. Sharp, R. Fine, B. Honig, Computer-Simulations Of The Diffusion Of A Substrate To An Active-Site Of An Enzyme, *Science*, 236 (1987) 1460-1463.
- [35] S.H. Northrup, J.O. Boles, J.C.L. Reynolds, Brownian Dynamics Of Cytochrome-C And Cytochrome-C Peroxidase Association, *Science*, 241 (1988) 67-70.
- [36] Z.X. Liang, J.M. Nocek, K. Huang, R.T. Hayes, I.V. Kurnikov, D.N. Beratan, B.M. Hoffman, Dynamic docking and electron transfer between Zn-myoglobin and cytochrome b(5), *Journal of the American Chemical Society*, 124 (2002) 6849-6859.
- [37] Z.X. Liang, I.V. Kurnikov, J.M. Nocek, A.G. Mauk, D.N. Beratan, B.M. Hoffman, Dynamic docking and electron-transfer between cytochrome b(5) and a suite of myoglobin surface-charge mutants. Introduction of a functional-docking algorithm for protein-protein complexes, *Journal of the American Chemical Society*, 126 (2004) 2785-2798.
- [38] D. Keilin, On cytochrome, a respiratory pigment, common to animals, yeast, and higher plants., *Proceedings of the Royal Society of London*, 98 (1925) 312-339.
- [39] E. Margoliash, Primary Structure And Evolution Of Cytochrome C, *Proceedings of the National Academy of Sciences of the United States of America*, 50 (1963) 672-&.
- [40] H. Roder, G.A. Elove, S.W. Englander, Structural Characterization Of Folding Intermediates In Cytochrome-C By H-Exchange Labeling And Proton Nmr, *Nature*, 335 (1988) 700-704.
- [41] W.H. Koppenol, J.D. Rush, J.D. Mills, E. Margoliash, The Dipole-Moment Of Cytochrome-C, *Molecular Biology and Evolution*, 8 (1991) 545-558.
- [42] H. Tian, R. Sadoski, L. Zhang, C.A. Yu, L. Yu, B. Durham, F. Millett, Definition of the interaction domain for cytochrome c on the cytochrome bc(1) complex - Steady-state and rapid kinetic analysis of electron transfer between cytochrome c and *Rhodobacter sphaeroides* cytochrome bc1 surface mutants, *Journal of Biological Chemistry*, 275 (2000) 9587-9595.
- [43] Y.J. Zhen, C.W. Hoganson, G.T. Babcock, S. Ferguson-Miller, Definition of the interaction domain for cytochrome c on cytochrome c oxidase - I. Biochemical, spectral, and kinetic characterization of surface mutants in subunit II of *Rhodobacter sphaeroides* cytochrome aa(3), *Journal of Biological Chemistry*, 274 (1999) 38032-38041.
- [44] K.F. Wang, Y.J. Zhen, R. Sadoski, S. Grinnell, L. Geren, S. Ferguson-Miller, B. Durham, F. Millett, Definition of the interaction domain for cytochrome c on cytochrome c oxidase - II.

- Rapid kinetic analysis of electron transfer from cytochrome c to *Rhodobacter sphaeroides* cytochrome oxidase surface mutants, *Journal of Biological Chemistry*, 274 (1999) 38042-38050.
- [45] A. Fago, A.J. Mathews, L. Moens, S. Dewilde, T. Brittain, The reaction of neuroglobin with potential redox protein partners cytochrome b(5) and cytochrome c, *Febs Letters*, 580 (2006) 4884-4888.
- [46] A.N. Volkov, N.A.J. van Nuland, Electron Transfer Interactome of Cytochrome c, *Plos Computational Biology*, 8 (2012).
- [47] S. Ferguson-Miller, D.L. Brautigan, E. Margoliash, Correlation Of Kinetics Of Electron-Transfer Activity Of Various Eukaryotic Cytochromes-C With Binding To Mitochondrial Cytochrome-C Oxidase, *Journal of Biological Chemistry*, 251 (1976) 1104-1115.
- [48] C.C. Moser, P.L. Dutton, Cytochrome-C And Cytochrome-C2 Binding-Dynamics And Electron-Transfer With Photosynthetic Reaction Center Protein And Other Integral Membrane Redox Proteins, *Biochemistry*, 27 (1988) 2450-2461.
- [49] J.B. Schenkman, I. Jansson, The many roles of cytochrome b(5), *Pharmacol. Ther.*, 97 (2003) 139-152.
- [50] Z.X. Liang, M. Jiang, Q. Ning, B.M. Hoffman, Dynamic docking and electron transfer between myoglobin and cytochrome b(5), *Journal of Biological Inorganic Chemistry*, 7 (2002) 580-588.
- [51] P. Xiong, J.M. Nocek, J. Vura-Weis, J.V. Lockard, M.R. Wasielewski, B.M. Hoffman, Faster Interprotein Electron Transfer in a Myoglobin, b(5) Complex with a Redesigned Interface, *Science*, 330 (2010) 1075-1078.
- [52] M. Ubbink, Dynamics in transient complexes of redox proteins, *Biochemical Society Transactions*, 40 (2012) 415-418.
- [53] A.N. Volkov, J.A.R. Worrall, E. Holtzmann, M. Ubbink, Solution structure and dynamics of the complex between cytochrome c and cytochrome c peroxidase determined by paramagnetic NMR, *Proceedings of the National Academy of Sciences of the United States of America*, 103 (2006) 18945-18950.
- [54] A.N. Volkov, O. Bashir, J.A.R. Worrall, M. Ubbink, Binding Hot Spot in the Weak Protein Complex of Physiological Redox Partners Yeast Cytochrome c and Cytochrome c Peroxidase, *Journal of Molecular Biology*, 385 (2009) 1003-1013.
- [55] X. Xu, P.H.J. Keizers, W. Reinle, F. Hannemann, R. Bernhardt, M. Ubbink, Intermolecular dynamics studied by paramagnetic tagging, *Journal of Biomolecular Nmr*, 43 (2009) 247-254.
- [56] L. Regan, D. Caballero, M.R. Hinrichsen, A. Virrueta, D.M. Williams, C.S. O'Hern, Protein Design: Past, Present, and Future, *Biopolymers*, 104 (2015) 334-350.
- [57] B. Kuhlman, G. Dantas, G.C. Ireton, G. Varani, B.L. Stoddard, D. Baker, Design of a novel globular protein fold with atomic-level accuracy, *Science*, 302 (2003) 1364-1368.
- [58] D. Rothlisberger, O. Khersonsky, A.M. Wollacott, L. Jiang, J. DeChancie, J. Betker, J.L. Gallaher, E.A. Althoff, A. Zanghellini, O. Dym, S. Albeck, K.N. Houk, D.S. Tawfik, D. Baker, Kemp elimination catalysts by computational enzyme design, *Nature*, 453 (2008) 190-U194.
- [59] L. Jiang, E.A. Althoff, F.R. Clemente, L. Doyle, D. Rothlisberger, A. Zanghellini, J.L. Gallaher, J.L. Betker, F. Tanaka, C.F. Barbas, D. Hilvert, K.N. Houk, B.L. Stoddard, D. Baker, De novo computational design of retro-aldol enzymes, *Science*, 319 (2008) 1387-1391.
- [60] C.A. Rohl, C.E.M. Strauss, K.M.S. Misura, D. Baker, Protein structure prediction using rosetta, *Methods Enzymol.*, 383 (2004) 66-+.
- [61] D. Baker, Protein folding, structure prediction and design, *Biochemical Society Transactions*, 42 (2014) 225-229.
- [62] J.M. Zou, J.G. Saven, Statistical theory of combinatorial libraries of folding proteins: Energetic discrimination of a target structure, *Journal of Molecular Biology*, 296 (2000) 281-294.

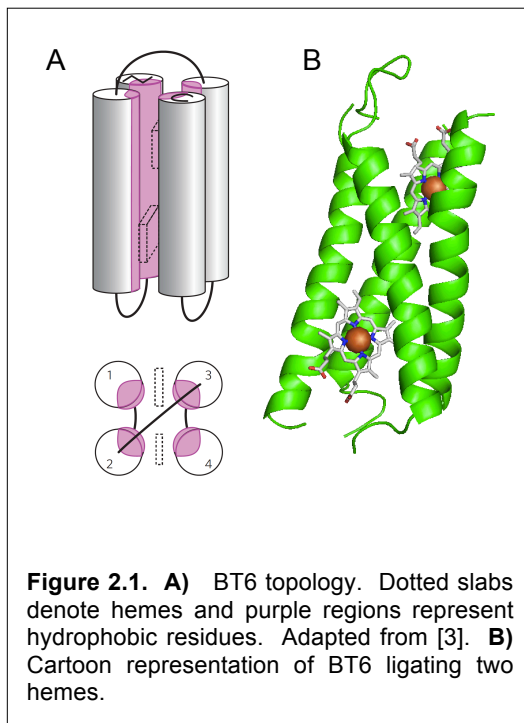
- [63] J.R. Calhoun, H. Kono, S. Lahr, W. Wang, W.F. DeGrado, J.G. Saven, Computational design and characterization of a monomeric helical dinuclear metalloprotein, *Journal of Molecular Biology*, 334 (2003) 1101-1115.
- [64] F.V. Cochran, S.P. Wu, W. Wang, V. Nanda, J.G. Saven, M.J. Therien, W.F. DeGrado, Computational de novo design and characterization of a four-helix bundle protein that selectively binds a nonbiological cofactor, *Journal of the American Chemical Society*, 127 (2005) 1346-1347.
- [65] H.C. Fry, A. Lehmann, J.G. Saven, W.F. DeGrado, M.J. Therien, Computational Design and Elaboration of a de Novo Heterotetrameric alpha-Helical Protein That Selectively Binds an Emissive Abiological (Porphinato)zinc Chromophore, *Journal of the American Chemical Society*, 132 (2010) 3997-4005.
- [66] H.C. Fry, A. Lehmann, L.E. Sinks, I. Asselberghs, A. Tronin, V. Krishnan, J.K. Blasie, K. Clays, W.F. DeGrado, J.G. Saven, M.J. Therien, Computational de Novo Design and Characterization of a Protein That Selectively Binds a Highly Hyperpolarizable Abiological Chromophore, *Journal of the American Chemical Society*, 135 (2013) 13914-13926.
- [67] A. Roy, I. Sarrou, M.D. Vaughn, A.V. Astashkin, G. Ghirlanda, De Novo Design of an Artificial Bis 4Fe-4S Binding Protein, *Biochemistry*, 52 (2013) 7586-7594.
- [68] G.M. Bender, A. Lehmann, H. Zou, H. Cheng, H.C. Fry, D. Engel, M.J. Therien, J.K. Blasie, H. Roder, J.G. Saven, W.F. DeGrado, De novo design of a single-chain diphenylporphyrin metalloprotein, *Journal of the American Chemical Society*, 129 (2007) 10732-10740.
- [69] I.V. Korendovych, A. Senes, Y.H. Kim, J.D. Lear, H.C. Fry, M.J. Therien, J.K. Blasie, F.A. Walker, W.F. DeGrado, De Novo Design and Molecular Assembly of a Transmembrane Diporphyrin-Binding Protein Complex, *Journal of the American Chemical Society*, 132 (2010) 15516-15518.
- [70] N.H. Joh, T. Wang, M.P. Bhate, R. Acharya, Y. Wu, M. Grabe, M. Hong, G. Grigoryan, W.F. DeGrado, De novo design of a transmembrane Zn²⁺-transporting four-helix bundle, *Science*, 346 (2014) 1520-1524.
- [71] G. Ulas, T. Lemmin, Y. Wu, G.T. Gassner, W.F. DeGrado, Designed metalloprotein stabilizes a semiquinone radical, *Nature Chemistry*, 8 (2016) 354-359.
- [72] M.S. Packer, D.R. Liu, Methods for the directed evolution of proteins, *Nature Reviews Genetics*, 16 (2015) 379-394.
- [73] P.S. Coelho, E.M. Brustad, A. Kannan, F.H. Arnold, Olefin Cyclopropanation via Carbene Transfer Catalyzed by Engineered Cytochrome P450 Enzymes, *Science*, 339 (2013) 307-310.
- [74] S.C. Patel, M.H. Hecht, Directed evolution of the peroxidase activity of a de novo-designed protein, *Protein Engineering Design & Selection*, 25 (2012) 445-451.
- [75] M. Hecht, Sustaining Life With Proteins Designed De Novo, *Protein Science*, 23 (2014) 66-66.
- [76] K.M. Digianantonio, M.H. Hecht, A protein constructed de novo enables cell growth by altering gene regulation, *Proceedings of the National Academy of Sciences of the United States of America*, 113 (2016) 2400-2405.
- [77] E.A. Althoff, L. Wang, L. Jiang, L. Giger, J.K. Lassila, Z. Wang, M. Smith, S. Hari, P. Kast, D. Herschlag, D. Hilvert, D. Baker, Robust design and optimization of retroaldol enzymes, *Protein Science*, 21 (2012) 717-726.
- [78] J.M. Cordova, P.L. Noack, S.A. Hilcove, J.D. Lear, G. Ghirlanda, Design of a functional membrane protein by engineering a heme-binding site in glycophorin A, *Journal of the American Chemical Society*, 129 (2007) 512-518.
- [79] S. Shinde, J. Cordova, G. Ghirlanda, Modulation Of Function In Heme Binding Membrane Protein, *Biopolymers*, 92 (2009) 343-343.

- [80] I.V. Korendovych, D.W. Kulp, Y. Wu, H. Cheng, H. Roder, W.F. DeGrado, Design of a switchable eliminase, *Proceedings of the National Academy of Sciences of the United States of America*, 108 (2011) 6823-6827.
- [81] L. Regan, W.F. DeGrado, Characterization Of A Helical Protein Designed From 1St Principles, *Science*, 241 (1988) 976-978.
- [82] M.H. Hecht, J.S. Richardson, D.C. Richardson, R.C. Ogden, Denovo Design, Expression, And Characterization Of Felix - A 4-Helix Bundle Protein Of Native-Like Sequence, *Science*, 249 (1990) 884-891.
- [83] B.R. Lichtenstein, T.A. Farid, G. Kodali, L.A. Solomon, J.L.R. Anderson, M.M. Sheehan, N.M. Ennist, B.A. Fry, S.E. Chobot, C. Bialas, J.A. Mancini, C.T. Armstrong, Z. Zhao, T.V. Esipova, D. Snell, S.A. Vinogradov, B.M. Discher, C.C. Moser, P.L. Dutton, Engineering oxidoreductases: maquette proteins designed from scratch, *Biochemical Society Transactions*, 40 (2012) 561-566.
- [84] D.E. Robertson, R.S. Farid, C.C. Moser, J.L. Urbauer, S.E. Mulholland, R. Pidikiti, J.D. Lear, A.J. Wand, W.F. DeGrado, P.L. Dutton, Design And Synthesis Of Multi-Heme Proteins, *Nature*, 368 (1994) 425-431.
- [85] S.S. Huang, B.R. Gibney, S.E. Stayrook, P.L. Dutton, M. Lewis, X-ray structure of a Maquette scaffold, *Journal of Molecular Biology*, 326 (2003) 1219-1225.
- [86] R.E. Sharp, C.C. Moser, F. Rabanal, P.L. Dutton, Design, synthesis, and characterization of a photoactivatable flavocytochrome molecular maquette, *Proceedings of the National Academy of Sciences of the United States of America*, 95 (1998) 10465-10470.
- [87] A.M. Grosset, B.R. Gibney, F. Rabanal, C.C. Moser, P.L. Dutton, Proof of principle in a de novo designed protein maquette: An allosterically regulated, charge-activated conformational switch in a tetra-alpha-helix bundle, *Biochemistry*, 40 (2001) 5474-5487.
- [88] R.L. Koder, J.L. Anderson, L.A. Solomon, K.S. Reddy, C.C. Moser, P.L. Dutton, Design and engineering of an O(2) transport protein, *Nature*, 458 (2009) 305-309.
- [89] B.M. Discher, D. Noy, J. Strzalka, S.X. Ye, C.C. Moser, J.D. Lear, J.K. Blasie, P.L. Dutton, Design of amphiphilic protein maquettes: Controlling assembly, membrane insertion, and cofactor interactions, *Biochemistry*, 44 (2005) 12329-12343.
- [90] D. Noy, B.M. Discher, I.V. Rubtsov, R.A. Hochstrasser, P.L. Dutton, Design of amphiphilic protein maquettes: Enhancing maquette functionality through binding of extremely hydrophobic cofactors to lipophilic domains, *Biochemistry*, 44 (2005) 12344-12354.

Chapter 2 Electron Transfer from Maquettes to Cyt *c*

2.1 Background and Introduction

An extensive biophysical literature investigates the electron-transfer between natural proteins, as discussed in **Chapter 1**. The majority of these publications focus on ET between physiological redox partners. A smaller subset examines *in vitro* ET between two natural proteins that may not interact in nature because they originate in different organisms [1] or because their physiological functions are incompletely understood [4]. Finally, some studies examine the ET in a fusion protein comprising two unnatural redox partners such as photosystem I and Fe hydrogenase [5], [6]. However, there are very few reports of interprotein ET involving a completely unnatural protein. The first such report was delivered in Reference [3], discussed in **Section 2.1.1**. Shortly thereafter the Ghirlanda lab described the reduction of cyt *c* by a computationally designed 4-helix bundle ligating a pair of 2Fe2S clusters [7]. Finally, prior Dutton lab member Lee Solomon has shown preliminary data on interprotein ET between two maquettes binding porphyrins of differing E_m . This chapter describes a more detailed kinetic analysis of cyt *c* reduction by a heme maquette, published in [8]. **Section 2.2** provides an overview of the maquettes, and **Section 2.3** summarizes the experimental methods. **Section 2.4** describes a series of straightforward stopped-flow experiments mixing dithionite-reduced maquettes with oxidized cyt *c*. **Section 2.5** presents another set of experiments using a photolysis-induced ET to improve upon the temporal resolution afforded by simple stopped-flow. All of these reactions involve ET from a ground-state maquette porphyrin, in contrast to the photo-activated ET from an excited cofactor discussed in **Chapter 4**.



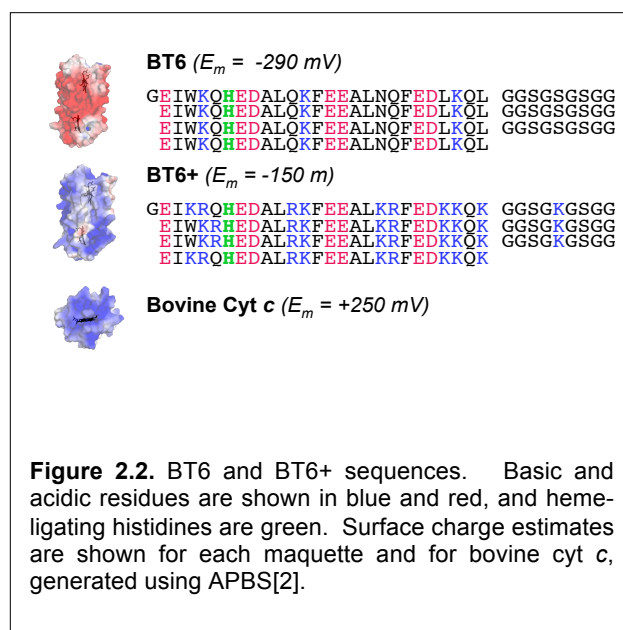
2.2 BT6 and BT6+ Maquettes

The Dutton lab maquettes known as “BT6” and “BT6+” were utilized for all experiments in this chapter. **Figure 2.1** illustrates the topology of the proteins. **Figure 2.2** shows the sequences and predicted surface charges for BT6 and BT6+, along with the surface charge map for bovine cytochrome *c* [9]. These designs were originally published in [3].

BT6 is a single-chain, water-soluble, 4- α -helical bundle with two bis-his sites for binding *b*-type or other iron porphyrins. The outward-facing portions of the helices are rich in glutamates and other charged residues, resulting in an expected overall charge of -16 at neutral pH. Both hemes bind tightly, with measured K_d values of < 5 nM for each heme. When 2 hemes are bound each has a midpoint potential of -290 mV [3]. In lieu of hemes, the bis-His sites of BT6 will also bind two molar equivalents of the synthetic porphyrin iron diacetyldeuteroporphyrin IX, or Fe DADPIX (structure shown in **Figure 1.2**). The two electron-withdrawing acetyl substituents of DADPIX raise the E_m to -140 mV, while maintaining $K_d < 100$ nM [10].

As in natural globins and some other maquettes, reduced iron porphyrins in BT6 will readily bind diatomic gaseous

ligands including O₂, nitric oxide, and carbon monoxide (CO) [3, 11, 12]. Bound CO stabilizes the reduced heme state, rendering it unable to transfer electrons to potential redox partners such as cytochrome *c*. However, electronic excitation from a visible photon will release the bound CO, enabling the maquette to reduce an electron acceptor. Natural globins and some (but not all) other heme proteins share this property for CO [13] and other diatomic ligands [14]. Britton Chance employed flash photolysis to study ET kinetics in cytochrome *c* oxidase [15]. Most of this chapter’s experiments rely upon this established photolysis technique to initiate ET reactions. The photolysis data presented here employ CO bound to BT6 / heme, although BT6 / DADPIX



will also bind and photolyze a CO ligand. **Figure 2.3** shows the UV-Vis spectra for the reduced, oxidized, and CO-bound species discussed in this chapter.

The BT6 scaffold has proven remarkably tolerant to mutation, binding a range of cofactors beyond iron porphyrins. One or both bis-His sites may be changed to single His to accommodate pentacoordinate zinc porphyrins or chlorins. Alternately, a cysteine may be introduced to bind a cytochrome P450-like heme or to provide a covalent flavin attachment[3].

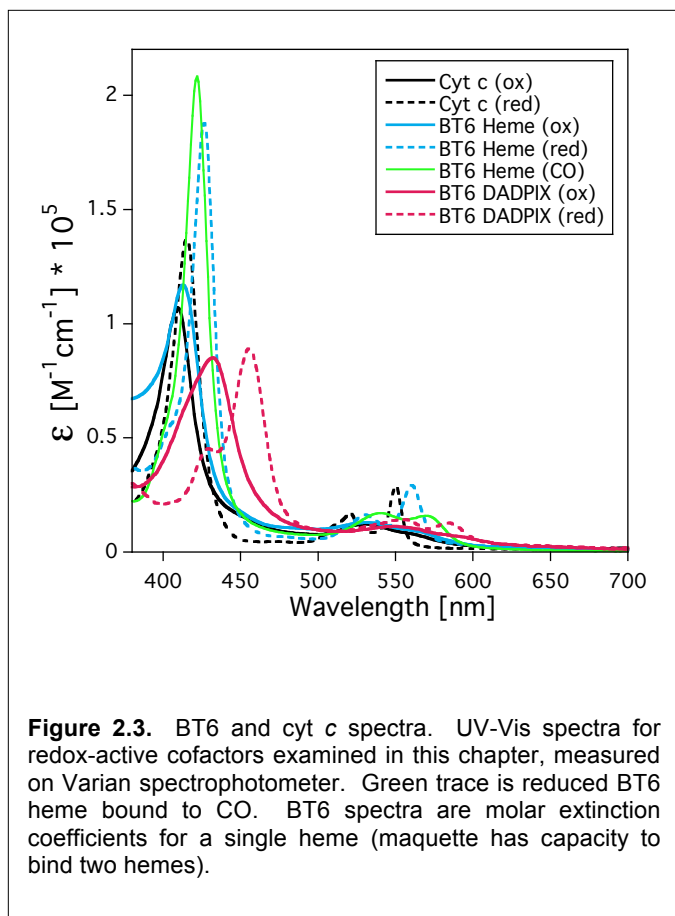


Figure 2.3. BT6 and cyt *c* spectra. UV-Vis spectra for redox-active cofactors examined in this chapter, measured on Varian spectrophotometer. Green trace is reduced BT6 heme bound to CO. BT6 spectra are molar extinction coefficients for a single heme (maquette has capacity to bind two hemes).

Preliminary evidence shows BT6 can also bind more exotic ligands such as the multi-metal nitrogenase cofactor FeMoCo[16]. The 9-residue glycine / serine loops can be extended or shortened with minimal functional impact to the protein[3, 17].

Importantly for this work, the solvent-facing glutamates may also be changed to other hydrophilic, helix-forming residues. This opens the possibility to examine how surface charge impacts the maquette's interaction with redox partners. Bovine cyt *c* contains a conspicuous patch of basic residues around its heme, yielding an overall charge of +7 units at physiological pH. This electrostatic feature influences its

approach and orientation with physiological redox partners cytochrome *bc1*[18] and cytochrome *c* oxidase (CcO) [19]. We expect a maquette's charge to similarly impact its redox interaction with cyt *c*. BT6 is strongly negative, and thus charge complimentary with cyt *c* this should produce a fast interprotein ET rate. Likewise, we would expect slower ET from a positive maquette.

The variant known as "BT6+" replaces many of the glutamates with lysines, and the overall impact is to raise the total predicted charge from -16 to -11 at neutral pH. The

preponderance of positive charge in BT6+ raises the heme E_m to -150 mV[3]. The E_m increase of +140 mV, despite a large electrostatic change of 27 units, is relatively modest compared with similar large-scale charge changes in natural proteins. [20]. BT6+ binds both hemes with a reasonably tight 365 nM K_d [3].

Finally, it should be noted that although BT6 and BT6+ both exhibit strong charge monopoles, they were not designed as dipoles. **Chapter 4** examines other maquettes with intentionally designed dipole moments.

2.3 Methods

2.3.1 Protein preparation

Protein maquettes were expressed and purified as described in [3], reviewed here briefly. His-tagged constructs linked to the maquette via a TEV cleavage site were expressed in BL-21 *E. coli* for 4 hours after IPTG induction. Following cell lysis and Ni-NTA gravity column purification, the constructs were incubated overnight at room temperature with recombinant TEV protease. A second Ni-NTA run removed cleavage fragments. The maquette was lyophilized after a final RP-HPLC purification step. Prior to ET experiments, porphyrin cofactors were added from DMSO stock solutions with concentrations measured using the hemochrome method[21]. Maquette proteins were dissolved in CHES buffer (20 mM CHES, 100 mM NaCl, pH 9.0) and protein concentrations were measured via 280 nm absorbance ($\epsilon = 5600 \text{ M}^{-1}\text{cm}^{-1}$ per tryptophan). 2.5 equivalents of heme stock solution were added and incubated at room temperature for 5 minutes. The heme-bound protein was passed through a PD-10 gravity column (GE Healthcare) to remove excess heme and exchange buffer. Finally, the protein was diluted to the desired experimental concentration, verified by tracking the 412nm Soret band of the bound cofactor ($\epsilon = 117000 \text{ M}^{-1}\text{cm}^{-1}$) [22].

Bovine heart cyt *c*, oxidized with $\text{K}_3\text{Fe}(\text{CN})_6$, was prepared as described in **Appendix A1.5**. The solution was diluted to the desired experimental concentration by following the 409 nm Soret band ($\epsilon = 107000 \text{ M}^{-1}\text{cm}^{-1}$) [23].

2.3.2 Degassing and CO binding

Prior to ET experiments, several mL of porphyrin-bound maquette solution and cyt *c* solution were placed in septum-sealed quartz cassettes with stir bars. The maquette was placed under either an argon or carbon monoxide (CO) gas flow, and cyt *c* was placed under argon. After 45 minutes, an oxygen scrubbing mixture of 80 nM glucose oxidase, 12 nM catalase, and 1 mM glucose was added to the maquette solution (see **Section A1.1** for more details on enzymatic O₂ scrubbing). The maquette protein was reduced by careful titration of sodium dithionite, observing 318 nm absorbance to avoid adding dithionite excess. For CO samples, dithionite was added until full CO binding was observed spectroscopically. The maquette was then placed under argon flow for 5 min with stirring to remove excess CO. Cyt *c* and reduced maquette (with or without CO) were transferred under positive argon pressure to 10 mL gastight syringes (SGE Analytical) equipped with stainless steel Luer valves (Cadence Science) and finally loaded into the stopped-flow apparatus.

2.3.3 Stopped-flow ET measurements without CO photolysis

ET measurements were run on an RSM-1000 UV-Vis stopped-flow spectrophotometer (OLIS, Inc.) equipped with a rapid-scan monochromator sampling the Q-band spectral region at 1000 spectra per second. 3900 scans (3.9 seconds) were acquired after mixing the maquette and cytochrome *c* reactants. Proteins were dissolved in 50 mM HEPES, 120 mM KCl, pH 8.0. All experiments were performed at 20 C. The electron transfer reaction was monitored at 550 nm, corresponding to the reduced α band of cyt *c*. Static measurements of the reduced and oxidized forms of the maquette and cyt *c* indicate an extinction coefficient change of 19040 M⁻¹cm⁻¹ for a single ET from maquette B-heme to cyt *c*. Note that BT6 binds two hemes, each potentially available to transfer an electron to cyt *c*.

The stopped-flow data were fit to second-order reaction trajectories. Any compromise of anaerobicity prior to the stopped-flow mixing introduces an uncertainty in the initial concentration of reduced maquette heme, but not in the oxidized cyt *c*. Thus, the initial concentration of maquette was allowed to float for fitting the reaction trajectory to account for the

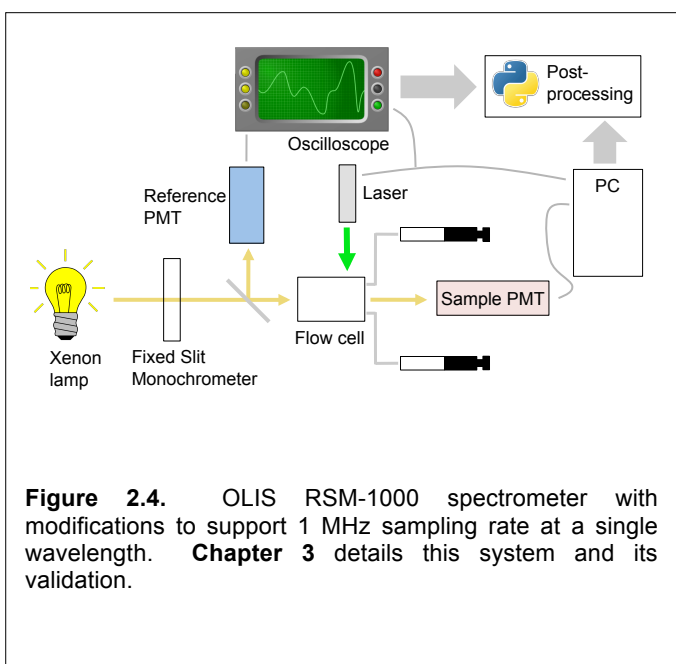
possibility of partial pre-oxidation. The resultant data were then normalized to the second-order fit at $t=0$ and $t=\infty$.

2.3.4 CO Photolysis-induced ET experiments

I made significant modifications to the OLIS RSM-1000 stopped flow apparatus for photolysis-induced ET measurements, as summarized in **Figure 2.4**. **Chapter 3** details the apparatus and how its performance was verified by comparing measured results to a published kinetic standard[24]. Briefly, a Q-switched frequency-doubled Nd:YAG laser (532 nm, Spectra

Physics) was focused on the flow cell to photolyze CO-bound reduced heme in BT6, rendering the maquette competent for ET to cyt *c*. The flow cell was exposed to a laser flash 200 to 300 mS after firing the stopped-flow to mix the two reactants. Due to limitations in the OLIS software, the reference photomultiplier tube (PMT) output was routed to an oscilloscope rather than to the PC controlling the OLIS instrument and capturing the sample PMT signal. A Python script, run after all data was collected,

removed laser flash artifacts and combined the two PMT voltage trajectories to calculate sample absorbance changes. All photolysis-induced ET experiments were performed at 20 C.



2.3.5 Kinetics computations for high-salt photolysis: 110 mM NaCl / 50 mM Na₂HPO₄

As explained in Section 2.4.2, the observed photolysis yield was always well below 100%. The effective concentration of photolyzed maquette heme available to reduce cyt *c* was computed from the 420 nm absorbance change at 1 ms following the laser flash. After 1 ms the histidine rebinding is essentially complete, and this interval is less than the much slower characteristic times of ET (see Figure 2.6) and CO re-binding (see Figure 2.7).

As seen in Figure 2.8, 420 nm is isosbestic for electron transfer but shows a large change for photolysis ($\epsilon_{\text{photolysis}} = -44000 \text{ M}^{-1}\text{cm}^{-1}$ per heme). The initial rate for the electron-transfer process was monitored by the essentially linear post-flash absorbance change at 424 nm from 1 to 5 ms. This wavelength is isosbestic for CO recombination and has an extinction change of $\epsilon_{\text{ET}} = -90000 \text{ M}^{-1}\text{cm}^{-1}$ (per electron) for electron ET; the isosbestic point and extinction coefficient were determined from static spectra of the maquette and of cyt *c*. To avoid possible spectral contamination by

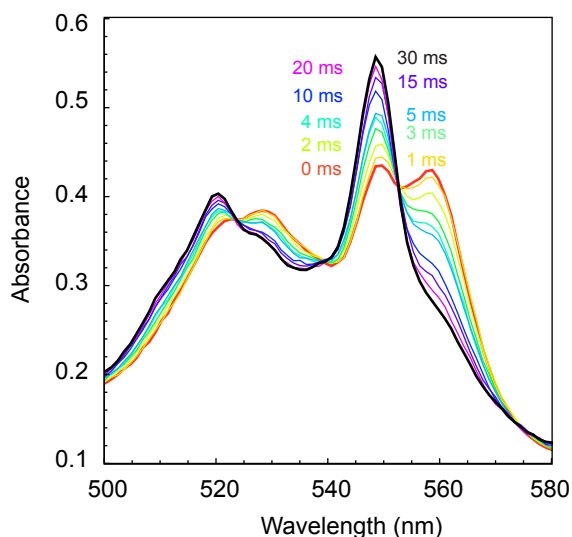


Figure 2.5. Stopped-flow mixing of 4.75 μM reduced BT6 with 8.5 μM oxidized cyt *c*. Over this timecourse the reduced *b* heme α band at 560 nm disappears and is replaced by the reduced α band of *c* heme at 550 nm.

sub-ms histidine recombination, the first 1 ms was excluded from calculation for initial rate.

2.3.6 Kinetics computations for low-salt photolysis: 11 mM NaCl / 5 mM Na₂HPO₄

At this lower ionic strength, post-photolysis ligand exchange was comparable to electron transfer rates and both were much faster than CO recombination. Thus the ligand exchange

isosbestic at 432 nm was chosen to measure the rate of electron-transfer kinetics. At this wavelength, differences in static spectra for known concentrations of oxidized, reduced, and CO-bound maquette and cyt *c* indicate extinction changes of $\epsilon_{\text{photolysis}} = 45000 \text{ M}^{-1}\text{cm}^{-1}$ per heme, $\epsilon_{\text{ET}} = -102000 \text{ M}^{-1}\text{cm}^{-1}$ per electron. The initial electron transfer rate was computed by measuring the slope from 100 μs to 300 μs after the laser flash. The photolysis yield was computed by linearly extrapolating the absorbance from 100 μs back to the time of the laser pulse. Best-fit single and double exponential functions (**Figure 2.10**) were computed using a Python script.

2.3.7 Protein Surface Charge Estimates, Visualization, and ET rate predictions

Visualizations use Pymol 1.7.5. [25]. Maquette structure figures are estimates generated from a 1 ns molecular dynamics trajectory in GROMACS[26] starting from four parallel helices connected by loops optimized in Modeler[27]. Cyt *c* uses PDB ID: 2DB7 [28]. Surface charge figures use the APBS plug-in for Pymol[2]. Theoretical inter-protein ET rate surfaces use a tunneling rate expression[29] embedded in a Pymol-integrated Python script.

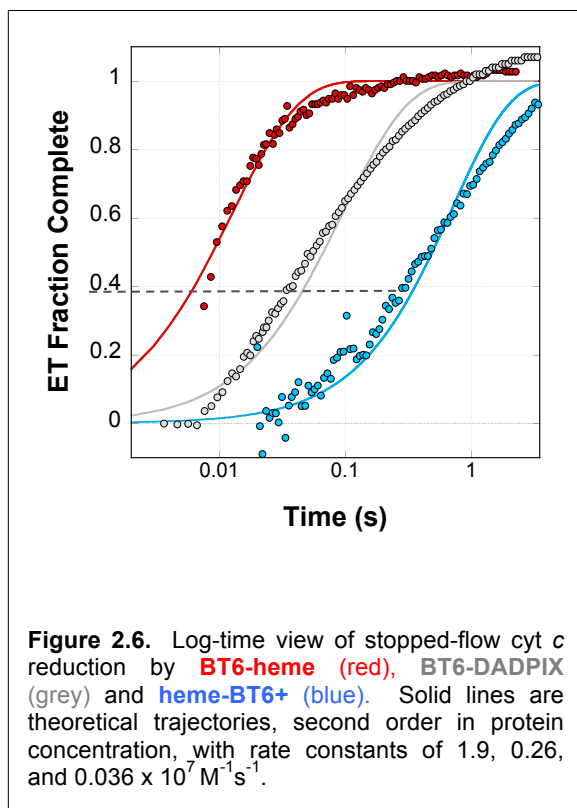
2.4 Results

2.4.1 Stopped-flow interprotein electron transfer

Figure 2.5 shows the spectral evolution of the heme Q-band region upon mixing reduced heme-BT6 with oxidized cyt *c*. This experiment is a simple mixing of two species in the stopped flow and does not involve CO photolysis. Over the 30 ms shown in the figure, the 560 nm feature of reduced B heme disappears and is replaced by the reduced α band of cyt *c* at 550 nm. This change is indicative of interprotein ET. The rate of cyt *c* reduction matches the rate of heme *b* oxidation, indicating that the cyt *c* is not being directly reduced by residual dithionite or some other electron source. (Furthermore, control experiments mixing oxidized cyt *c* with $\sim 20 \mu\text{M}$ dithionite yielded slower cyt *c* reduction over several hundred ms). The red points in **Figure 2.6** show the cyt *c* reduction on a log time scale, fit to a theoretical trajectory with a second order rate constant of $1.9 \times 10^7 \text{ M}^{-1}\text{s}^{-1}$. This is a fast electron transfer, as we would expect given that it is

highly exothermic ($\Delta G = -550$ meV) and that the monopole charges of the two reactants are complimentary.

The blue points in **Figure 2.6** show the ET results when BT6 (-20 net charge with 2 bound hemes) is replaced with the lysine-rich BT6+ variant (+7 net charge). The computed rate constant drops to 3.6×10^5 $M^{-1}s^{-1}$, 50-fold slower. There are two reasons to expect slower *cyt c*



reduction from BT6+ than from BT6. First, the midpoint potential of BT6+ is 150 mV greater, yielding a less exothermic but still quite favorable reaction ($\Delta G = -410$ meV). More importantly, the positive surface no longer compliments the charge of *cyt c*. The Moser-Dutton Ruler (**Eqn. 1.5**) predicts only a 3-fold decrease in rate for this change in energy change, suggesting that the change in electrostatic interaction makes the dominant contribution. We tested this hypothesis by replacing the heme cofactors of the original BT6 maquette (-20 charge) with the higher potential synthetic porphyrin DADPIX (**Figure 2.3**). ΔG for ET from BT6/DDADPIX \rightarrow *cyt c* is -400 meV, very

close to the -410 meV for BT6+/Heme \rightarrow *cyt c*. **Figure 2.6** show the results of *cyt c* reduction by BT6/DADPIX, fit to a second-order trajectory for a rate of 2.6×10^6 $M^{-1}s^{-1}$. This result is slower by about a factor of three than the Moser-Dutton prediction, assuming the driving force change to be the only difference between the BT6 / heme and BT6 / DADPIX systems. Nevertheless, it is clear that surface electrostatics play a significant role in the difference in the rates of *cyt c* reduction by BT6 / heme and BT6+ / heme.

2.4.2 BT6 CO flash photolysis

The CO flash photolysis method for inducing ET, detailed in **Chapter 3**, provides two important advantages over the simple stopped-flow mixing described above. First, the OLIS stopped-flow cannot resolve reactions faster than a few ms, making it unsuitable for the faster inter-protein ET rates at reduced ionic strength. Secondly, the process of titrating dithionite into the maquette sample to pre-reduce it while avoiding the presence of excess dithionite is challenging and difficult to repeat reliably. For these reasons we employed the CO-photolysis method for all the remaining experiments in this chapter. This section shows typical results at two ionic strengths and explains the spectral interpretation of these experiments.

In the absence of a gaseous ligand, two histidine N ϵ atoms ligate each BT6 heme. Bound O₂ or CO, if present, displaces one of these histidine sidechains [3, 11]. The heme maquette functions much like the natural hexacoordinate oxygen transporter neuroglobin. Upon absorbing a photon, a bound CO ligand photo-dissociates yielding a ferrous heme ligated by only a single histidine. This is seen as a red shift in the Soret difference spectrum (red spectrum **Figure 2.7**) with a 435 nm peak and an isosbestic at 427 nm. The heme iron undergoes ligand exchange

to rebind the second histidine in about a millisecond, yielding the typical B-heme reduced spectrum with a Soret peak around 429 nm (black spectrum in **Figure 2.7**). The isosbestic wavelength for this histidine rebinding event is 432 nm. Over the course of ~ 1 sec the

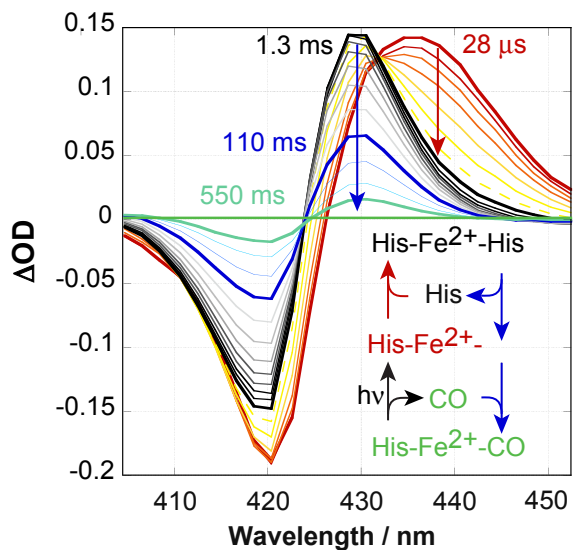


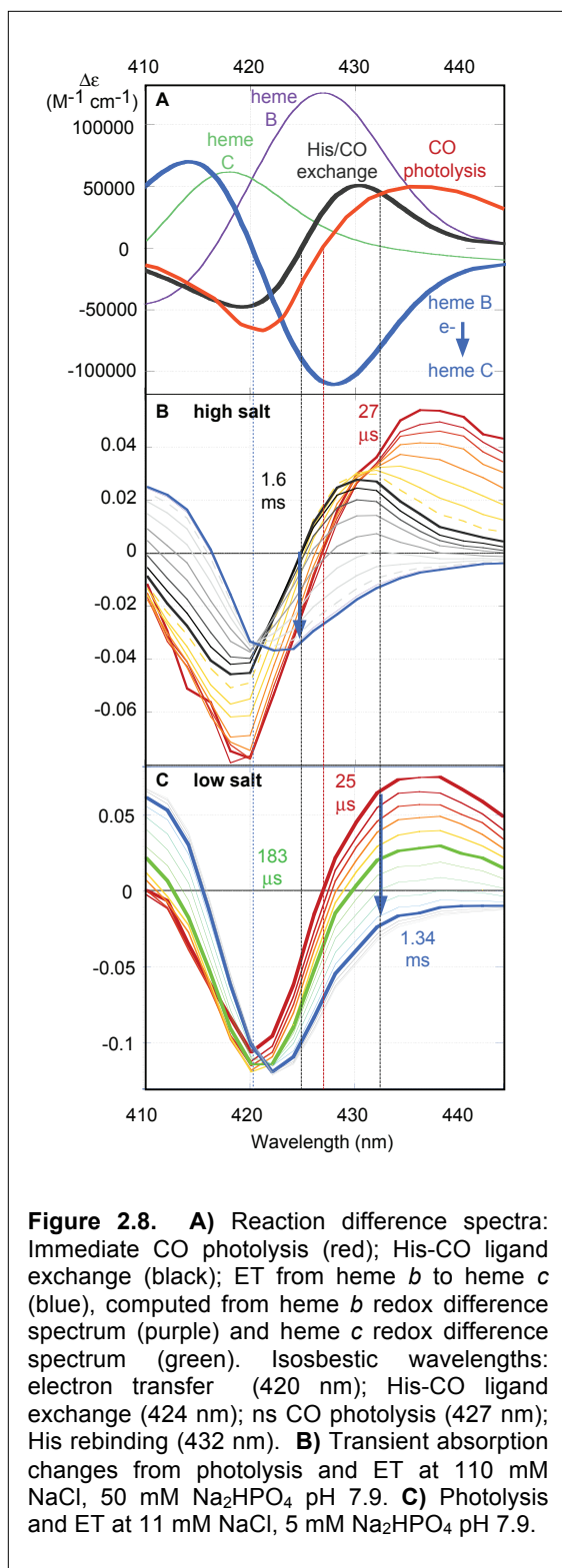
Figure 2.7. Soret region spectral changes following CO flash photolysis, relative to initial state with CO bound to reduced BT6. There is no ET in this system; this figure shows only CO photolysis, heme ligand exchange, and CO rebinding. Immediately after photolysis, the heme is in a **pentacoordinate state with only one histidine bound (red trace)**. The distal histidine rebinds in **about 1 ms (black trace)**. At minimal CO concentrations in the argon-purged sample, **CO slowly rebinds to restore the original pre-flash carboxy-heme state (green trace)**. Post-flash times are given for bold traces. 110 mM NaCl, 50 mM Na₂HPO₄, pH 7.9. The red arrow shows the evolution of the ligand exchange event, and the blue arrow shows CO rebinding and replacing the second Fe-ligating histidine.

dissociated CO returns (at low CO concentration), displacing the second histidine and restoring the original carboxy heme state. 424 nm is isosbestic for the CO-rebinding event. Dutton lab member Molly Sheehan has previously shown the BT6 unimolecular rate constants $k_{\text{His-on}}$ and $k_{\text{His-off}}$ and the bimolecular CO rebinding rate $k_{\text{CO-on}}$ to be 210 s^{-1} , 50 s^{-1} , and $4.3 \mu\text{M}^{-1}\text{s}^{-1}$ respectively[30].

Using this photolysis scheme, the observed CO photolysis yield was typically ~13%. This result was computed by comparing the transient absorption change at about 1 ms after histidine ligand exchange (black trace, **Figure 2.7**) to the difference between static reduced and carboxy-BT6 at the same protein concentration, as measured on the Varian spectrophotometer. The photolysis yield proved insensitive to small adjustments in the laser optics and to moderate reductions in laser intensity, suggesting that laser energy was not the limiting factor. Instead, the observed yield is probably limited by “geminate recombination” where a large fraction of the photolyzed CO re-binds to reduced heme on a sub- μs timescale that cannot be resolved by this apparatus[31]. Since the photolysis scheme was used to measure ET rates over a range of ionic strengths, we tested the photolysis yield at several salt concentrations. There was little change in yield between 5 mM Na_2HPO_4 / 11 mM NaCl and 50 mM Na_2HPO_4 / 330 mM NaCl. Interestingly, however, almost no photolysis was visible at 1.1 M NaCl despite robust binding of CO. Perhaps very high ionic strength induces a change in the protein structure that favors increased CO geminate recombination.

2.4.3 Photolysis-induced inter-protein electron transfer

Bound CO stabilizes the maquette heme, essentially raising its midpoint potential and rendering it incompetent to reduce *cyt c*. I did observe CO-bound BT6 to reduce *cyt c* over the timespan of a few minutes even in the absence of light, presumably due to the slow thermal dissociation of CO. In contrast, flash photolysis releases a large fraction of the bound CO molecules, making this BT6 population immediately available for energetically favorable ET. At the minimal CO concentrations in these experiments, CO recombination is significantly slower than the electron transfer. (**Figure 2.7** shows that the half-time for CO recombination is about 110 mS, while half-time for BT6 \rightarrow *cyt c* ET is ~ 9 ms in **Figure 2.6**). In the experiments that follow, the CO-bound ferrous maquette donor BT6 mixes with oxidized *cyt c* in the stopped-flow



apparatus about 200 ms prior to laser photo-activation, initiating CO photolysis and subsequent inter-protein electron transfer.

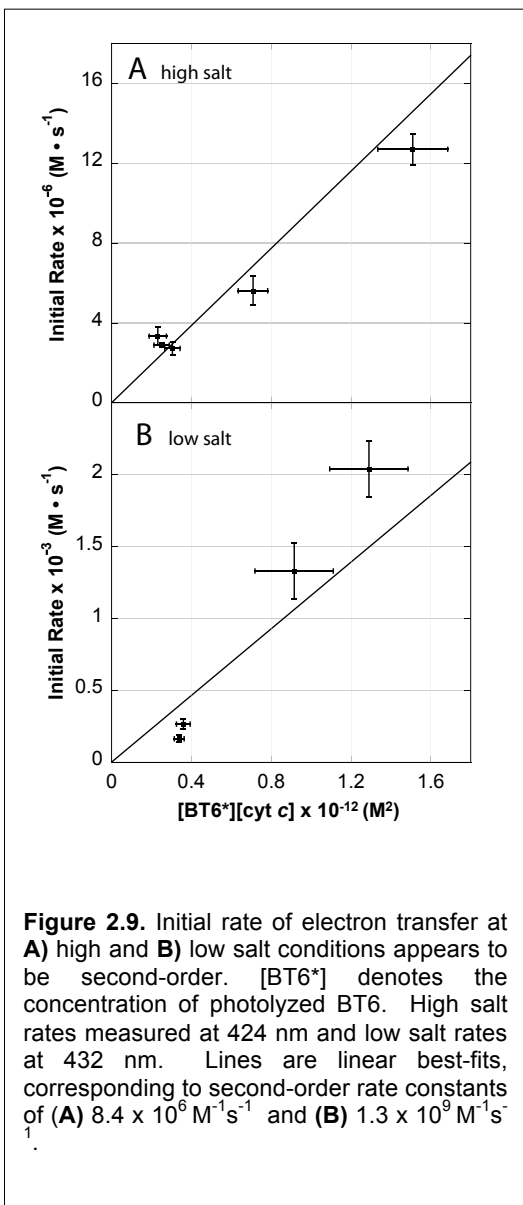
Figure 2.8 illustrates the spectral changes in photolysis-induced ET. **2.8-A** shows the difference spectra expected for CO photolysis (red), His-CO ligand exchange (black), and BT6 B heme to cyt *c* electron transfer (blue). The blue ET spectrum was computed by subtracting the redox difference spectrum of BT6 (purple) from the redox difference spectrum of cyt *c* (green).

Figure 2.8-B shows observed photolysis, ligand exchange, and electron-transfer kinetics under the high salt condition of 110 mM NaCl, 50 mM Na₂HPO₄ pH 7.9. The ~260 mM ionic strength for this environment is somewhat greater than typical *in vivo* conditions. In this regime the inter-protein ET is significantly slower than the ~1 ms histidine ligand exchange directly following CO photolysis, and the two processes are easily distinguishable by eye (red / yellow traces dominated by ligand exchange vs. black / gray traces dominated by ET). As explained in **Section 2.3.5**, photolysis yield was measured at 1 ms at 420 nm, a wavelength isobestic for ET ($\Delta\epsilon_{\text{his-on},420} = -44000 \text{ M}^{-1}\text{cm}^{-1}$). The ET process was tracked at 424 nm, isobestic for CO recombination ($\Delta\epsilon_{\text{ET},424} = -90000 \text{ M}^{-1}\text{cm}^{-1}$).

Figure 2.8-C illustrates CO photolysis-

induced ET at the low salt condition of 11 mM NaCl, 5 mM Na₂HPO₄ pH 7.9. ET is much faster

in this ionic strength regime, at least as fast as the characteristic ms time for His rebinding. In comparison to ET, the CO rebinding rate is negligible. Thus, to track ET we measure change at the ligand exchange isosbestic of 432 nm since this wavelength is insensitive to the simultaneously histidine rebinding ($\Delta\epsilon_{\text{ET},424} = -90000 \text{ M}^{-1}\text{cm}^{-1}$).



2.4.4. Concentration dependence of ET rates

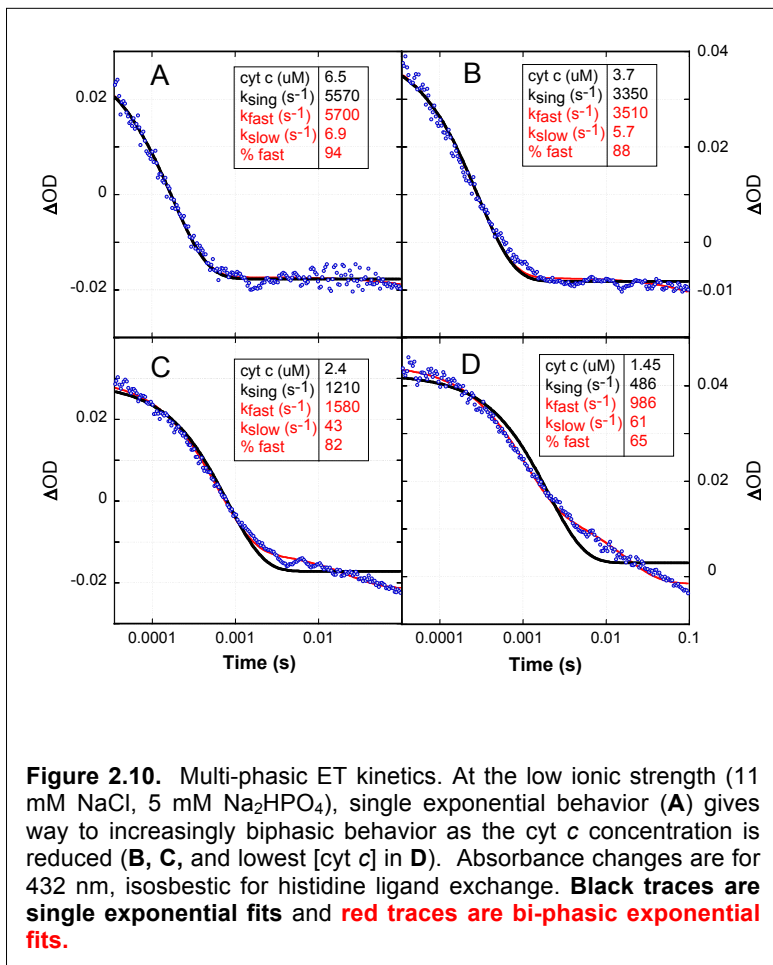
Figure 2.9 shows the initial ET rates as a function of the product of the concentrations of cyt *c* and flash-photolyzed, ET-competent BT6 (“BT6*”). The initial rates for the high salt conditions are shown in **Figure 2.9-A**, fit to a second-order rate constant of $9.7 \times 10^6 \text{ M}^{-1}\text{s}^{-1}$. For each experiment the ET trajectories fit well to a simple exponential function (not shown). Exponential behavior is unsurprising in the system since in each case [cyt *c*] is in significant excess when compared to [BT6*]. At the minimal [cyt *c*] value tested here, the [cyt *c*]:[BT6] ratio is 1::2. However, given a 17% photolysis yield computed for this experiment, the effective ratio for ET-competent maquettes becomes 3.4::1, large enough for the reaction to approach pseudo-first order behavior.

The low-salt kinetics in **Figure 2.9-B** are much faster, with a best-fit second-order rate constant of $1.2 \times 10^9 \text{ M}^{-1}\text{s}^{-1}$ approaching the diffusion limit[32]. This very high rate may follow

from ET within pre-formed multi-molecular complexes rather than between freely diffusing molecules, as discussed in **Section 2.5**. As in the high-salt experiments, we would expect the trajectories to mimic simple exponentials in each case, given the excess of [cyt *c*] in comparison

to [BT6*]. **Figure 2.10** plots the 432 nm ET trajectories for low-salt experiment, along with single and double best-fit exponentials. The double exponential functions are of the form:

$$f(t) = f_0 - A_{fast} \exp(-k_{fast} t) - A_{slow} \exp(-k_{slow} t) \quad \text{Eqn. 2.1}$$



The “% fast” values given for each biphasic fit in **Figure 2.10** correspond to the ratio of $A_{fast}/(A_{fast} + A_{slow})$. As [cyt c] is reduced, the “% fast” value falls, indicating that a single fast exponential function offers a less accurate description of the behavior as the slower phase becomes more significant. This suggests that some cyt c may be associated with CO-bound maquettes when the laser flash occurs; these cyt c molecules would need to dissociate and diffuse to photolyzed maquettes before they could be reduced. This

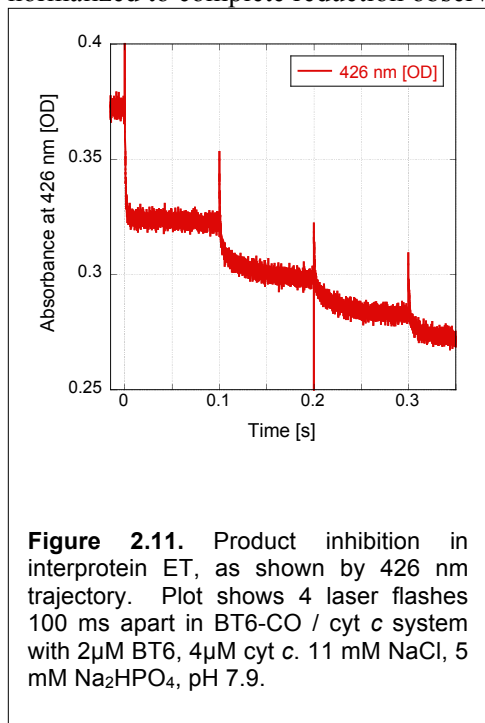
behavior would tend to reduce the observed initial rate at lower [cyt c] concentrations, consistent with the low-concentration points lying below the linear fit in **Figure 2.9-B**.

Figure 2-11 illustrates an additional point supporting the hypothesis that BT6 and cyt c form complexes at low ionic strength. This plot shows the absorbance changes at 426 nm associated with a series of four repeated laser flashes separated by 100 ms. (This data was taken on a preliminary experimental setup with only 1 ms resolution and significant flash artifacts). The first flash shows a fast absorbance change ending in a few ms. Subsequent flashes, however,

show a notable slow phase extending for many ms after the flash. This suggests product inhibition, where some activated maquettes are associated with already-reduced *cyt c* after the first flash; the slow phase corresponds to the time needed for them to dissociate and diffuse to an oxidized, ET-competent partner. Similar behavior has been reported for bacterial photosynthetic bacterial reaction centers and *cyt c*₂ at low ionic strength[33].

2.4.5 Ionic strength dependence of inter-protein electron transfer

Figure 2.12-A shows the ET timecourses after BT6 photolysis for a range of ionic strengths between the “high-salt” and “low-salt” conditions discussed above. Kinetics are normalized to complete reduction observed at 100 ms. At the lowest ionic strength (11 mM NaCl,



5 mM Na₂HPO₄), the halftime for the electron transfer is about 160 μs and the reaction is essentially complete in 2 ms. The ionic strength in the photolysis experiment at 70 mM NaCl and 32 mM Na₂HPO₄ (**Figure 2.11**, light green trace) is similar to that in the mixing experiments at 120 mM NaCl and 50 mM HEPES (**Figure 2.6**). Treating the light green trace as a simple exponential as a pseudo-first order with excess *cyt c*, the photolysis experiment exhibits a second-order rate constant of $3.3 \times 10^7 \text{ M}^{-1}\text{s}^{-1}$. This agrees reasonably well with the $1.9 \times 10^7 \text{ M}^{-1}\text{s}^{-1}$ fit for the simple mixing trajectory, confirming that there is no large inherent difference between these two measurement schemes.

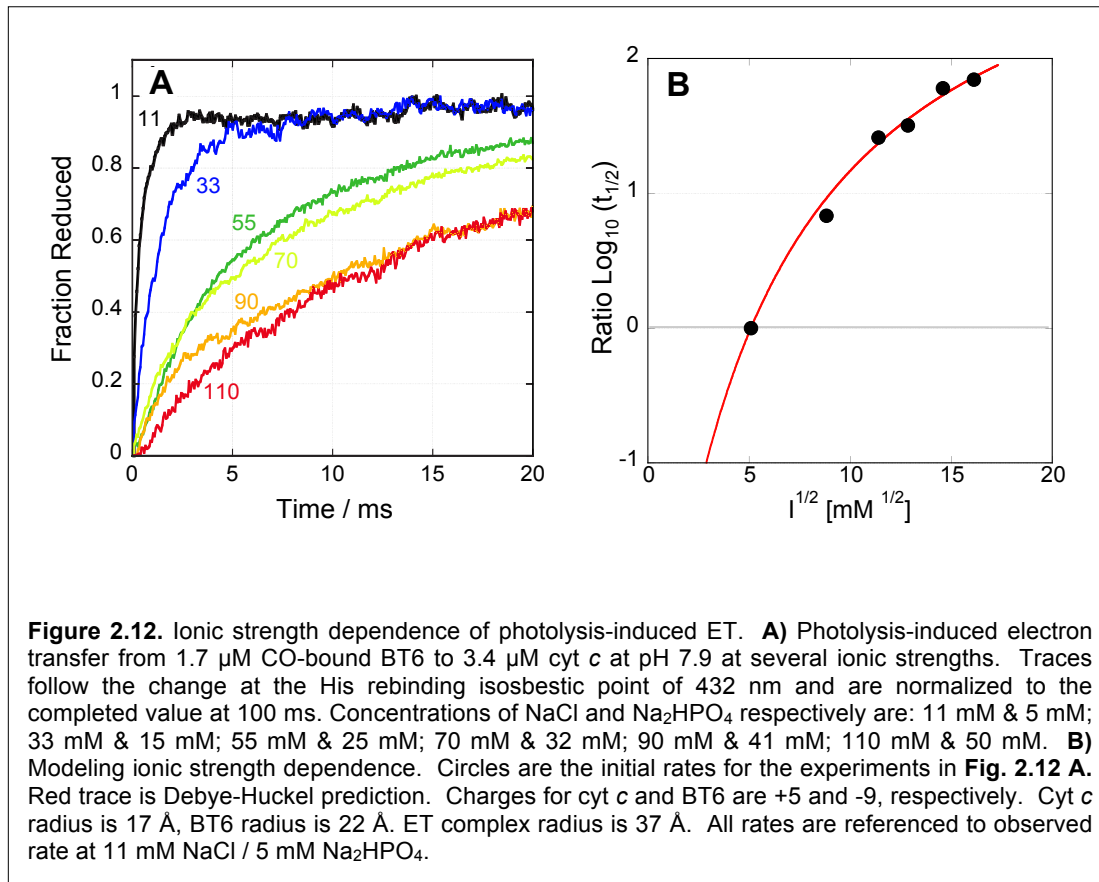


Figure 2.12-B plots the logarithm of each trajectory's half-time against the square root of the ionic strength. The log is expressed in terms of a ratio referenced to the lowest ionic-strength experiment (11 mM NaCl and 5 mM Na_2HPO_4). Assuming that the half-time is inversely proportional to the reaction rate, the red line shows the same ratio predicted by the Brønsted-Debye-Hückel relation (**Eqn 1.6**) for the following parameters: Cyt *c* radius = 17 Å [34], BT6 = 22 Å, ET complex radius = 37 Å, and charges for cyt *c* and BT6 are +5 and -9, respectively. The model does provide a reasonable fit using these parameters, but the protein charges inferred from this analysis are unrealistically small. One possible explanation for this discrepancy could be the presence of the phosphate buffer in the experiments. At the pH 7.9 the phosphate ions are primarily divalent (HPO_4^{2-}), and some experiments have suggested that this species may bind somewhat specifically to cyt *c*[35], possibly reducing the effective charge. This hypothesis could be tested by repeating the experiments in a monovalent buffer. Phosphate was chosen because

unlike organic buffers it is always redox-inactive, but in retrospect HEPES or TRIS would have been the better choice.

2.5 Discussion

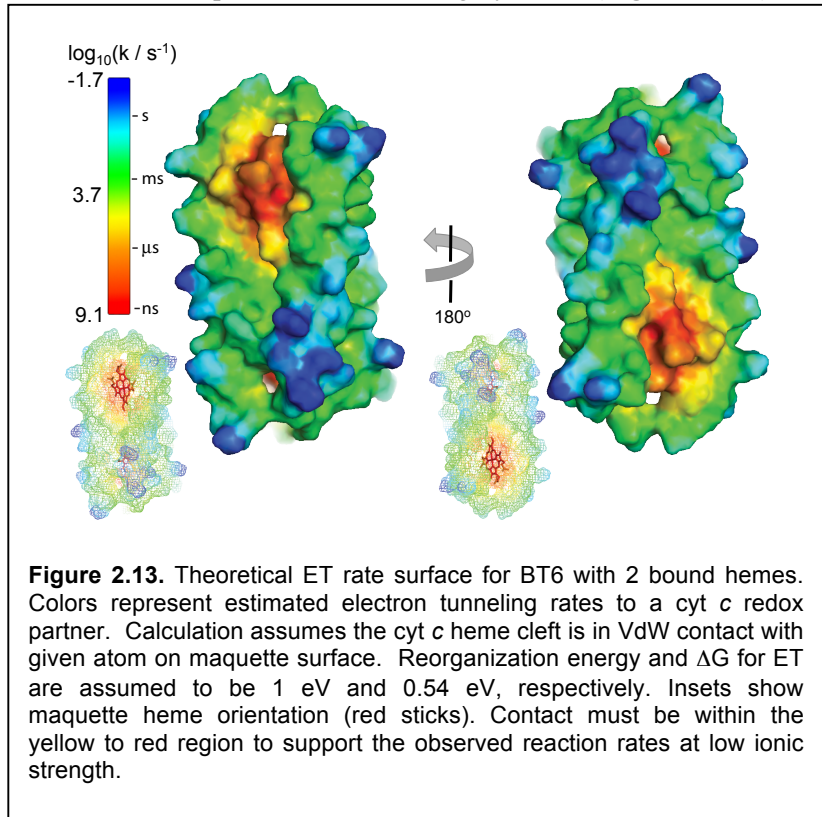
The initial experiments presented in **Section 2.4.1** give the first published report of interprotein ET between synthetic and natural protein redox partners. It has long been understood that successful ET between natural proteins can be guided by complimentary surface electrostatics [34, 36, 37]. By comparing cyt *c* reduction from charge-complimentary BT6 and anti-complimentary BT6+ maquettes, we conclude that this general principle also applies to ET between engineered maquettes and natural electron transporters.

BT6 reacts with cyt *c* sufficiently quickly for effective function *in vivo*. Indeed, it is fast enough that simple stopped-flow measurements provide inadequate time resolution and the faster method of CO photolysis-initiated electron transfer is needed to describe the ionic strength dependence of the reaction. The photoreduction of cyt *c* by CO-bound maquette BT6 is analogous to the natural diffusive photooxidation of cyt *c* by bacterial photosynthetic reaction centers [43]. Photo-excited reaction centers of *Rhodobacter sphaeroides* oxidize cyt *c* with a second-order rate constant of $1.4 \times 10^8 \text{ M}^{-1}\text{s}^{-1}$ in 30 mM NaCl, 10 mM Tris [33], similar to the $1.8 \times 10^8 \text{ M}^{-1}\text{s}^{-1}$ observed between **1** and cyt *c* at 33 mM NaCl, 15 mM K_2HPO_4 pH 7.9 (**Figure 2.12**, blue trace). Because not every contact between BT6 and cyt *c* will have appropriate distances for rapid electron transfer, we expect electrostatic attraction to increase the effective collisional frequency and significantly enhance the electron-transfer rate.

There are differing views on the precision of the electrostatic interactions required by biological electron-transfer networks, ranging from specific arrangements of inter-protein amino acid salt bridges[38] to a broader delocalized charge complimentarity [39]. We propose that the maquette-cyt *c* electron-transfer system supports the latter view. **Figure 2.13** displays the expected first-order electron-tunneling rates from BT6 to an optimally-oriented cyt *c* located at points along the maquette surface. These rates were computed from a Python script that measured the distance from each surface atom on the maquette to the nearest heme ring atom, and then added 9 Å to account for the estimated Van der Waals packing of the cyt *c* heme cleft. From this result, we may infer that productive electron transfer at low salt conditions is limited to cyt *c*

heme edge contacting a maximum of 15%-20% of the maquette surface; these are the yellow through red regions with a calculated half-time less than 200 μs as observed in the low-salt experiments. As this is a significant fraction of the maquette surface, there was no need to design a highly specific docking site for successful ET beyond a coarse scale electrostatic attraction.

At the high salt condition, the concentration dependence of initial ET rates is well fit by a linear relation, indicating a diffusive second-order reaction (**Figure 2.9-A**). At the low salt condition, this dependence is also roughly linear (**Figure 2.9-B**). However, several observations



call into question the possibility of a freely diffusing system at this low ionic strength. First, the best fit for a second-order reaction is extremely fast at $1.3 \times 10^9 \text{ M}^{-1}\text{s}^{-1}$. Second, as shown in **Figure 2-10**, these timecourses begin to take on biphasic character as the concentration of *cyt c* is reduced. Finally, the initial rates for the greater [*cyt c*] experiments are faster than predicted by a

linear relation. All of these features are consistent with a fraction of maquettes and *cyt c* partners that are “pre-bound” in loose complexes prior to CO release. No *cyt c* binding site was explicitly designed in the BT6 protein. However, it does exhibit a strong and relatively uniform negative surface charge complementing the lysine-rich heme pocket of *cyt c*. As **Figure 2.13** shows a large portion of the surface appears to be able to theoretically support fast ET, based on the Moser-Dutton relation. **Figure 2.14** shows a hypothetical construct in which four separate *cyt c* molecules are docked to a single two-heme maquette. This figure highlights the possibility that observed ET rates could increase roughly linearly with excess [*cyt c*] up to a 1:4 molar ratio even if the protein population is dominated by associated complexes rather than by freely diffusing

reactants. The experiments presented here do not conclusively distinguish between these possibilities at low ionic strength. In principle, reducing both reactant concentrations while maintaining low ionic strength could help to resolve this question. As the protein concentration drops below the K_d for complex dissociation, we would expect to see more pronounced biphasic character that ultimately is dominated by a slower diffusional phase. Further refinements in the apparatus would likely be needed to resolve the smaller OD changes expected in such experiments.

Another interesting open question is how the ligation state of post-photolysis maquette heme impacts the rate of cyt *c* reduction. **Figure 2.7** shows that after CO photolysis, a pentacoordinate heme state ligated by a single histidine Ne persists for up to a ms. This transient state is probably insignificant at the high ionic strength condition where the half-time for cyt *c* reduction is 10 or more ms; most of the reduced heme will have reverted to standard bis-his coordination prior to ET. However, this assumption is invalid at the low-salt condition where the cyt *c* reduction rate is comparable (or faster) than ligand exchange. In general, the midpoint potential for pentacoordinate globins such as myoglobin is greater than for hexacoordinate globins like GLB-12 or neuroglobin [40], [41]. This would serve to reduce the ET driving force. Directly measuring the pentacoordinate E_m in BT6

could prove challenging, since past attempts to bind heme in an obligate pentacoordinate single-His BT6 site have proven unsuccessful.

In conclusion, the results discussed here show the redox reactions between BT6 and cyt *c* share two major features with most physiological interprotein ET. First, complimentary monopole

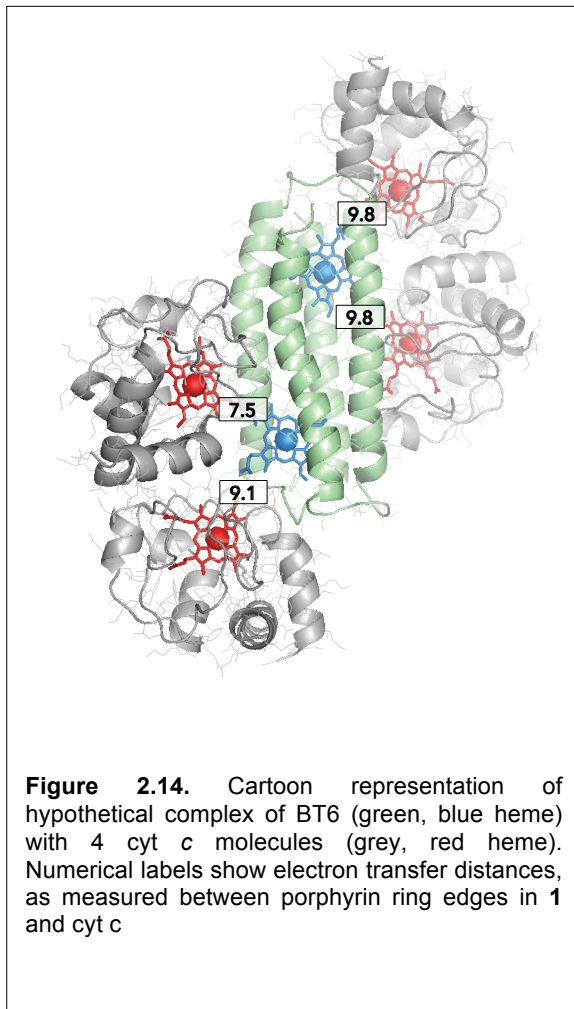


Figure 2.14. Cartoon representation of hypothetical complex of BT6 (green, blue heme) with 4 cyt *c* molecules (grey, red heme). Numerical labels show electron transfer distances, as measured between porphyrin ring edges in 1 and cyt *c*

charge distributions play an important role. Second, the reaction rate depends strongly on ionic strength (although the ionic strength dependence is less pronounced than the Debye-Huckel relation would predict). Other maquette designs allow a more detailed investigation into this interaction. The “GL” proteins introduced in **Chapter 4** display significant dipolar character. In lieu of CO-bound heme, the GL maquettes employ a light-activated synthetic cofactor to reduce cyt *c* directly from an excited electronic state. This avoids the spectroscopic complications of ligand rearrangement in analyzing the kinetics, along with questions of E_m for the transient post-photolysis pentacoordinate heme state.

2.6 References

- [1] S. Fergusonmiller, D.L. Brautigan, E. Margoliash, Correlation Of Kinetics Of Electron-Transfer Activity Of Various Eukaryotic Cytochromes-C With Binding To Mitochondrial Cytochrome-C Oxidase, *Journal of Biological Chemistry*, 251 (1976) 1104-1115.
- [2] N.A. Baker, D. Sept, S. Joseph, M.J. Holst, J.A. McCammon, Electrostatics of nanosystems: Application to microtubules and the ribosome, *Proceedings of the National Academy of Sciences of the United States of America*, 98 (2001) 10037-10041.
- [3] T.A. Farid, G. Kodali, L.A. Solomon, B.R. Lichtenstein, M.M. Sheehan, B.A. Fry, C. Bialas, N.M. Ennist, J.A. Siedlecki, Z. Zhao, M.A. Stetz, K.G. Valentine, J.L.R. Anderson, A.J. Wand, B.M. Discher, C.C. Moser, P.L. Dutton, Elementary tetrahelical protein design for diverse oxidoreductase functions, *Nature Chemical Biology*, 9 (2013) 826-+.
- [4] A. Fago, A.J. Mathews, L. Moens, S. Dewilde, T. Brittain, The reaction of neuroglobin with potential redox protein partners cytochrome b(5) and cytochrome c, *Febs Letters*, 580 (2006) 4884-4888.
- [5] C.E. Lubner, R. Grimme, D.A. Bryant, J.H. Golbeck, Wiring Photosystem I for Direct Solar Hydrogen Production, *Biochemistry*, 49 (2010) 404-414.
- [6] C.E. Lubner, P. Knorz, P.J.N. Silva, K.A. Vincent, T. Happe, D.A. Bryant, J.H. Golbeck, Wiring an FeFe -Hydrogenase with Photosystem I for Light-Induced Hydrogen Production, *Biochemistry*, 49 (2010) 10264-10266.
- [7] A. Roy, D.J. Sommer, R.A. Schmitz, C.L. Brown, D. Gust, A. Astashkin, G. Ghirlanda, A De Novo Designed 2 4Fe-4S Ferredoxin Mimic Mediates Electron Transfer, *Journal of the American Chemical Society*, 136 (2014) 17343-17349.
- [8] B.A. Fry, L.A. Solomon, P.L. Dutton, C.C. Moser, Design and engineering of a man-made diffusive electron-transport protein, *Biochimica Et Biophysica Acta-Bioenergetics*, 1857 (2016) 513-521.
- [9] N. Mirkin, J. Jaconic, V. Stojanoff, A. Moreno, High resolution X-ray crystallographic structure of bovine heart cytochrome c and its application to the design of an electron transfer biosensor, *Proteins-Structure Function and Bioinformatics*, 70 (2008) 83-92.
- [10] L.A. Solomon, G. Kodali, C.C. Moser, P.L. Dutton, Engineering the assembly of heme cofactors in man-made proteins, *J Am Chem Soc*, 136 (2014) 3192-3199.
- [11] R.L. Koder, J.L. Anderson, L.A. Solomon, K.S. Reddy, C.C. Moser, P.L. Dutton, Design and engineering of an O(2) transport protein, *Nature*, 458 (2009) 305-309.
- [12] J.L.R. Anderson, C.T. Armstrong, G. Kodali, B.R. Lichtenstein, D.W. Watkins, J.A. Mancini, A.L. Boyle, T.A. Farid, M.P. Crump, C.C. Moser, P.L. Dutton, Constructing a man-made c-type cytochrome maquette in vivo: electron transfer, oxygen transport and conversion to a photoactive light harvesting maquette, *Chemical science*, 5 (2014) 507-514.
- [13] J.S.a.S. Haldane, L., *Journal of Physiology*, 20 (1896).
- [14] Q.H. Gibson, Hemoproteins, Ligands, And Quanta, *Journal of Biological Chemistry*, 264 (1989) 20155-20158.
- [15] B. Chance, N. Graham, V. Legallais, Low-Temperature Trapping Method For Cytochrome-Oxidase Oxygen Intermediates, *Analytical Biochemistry*, 67 (1975) 552-579.
- [16] J.S. Kim, D.C. Rees, Structural Models For The Metal Centers In The Nitrogenase Molybdenum-Iron Protein, *Science*, 257 (1992) 1677-1682.
- [17] J.A.M. G. Kodali, L. A. Solomon, T. Episova, N. Roach, C. J Hobbs, P. Wagner, O. A. Mass, K. Aravindu, J. E. Barnsley, K. Gordon, D. L. Officer, P. L. Dutton, C. C. Moser Design and

- engineering of water-soluble light-harvesting protein maquettes *Chemical Science* (In Review), (2016).
- [18] H. Tian, R. Sadoski, L. Zhang, C.A. Yu, L. Yu, B. Durham, F. Millett, Definition of the interaction domain for cytochrome c on the cytochrome bc(1) complex - Steady-state and rapid kinetic analysis of electron transfer between cytochrome c and *Rhodobacter sphaeroides* cytochrome bc1 surface mutants, *Journal of Biological Chemistry*, 275 (2000) 9587-9595.
- [19] S. Ferguson-Miller, D.L. Brautigan, E. Margoliash, Correlation Of Kinetics Of Electron-Transfer Activity Of Various Eukaryotic Cytochromes-C With Binding To Mitochondrial Cytochrome-C Oxidase, *Journal of Biological Chemistry*, 251 (1976) 1104-1115.
- [20] M.S. Caffrey, M.A. Cusanovich, The Effects Of Surface-Charges On The Redox Potential Of Cytochrome-C2 From The Purple Phototrophic Bacterium *Rhodobacter-Capsulatus*, *Archives of Biochemistry and Biophysics*, 285 (1991) 227-230.
- [21] E.A. Berry, B.L. Trumpower, Simultaneous determination of hemes a, b, and c from pyridine hemochrome spectra, *Anal Biochem*, 161 (1987) 1-15.
- [22] T.A. Farid, Engineering a artificial, multifunctional oxidoreductase protein maquette, Publicly accessible Penn Dissertations, (2012).
- [23] E. Margoliash, N. Frohwirt, Spectrum Of Horse-Heart Cytochrome-C, *Biochemical Journal*, 71 (1959) 570-578.
- [24] J.G.P.i. Peter D. Wildes, Gether Irick, Jr., D. G. Whitten, Solvent and Substituent Effects on the Thermal Isomerization of Substituted Azobenzenes. A Flash Spectroscopic Study, *Journal of the American Chemical Society*, 93 (1971).
- [25] L. Schrodinger, The PyMOL molecular graphics system, Version 13r1, (2010).
- [26] H.J.C. Berendsen, D. Vandespoel, R. Vandrunen, GROMACS - A Message-Passing Parallel Molecular-Dynamics Implementation, *Computer Physics Communications*, 91 (1995) 43-56.
- [27] A. Sali, T.L. Blundell, Comparative Protein Modeling By Satisfaction Of Spatial Restraints, *Journal of Molecular Biology*, 234 (1993) 779-815.
- [28] N. Mirkin, J. Jaconcic, V. Stojanoff, A. Moreno, High resolution X-ray crystallographic structure of bovine heart cytochrome c and its application to the design of an electron transfer biosensor, *Proteins*, 70 (2008) 83-92.
- [29] C.C. Page, C.C. Moser, X.X. Chen, P.L. Dutton, Natural engineering principles of electron tunnelling in biological oxidation-reduction, *Nature*, 402 (1999) 47-52.
- [30] M.M. Sheehan, Engineering oxygen reactivity in heme-protein maquettes, Publicly accessible Penn Dissertations, (2014).
- [31] E.R. Henry, J.H. Sommer, J. Hofrichter, W.A. Eaton, Geminate Recombination Of Carbon-Monoxide To Myoglobin, *Journal of Molecular Biology*, 166 (1983) 443-451.
- [32] R.A. Alberty, G.G. Hammes, Application Of The Theory Of Diffusion-Controlled Reactions To Enzyme Kinetics, *Journal of Physical Chemistry*, 62 (1958) 154-159.
- [33] C.C. Moser, P.L. Dutton, Cytochrome-C And Cytochrome-C2 Binding-Dynamics And Electron-Transfer With Photosynthetic Reaction Center Protein And Other Integral Membrane Redox Proteins, *Biochemistry*, 27 (1988) 2450-2461.
- [34] J.W. van Leeuwen, The Ionic-Strength Dependence Of The Rate Of A Reaction Between 2 Large Proteins With A Dipole-Moment, *Biochimica et biophysica acta*, 743 (1983) 408-421.
- [35] G. Taborsky, K. McCollum, Phosphate Binding By Cytochrome-C - Specific Binding-Site Involved In The Formation And Reactivity Of A Complex Of Ferricytochrome-C, Ferrous Ion, And Phosphate, *Journal of Biological Chemistry*, 254 (1979) 7069-7075.
- [36] W.H. Koppenol, C.A.J. Vroonland, R. Braams, Electric-Potential Field Around Cytochrome-C And Effect Of Ionic-Strength On Reaction-Rates Of Horse Cytochrome-C, *Biochimica et biophysica acta*, 503 (1978) 499-508.

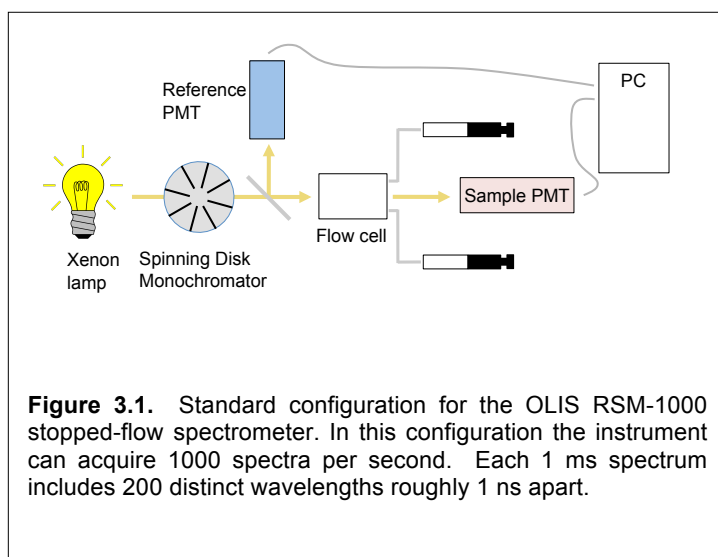
- [37] D.W. Dixon, X. Hong, S.E. Woehler, Electrostatic And Steric Control Of Electron Self-Exchange In Cytochromes C, C551, And B5, *Biophysical Journal*, 56 (1989) 339-351.
- [38] E. Margoliash, H.R. Bosshard, Guided By Electrostatics, A Textbook Protein Comes Of Age, *Trends in Biochemical Sciences*, 8 (1983) 316-320.
- [39] D.M. Tiede, A.C. Vashishta, M.R. Gunner, Electron-Transfer Kinetics And Electrostatic Properties Of The Rhodobacter-Sphaeroides Reaction Center And Soluble C-Cytochromes, *Biochemistry*, 32 (1993) 4515-4531.
- [40] S. De Henau, L. Tilleman, M. Vangheel, E. Luyckx, S. Trashin, M. Pauwels, F. Germani, C. Vlaeminck, J.R. Vanfleteren, W. Bert, A. Pesce, M. Nardini, M. Bolognesi, K. De Wael, L. Moens, S. Dewilde, B.P. Braeckman, A redox signalling globin is essential for reproduction in *Caenorhabditis elegans*, *Nature Communications*, 6 (2015).
- [41] L. Kiger, L. Tilleman, E. Geuens, D. Hoogewijs, C. Lechauve, L. Moens, S. Dewilde, M.C. Marden, Electron Transfer Function versus Oxygen Delivery: A Comparative Study for Several Hexacoordinated Globins Across the Animal Kingdom, *Plos One*, 6 (2011).

Chapter 3 Photolysis-Induced Electron Transfer Apparatus

3.1 Background

In this chapter I describe and validate hardware modifications to the Dutton laboratory's OLIS stopped-flow spectrometer. The CO-photolysis data presented in **Chapter 2** and published in [1] were acquired using this modified spectrometer system. No new scientific conclusions are presented in this chapter. Instead it presents an extended discussion and validation of the experimental methods employed for these experiments.

Figure 3.1 illustrates the standard configuration of the OLIS RSM-1000 spectrometer. Two air-driven pistons drive the sample through a mixing jet and into a 2 cm-pathlength flow cell.



Two photomultiplier tubes (PMTs) capture light at a given wavelength before and after the sample, and both of these PMTs are captured by a digitizer card in the PC. The only unusual feature is this arrangement is a “spinning disk monochromator,” a wheel with thin slits near its periphery that slice through the probe beam downstream of the fixed monochromator. This allows the

instrument to quickly sample many wavelengths.

This system is ideal for providing broad spectral resolution on a ms timescale but is not sufficient to resolve the fast kinetics of interprotein ET at low ionic strength. There are two kinetic limitations. The first is “dead-time” imposed by the plumbing of the stopped-flow apparatus. Since the reaction begins during the initial turbulent mixing before the samples enter the flow cell, the first ~3 ms of the reaction cannot be resolved. Even in a specialized low-volume stopped-flow apparatus designed specifically to minimize this deadtime, the first ~100 μ S

is unavailable. [3]. The second limitation is in the spinning disk monochromator, which samples each wavelength at minimal interval of 1 ms.

Using flash photolysis rather than mixing to initiate the reaction overcomes dead-time limitation. The second limitation, imposed by the speed of the spinning disk monochromator, can in principle be overcome by simply replacing the disk with a fixed slit, passing only a single narrow wavelength band. This is a trivial change, but unfortunately the OLIS electronics do not support acquiring both the sample and reference PMTs together at less than a 100 μ S sample time. However, I was able to achieve a sample time of 1 μ S by using the OLIS digitizer and an oscilloscope to capture the sample and reference PMTs, respectively. These modifications are detailed below.

3.2 Spectrometer Modifications

As discussed in section 2.2, the reduced hemes in the BT6 maquette readily bind CO. This raises heme E_m such that direct ET from carboxy-BT6 to cyt *c* becomes negligible. As in natural globins, the CO is subject to photolysis upon heme excitation [4]. The “naked” ferro-BT6 becomes ET-competent upon CO photolysis. Thus, carboxy-BT6 offers a system for photoactivatable reduction of cyt *c* with a fast laser pulse to initiate ET, avoiding the limitation imposed by stopped-flow dead-time. In this setup, the stopped-flow syringes are loaded with carboxy-BT6 and oxidized cyt *c*. A Spectra Physics frequency-doubled Nd::YAG laser was pulsed at 10 Hz. A mechanical shutter (Thor Labs) is triggered to deliver one or more laser pulses to the flow cell 200 mS after the stopped-flow has fired.

Figure 3.2 shows photolysis-induced ET from 22 μ M carboxy-BT6 to 44 μ M oxidized cyt *c* at a range of salt concentrations. These data were acquired at 1 mS intervals using the spinning-disk monochromator. These experiments yield well-defined trajectories even at the first mS following

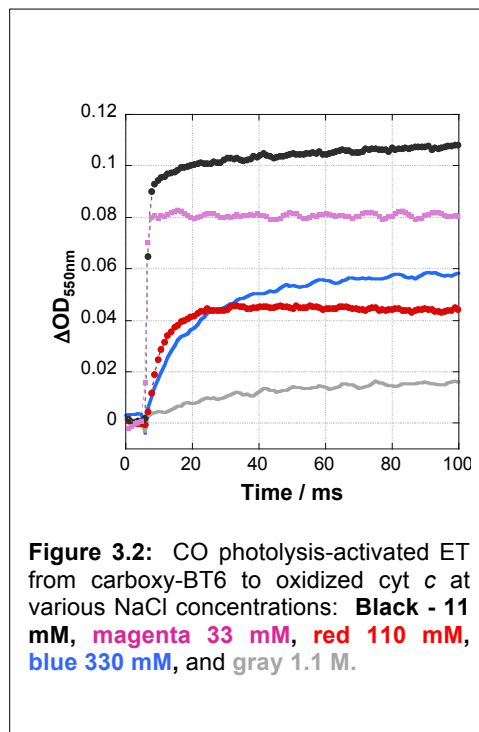


Figure 3.2: CO photolysis-activated ET from carboxy-BT6 to oxidized cyt *c* at various NaCl concentrations: **Black - 11 mM**, **magenta 33 mM**, **red 110 mM**, **blue 330 mM**, and **gray 1.1 M**.

the laser excitation, in contrast to the 3 ms dead-time seen with the simple stopped-flow method.

Monochrometer	PMTs digitized	Min. Sampling Interval
Spinning disk	Sample + Ref	1 mS
Fixed slit	Sample + Ref	100 μ S
Fixed slit	Sample only	1 μ S

Table 3.1. OLIS spectrometer configurations.

However, the reference PMT is still operational and so can be acquired by another device. I connected a Tektronix DPO2024B oscilloscope to capture the reference PMT signal, triggered by the same signal driving the laser shutter. Since this arrangement acquires only one wavelength at a time, the fixed slit monochrometer cycles through a range of wavelengths for each experiment: 430 nm to 400 nm to cover the Soret range of the hemes *b* and *c*. A 450 nm short-wave pass optical filter was placed in front of the sample PMT. This diminishes scattered 532 nm laser light reaching the PMT without impacting the probe beam in the Soret wavelength range, although additional processing was still needed to remove the residual flash artifact (see **Section 3.3**). After the experiment was completed, a Python script reads the saved sample and reference PMT voltage records at each wavelength and processes them to remove flash artifacts and compute μ S Δ OD values. **Figure 2.4** (*previous chapter*) illustrates these hardware changes.

However, the 1 mS sampling time used here is too slow to resolve the trajectories for lower ionic strengths.

Table 3.1 summarizes the sampling rate limits for the OLIS device. Clearly the 1 μ S sampling rate is desirable to resolve fast kinetics, but the OLIS software will only digitize the sample PMT output in this case.

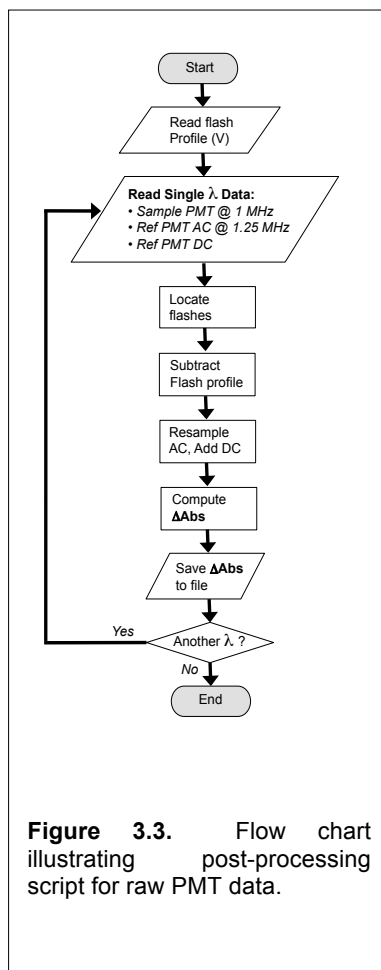
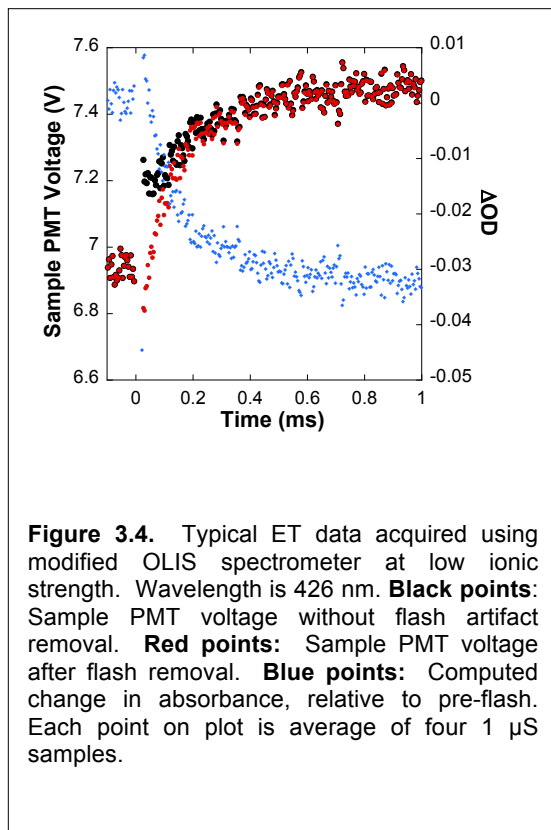


Figure 3.3. Flow chart illustrating post-processing script for raw PMT data.

3.3 Post-Processing Script

Figure 3.3 summarizes the functions of the post-processing script in a flow chart. First, one or more saved “flash profiles” file read from file. These are raw sample PMT voltage trajectories where the laser is pulsed several times with only water in the flow cell. The script identifies the flashes and averages 10 ms of data after each to form a profile of the voltage flash artifact. Additional profiles are provided if the high-voltage supply to the sample PMT is changed over the course of the experiment.

For each wavelength, three data files are read from file: the sample PMT signal (1 μ S sample interval from digitizer card), the AC component of the reference PMT signal (800 ns interval from oscilloscope), and the DC component of the reference PMT. Next, laser flashes are located in the sample PMT signal, and the flash profile is subtracted at each location. The DC component of the reference PMT is averaged and then added to the AC component. Finally, the



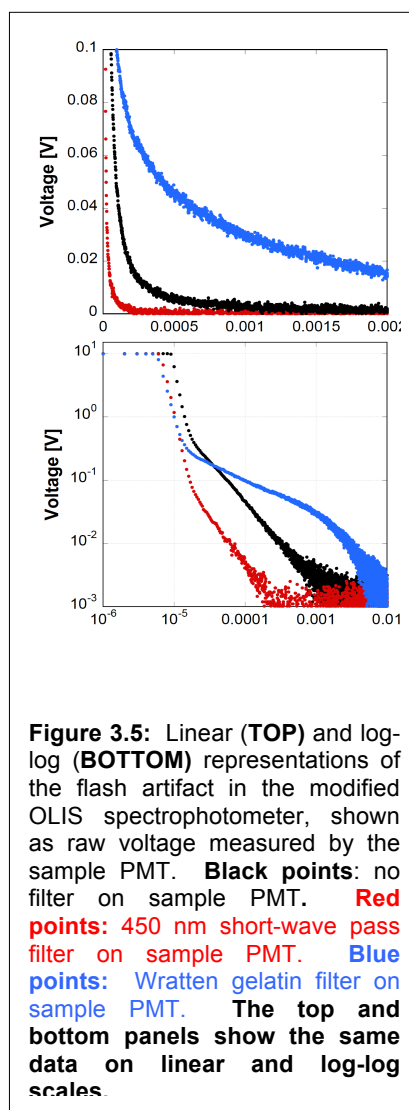
reference signal is interpolated to yield a 1 μ S sample with timepoints matching those of the sample signal. At this point processed records are available for both the sample and reference PMTs at matching timepoints, so they are divided to give the absorbance. This calculation is repeated for each wavelength. **Figure 3.4** shows a typical result from the post-processing script for interprotein ET at low ionic strength with fast kinetics. The visible difference between the red and black points at times $< \sim 150 \mu$ S indicates that the flash artifact is significant in this region.

Figure 3.5 shows the magnitude of the sample PMT flash artifact at a PMT voltage level of 400 V, typically for high OD portions of the Soret band. The data were obtained by flashing the laser without reactants in the flow cell. Comparing the red and black points shows the impact of the 450 nm SWP filter used for all protein ET experiments; clearly this filter helps

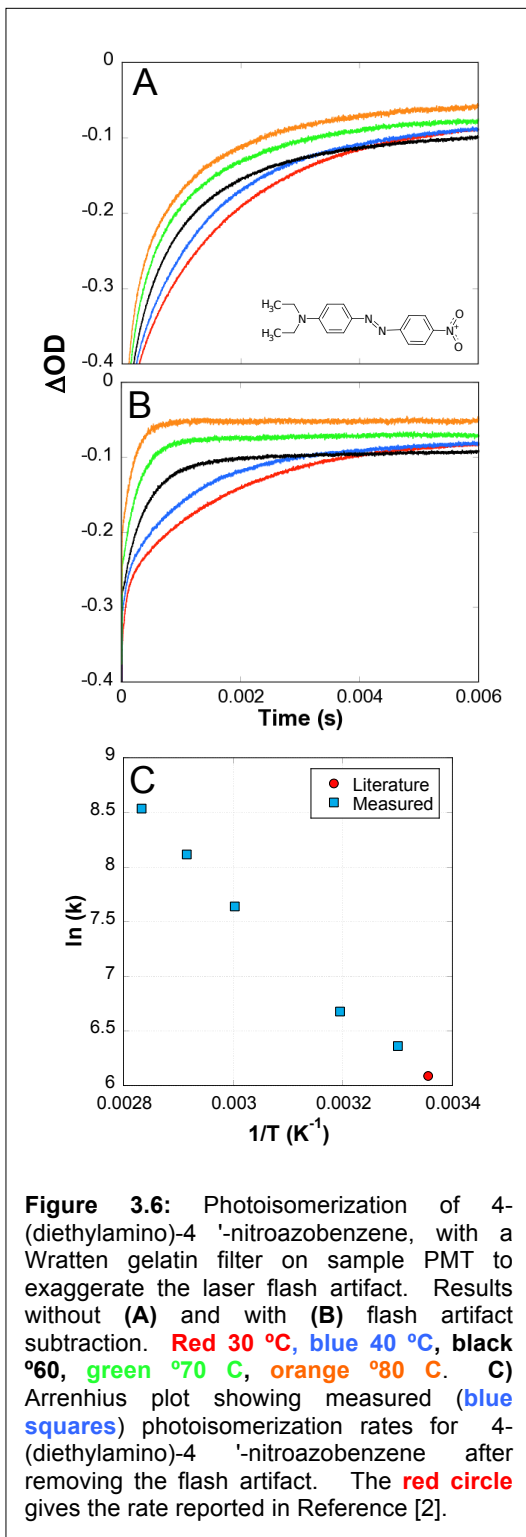
to cut the intensity and duration of the flash artifact. For the blue points, I replaced the SWP pass filter with a Kodak Wratten #35 gelatin filter, with transmittance between roughly 320 nm and 470 nm [5]. Surprisingly, adding the Wratten greatly enhanced the impact of the flash, resulting in a noticeable impact on the ms timescale. This is likely due the strong phosphorescence reported for some organic filters. Clearly the Wratten filter does not help to reduce the impact of the flash. However, it does provide a method to actually exaggerate the artifact, providing a more stringent test for its removal, as discussed below.

3.4 Validating laser artifact removal

To validate the scheme for removing the flash artifact, I attempted to reproduce expected kinetics for a unimolecular photo-isomerization reaction in the presence of the flash-enhancing Wratten filter. Upon photoexcitation, the azo dye 4-(diethylamino)-4'-nitrobenzene (inset, **Figure 3.6-A**) undergoes a *trans*-to-*cis* transition followed by thermally driven change back to the *trans* isomer. The rate of the thermal isomerization follows typical Arrhenius behavior. **Figure 3.6-A** shows the measured DOD trajectories of the photoisomerization at a range of temperatures in the presence of the Wratten filter *without* subtracting the flash profile. The flash artifact persists for longer than the isomerization half-time at most temperatures here, so there is little difference between the traces. **Figure 3.6-B** shows the same data after subtracting the flash, showing a distinct difference in kinetics with temperature variation. **Figure 3.6-C** shows an Arrhenius plot for the first-order rate constants fit to the measured flash-corrected trajectories, along with the previously reported rate[2]. Recovery of the underlying Arrhenius behavior verifies the



design and implementation of this scheme to remove the flash artifact.



3.5 References

- [1] B.A. Fry, L.A. Solomon, P.L. Dutton, C.C. Moser, Design and engineering of a man-made diffusible electron-transport protein, *Biochimica Et Biophysica Acta-Bioenergetics*, 1857 (2016) 513-521.
- [2] J.G.P.i. Peter D. Wildes, Gether Irick, Jr., D. G. Whitten, Solvent and Substituent Effects on the Thermal Isomerization of Substituted Azobenzenes. A Flash Spectroscopic Study, *Journal of the American Chemical Society*, 93 (1971).
- [3] H. Roder, K. Maki, H. Cheng, M.C.R. Shastry, Rapid mixing methods for exploring the kinetics of protein folding, *Methods*, 34 (2004) 15-27.
- [4] Q.H. Gibson, Hemoproteins, Ligands, And Quanta, *Journal of Biological Chemistry*, 264 (1989) 20155-20158.
- [5] E.K. Company, Wratten Light Filters, (1920).

Chapter 4 Interprotein Electron-Transfer with Photoactivatable Maquettes

4.1 Introduction: Motivation and Experimental Considerations

Chapter 2 discusses two experimental methods to probe ET from maquette-bound porphyrins to natural cyt *c*. The first method is simply stopped-flow spectroscopy where the reactants are rapidly mixed to initiate a thermodynamically favorable reaction. The second method is CO photolysis-induced ET. Here, we use a laser flash to release bound CO from a reduced maquette in the presence of oxidized cyt *c*. The reduced heme becomes ET-competent upon the loss of its CO ligand. We may think of the laser as removing a kinetic barrier to a downhill ET. This chapter introduces a third experimental system for the study of maquette-cyt *c* ET. This method is *light-activated electron transfer*, relying on the same laser used for the photolysis experiments. The physical basis of the reaction is quite different, however. In this system the laser produces a long-lived triplet state in a maquette-bound zinc porphyrin. This excited triplet is highly reducing, thus driving interprotein ET to oxidized cyt *c* or intraprotein ET to another cofactor present in the maquette.

This chapter describes photo-activated interprotein ET from several maquettes to natural bovine cyt *c*. Like **Chapter 2**, this work examines the impact of external maquette charge patterning, concentration, and ionic strength on interprotein rates. It also demonstrates a design to photo-oxidize (rather than reduce) cyt *c* in solution. The work in **Chapter 4** is being written up for submission to *Chemical Science* [4].

4.1.1 Zinc Porphyrin and Photoactivated ET

The Zn atom is typically pentacoordinate. As part of a protein-bound tetrapyrrole, Zn is ligated by the four pyrrole nitrogens and a single histidine N ϵ atom. This contrasts with the hexacoordinate bis-His ligation of the B heme in BT6 (**Chapter 2**). An extensive literature examines the photophysical properties of Zn tetrapyrroles in proteins. Some studies replace naturally-occurring porphyrin metals such as iron[5] or magnesium[6] with zinc. Others use

synthetic zinc porphyrins employing phenyl groups or other ring substituents [7, 8]. To our knowledge, however, these experiments are the first to investigate photo-activated interprotein ET involving a zinc porphyrin bound in a completely artificial protein. The photophysical properties of Zn porphyrins make them well suited for these studies. Photoexcitation produces a strongly-reducing singlet state. The singlet has a ~ 1 ns lifetime, returning quickly to the ground state through fluorescence or non-radiative decay. However, a significant fraction of the singlet population undergoes intersystem crossing (ISC) to the much longer-lived triplet state. The triplet is still energetic enough to readily reduce most biological redox partners, and unlike the ephemeral singlet it persists for several ms. This long lifetime makes a zinc porphyrin triplet ideal to probe ET on timescales ranging from ns to a few ms.

A porphyrin cation is left behind when the excited Zn porphyrin reduces a redox partner. This cation is highly oxidizing, and in the absence of additional redox centers in the system the porphyrin may quickly reclaim the electron it has just donated. Photosynthetic reaction centers are similar in this regard, and fast ET steps following the initial charge separation serve to discourage immediate recombination[9, 10]. No special design features slow the back-ET in this chapter's experiments, but the charge-separated states described here still persist for 100 μ S or longer. Moreover, the cyclic nature of this reaction offers a significant experimental advantage when compared to the downhill ET in **Chapter 2**. Because the system reverts to its original state quickly after excitation, the experiment may be repeated quickly; this permits extensive averaging to reduce measurement noise.

The photoactivatable cofactor employed in all ET experiments in **Chapter 4** is the synthetic zinc porphyrin Zn-3-phenyl-9-para-carboxyphenyl-porphine, hereafter called "ZnP". **Figure 4.1** illustrates this molecule. Tatiana Esipova of the Vinogradov lab generously provided

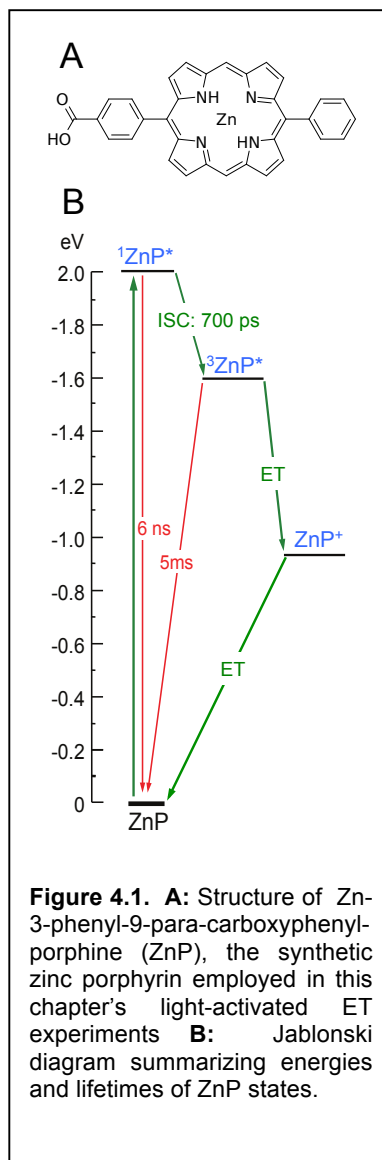
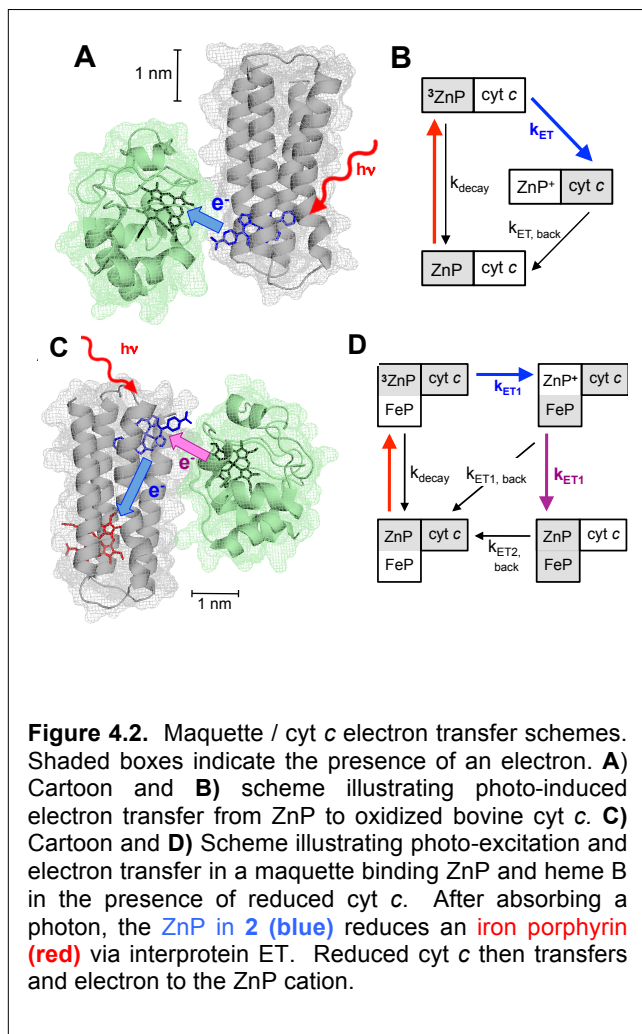


Figure 4.1. A: Structure of Zn-3-phenyl-9-para-carboxyphenyl-porphine (ZnP), the synthetic zinc porphyrin employed in this chapter's light-activated ET experiments **B:** Jablonski diagram summarizing energies and lifetimes of ZnP states.

us with ZnP, and it has also seen extensive use by Dutton lab members Nate Ennist, Zhenyu Zhao, and Josh Mancini. Zhenyu Zhao has characterized the basic photophysics of ZnP, summarized in the Jablonski diagram **Figure 4.1-B**. Importantly, the singlet state is ignored for purposes of all experimental analyses in this chapter. This is justified by the singlet's short 1 ns lifetime, combined with the absence of any spectroscopic signs of electron transfer at the initial 1



μS data point in the transient absorption experiments (see **Figure 4.12-D**, for instance). Zhenyu Zhao measured the $\text{ZnP}^+ / \text{ZnP}^0$ couple to be +800 mV in GL-H96, and this value is employed in subsequent ET calculations.

Figure 4.2 A/B shows a cartoon and kinetic scheme describing most of the experiments in this chapter. Since this system contains two redox centers (a photoexcitable pigment and an electron acceptor), it is an example of a *photochemical dyad*. Upon absorbing a photon (red arrow), the ZnP ground state becomes a $^3\text{ZnP}^*$ triplet. This state may decay or reduce an oxidized cyt *c* molecule (blue arrow). Finally, the ZnP^+ will re-oxidize the cyt *c*, recovering the initial state prior to excitation. **Figure 4.2 C/D** illustrates a second experimental system, a *photochemical triad*. The

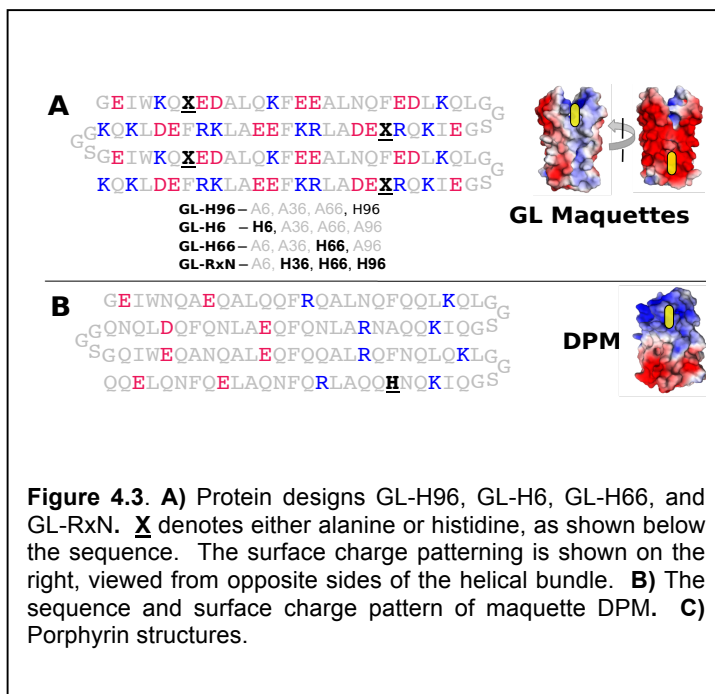
maquette binds a heme B in addition to a ZnP, and in this system the cytochrome *c* is initially reduced. $^3\text{ZnP}^*$ reduces the heme B, and the resulting ZnP^+ cation subsequently oxidizes cyt *c*. This system is analogous to a simplified bacterial reaction center where ZnP, heme B, and cyt *c* function as the bacteriochlorophyll special pair, bacteriopheophytin, and cyt c_2 , respectively. The work of Zhenyu Zhao in the Dutton lab focuses on a photochemical triad where all three cofactors

reside in the same protein, while the experiment presented here in **Section 4.5.5** is the lab's first effort toward a triad where the charge-separated state residues across two separate proteins.

4.2 Protein Design, Expression and Purification

4.2.1 Design

This chapter addresses five maquette designs, shown in **Figure 4.3**. All of these proteins are monomeric 4- α -helical designs expanding upon the wide range of earlier maquettes sharing this topology. Like the BT6 protein discussed in **Chapter 2**, each of these maquettes is based upon a “binary patterning” scheme in which helix-forming hydrophilic and hydrophobic residues are arranged in a heptad pattern. Inward-facing histidines are selected to bind metal porphyrin cofactors in the bundle interior.



Four of the proteins are given the prefix “GL”. Helices 1 and 3 in these designs are identical in sequence to the helices of the negatively charged BT6 protein from Chapter 2. However, helices 2 and 4 possess a net positive charge. Thus, the GL designs display a moderate dipole moment roughly perpendicular to the bundle axis. The GL proteins also differ from BT6 their loops. Rather than the long 9-residue glycine and serine loops of BT6, each of the GL proteins employs shorter GGSG loops. Previous work in the Dutton lab has shown that melting temperature increases as the interhelical loops are shortened, given identical helical sequences[11].

Importantly, maquettes also differ from BT6 in their histidine placement. BT6 contains 4 histidines, thus accommodating bis-histidine binding for two heme cofactors. Previous work has shown that the BT6 scaffold may be modified to bind a single heme, and also that one or both of the bis-his heme sites may be replaced with a single histidine[12]. A single his site will not bind heme, but may instead offer a binding site for a zinc porphyrin (ZnP). The first three maquettes discussed here are named “GL-H96”, “GL-H6”, and “GL-H66”, corresponding to the location of their single histidine residue. The histidine in GL-H96 is located such that it will bind a ZnP in the positively charged face of the maquette, while GL-H6 and GL-H66 will bind a ZnP in the negative portion. The fourth maquette, called here GL-RxN (to denote “reaction center”), contains three histidines at sequence positions 36, 66, and 96. This arrangement provides one bis-his heme site between H36 and H96, along with a single-his ZnP site at H66. A similar 3-histidine BT6 variant has been shown to support photo-activated intraprotein ET between a zinc porphyrin and heme[12]. Additional experiments have shown intraprotein ET between a zinc porphyrin and heme in a detergent solubilized amphiphilic maquette (See **Chapter 5** and reference [13]).

The final design is “DPM”, short for “Dipole Maquette”. It contains a single histidine at position 96 to accommodate a ZnP. The

inward-facing hydrophobic residues, primarily Leu and Ala, are unchanged from the sequences of GL and BT6. However, the charge patterning on the outward-facing residues has been altered significantly with the goal of producing a strong dipole moment roughly parallel to the bundle axis. DPM was engineered in an effort to use dipolar charge patterning to suppress *cyt c* photoreduction. The DPM protein is not the first effort to engineer a dipole moment parallel the bundle axis. Previous Dutton lab member Xiaochi Chen designed a somewhat similar 4-helix dimer dubbed the “*cyt b* maquette” [14]. The Chen protein maintained the total number of

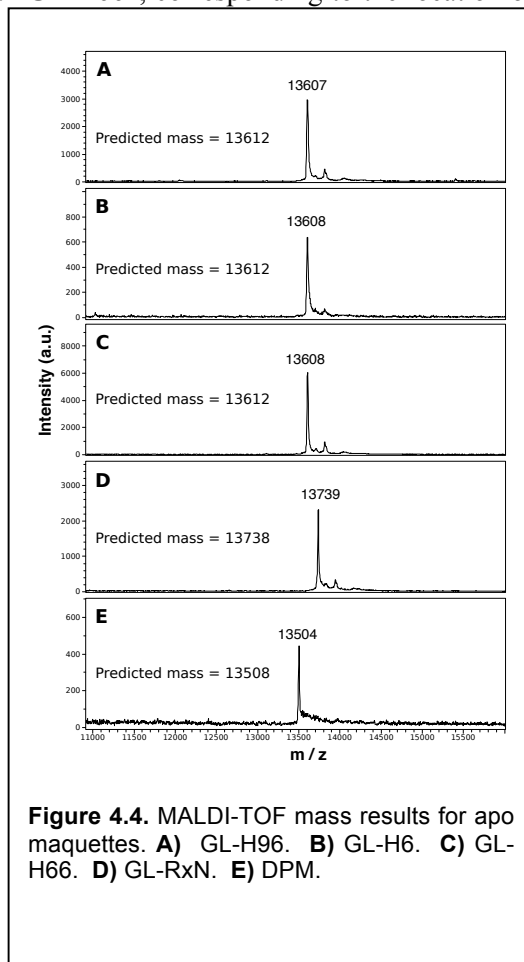
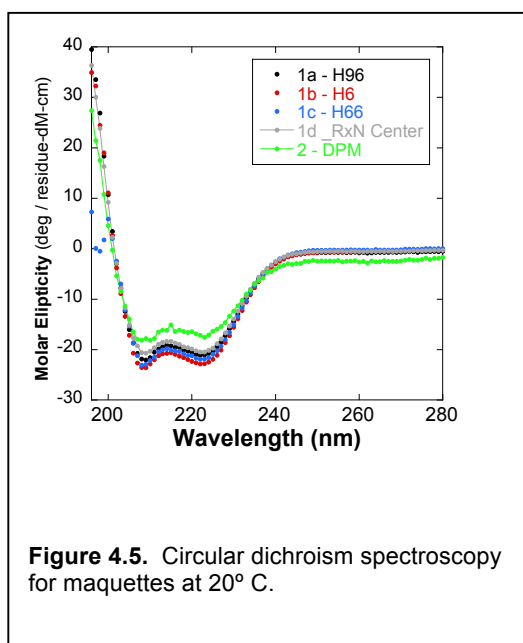


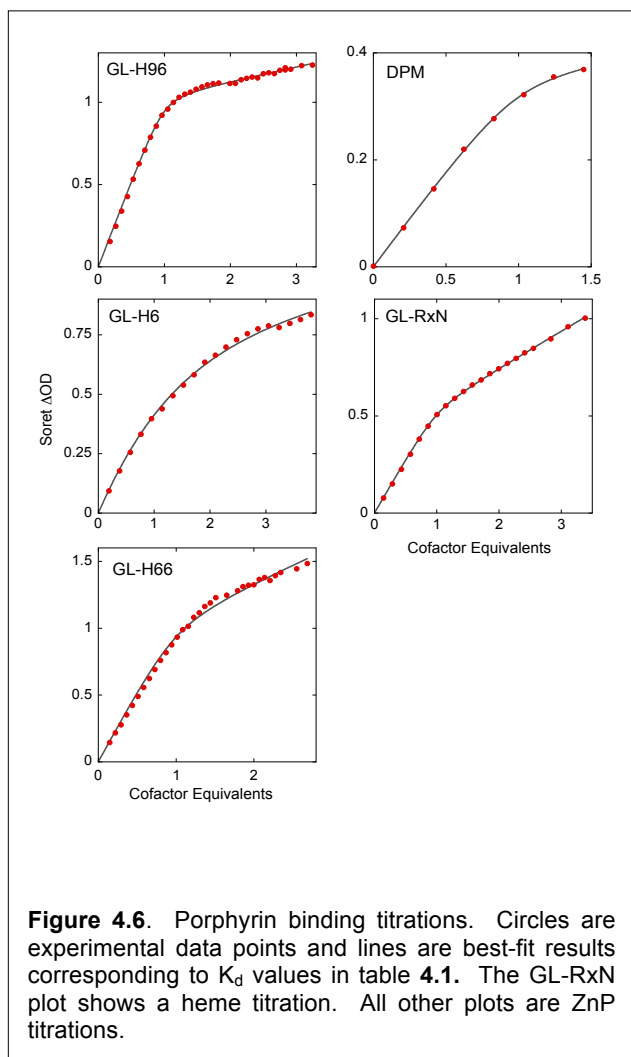
Figure 4.4. MALDI-TOF mass results for apo maquettes. **A)** GL-H96. **B)** GL-H6. **C)** GL-H66. **D)** GL-RxN. **E)** DPM.

glutamates and lysines typically employed on the exterior of soluble maquettes but aggressively segregated them on opposite ends of the bundle, producing a very strong dipole. Although the *cyt b* maquette did bind heme and otherwise function as designed, it proved to be insoluble in less than 1.5 M KCl. Presumably extreme ionic strength was needed to overcome the strong interprotein dipolar interactions. Hoping to circumvent this solubility issue, I reduced the total number of charged residues in DPM as compared to the GL, BT6, and “*cyt b* maquette” designs. DPM replaces many of these charged residues with polar uncharged glutamines, thus maintaining a hydrophilic exterior while reducing total charge count. This approach appears to have succeeded, as DPM dissolves to several μM concentration at 4mM ionic strength (see **Section 4.2.2** below).



4.2.2 Protein Expression, purification, and solubilization

DNA 2.0 provided an initial gene template for the four GL protein maquettes in the pET-32b+ vector. Enzyme-free PCR cloning [15] was used to produce genes for the four histidine variants. GenScript provided a pUC57 vector with the gene for the DPM maquette. Expression and purification were performed using the same methods described in **Chapter 2**.



The four dry GL proteins were readily solubilized in 2 mM Tris / 3 mM NaCl at pH 8.0, the condition used for transient absorption (TA) experiments. Lyophilized DPM proved to be only sparingly soluble at these conditions ($\sim 7 \mu\text{M}$) and exhibits a UV peak around 265 nm rather than the 280 nm expected for tryptophan, suggesting misfolding and/or aggregation. However, DPM is soluble to at least $30 \mu\text{M}$ under the higher ionic strength condition of 40 mM Tris, 200 mM NaCl at pH 8.0 with a typical tryptophan UV signature. This spectrum was maintained upon buffer exchange into 2 mM Tris / 2 mM NaCl for TA experiments.

4.3 Biophysical characterization

4.3.1 MALDI-TOF

MALDI-TOF spectroscopy verified the mass of the purified proteins. Lyophilized protein was dissolved in 1:1 acetonitrile and water and mixed with sinapinic acid and then dried on the MALDI plate under vacuum. Masses measured by MALDI matched the predicted masses based on sequence within 4 daltons, as shown in **Figure 4.4**.

4.3.2 Circular dichroism

Circular dichroism (CD) spectroscopy verified the maquettes' secondary structure, as described in **Appendix A1.2**. **Figure 4.5** shows the results of circular (CD) on 20 μM apo-maquettes at 20 °C. These data were obtained at pH 8.0 with 3 mM NaCl / 2 mM Tris, the lowest ionic strength condition employed for subsequent electron transfer experiments. CD experiments on GL-H96 and DPM at 20 mM NaCl and 5 mM Tris at pH 8.0 yielded similar results (data not shown). These CD spectra indicate that the secondary structures are predominantly α -helical.

4.3.3 Porphyrin binding

All maquettes described here are designed to bind a ZnP cofactor. In addition, the GL-RxN includes a bis-his heme site. ZnP or heme were titrated into 1 mL maquette samples, as described in **Appendix A1.3**. **Figure 4.6** shows the data and best-fit binding curves from these

titration, and **Table 4.1** shows the binding constants and extinction coefficients corresponding to these fits. Except for GL-H6, all of these systems exhibit dissociation constants in the nM range. GL-H6 ($K_d \sim 1.8 \mu\text{M}$) is a weaker binder, and its parameters could be better resolved with a second titration at higher protein concentration.

Maquette	Porphyrin	[Maq] (μM)	$\lambda_{\text{Soret, max}}$ (nm)	ϵ_{bound} ($\text{M}^{-1}\text{cm}^{-1}$)	ϵ_{free} ($\text{M}^{-1}\text{cm}^{-1}$)	K_d (nM)
GL-H96	ZnP	2.5	421	420000	34000	35
GL-H6	ZnP	2.0	420	490000	13000	1800
GL-H66	ZnP	3.0	420	370000	87000	160
DPM	ZnP	1.2	419	310000	34000	41
GL-RxN	Heme	4.5	412	125000	42000	140

Table 4.1: Porphyrin binding titration parameters for fits in **Figure 4.6**. Parameters were computed as described in **Section A1.3**

The various maquettes exhibit significantly different extinction coefficients for the bound ZnP cofactor, as well as slight shifts in the wavelength of the Soret peak. There is in fact a visible color discrepancy between the GL-H96 and GL-H66 maquettes at concentrations of ZnP yielding ~1 OD absorbance. These differences suggest that ZnP cofactors reside in different binding/solvation environments. Note that the titration shown here for GL-RxN is for heme; no titration has been performed for ZnP. However, at 3 μ M protein concentration GL-RxN does reliably bind 0.9 equivalents of ZnP after binding a heme. The difference spectrum between (GL-RxN + heme + ZnP) – (GL-RxN + heme) is similar to that for GL-H66 + ZnP, as expected.

4.4 Methods: ET Experiments and Analysis

4.4.1 Transient Absorption Spectroscopy

All protein solutions were prepared with NaCl and Tris buffer at pH 8.0. Oxidized or reduced cyt *c* was prepared using either $K_3Fe(CN)_6$ or sodium ascorbate as described in **Appendix A1.5**. Unless otherwise noted, the experiments were run at the low ionic strength condition of 2 mM Tris / 3 mM NaCl. The experiments described in **Section 4.5.4** examine two other ionic strength conditions: 5 mM Tris / 20 mM NaCl and 25 mM Tris / 100 mM NaCl. The protein samples were placed in a quartz fluorescence cuvette with a foil-lined septum and degassed under O_2 -scrubbed argon with stirring for 1 hr. For experiments using cyt *c*, either oxidized or reduced 300 μ M cyt *c* stock was injected into the maquette solution using a gas-tight syringe, followed by an additional 5 min of degassing. For maquette-only or oxidized cyt *c* experiments, a cocktail of 80 nM glucose oxidase, 12 nM catalase, and 1.5 mM glucose was added to scrub residual O_2 . [16]. For experiments using reduced cyt *c*, the O_2 scrubbing system of 40 μ M protocatechuate deoxygenase (PCD) and 1.5 mM protocatechuic acid was used instead [17]. PCD was employed for the reduced cyt *c* experiments because the glucose oxidase scrubbing system appears to slowly oxidize cyt *c*.

The anaerobic cuvette was transferred to the transient absorption apparatus outlined in **Figure 4.7**. A Peltier-equipped stage maintained a constant sample temperature 20° C. A 10

Hz frequency-doubled Nd:YAG laser (Spectra Physics) provided optical excitation at 532 nm, and a mechanical shutter (ThroLabs) limited laser exposure to one pulse per second. A split fiber-optic cable routed the output of a xenon flash source through two parallel paths in the cuvette and then to an Acton SP-2156 spectrograph; one path overlapped the region of laser

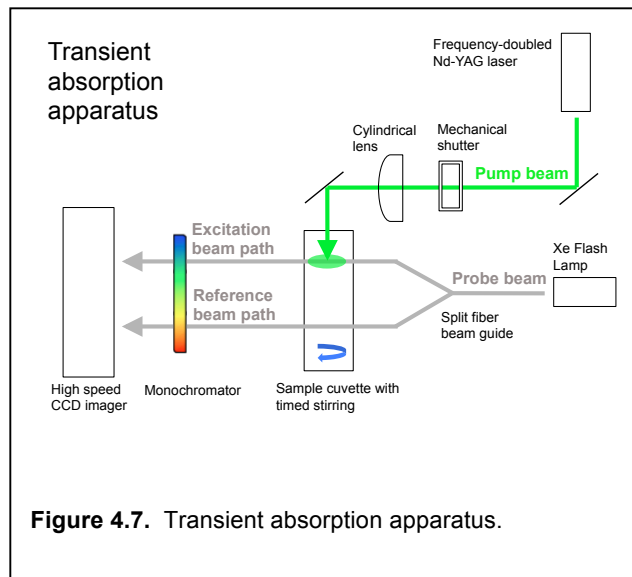


Figure 4.7. Transient absorption apparatus.

excitation while the second provided a “dark” reference. The monochromator outputs were focused onto a Princeton Instruments PiMax-3 ICCD camera using a 1 μ S integration time. A Stanford Research System DG 535 digital delay generator, driven by the laser lamp sync output signal, provided triggers to the laser Q-switch, xenon flash, and camera exposure. Transient absorption spectra were computed by subtracting the averages of 60 acquisitions, with and without laser exposure, at each timepoint.

4.4.2 Stretched Exponential Fits

Plotting the rate of post-excitation Soret bleach recovery provides a simple, semi-quantitative method to compare rates of electron transfer between different reactions (given that electron transfer is indeed the dominant mechanism of triplet quenching). Superficially, these traces resemble simple exponential decay functions. However, there is no theoretical basis to expect a single exponential behavior in a second-order reaction unless one reactant is present in large excess. Even in this case, conformational anisotropies and multiple orientations for ET-competent complexes could complicate the kinetics. Instead, I used normalized stretched functions of the form

$$f(t) = \exp(-(kt)^\beta) \quad \text{Eqn. 4.1}$$

to fit the bleach trajectories. β ranges from 0 to 1, with 1 indicating a standard single exponential and values < 1 indicating increasingly large stretch. The half-time such a function is given by:

$$t_{1/2} = \frac{(\ln 2)^{-\beta}}{k} \quad \text{Eqn. 4.2}$$

This half-time provides a simple metric to compare reaction kinetics between experiments where discrete rate constants are not readily available.

4.4.3 Singular Value Decomposition and Kinetics Model Fitting

To examine the dependence of cyt *c* photoreduction rate on concentration, Singular Value Decomposition (SVD) analysis was combined with a chemical kinetics scheme shown in **Figure 4.2-B**. Henry and Hofrichter provide a thorough description of this approach [18]. Given a particular kinetic model with unknown rates, this scheme solves for these rates directly from time-evolving spectra. There is no need to assume *a priori* the spectra of the specific species in the reaction. I implemented the analysis in Python using the SVD and function minimization tools of the Scipy package.

Results from the TA experiment are represented by the $n_\lambda \times n_t$ matrix A , with rows and columns representing individual wavelengths and timepoints. SVD decomposes the matrix into three components:

$$A = USV \quad \text{Eqn. 4.3}$$

where the columns of U and rows of V represent linear combinations of the spectra of individual states in the system and fractional populations of these states, respectively. S is a monotonically decreasing diagonal matrix whose terms denote the “significance” of the corresponding rows and columns of V . For each experiment the first two S values are much greater than the subsequent values, indicating that most of the non-random information in U and V are present in the first two columns and rows; this is consistent with the kinetic scheme in **Figure 4.2-B** containing two visible states (the ZnP ground state is spectrally silent). Thus, U and V were truncated to the first two columns and rows and S was limited to its first two components.

The 2x2 transformation matrix C gives coefficients to transform V^T (matrix transpose of V) to the fractional populations of the ZnP triplet and charge-separated state at each timepoint; these populations are given by the unknown $n \times 2$ matrix P :

$$P = CV^T \quad \text{Eqn. 4.4}$$

For any given time delay t , solving the rate equations defined by the model in **Figure 2** yields fractional populations for the ZnP triplet state and charge separated states as follows:

$$P_{trip}(k_{ET}) = \exp(-(k_d + k_{ET})t) \quad \text{Eqn. 4.5}$$

$$P_{CSS} = \frac{k_d}{k_d + k_{ET} - k_{ET,back}} \left(\exp(-k_{ET,back}t) - \exp(-(k_{ET} + k_d)t) \right) \quad \text{Eqn. 4.6}$$

Minimizing the sum of squared differences between the population matrices defined by **Eqn. 4.4** and **Eqns. 4.5 / 4.6**, yields best-fit parameters for the unknown rate parameters k_{ET} and $k_{ET,back}$ and for the 4 coefficients of the transformation matrix C . Powell's method for multivariate optimization was run in a Python script to perform this minimization [19]. In analyzing the transient absorption results, the direct triplet decay rate k_d was fixed at 210 s^{-1} , as observed for the ET-incompetent system of maquette GL-H96 with pre-reduced cyt c (Figure **4.10**, red trace).

Figure 4.8 outlines a series of tests using simulated transient absorption data to test this optimization scheme. k_1 , k_2 , and k_3 are equivalent to k_{ET} , $k_{ET,back}$, and k_d in the ET scheme. A Python script generates synthetic transient absorption spectra based on given rates in the model and arbitrary, overlapping spectra for the first two species (**Figure 4.8-A**). Several amplitudes of random Gaussian noise were added to the synthetic spectra, and the algorithm was then run multiple times to test its ability to correctly extract the first two rates in the presence of noise. 32 iterations (with different noise patterns) were run at noise levels ranging from 0.001 to 0.1. Table **4.2** summarizes these results.

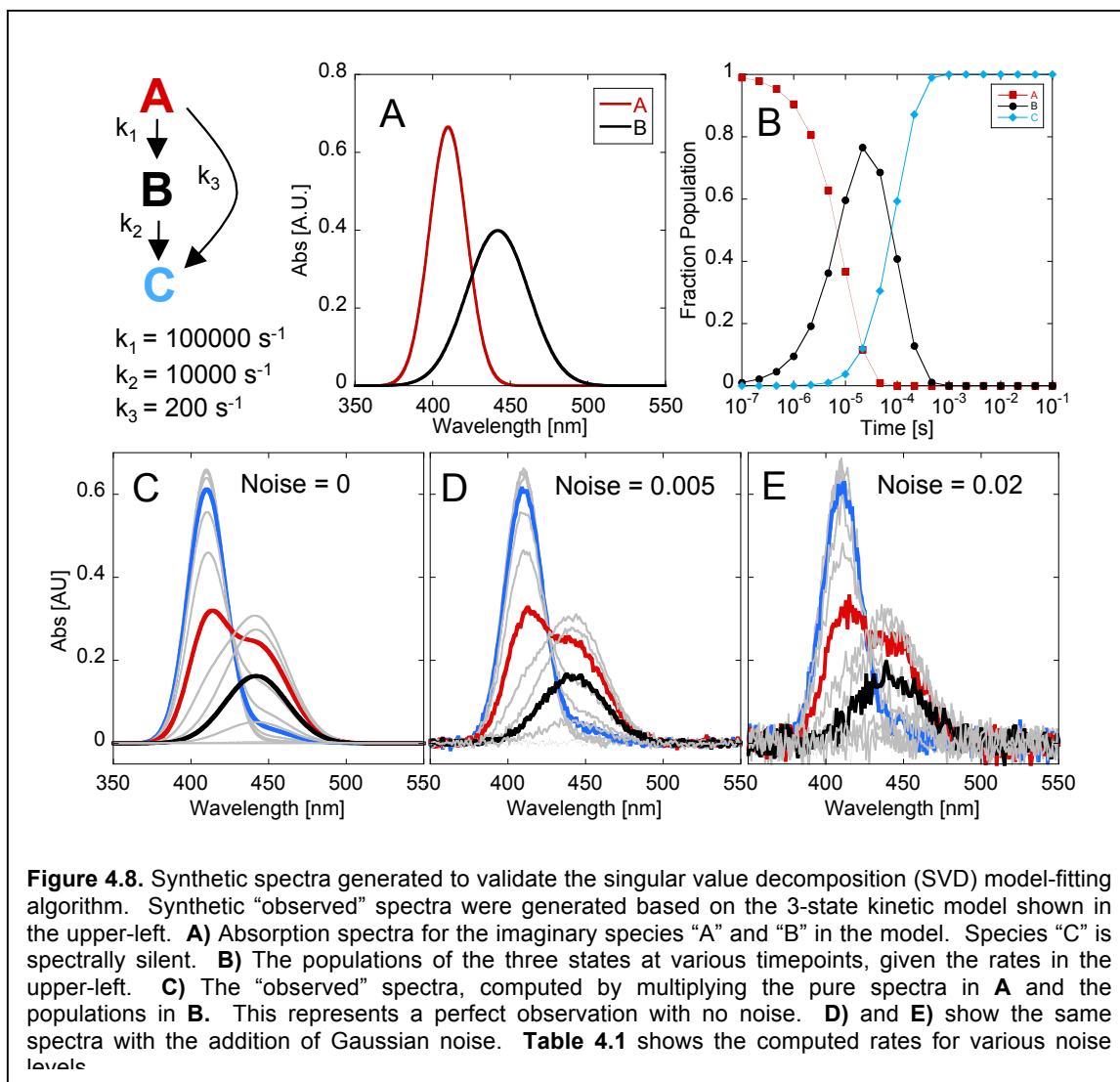


Figure 4.8. Synthetic spectra generated to validate the singular value decomposition (SVD) model-fitting algorithm. Synthetic “observed” spectra were generated based on the 3-state kinetic model shown in the upper-left. **A)** Absorption spectra for the imaginary species “A” and “B” in the model. Species “C” is spectrally silent. **B)** The populations of the three states at various timepoints, given the rates in the upper-left. **C)** The “observed” spectra, computed by multiplying the pure spectra in **A** and the populations in **B**. This represents a perfect observation with no noise. **D)** and **E)** show the same spectra with the addition of Gaussian noise. **Table 4.1** shows the computed rates for various noise levels.

Noise Level	$k_1 = 100000 \text{ s}^{-1}$			$k_2 = 10000 \text{ s}^{-1}$		
	%Err ($\overline{k_1}$)	%Stdev (k_1)	Max %Err (k_1)	%Err ($\overline{k_2}$)	%Stdev (k_2)	Max %Err (k_2)
0.001	0.006	0.10	0.22	0.036	0.12	0.28
0.002	0.009	0.22	0.62	0.041	0.24	0.67
0.005	0.095	0.70	1.7	0.15	0.56	1.5
0.01	0.32	0.97	2.2	0.31	1.1	2.4
0.02	0.014	2.1	4.5	0.10	2.7	8.1
0.05	3.8	5.0	16.5	4.1	6.2	15.0
0.1	22.3	23.3	80.5	71.3	129	400

Table 4.2: Summary of SVD model test results rates with varying amplitudes of Gaussian noise.

Matlab. Our programs produced identical results, within numerical precision, when run on the same input data.

4.4.4 SVD with Log-Normal Reaction Rate Distributions

Dutton lab member Zhenyu Zhao has successfully applied the SVD scheme described above to *intraprotein* ET maquette systems where all ETs occur between specific cofactor positions in a well-structured protein. However, this three-state model with discrete ET rates did not yield a good fit in analyzing my *interprotein* *cyt c* photoreduction experiments (see **Figure 4.12-B**). The work of Ubbink and others, introduced in **Chapter 1**, shows that interprotein ET may occur over a range of distances rather than simply from a single well-defined ET complex [20, 21] [22]. This situation seems likely in a maquette / *cyt c* system lacking a specifically engineered binding site. Given a range of possible distances, it follows that the ET may be better described by a continuous distribution of rates rather than a by single discrete rate. To account

These results show that the SVD model fitting scheme yields rates that are correct within a few percent even in the face of noise levels that appear by eye to dominate the useful spectral signals. Furthermore, Zhenyu Zhao of the Dutton lab independently developed a separate implementation of this scheme using

for this, I revisited the 3 state-model, replacing the discrete rates with continuous log-normal distribution functions. If a variable X follows a normal distribution, then $\exp(X)$ will follow a log-normal distribution. Thus, given the (somewhat arbitrary) assumption that ET-competent encounters occur at a normally-distributed range of distances, the resulting distribution of ET rates will be described by a log-normal distribution; this follows from the exponential rate dependence in the Moser-Dutton expression. A general log-normal probability distribution function of ET rates k_{ET} is given as $p(\mu, \sigma)$, where μ and σ denote the most probable $\ln(K_{ET})$ and the “spread” of the distribution, is:

$$p(\mu, \sigma) = \frac{1}{k\sigma\sqrt{2\pi}} \exp\left(-\frac{(\ln k_{ET} - \mu)^2}{\sqrt{2}\sigma}\right) \quad \text{Eqn. 4.7}$$

Furthermore, we may assume that both forward (${}^3\text{ZnP}^* \rightarrow \text{cyt } c$) and reverse ($\text{cyt } c \rightarrow \text{ZnP}^+$) interprotein ET will occur over the same distribution of distances. According to the Moser-Dutton ruler expression, this means that the distribution of forward and reverse rates will differ simply by a fixed ratio, defined by the ΔG and the reorganization energy λ for the two ETs. Given the values estimated in **Section 4.1** ($\Delta G_{\text{forward}} = -0.95$ eV, $\Delta G_{\text{back}} = -0.65$ eV, $\lambda = 1$ eV), this ratio, denoted here by γ , is about 0.5. Adjusting Eqn 4.4 to account for a single discrete rate k_{ET} and back ET rate of γk_{ET} yields:

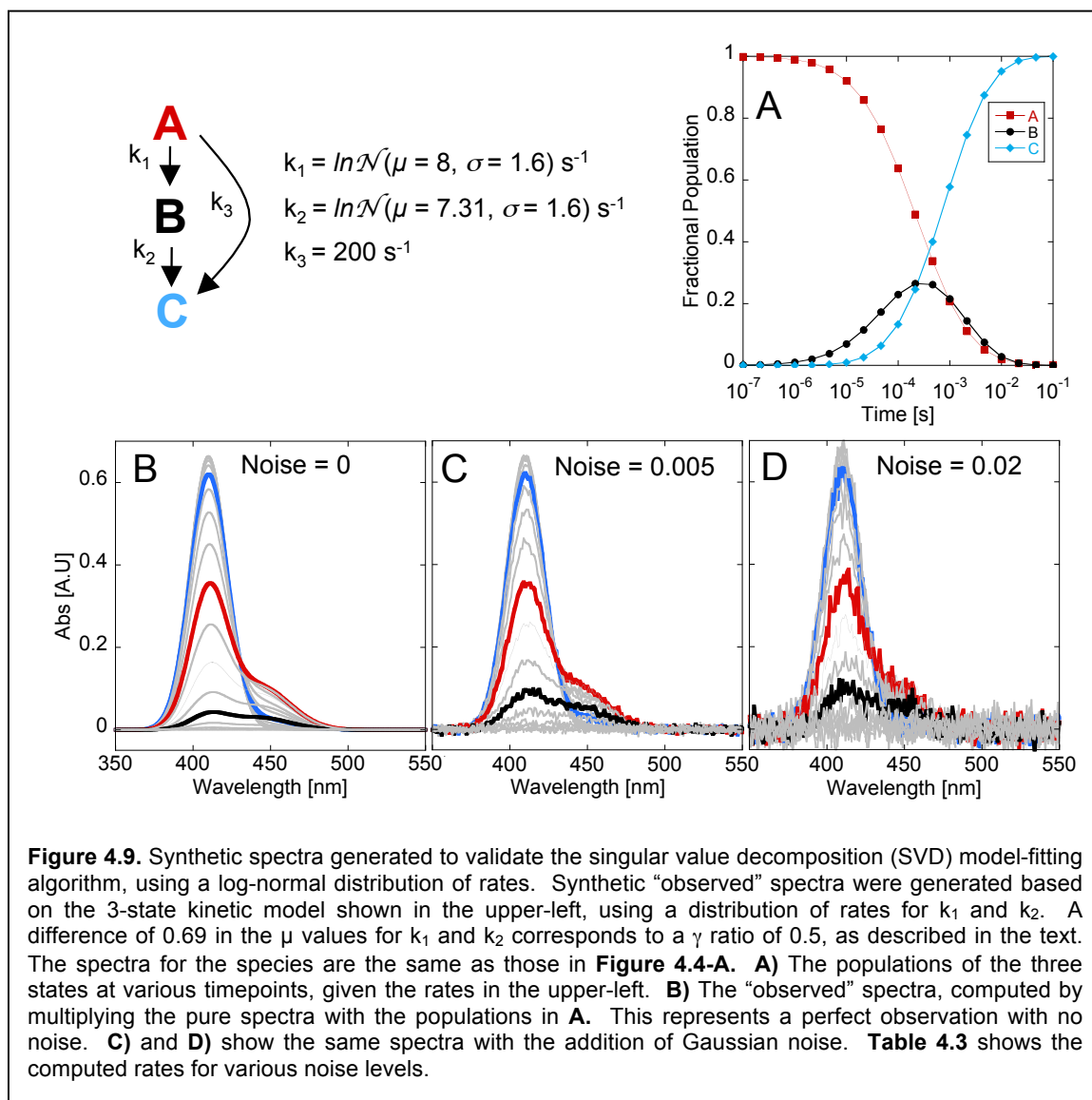
$$P_{CSS}(k_{ET}) = \frac{k_d}{k_d + (1 - \gamma)k_{ET}} \left(\exp(-\gamma k_{ET} t) - \exp(-(k_{ET} + k_d)t) \right) \quad \text{Eqn. 4.8}$$

Replacing the discrete rate by the log-normal distribution yields the following two integrals for the triplet and charge-separated populations; these integrals may be solved numerically:

$$P_{trip}(\mu, \sigma, t) = \int_0^{\infty} P_{trip}(k_{ET}, t) p(\mu, \sigma) dk_{ET} \quad \text{Eqn. 4.9}$$

$$P_{CSS}(\mu, \sigma, t) = \int_0^{\infty} P_{CSS}(k_{ET}, t) p(\mu, \sigma) dk_{ET} \quad \text{Eqn. 4.10}$$

Best-fit parameters for the distribution parameters μ and σ , and for the 4 coefficients of the transformation matrix C , were found by minimizing the sum of squared differences between the population matrices defined by Eqn. 4.2 and Eqns. 4.7 and 4.8. Powell’s direction conjugation algorithm performed this minimization [19]. As with the discrete rate optimization described in **Section 4.2.3**, I wrote a Python script to test the accuracy of this scheme using simulated transient absorption data with random noise. **Figure 4.9** shows the kinetic system,



populations, and sample spectra with noise. **Table 4.3** gives the results of the test for various noise levels. 8 test iterations were run for each noise condition.

Noise Level	$\mu = 8$			$\sigma = 1.6$		
	%Err (μ)	%Stdev (μ)	Max %Err (μ)	%Err (σ)	%Stdev (σ)	Max %Err (σ)
0.005	0.015	0.05	0.093	0.19	0.10	1.2
0.01	0.14	0.031	0.58	0.36	0.018	2.1
0.02	0.058	0.048	0.87	0.66	0.017	2.0
0.05	2.1	0.11	4.4	4.97	0.099	13
0.1	.71	0.26	5.9	52	0.43	88

Table 4.3: Summary of SVD model test results using log-normal rates

4.5 Electron Transfer Results

4.5.1 GL-H96 photoreduces cyt *c*

After photoexcitation, the ZnP quickly forms a reducing triplet state ($E_m \sim -700$ mV for the ${}^3\text{ZnP}^* / \text{ZnP}^+$). ET to cyt *c* ($E_m = +250$ mV) is thus highly favorable. The resulting ZnP^+ cation has $E_m +900$ mV, favoring a reoxidation of the cyt *c* to return the ZnP to its ground state.

The transient absorption spectra of both the ${}^3\text{ZnP}^*$ and ZnP^+ states are dominated by a conspicuous bleach of the ground state Soret band. In the absence of an ET partner, the triplet will decay to the ground state through a non-radiative decay and weak phosphorescence, producing Soret bleach recovery on a ms timescale. Fast ET to a redox partner is expected to accelerate this recovery. **Figure 4.10** plots the Soret bleach recovery for GL-H96 alone and with stoichiometric concentrations of reduced and oxidized cyt *c*. In

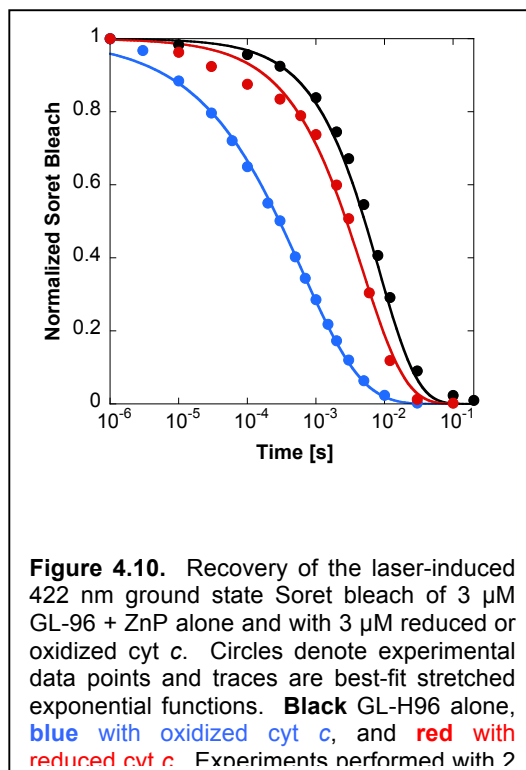
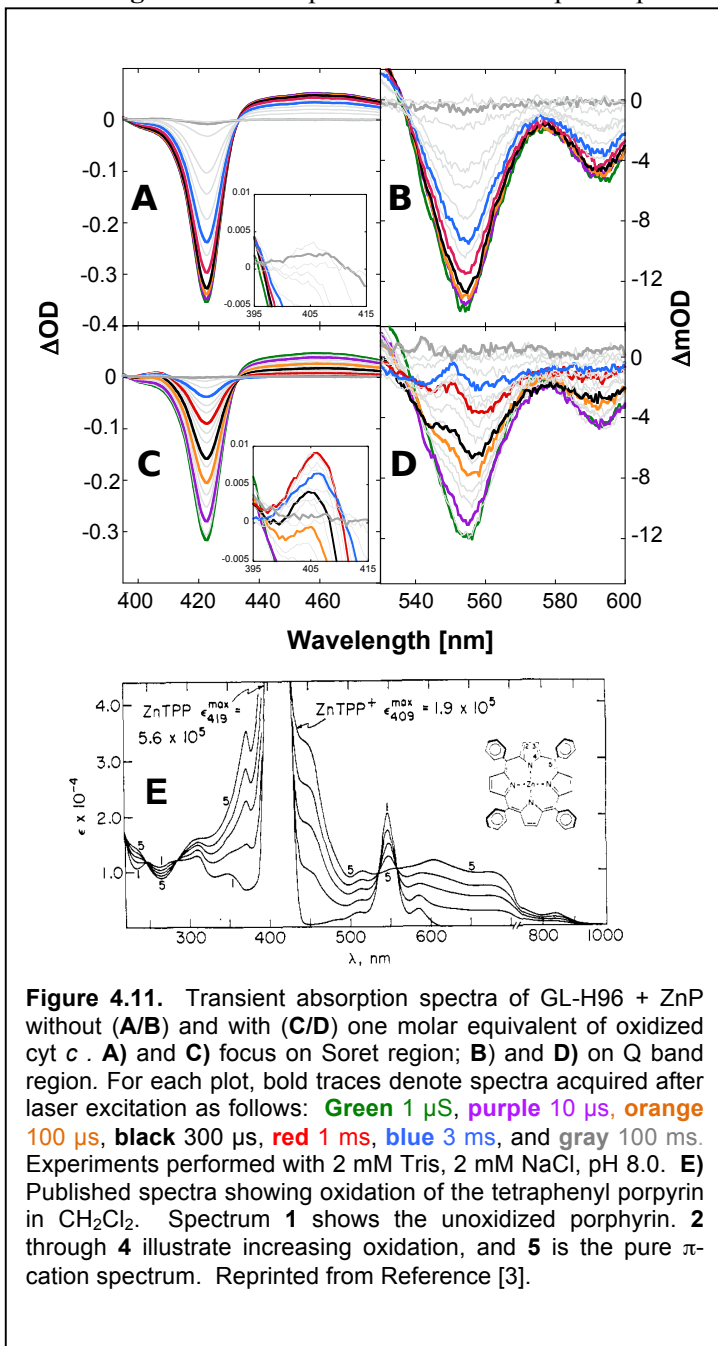


Figure 4.10. Recovery of the laser-induced 422 nm ground state Soret bleach of 3 μM GL-96 + ZnP alone and with 3 μM reduced or oxidized cyt *c*. Circles denote experimental data points and traces are best-fit stretched exponential functions. **Black** GL-H96 alone, **blue** with oxidized cyt *c*, and **red** with reduced cyt *c*. Experiments performed with 2

the absence of an electron acceptor, the triplet decays at a rate of 110 s^{-1} . This increases modestly to 210 s^{-1} with a stoichiometric concentration of reduced *cyt c*. The presence of oxidized *cyt c* raises the bleach recovery rate to 1600 s^{-1} . Significantly faster Soret bleach recovery in the presence of oxidized *cyt c* is consistent with interprotein ET from the reducing ^3ZnP .

Figure 4.11 compares transient absorption spectra for GL-H96 alone and with oxidized



cyt c. With *cyt c*, the Q-band region develops a distinct peak at 550 nm, the signature of *cyt c* reduction. Furthermore, experiments with *cyt c* show a 405 nm peak on the same timescale as the 550 nm *cyt c* α-band, a feature consistent with the spectrum of the ZnP^+ cation. **Figure 4.11-E**, taken from the literature [3], shows spectrum of a synthetic zinc porphyrin and its π -cation. In comparison to the unoxidized spectrum, the cation Soret exhibits a blue shift of 10 nm and a drop in extinction by about a factor of 3.

Importantly, both the 405 nm and 550 nm features, indicative of reduced *cyt c* and oxidized ZnP, are visible only when oxidized *cyt c* is present. Thus, the faster Soret bleach recovery with oxidized *cyt c* in **Figure 4.10** is in fact due to triplet quenching via interprotein ET.

4.5.2 Cyt *c* photoreduction rate is linear with [cyt *c*]

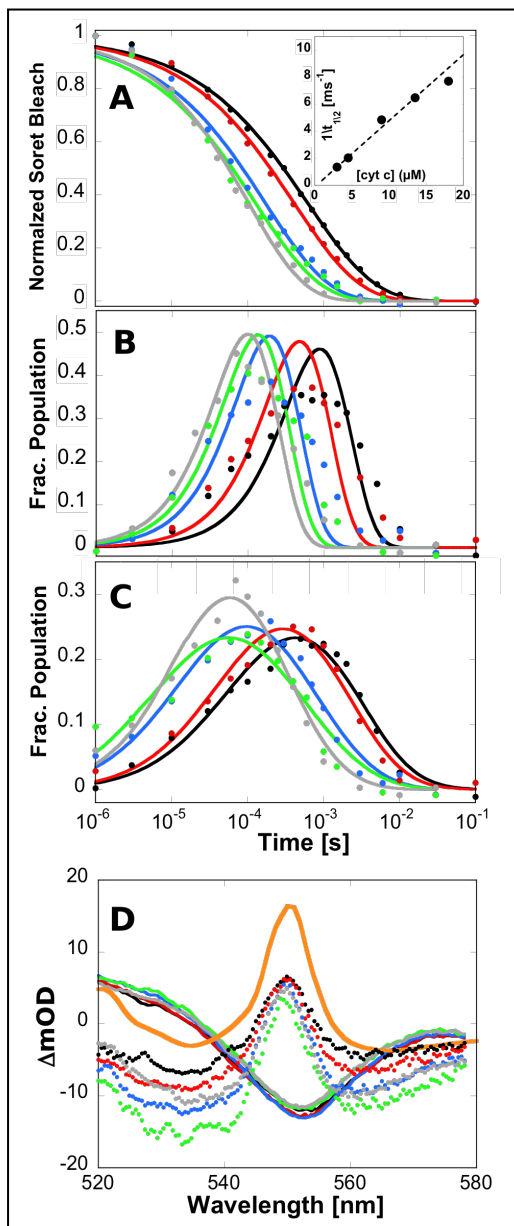


Figure 4.12. Transient absorption-for laser-activated 3 μM ZnP-GH96 with varying concentrations of cyt *c*: **black** 3 μM , **red** 4.5 μM , **blue** 9 μM , **green** 13.5 μM , **gray** 18 μM . **A)** ZnP Soret bleach recovery on a log time scale fit to stretched exponentials. **Inset:** Fit recovery half-times vs. cyt *c* concentration. The dotted line corresponds to a second-order rate constant of $3.4 \times 10^8 \text{ M}^{-1}\text{s}^{-1}$.

B) SVD kinetics model fitting showing charge-separated population relative to the initial excited $^3\text{ZnP}^*$ population for each time point. The kinetic model uses a discrete rate for each state transition, as introduced in Figure 4.4.

C) SVD kinetics model fitting same data, using a log-normal rate distribution as in Figure 4.5. This provides a better fit than the single-rate model in B.

D) Difference spectra for the $^*\text{ZnP}^3$ and the charge separated states, derived from the SVD model in C. Solid lines show spectra for the $^*\text{ZnP}^3$ excited state. Circles show spectra for the charge-separated state consisting of ZnP^+ and reduced cyt *c*. The latter

We repeated the transient absorption experiment with cyt *c* and GL-H96, varying the cyt *c* / maquette molar ratio between 1::1 and 6::1. **Figure 4.12** summarizes these experiments. **Figure 4.12-A** fits the kinetics of bleach recovery to stretched exponentials of the form $y = \exp(- (kt)^\beta)$. In each case the value β is less than 0.5, indicating a significant departure from simple exponential behavior. The inverse half-time increases linearly over the whole concentration

range, (**A-insert**). This concentration dependence is not expected if ET is dominated by maquettes bound to cyt *c* partners in a well-defined complex. A stable ET complex between the maquette and *N* identically-bound cyt *c* molecules, for example, would instead show a biphasic dependence on [cyt *c*], with a breaking point at the 1::*N* stoichiometry. Instead, the reaction appears to be diffusive, despite the very low 4 μM ionic strength conditions employed here. The inverse-half time plot in **A-insert** implies a second order rate constant of $3.4 \times 10^8 \text{ M}^{-1}\text{s}^{-1}$. This numerical result follows from the clearly oversimplified assumption of a simple exponential, pseudo-first order trajectory. But it should represent an order-of-magnitude estimate, and the main conclusion is the inverse relationship between half-time and [cyt *c*].

Figure **4.12-B** shows the charge-separated populations derived from these experiments using the discrete-rate SVD-model fitting scheme described in **Section 4.2.2**. The ratio between back and forward ET was fixed at 0.5, as described previously. I also fixed the direct triplet decay rate at 210 s⁻¹ (**Figure 4.10**, red trace). The points in the plot are the populations derived from **Eqn. 4.2**, while the traces are the populations predicted by the best-fit discrete rates for the model (**Eqn. 4.4**). The populations computed from the SVD and from the best-fit kinetic model are clearly dissimilar.

I re-analyzed the data using the log-normal rate distribution model described in **Section 4.2.3**, and **Figure 4.12-C** shows these results. The traces in **Figure 4.12-C** follow from **Eqn. 4.8**. The log-normal model gives a better fit, as expected in a diffusing system where ET occurs over a range of distances. Finally, **Figure 4.12-D** shows the difference spectra for the triplet state and charge-separated state extracted from SVD for the best-fit models. The reduced cyt *c* α-band at 550 nm is evident for each experiment. The amplitude of this feature matches that expected for complete maquette electron transfer, given the ~ 30% triplet yield as measured by Soret bleach at 1 μS (orange trace).

4.5.3 Comparing cyt *c* photoreduction from among maquette designs

The ZnP-ligating His in GL-H96 is located closest to the more positive maquette face. Designs GL-H6 and GL-H66 move the ligating His to the net negative face of the protein. **Figure 4.13-A** compares the Soret bleach kinetics of GL-H96, GL-H6, and GL-H66. When cyt *c* is absent, the triplet decay rates for the three maquettes agree within a factor of 2: 110 s⁻¹, 130 s⁻¹, and 210 s⁻¹ for GL-H96, GL-H6, and GL-H66 respectively. All three maquettes show a

significant increase in bleach recovery when equimolar 3 μM cyt *c* is present, with rates of 1900 s^{-1} , 590 s^{-1} , and 1700 s^{-1} . **Figure 4.13-B** and **4.13-C** show the Q-band transient absorption spectra for GL-H6 and GL-H66 with cyt *c*. Both clearly display the 550 nm signature of cyt *c* reduction. The rate of this ET shows little change in moving the ZnP ligation site from the positive maquette face in GL-H96 to the negative face in GL-H6 and GL-H66, suggesting the interaction of the modest dipole of **1x** with cyt *c* is not a major factor driving ET kinetics.

In contrast to the lateral dipolar arrangement in the GL maquettes, the axial charge patterning of the DPM yields a stronger dipole moment. Since the cofactor lies in the positive side of the maquette, the dipole-dipole interaction with the similarly positioned heme in cyt *c* is expected to slow interprotein ET. **Figure 4.13-D** shows the Soret bleach recovery kinetics for DPM alone and with oxidized and reduced cyt *c*. In the absence of cyt *c*, DPM exhibits a triplet decay rate of 230 s^{-1} , similar to that of the GL proteins. As with the laterally-patterned GL maquettes, adding oxidized cyt *c* accelerates the DPM triplet decay; in this system the rate with oxidized cyt *c* is 8500 s^{-1} . Surprisingly, the DPM excited state is also significantly quenched by reduced cyt *c*, with a rate of 2550 s^{-1} ; this quenching by both oxidized and reduced cyt *c* is much more pronounced in DPM than in the GL proteins. Since reduced cyt *c* is not competent for photo-reduction in this system, this result suggests that an energy transfer mechanism may be behind the triplet quenching. The Q-band transient absorption spectra for isolated DPM (**Figure 4.13-E**) and for DPM with one equivalent of oxidized cyt *c* (**Figure 4.13-F**) evolve with different rates but are otherwise similar; unlike the lateral dipolar maquettes of **Figures 4.11-D** and **4.13-B** and **4.13-C**, the 550 nm peak characteristic of cyt *c* reduction is absent in DPM. This suggests that placing ZnP in the positive end of the strongly dipolar DPM maquette suppresses interprotein ET, despite the fact that oxidized cyt *c* quenches the excited DPM triplet more effectively than does reduced cyt *c*.

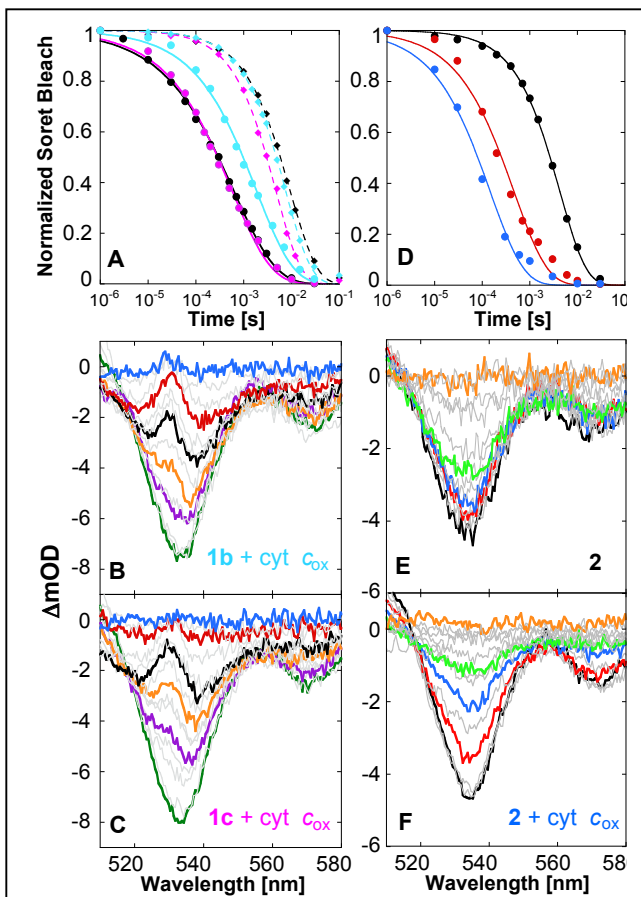


Figure 4.13. Comparing photoreduction of cyt c by ZnP + GL-H96, GL-H6, GL-H66 and DPM. **A)** Soret bleach recovery for 3 μM proteins GL-H96 (**black**), GL-H6 (**blue**), and GL-H66 (**red**) without (diamonds) and with (circles) 1 equivalent of oxidized cyt c.

B/C) Q-band transient absorption spectra of 3 μM oxidized cyt c with 3 μM GL-H6 (**B**) or 3 μM GL-H66 (**C**). Colored traces are: **green** 1 μs , **purple** 100 μs , **orange** 400 μs , **black** 1 ms, **red** 4 ms, and **blue** 30 ms.

D) Soret bleach recovery for 3 μM DPM alone (**black**) and with 3 μM **reduced** (**red**) or **oxidized** cyt c (**blue**).

E/F) Q band changes for DPM alone (**E**) and with one molar equivalent of oxidized cyt c (**F**). Colored traces are: **1 μs** (**black**), **100 μs** (**red**), **400 μs** (**blue**), **1.5 ms** (**green**), and **30 ms** (**orange**).

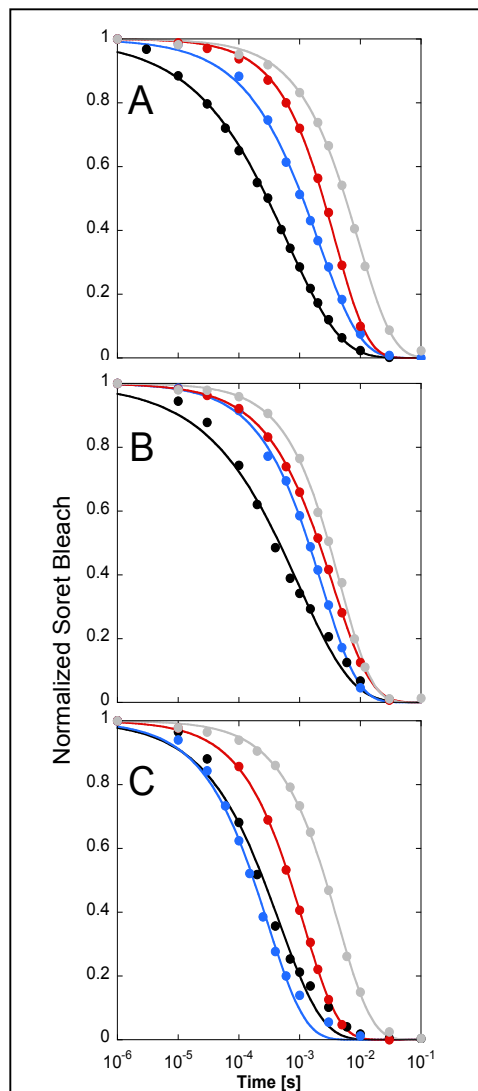


Figure 4.14. Ionic strength dependence of Soret bleach recovery rate for 3 μM maquettes: **A)** GL-H96. **B)** GL-H66. **C)** DPM. Circles show experimental data points and traces are best-fit stretched exponentials. Gray data are maquettes alone at 20 mM ionic strength. Other data also include 3 μM cyt c at the following ionic strengths: **black: 4 mM**, **blue: 22.5 mM**, **red: 110 mM**.

4.5.4 Ionic strength dependence of cyt *c* photoreduction

All of the transient absorption experiments discussed to this point were performed at the very low, non-physiological ionic strength of 4 mM. At this low salt concentration, it is expected that electrostatic interactions between the maquette and cyt *c* redox partners will be quite strong, and moreover that longer-range monopole interactions may overwhelm shorter-range dipole effects (please see **Section 4.6** for elaboration). Because the ^3ZnP decays on the order of several ms, the experimental system employed here is not useful for probing very slow interprotein ET. Thus, I chose to focus largely on the low-salt condition to hasten the ET (and improve the yield) for systems where ET was expected.

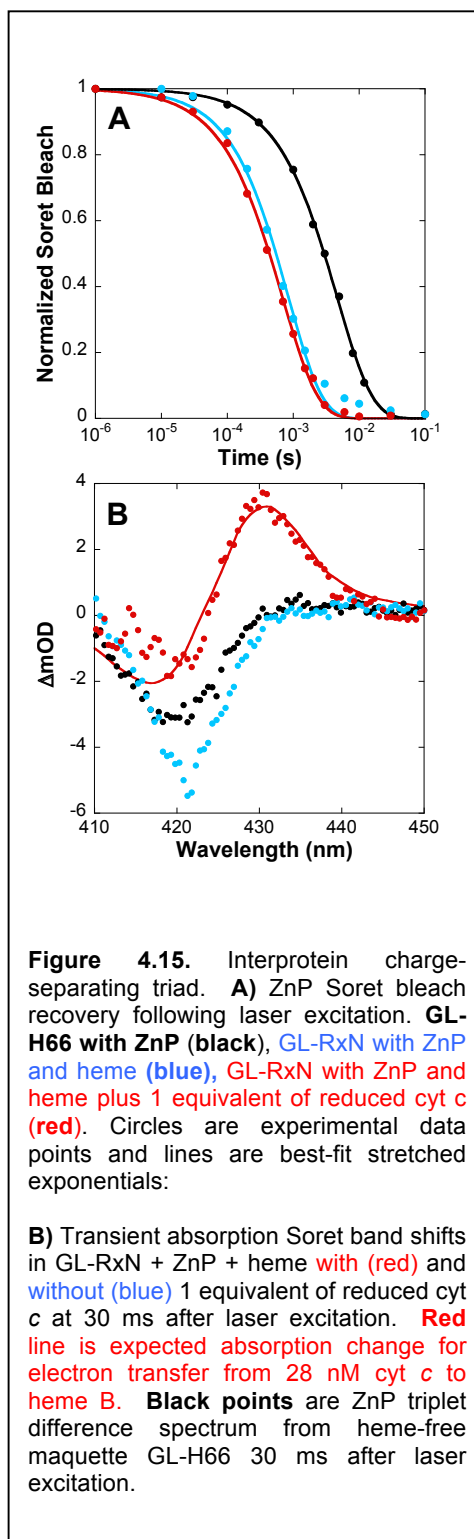
However, the ionic strength dependence is an important consideration in understanding the electrostatic interaction between redox pairs. The following experiments extend the cyt *c* photoreduction to 22 mM and 110 mM ionic strengths, using pH 8.0 solutions with 20 mM NaCl / 5 mM Tris and 100 mM NaCl / 25 mM Tris, respectively. **Figure 4.14** shows the Soret bleach recovery kinetics for GL-H96 (**A**), GL-H66 (**B**) and DPM (**C**) at each salt concentration. To summarize, the triplet quenching slows with increasing ionic strength in GL-H96 and GL-H66, and seems to behave non-monotonically in DPM, with 22 mM showing slightly faster quenching than 4 mM and 110 mM. **Section 4.6** discusses these results in the context of the monopole / dipole interaction theory of Van Leeuwen [23]. Note that the spectra for GL-H96 and GL-H66 both showed distinct cyt *c* 550 nm reduction bands at all ionic strengths (as in **Figures 4.11-D** and **4.13-C**), while DPM did *not* show this signature at any ionic strength (shown in **Figure 4.13-F**).

4.5.5 Cyt *c* photo-oxidation

Unlike the other maquettes discussed in this chapter, the GL-RxN maquette simultaneously binds a heme and a ZnP. The expected edge-to-edge separation of the Zn and Fe porphyrins is about 16 Å, short enough to support light-activated ET within the ~5 ms lifetime of the isolated ZnP triplet state. In the presence of reduced cyt *c*, some population of resulting ZnP⁺ cations may abstract an electron from cyt *c*, as illustrated in **Figure 4.3**. This section describes the results of experiments probing cyt *c* photo-oxidation by the GL-RxN protein.

In the absence of cyt *c*, the black and blue traces in **Figure 4.15-A** compare the ZnP³ quenching in GL-H66 (ZnP at H66) and GL-RxN (ZnP at H66 plus heme ligated between H36 and H96). The presence of oxidized heme in GL-RxN increases the ZnP³ quenching rate from 210 s⁻¹ to 1170 s⁻¹. This heme-driven acceleration of the zinc porphyrin quenching is similar to that observed previously in a BT-6 Zn / Heme variant [12] and in an amphiphilic maquette binding ZnPIX and heme (**Figure 5.15**, reference [13]). The red trace in **Figure 4.15-A** shows GL-RxN with one molar equivalent of reduced cyt *c*; there is essentially no change in the triplet quenching when compared the GL-RxN alone.

Figure 4.15-B examines the transient absorption spectra of these same three systems 30 ms after the laser flash. In each case, the system has mostly returned to the quiescent ground state by this time; the residual signals of a few mOD are two orders of magnitude smaller than the initial bleach 1 μs after the laser flash. The black points show the spectrum of the heme-free GL-H66 maquette. The blue points show GL-RxN, binding heme and ZnP but without cyt *c*. The red points add one molar equivalent of cyt *c* to the GL-RxN center. The 428 nm peak is characteristic of cyt *c* oxidation. The red trace is the spectrum predicted for 28 nM reduced heme B and oxidized cyt *c*; this concentration corresponds to a 3% yield in the charge-separated state at this time point. Despite the marginal yield, the spectral evidence does suggest that this maquette has replicated an



essential function of the bacterial photosynthetic reaction center by photo-oxidizing cyt *c* in solution. We were unsuccessful in deconvolving the cyt *c* oxidation from the other states in the system using SVD, but by 30 ms after the flash essentially only the charge-separated state remained.

4.6 Discussion

The interprotein ET reactions examined in this chapter differ from those in **Chapter 2** in two important respects. First, this chapter's experiments are cyclic ETs driven by maquette cofactor excitation, whereas the ET in **Chapter 2** are exothermic, non-cyclic, ground state reactions. Much of the literature addressing time-resolved protein electron transfer examines similar cyclic, photoactivated systems including natural photosynthetic reaction centers [24] [25] and modified proteins using photoactivatable zinc cofactors [26] [27] or ruthenium labels [28] [29]. Second, this chapter's maquettes are designed with a dipole moment whereas the BT6 protein addressed earlier has a fairly uniform charge distribution.

ET from GL-H96 shows second-order behavior with respect to [cyt *c*]. **Figure 4.13-A** demonstrates that, at 4 mM ionic strength, the rate of cyt *c* photoreduction by GL-H96 to cyt *c* is linear with cyt *c* concentration in up to 6x excess, yielding a second-order rate constant of $3.4 \times 10^8 \text{ M}^1\text{s}^{-1}$. Clearly this is a fast reaction, approaching the diffusion limit if the reactants are in fact freely diffusing. The reaction half-time in **1d** decreases inversely with [cyt *c*] out to six equivalents of cyt *c*, suggesting the absence of a well-defined bound complex for ET in this system. Such behavior is consistent with some other interprotein electron transfer complexes including Adrenodoxin / cyt *c* [30] and myoglobin / cyt *b5* [26]. Notably, both partners in these two “pure encounter complex” systems are small, single-cofactor proteins, as is the case here. It is somewhat surprising that the reactants appear to be freely diffusing at the unphysiologically low 4 μM ionic strength. The oxidation of cyt *c2* by the *R. sphaeroides* reaction center, for example, shows a change from diffusional to partially-bound kinetics upon changing the reaction conditions from 30 mM NaCl / 10 mM Tris to 10 mM Tris alone [24].

Estimating the maquette dipole moments provides some insight into the ionic strength dependence of ET rates. A public web-based tool, the Protein Dipole Moments Server, computed the dipole moment of each maquette from a rough PDB from an estimated structure. The server returns the magnitude and direction of the dipole vector, allowing a rough calculation of the angle expected with respect to a well- aligned cyt *c* molecule. **Table 4.5** summarizes these results. It is important to note that the structures employed for these calculations are purely estimates: they are the result of a 10 ns molecular dynamics run on the GL-H66 maquette (starting from parallel helices), followed by Pymol “mutagenesis” to the sequences of the H96 and DPM maquettes.

Thus, the structures and resulting dipoles should only be considered approximations in the subsequent calculations.

Van Leeuwen presented a theory addressing the ionic strength dependence of interprotein electron transfer, accounting for both monopolar and dipolar electrostatic effects (**Eqn. 1.8**). The quantities in **Table 4.4** are sufficient to solve **Eqn 1.8** for each maquette / cyt *c* system, offering a prediction of the ionic strength dependence. **Figure 4.16** shows these results, along with the experimental half-times of the stretched-exponential fits of **Figure 4.14**. Please note that the figure shows half-times, not rates, so larger values correspond to slower ET. Frame **A** shows the overall predictions for each maquette to the experimental observations. Frames **B-D** separate the overall theoretical interaction into monopolar and dipolar components.

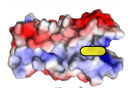
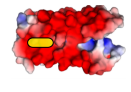
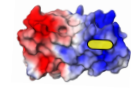
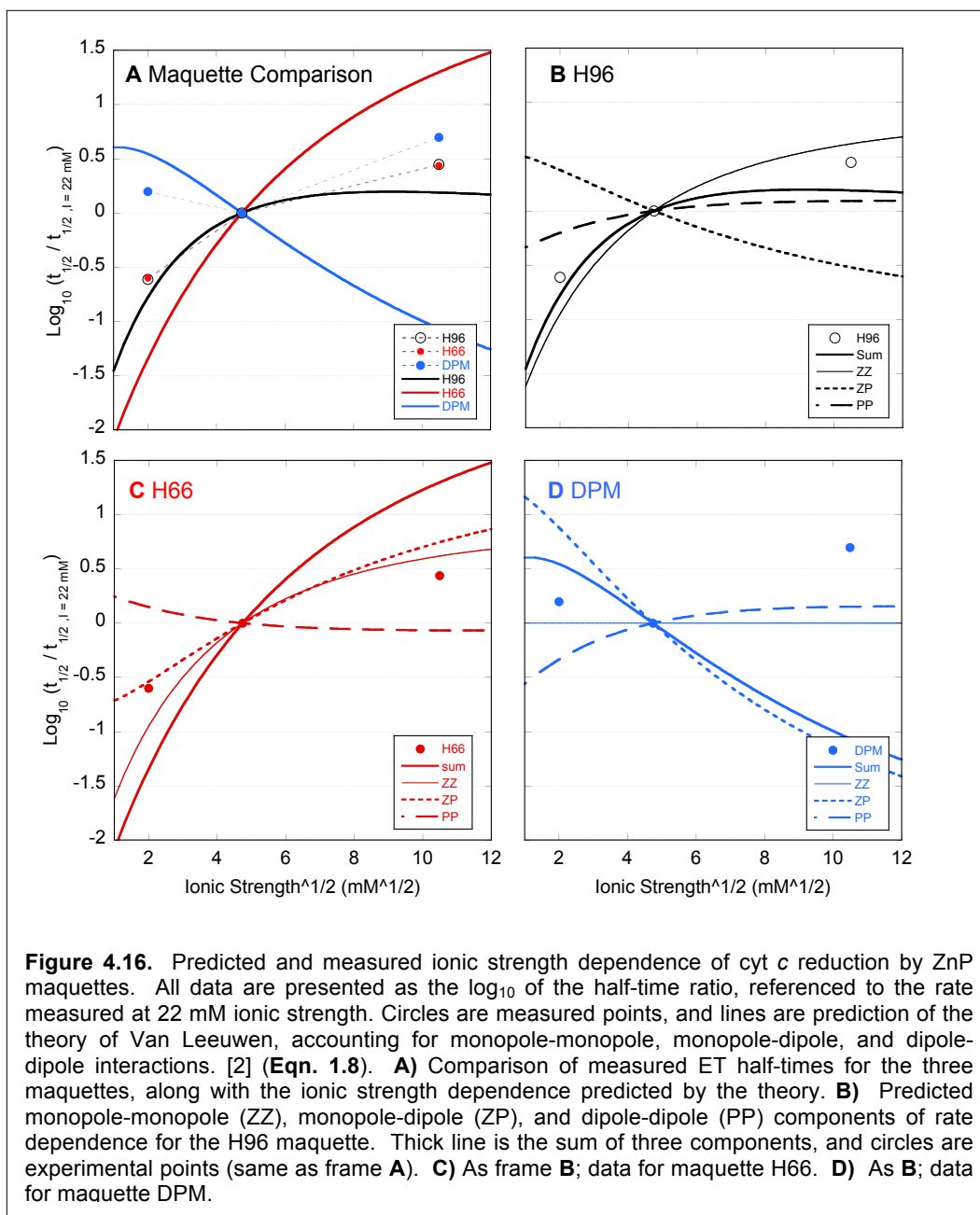
Protein	Charge	APBS Charge Visualization	Dipole moment (debye)	Estimated dipole θ
GL-H96	-7		433	- 135 deg
GL-H66	-7		318	+ 45 deg
GL-DPM	0		723	-180 deg
Cyt <i>c</i>	+6		304	0 deg

Table 4.4. Maquette dipole estimates from Protein Dipole Moments Server[1]. Yellow boxes indicate locations of ZnP in protein



Of the three maquettes in **Frame A**, only H96 (black line) fits reasonably with the predicted ionic strength dependence. H96 has a favorable monopole but moderately unfavorable dipole for interaction with *cyt c*; its overall charge is negative but the cofactor resides on the net positive side of the protein. H66 (red) has both a favorable charge and dipole vector. Yet the ionic strength dependence of H66 is very close to that of H96, even at the highest ionic strength. The “narrow” geometry of the 4-helix maquette bundle may explain this result, as illustrated in

Figure 4.17. The unfavorable dipole geometry assumes that a *cyt c* molecule could only engage in ET from the left side of the protein, near the “+” side. However, even a *cyt c* engaging from the bottom or right side of the protein may come within reasonable ET distance. If this is significant, the left-to-right dipole orientation on the H66 and H96 designs would be expected to have a smaller impact on the ET rate.

The glutamine-rich amino acid composition of DPM is a large departure from previous maquette designs, and its ability to maintain structure and cofactor binding despite a major sequence overhaul is a testament to the maquette concept. The dipole moment of the DPM maquette is parallel to the long maquette axis and thus should not be subject to the *cyt c* “wraparound” pictured in **Figure 4.17**. DPM has no net charge but possesses a strong and unfavorably oriented dipole for interaction with *cyt c*.

Figure 4.16-D predicts the half-time to decrease monotonically with ionic strength, as more salt will screen the unfavorably dipolar interaction. This was not observed however; the 22 mM ionic strength shows a shorter half-time than either 4 mM or 110 mM. As discussed in **Section 4.5.3**, the absence of a reduced *cyt c* α band along with quenching by pre-reduced *cyt c* suggests that the *cyt c*-dependent quenching in these experiments may be occurring through a non-ET mechanism. If a Forster-type energy transfer is responsible for this quenching, we would still expect some ionic strength dependence in this interaction. Because the Forster exchange is a longer-range interaction, its ionic strength dependence would likely be weaker than that for ET. It is difficult to draw conclusions from the salt dependence of quenching for DPM, given the open question of the triplet quenching mechanism.

The RxN maquette, ligating both ZnP and heme, performs photooxidation of pre-reduced *cyt c*. The 3% yield computed from **Figure 4.15** clearly offers room for improvement, but it is notable that the H66 design changes from a photo-reducing to photo-oxidizing construct simply

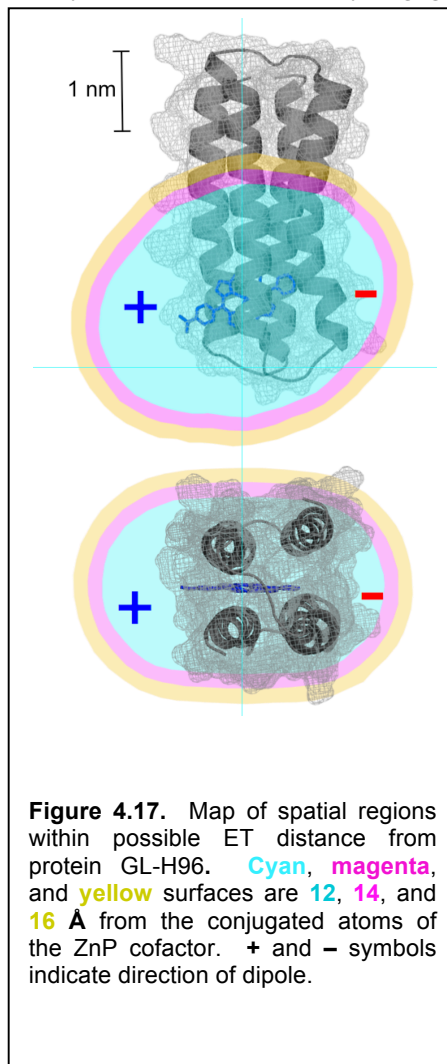


Figure 4.17. Map of spatial regions within possible ET distance from protein GL-H96. Cyan, magenta, and yellow surfaces are 12, 14, and 16 Å from the conjugated atoms of the ZnP cofactor. + and - symbols indicate direction of dipole.

through the addition of two histidines and a heme. Moreover, the ZnP / heme charge-separated dyad is very short lived both in this protein and in similar designs [12]. The work of Zhenyu Zhao and others in the Dutton lab in engineering a long-lived intra-protein charge separation could certainly be applied to this system to improve the cyt *c* oxidation yield. The photooxidation shown here represents a proof-of-principle for such an effort.

4.7 Conclusions

The experiments show that simple protein maquettes may be rationally designed to bind a photoactivatable cofactor and to perform photoreduction of natural bovine cyt *c*. At 4 mM ionic strength the k_{ET} for this system is $3.4 \times 10^8 \text{ M}^{-1}\text{s}^{-1}$, with second-order kinetics out to 6 stoichiometric equivalents of cyt *c*. As in **Chapter 2**, these maquettes were designed only with rough geometry and surface charge patterning in mind, and they show that detailed structural design is not necessary for fast interaction with a natural protein. The robust ET behavior of H96 was somewhat surprising given that it was designed with an unfavorably oriented dipole; H66 was expected to be faster. Certainly the favorable monopole interaction plays a role in H96, apparently outweighing the dipole influence at the salt levels examined here. In contrast, the strongly unfavorable dipole of the DPM maquette does appear to suppress ET, although it still does exhibit cyt *c* – dependent quenching, perhaps resulting from an energy transfer mechanism. Finally, the H66 maquette can be changed from a reducing to oxidizing protein with the simple addition of a second cofactor.

Additional protein designs would offer more insight into the details of maquettes' electrostatic interactions. Specifically, the dipole impacts in H66 and H96 would be easier to characterize in monopole-free proteins. The large count of polar uncharged residues in DPM suggests that such a change could be made with little disruption to behavior. A favorably-oriented DPM variant would offer additional insight into the impact of an “aggressive” dipolar design to enhance ET. Finally, additional experiments at higher ionic strengths would provide more physiologically relevant data. Importantly, this would also aid in deconvolving the impact of dipole effects from the monopoles, as the dipolar interactions become proportionately more significant with the ionic screening of longer-ranged monopole effects.

4.8 References

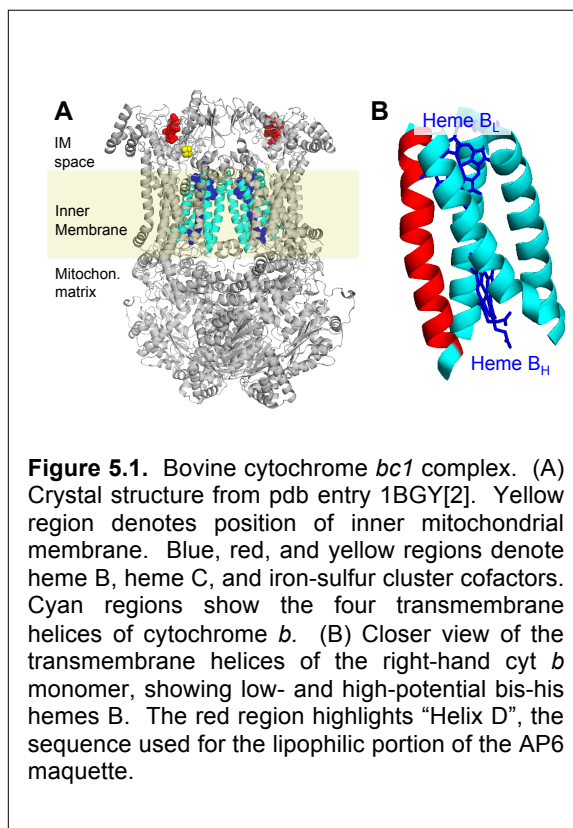
- [1] C.E. Felder, J. Prilusky, I. Silman, J.L. Sussman, A server and database for dipole moments of proteins, *Nucleic Acids Research*, 35 (2007) W512-W521.
- [2] J.W. Vanleeuwen, The Ionic-Strength Dependence Of The Rate Of A Reaction Between 2 Large Proteins With A Dipole-Moment, *Biochimica et biophysica acta*, 743 (1983) 408-421.
- [3] J. Fajer, D.C. Borg, A. Forman, D. Dolphin, R.H. Felton, Pi-Cation Radicals And Dications Of Metalloporphyrins, *Journal of the American Chemical Society*, 92 (1970) 3451-&.
- [4] B.A.M. Fry, Joshua A.; Esipova, Tatiana V.; Vinogradov, Sergei, A.; Dutton, P. Leslie; Moser, Christopher C., Light-activated electron transfer between de novo and natural proteins, *Chemical science*, (2016).
- [5] J.M. Vanderkooi, F. Adar, M. Erecinska, Metallocytochromes-C - Characterization Of Electronic Absorption And Emission-Spectra Of Sn-4+ And Zn-2+ Cytochromes-C, *European Journal of Biochemistry*, 64 (1976) 381-387.
- [6] Y. Takeuchi, Y. Amao, Light-harvesting properties of zinc complex of chlorophyll-a from spirulina in surfactant micellar media, *Biometals*, 18 (2005) 15-21.
- [7] H.C. Fry, A. Lehmann, J.G. Saven, W.F. DeGrado, M.J. Therien, Computational Design and Elaboration of a de Novo Heterotetrameric alpha-Helical Protein That Selectively Binds an Emissive Abiological (Porphinato)zinc Chromophore, *Journal of the American Chemical Society*, 132 (2010) 3997-4005.
- [8] H.C. Fry, A. Lehmann, L.E. Sinks, I. Asselberghs, A. Tronin, V. Krishnan, J.K. Blasie, K. Clays, W.F. DeGrado, J.G. Saven, M.J. Therien, Computational de Novo Design and Characterization of a Protein That Selectively Binds a Highly Hyperpolarizable Abiological Chromophore, *Journal of the American Chemical Society*, 135 (2013) 13914-13926.
- [9] W. Holzappel, U. Finkle, W. Kaiser, D. Oesterhelt, H. Scheer, H.U. Stolz, W. Zinth, Initial Electron-Transfer In The Reaction Center From Rhodobacter-Sphaeroides, *Proceedings of the National Academy of Sciences of the United States of America*, 87 (1990) 5168-5172.
- [10] Y. Kakitani, A. Hou, Y. Miyasako, Y. Koyama, H. Nagae, Rates of the initial two steps of electron transfer in reaction centers from Rhodobacter sphaeroides as determined by singular-value decomposition followed by global fitting, *Chemical Physics Letters*, 492 (2010) 142-149.
- [11] J.A.M. G. Kodali, L. A. Solomon, T. Esipova, N. Roach, C. J Hobbs, P. Wagner, O. A. Mass, K. Aravindu, J. E. Barnsley, K. Gordon, D. L. Officer, P. L. Dutton, C. C. Moser Design and engineering of water-soluble light-harvesting protein maquettes *Chemical Science (In Review)*, (2016).
- [12] T.A. Farid, G. Kodali, L.A. Solomon, B.R. Lichtenstein, M.M. Sheehan, B.A. Fry, C. Bialas, N.M. Ennist, J.A. Siedlecki, Z. Zhao, M.A. Stetz, K.G. Valentine, J.L.R. Anderson, A.J. Wand, B.M. Discher, C.C. Moser, P.L. Dutton, Elementary tetrahelical protein design for diverse oxidoreductase functions, *Nature Chemical Biology*, 9 (2013) 826-+.
- [13] G. Goparaju, B.A. Fry, S.E. Chobot, G. Wiedman, C.C. Moser, P.L. Dutton, B.M. Discher, First principles design of a core bioenergetic transmembrane electron-transfer protein, *Biochimica Et Biophysica Acta-Bioenergetics*, 1857 (2016) 503-512.
- [14] X.X. Chen, B.M. Discher, D.L. Pilloud, B.R. Gibney, C.C. Moser, P.L. Dutton, De novo design of a cytochrome b Maquette for electron transfer and coupled reactions on electrodes (vol 106, pg 617, 2002), *J. Phys. Chem. B*, 106 (2002) 2812-2812.
- [15] D. Tillett, B.A. Neilan, Enzyme-free cloning: a rapid method to clone PCR products independent of vector restriction enzyme sites, *Nucleic acids research*, 27 (1999) e26-e28.

- [16] L. Risinger, X.R. Yang, G. Johansson, Deoxygenation Of Supporting Electrolytes In Stripping Voltammetry By Glucose And Co-Immobilized Glucose-Oxidase And Catalase In A Flow System, *Analytica Chimica Acta*, 200 (1987) 313-318.
- [17] C.E. Aitken, R.A. Marshall, J.D. Puglisi, An oxygen scavenging system for improvement of dye stability in single-molecule fluorescence experiments, *Biophysical Journal*, 94 (2008) 1826-1835.
- [18] E.R. Henry, J. Hofrichter, Singular Value Decomposition - Application To Analysis Of Experimental-Data, *Methods in Enzymology*, 210 (1992) 129-192.
- [19] M.J.D. Powell, An efficient method for finding the minimum of a function of several variables without calculating derivatives, *Computer Journal*, 7 (1962).
- [20] Q. Bashir, A.N. Volkov, G.M. Ullmann, M. Ubbink, Visualization of the Encounter Ensemble of the Transient Electron Transfer Complex of Cytochrome c and Cytochrome c Peroxidase, *Journal of the American Chemical Society*, 132 (2010) 241-247.
- [21] J. Schilder, M. Ubbink, Formation of transient protein complexes, *Current Opinion in Structural Biology*, 23 (2013) 911-918.
- [22] S.H. Northrup, J.O. Boles, J.C.L. Reynolds, Brownian Dynamics Of Cytochrome-C And Cytochrome-C Peroxidase Association, *Science*, 241 (1988) 67-70.
- [23] J.W. van Leeuwen, The Ionic-Strength Dependence Of The Rate Of A Reaction Between 2 Large Proteins With A Dipole-Moment, *Biochimica et biophysica acta*, 743 (1983) 408-421.
- [24] C.C. Moser, P.L. Dutton, Cytochrome-C And Cytochrome-C2 Binding-Dynamics And Electron-Transfer With Photosynthetic Reaction Center Protein And Other Integral Membrane Redox Proteins, *Biochemistry*, 27 (1988) 2450-2461.
- [25] M. Tetreault, M. Cusanovich, T. Meyer, H. Axelrod, M.Y. Okamura, Double mutant studies identify electrostatic interactions that are important for docking cytochrome c(2) onto the bacterial reaction center, *Biochemistry*, 41 (2002) 5807-5815.
- [26] Z.X. Liang, M. Jiang, Q. Ning, B.M. Hoffman, Dynamic docking and electron transfer between myoglobin and cytochrome b(5), *Journal of Biological Inorganic Chemistry*, 7 (2002) 580-588.
- [27] P. Xiong, J.M. Nocek, A.K.K. Griffin, J. Wang, B.M. Hoffman, Electrostatic Redesign of the Myoglobin, Cytochrome b(5) Interface To Create a Well-Defined Docked Complex with Rapid Interprotein Electron Transfer, *Journal of the American Chemical Society*, 131 (2009) 6938-+.
- [28] D.N. Beratan, J.N. Onuchic, J.R. Winkler, H.B. Gray, Electron-Tunneling Pathways In Proteins, *Science*, 258 (1992) 1740-1741.
- [29] R. Langen, I.J. Chang, J.P. Germanas, J.H. Richards, J.R. Winkler, H.B. Gray, Electron-Tunneling In Proteins - Coupling Through A Beta-Strand, *Science*, 268 (1995) 1733-1735.
- [30] M. Ubbink, Dynamics in transient complexes of redox proteins, *Biochemical Society Transactions*, 40 (2012) 415-418.

Chapter 5 Amphiphilic Maquettes Designed for Transmembrane Electron Transfer

5.1 Introduction: Cytochrome *b* and Amphiphilic Maquettes

Mitochondrial coenzyme Q – cytochrome *c* oxidoreductase, also known as cytochrome *bc1* or Complex III, is one of the integral membrane protein complexes of the respiratory electron transport chain, or ETC. Like the other complexes I, II, IV, and adenosine triphosphate (ATP) synthase, *cyt bc1* resides in the mitochondrial inner membrane. Its bioenergetic function is to move electrons from reduced ubiquinone in the membrane to soluble cytochrome *c* in the aqueous mitochondrial intermembrane space. In doing so, *cyt bc1*, along with the other ETC complexes, transfers protons from the mitochondrial matrix to the intermembrane space. **Figure 5.1-A** illustrates the crystal structure of the bovine *bc1* complex[2]. The protein is large homodimer with each half consisting of multiple peptide chains. Photosynthetic bacteria support a similar *bc1* complex, residing in the periplasmic membrane with the photosynthetic reaction center. Its function and cofactors mirror those of the mitochondrial complex: electrons from photo-reduced quinone drive protons across the membrane. The electrons are then transferred to soluble cytochrome *c*₂ and cycled back to the reaction center.



to heme c_1 , and finally to soluble cytochrome c . The other electron is carried to through the two B-type hemes of the cytochrome b subunit, and finally to a second oxidized quinone bound at a separate site. This transmembrane ET through the two cyt b hemes is coupled with the proton-pumping transfer function of the complex. The heme-binding helices of cytochrome b form a well-defined coiled-coil spanning the membrane. This tetrahelical bundle provides a natural structural and functional prototype for developing *de novo* proteins supporting transmembrane ET. **Figure 5.1-B** highlights these helices in the structure of the much larger *bcl* complex. This chapter addresses the design and function of several amphiphilic maquettes that draw on structure and sequence of the cyt b subunit of *bcl*. (Please note that the term “cyt b ” refers here to the *bcl* subunit, not to B-type cytochromes in general).

To date, most maquette designs have been water-soluble proteins. Binary patterning, introduced in **Chapter 1**, provides a straightforward and reliable guide for the design of soluble α -helical bundle proteins. The previous two chapters address interprotein ET with maquettes, and this discussion has so far been limited to water-soluble designs. Indeed, nature does provide many examples of biologically essential interprotein ET between two soluble partners including ferredoxin / ferredoxin-NADP+ reductase [6], cyt $b5$ / hemoglobin [7], and cyt c / neuroglobin [9]. Yet the major bioenergetic interprotein electron-transfers involve a large membrane-bound photosynthetic or respiratory complex and a small soluble electron transporter: plastocyanin, ferredoxin / flavodoxin, or cyt c . In each case the small diffusing transporter interacts with an aqueous domain of the membrane-bound partner. So in order to model the full range of biological ET, the maquette concept should be extended to include amphiphilic, membrane-bound proteins.

Qualitatively, the principles of electron transfer do not differ between soluble and membrane-bound proteins [10], and the Moser-Dutton Ruler (**Eqn. 1.5**) should offer guidance in cofactor placement in an amphiphilic maquette just as in a soluble design. Experimental work with amphiphilic proteins requires detergent solubilization or incorporation into liposomes or other membranes. Thus, working with amphiphilic proteins is often more demanding than similar experiments with water-soluble proteins. Given these challenges, and the fact that many inquiries into electron transfer and other functions may be addressed by focusing purely on soluble proteins, it is unsurprising that there are relatively few *de novo* membrane protein designs in the literature. The first of these focused on transmembrane peptides mimicking the structure of ion channels [3], [11]. These were purely lipophilic molecules with minimal protrusion beyond the

membrane into the aqueous space. Discher et. al. presented the first amphiphilic, heme-binding maquette designs[8]. These four proteins, termed AP0 thru AP3, were homo-tetrameric four- α -helix bundles combining sequence from a dimeric soluble maquette with residues from a known transmembrane helix as shown in **Table 5.1**.

Ghirlanda and coworkers have demonstrated that minimal mutations confer heme binding [12] and midpoint potential modulation [13] in the natural transmembrane protein glycophorin A. This interesting result suggests that incorporating cofactor binding in membrane proteins may in general be fairly straightforward. Korendovych et. al. computationally designed a helical transmembrane homotetramer protein with two bis-histidine non-biological iron

Maquette	Lipophilic region	Aqueous region	Heme sites
AP0	<i>De novo</i> proton channel LS2 [3]	HP1 maquette [4]	4 aqueous
AP1	Influenza M2 proton channel	HP1 maquette[4]	2 aqueous, 2 membrane
AP2	Bovine cyt <i>b</i>	HP1 maquette[4]	2 membrane
AP3	Bovine cyt <i>b</i>	HP1 maquette[4]	2 membrane

Table 5.1: Previous amphiphilic maquette designs[8].

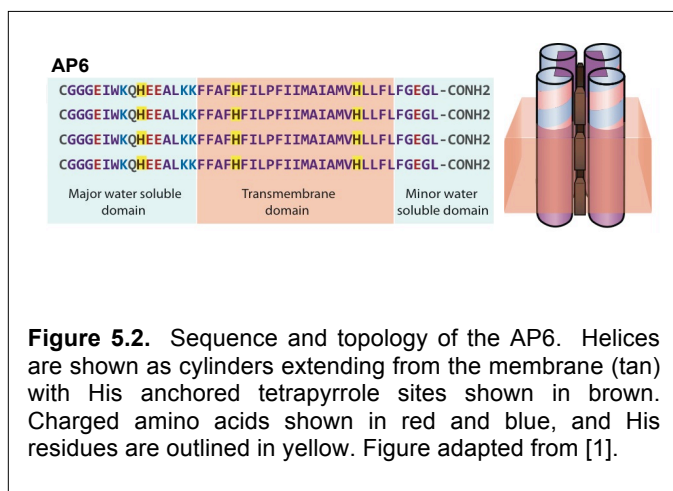
porphyrins in lieu of heme B [14]. The stated goal of this design was to demonstrate transmembrane ET. However, no electron-transfer was reported despite successful bundle assembly and cofactor binding in a phospholipid membrane. Indeed, to our knowledge there have been no reports in the literature of transmembrane ET mediated by a manmade protein.

This chapter describes my efforts and those of other Discher group members to reproduce the transmembrane ET function of cyt *b* using heme-binding amphiphilic maquettes. Two designs are presented here, denoted **AP6** and **AM1**. The production, purification, and biophysical characterization of these maquettes, as well as light-induced intraprotein ET, have been published in the May 2016 issue of *BBA Bioenergetics* [1]; these results are briefly described here. We also describe inconclusive but promising efforts to use these maquettes to catalyze ET between soluble small molecules separated by a bilayer. Finally, the chapter concludes with an additional design, **AM2**, drawing from sequence features in a new Dutton lab soluble maquette structure as well as from specific conserved features of cyt *b*.

5.2 AP6 Maquette

5.2.1 Design, synthesis, and liposome assembly of AP6

Figure 5.2 shows the sequence and cartoon representation of the AP6 protein. Like the earlier “AP-series” maquettes summarized in **Table 5.1**, AP6 is a homotetrameric 4- α -helix bundle. The membrane-spanning domain consists of 23 residues from the fourth helix of bovine cyt *b* (red region of **Figure 5.1-B**); in the natural protein this span encompasses histidines binding both heme B_L and B_H. This is the straightest of the four cyt *b* transmembrane helices. The



sequence of the aqueous region is derived from the soluble maquette HP7, a protein that has previously been shown to bind heme with a K_d of less than 5 nM[15]. As shown in **Figure 5.2**, AP6 offers three distinct positions for heme ligation: two lie within the membrane (corresponding to hemes B_L and B_H of cyt *b*) and one lies in the aqueous region. Given

three histidines on each helix, the bundle can potentially accommodate bis-histidine ligation for up to 6 hemes, two at each position along the bundle axis. Assuming a typical helical rise of 1.5 Å per residue, the expected separations of 16.5 and 21Å between adjacent histidine positions should yield heme edge-to-edge distances of roughly 11 and 16 Å. This separation is small enough to support fast intraprotein ET[16].

AP6 was synthesized on a Pioneer continuous flow solid phase synthesizer (Applied Biosystems) using a standard Fmoc/tBu protection strategy on a Fmoc-PEG-PAL-PS resin (Applied Biosystems) at 0.1 mmole scale. The synthesized peptide was purified on a reversed-phase C₁₈ HPLC column (Vydac) using gradients of acetonitrile (Fisher) and water both containing 0.1% (v/v) trifluoroacetic acid (TFA). The purity and molecular weight of the peptide was confirmed by MALDI-TOF mass spectrometry (Bruker) to be 5,022 Da. The purified protein dissolves readily in 2 mM dodecylphosphocholine (DPC) and in methanol.

5.2.2 Biophysical Characterization of AP6

Environment	Max. # Heme	K _{d1} (nM)	K _{d2} (nM)	K _{d3} (nM)	K _{d4} (μM)
Detergent: 2 mM DPC	5-6	< 5	50	400	>1
Lipid: POPC/POPS	5-6	< 5	50	400	1

Table 5.2 Heme binding in AP6.

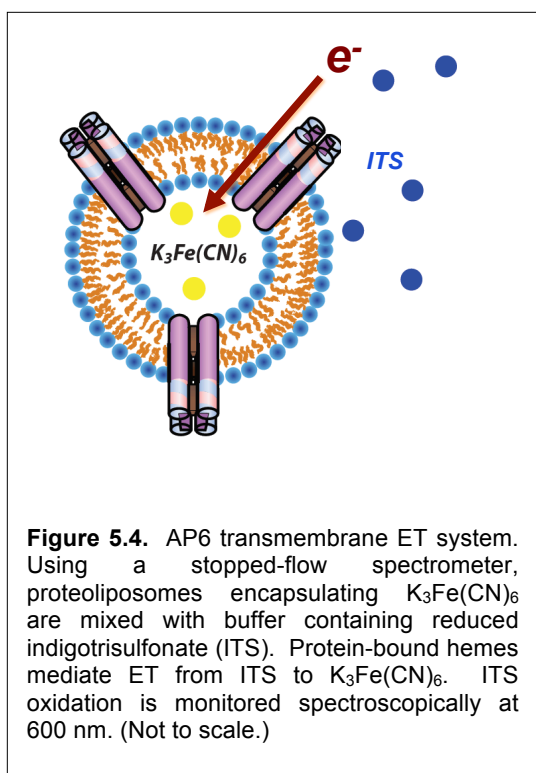
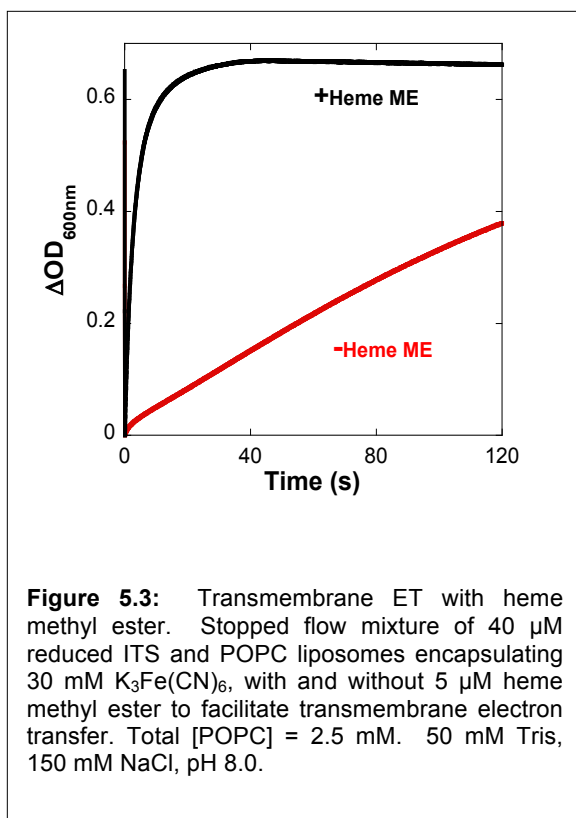
Ultracentrifugation experiments performed by Sarah Chobot have shown AP6 in 2 mM DPC to be roughly 50% tetrameric in the apo form at 1 μM concentration, increasing to ~80% at 10 μM. Adding heme promotes bundle association, yielding essentially 100% tetrameric

protein even at 100 nM concentration[17]. Dr. Geetha Goparaju performed further characterization of AP6, with data shown in **Appendix A2**. Circular dichroism spectroscopy on AP6 in 2 mM DPC estimates alpha-helical content to be ~56% at 25 C°. **Figure A2.1-A** shows the CD spectrum. Titrations to estimate heme K_d were performed for AP6 in 2 mM DPC and in phospholipid vesicles (80% POPC, 20% POPS). The data were fit to an analytical expression describing independent binding sites. **Figure A2.1-B** shows heme titrations in SDS and vesicles, and **Table 5.2** gives the computed K_d values.

Redox potentials of AP6 with 2 hemes in 80::20 POPC/POPS vesicles were measured by redox potentiometry[18], as described in **Appendix A1.4**. A redox titration pH 8.0 (100 mM NaCl, 20 mM Tris) yielded E_m values of -30 mV and -130 mV. Sarah Chobot previously measured the pH 8.0 midpoint of 2 heme in DPC-solubilized AP6 at -70 ± 8 mV and -150 ± 5 mV [19]. The slightly greater values observed in vesicle-incorporated AP6 suggests the bilayer environment may provide better heme sequestration from water than does the detergent micelle.

5.2.3 Developing an AP6 Proteoliposome System for Transmembrane ET

Transmembrane ET is a major functional goal of amphiphilic maquettes. A series of redox-active cofactors, anchored at discrete positions across a bilayer within mutual electron transfer distance, should ferry electrons downhill along a potential gradient. This section discusses the development of an experimental system to demonstrate maquette-mediated transmembrane ET.



In 1982 Loach et. al.[20] showed that heme methyl ester embedded in a bilayer mediates transmembrane ET. Esterifying the heme propionates increases the porphyrin's hydrophobicity, allowing it to traverse the inner portion of the bilayer. Loach showed that heme methyl ester catalyzes ET from the redox dye indigotrisulfonate (ITS) in bulk solution to $\text{K}_3\text{Fe}(\text{CN})_6$ encapsulated in palmitoyl-oleoyl-sn-glycero-phosphocholine (POPC) vesicles. In contrast, unmodified heme associates with the bilayer but cannot easily cross it, and Loach showed minimal ITS oxidation with ordinary heme. The ITS / $\text{K}_3\text{Fe}(\text{CN})_6$ vesicle system seemed simple to adapt to protein-mediated ET. We repeated the Loach experiment to verify the expected

function of the ITS redox dye; results are shown in **Figure 5.3**. As expected, heme methyl ester readily catalyzes the ITS oxidation, so we moved forward in adapting this system to problem maquette-mediated transmembrane ET. **Figure 5.4** presents a cartoon illustrating this maquette system.

A second potential source for anomalously fast oxidation is the leakage of $\text{K}_3\text{Fe}(\text{CN})_6$ from the proteoliposomes. Drawing from Loach's earlier work [20], our initial transmembrane experiments used only POPC lipid. However, the literature reports that other lipid formulations may better prevent the leakage of encapsulated small molecules. Charged

phospholipids such as palmitoyl-oleoyl-sn-glycero-phosphoserine (POPS) impart a degree of Coulombic repulsion between vesicles, limiting fusion and dynamics[21]. Cholesterol modulates lipid packing and plays an essential biological role in maintaining cell membrane integrity[22].

We first used dynamic light scattering (DLS) to make a qualitative comparison of holo-AP6 proteoliposome formulations.

Vesicles were prepared using 3 lipid mixtures: POPC, 80% POPC / 20% POPS, and 70% POPC / 15% POPS / 15% cholesterol. DLS measurements were taken on these samples directly after production and again after a 24-hour incubation at room temperature.

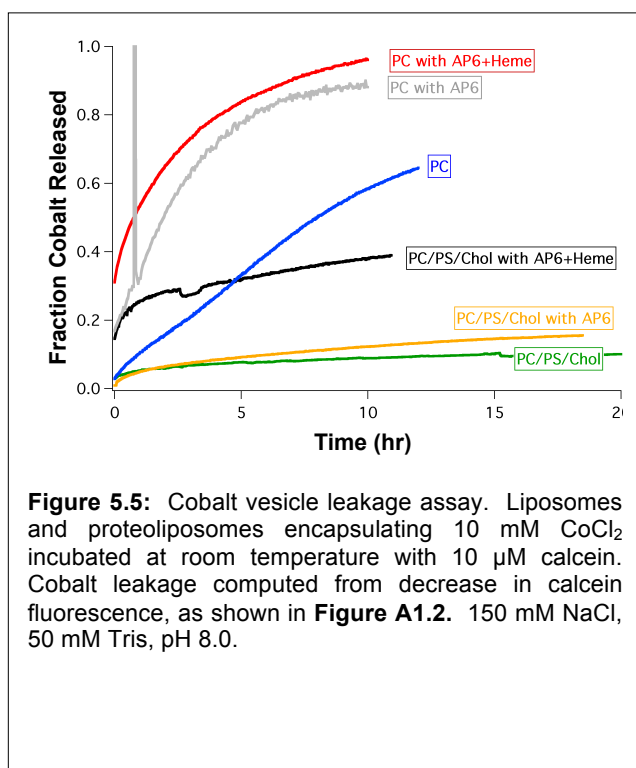
Table 5.3 summarizes these results. The mixture of POPC / POPS / cholesterol shows the lowest initial

	PC	PC / PS 80::20	PC/PS/Chol 70::15::15
\bar{R}	54.3 nm	59.4 nm	56.7 nm
Polydispersity	15.2%	19.3%	11.4%
\bar{R} , overnight	59.3 nm	60.4 nm	56.8 nm
Polydispersity, overnight	27.9%	22.3%	14.1%
$\Delta \bar{R}$	+ 5.0 nm	+ 1.0 nm	+ 0.1 nm
Δ Polydispersity	+ 12.7%	+ 3.0%	+ 2.7 %

Table 5.3. Dynamic light scattering with AP6 proteoliposomes using various lipid compositions.

polydispersity, as well as the smallest overnight change. This result suggests that the 3-lipid formulation may reduce vesicle dynamics and associated leakage.

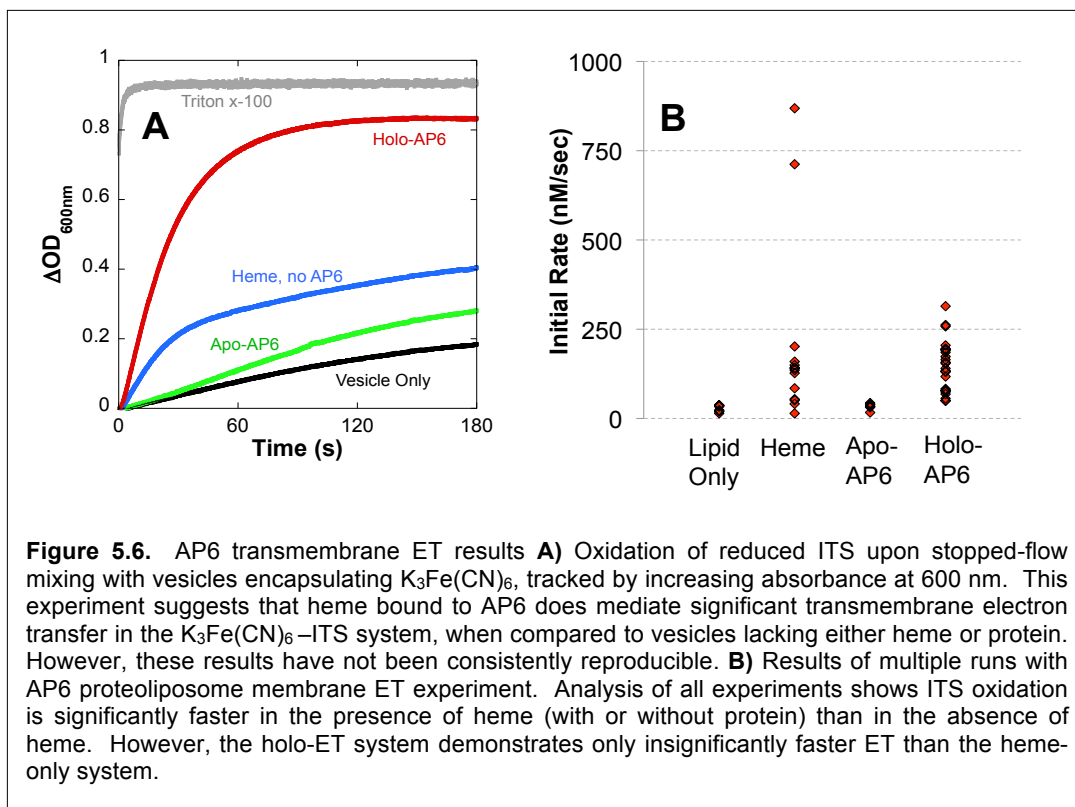
We also used a fluorescence-quenching assay to more directly compare the leakiness of various vesicle formulations. Liposomes encapsulating CoCl_2 (in place of $\text{K}_3\text{Fe}(\text{CN})_6$) were incubated in a fluorimeter with calcein in the surrounding buffer. In aqueous solution, the cobalt cation exists primarily as the $\text{Co}^{2+}(\text{H}_2\text{O})_6$ complex; this complex is similar in size to $\text{K}_3\text{Fe}(\text{CN})_6$ and should provide a reasonable proxy for ferricyanide leakage. Calcein, a fluorophore that is efficiently quenched by Co^{2+} and other divalent cations, was added to the medium outside the vesicles. I calibrated this quenching to $[\text{Co}^{2+}]$ through an initial titration of Co^{2+} in the absence of vesicles. **Figure A1.2** illustrates this quenching calibration in comparison to a similar experiment from the literature[23]. Applying the calibration to the results of overnight quenching experiments with vesicles yielded the results in **Figure 5.5**. These experiments show that for lipid-only vesicles, as well as apo- or holo-AP6 proteoliposomes, the 3-lipid mixture releases less Co^{2+} than does the pure POPC system. Thus, the 70::15::15 POPC / POPS / cholesterol lipid mixture was used for all subsequent AP6 transmembrane ET experiments.



5.2.4 AP6 Transmembrane Electron-Transfer Results

Vesicles encapsulating 30 mM $\text{K}_3\text{Fe}(\text{CN})_6$ were mixed with reduced 40 μM ITS in an OLIS stopped-flow spectrometer, as detailed in **Appendix A1.7**. ITS oxidation rates were compared between vesicles with AP6 and heme, AP6 only, heme only, or neither. **Figure 5.6-A** shows a representative result for AP6 transmembrane ET. The four vesicle samples shown here were prepared together and run sequentially in the stopped-flow in the same day. Vesicles lacking both protein and heme show the slowest ITS oxidation. The apo protein raises this rate only slightly, while heme in the absence of protein shows a more significant increase and biphasic behavior. In this experiment the holo-AP6 shows faster ITS oxidation that is nearly complete by one minute. Finally, lysing the vesicles with detergent prior to mixing yields nearly complete oxidation within the first few seconds, as expected given excess $\text{K}_3\text{Fe}(\text{CN})_6$. However,

these results have not been consistently repeatable. **Figure 5.6-B** summarizes the results of multiple experiments. Running a Welch ANOVA test[24] on these data indicates that the presence of protein does not yield a statistically significant increase in initial ITS oxidation rate; essentially one cannot conclude from these data that holo-AP6 is a better mediator of transmembrane ET than heme alone.



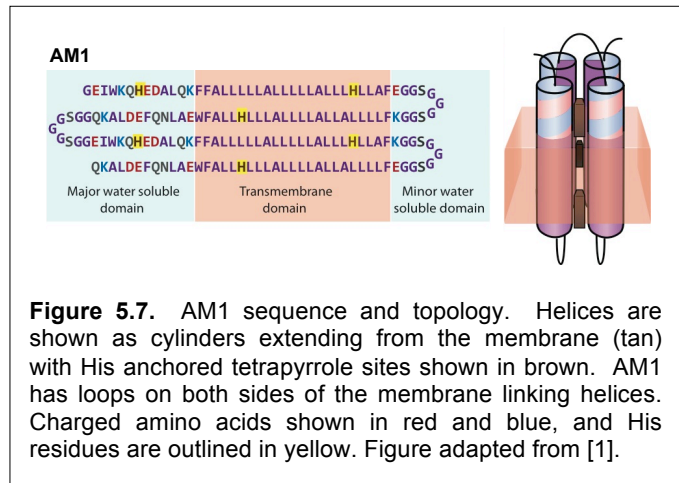
Some features of AP6 might render it unable to reliably shuttle electrons across the membrane. The heme binding tests showed that, in vesicles, AP6 ligates four hemes with K_d values of 1 μM or less. The tetrameric bundle offers six bis-his heme sites at three locations along the membrane. It is possible that the four hemes are binding in such a way that one of these locations is not occupied, breaking the ET chain. Furthermore, one could imagine a tetrameric bundle assembly where not all helices share the same vectorial orientation in the membrane, perhaps making hemes inaccessible to soluble redox molecules on one or both sides of the membrane. The monomeric AM1 design discussed in the next section seeks to address these concerns.

5.3 AM1 Maquette

5.3.1 Design of Amphiphilic Monomer Maquette AM1

The soluble monomeric maquette BT6, described in **Chapter 2**, was a step forward in “maquette evolution” from its predecessor, the dimeric helix-loop-helix construct known as HP7[15], [25]. A primary motivation in the development of a single-chain maquette was to break the sequence symmetry imposed by an oligomeric topology, allowing increased flexibility in making single-

point mutations. Similarly, the AM1 maquette (for “Amphiphilic Monomer”) was designed as a successor to AP6 to provide similar improvements in the family of amphiphilic maquettes. **Figure 5.7** shows the AM1 sequence, along with a structural cartoon. The hydrophilic domain of AM1 duplicates the top half of BT6, specifically 12 N-terminal amino acids from helices one and three, 12 C-terminal amino acids from helices two and four, and the loop connecting helices two and three. Each helix was then extended into the membrane with a 23 amino acid long “generic” transmembrane sequence rich in leucine and alanine residues. These residues were selected for their high α -helical propensity. The leucine-to-alanine ratio was chosen to match the overall hydrophobicity of the cyt *b* helices, as determined from the Wimley-White whole-residue octanol scale[26]. The hydrophilic domain contains a pair of heme ligating histidines between helices one and three. The sequences of the four helices were plotted on polar graphs with a 100° angle per residue, corresponding to straight α -helices with a typical pitch of 3.6 residues per helical turn[8]. The polar graphs revealed that the binary-patterned heptad repeat that has been used for the design of the water-soluble maquette **A** brings the amino acids out of register for longer helices, specifically for helices two and four. Therefore an extra alanine was introduced



near the C-terminal end of helices two and four. Additionally, phenylalanines and tryptophans were added near the edges of the membrane region, consistent with the lower insertion energy of aromatic residues near the aqueous-membrane interface[26].

5.3.2 Expression, Purification and TEV Cleavage of AM1

Like the soluble monomers BT6 and GL, AM1 is too large to be reliably synthesized and instead was expressed in *E. coli*. However, there are important differences in the expression and purification scheme for AM1. Geetha Goparaju carried out the bulk of method development leading to reliable expression and purification of the amphiphilic monomer.

Initial efforts to express amphiphilic maquettes resulted in poor yields, accompanied by very slow growth upon induction, suggesting protein toxicity. Driving the expressed protein into inclusion bodies offers a method to overcome product toxicity, and building a KSI fusion construct is a common technique to promote inclusion body formation [27]. Thus, the AM1 gene was cloned into a pET31b(+) vector (Novagen), producing a fusion with Δ^5 -3-ketosteroidisomerase (KSI). **Appendix A1.8.1** provides more detail on the gene design and fusion protein expression. A modified TEV cleavage procedure was developed to remove the His-tag and KSI domain from the maquette. This involved finding detergent conditions where the maquette did not aggregate before or after cleavage while still maintaining competent TEV protease function. Running the cleavage overnight in the presence of 2% Tween-20 and 2M urea produced good yields. **Appendix A1.8.2** details the inclusion body and fusion product purification, along with the TEV cleavage.

5.3.3 AM1 Solubilization, Detergent Exchange, and Vesicle Incorporation

In combination with sonication, SDS proved more effective than other detergents for solubilizing lyophilized AM1. For some experiments SDS was exchanged with dodecylmaltoside (DDM), a milder nonionic detergent that often better preserves native structure in membrane proteins. Adding lipids and removing detergent with polystyrene beads (Bio-Beads) allowed incorporation of AM1 into lipid vesicles. **Appendix A1.8.3** explains each of these procedures in more detail.

5.3.4 Biophysical Characterization of AM1

Dr. Geetha Goparaju performed much of the AM1 characterization work. Data are shown in **Appendix A2**, and this section gives a summary of the results. **Figure A2.2** shows a MALDI-TOF mass spectrum for AM1 after TEV cleavage. Two peaks are clearly visible. One corresponds to the mass of the cleaved maquette and the other to the mass of the cleavage fragment comprising KSI, His-tag, and TEV protease target sequence. **Figure A2.3-C** shows the CD spectrum of AM1 in SDS at 25 °C, corresponding to an α -helical content of 49%. Interestingly, the CD shows helical content increases to 58% upon detergent exchange to DDM (data not shown). Other reports have shown that CD may underestimate total helicity 9 to 31% in

SDS-solubilized proteins. [28]. The protein is relatively thermostable; thermal melt experiments show loss of 5% helicity upon raising the temperature from 25 °C to 55 °C.

Heme titrations into detergent-solubilized and liposome-incorporated AM1 were

Detergent	Lipid	Cofactor	Max. # cofactor	K _{d1} (nM)	K _{d2} (nM)	K _{d3} (μM)
3 mM SDS		Heme	3	< 5	400	4
DDM		Heme	3	< 5	400	0.4
	POPC/POPS	Heme	3	Pre-bound	150	4
3 mM SDS		Zn-PPIX	5	All < 50 nM		

Table 5.4: AM1 cofactor binding titrations. K_d values for heme and ZnPPIX in AM1, computed from titrations in **Figure A2.3**.

performed using the same procedures employed for AP6. **Figure A2.3-A** shows the results of heme binding titrations into AM1 solubilized in SDS and DDM as well as in POPC proteoliposomes. **Table 5.4** gives the K_d values computed from these experiments. Notably, the third K_d is improved by an order of magnitude, from 4 μM to 400 nM, upon replacing SDS with DDM. In the liposome case, the first heme equivalent was added to SDS-solubilized protein prior to detergent depletion as explained in **Appendix A1.8.3**.

We also examined binding of zinc protoporphyrin IX (ZnPPIX) in AM1. The porphyrin ring of ZnPPIX is identical to that of heme, but the Fe is replaced with Zn²⁺. ZnPPIX binds only to a single histidine, so AM1 has the potential capacity to ligate up to six ZnPPIX equivalents.

ZnPPIX was dissolved in DMSO and titrated into SDS-solubilized AM1 (**Figure A2.3-C**). The protein ligates 5 equivalents of ZnPPIX with $K_d < 50$ nM (**Table 5-4**). Finally, one equivalent each of heme and ZnPPIX were added to DDM-solubilized AM1. The spectra of these cofactors were additive, indicating successful binding of both (**Figure A2.4**).

Heme midpoint potential was measured for AM1 binding 2 hemes in proteoliposomes with a 80::20 POPC/POPS lipid mixture. Two hemes bound to AM1 exhibit distinct midpoint potentials at pH 7.0 and pH 8.0. Midpoint potential splitting is to be expected, if only because hemes buried far from the aqueous phase are generally easier to reduce and have higher midpoint potentials compared to hemes more exposed to water; this principle is supported by mutations impacting heme solvent accessibility in earlier maquette designs[29]. At pH 8.0 the ~120 mV difference between the two heme E_m values of -60 mV and +60 mV splitting approaches that observed between hemes b_H and b_L in cytochrome bc_1 complex[30]. Both hemes in native cyt b are very well sequestered from water, however; their potentials are modulated by direct interactions with neighboring residues, not by differences in solvent accessibility.

5.3.5 Light-Activated Intraprotein ET in AM1

Zinc protoporphyrin IX, or ZnPPIX, is a heme molecule in which the central iron atom has been replaced by zinc. Like other zinc porphyrins including the synthetic ZnP used in **Chapter 4**, ZnPPIX becomes strongly reducing upon photo-activation. The excited singlet state converts to the triplet on a ns timescale, and the E_m for the ${}^3\text{ZnPPIX}^*/\text{ZnPPIX}^+$ couple is about -800 mV[31]. AM1, binding both heme and ZnPPIX, provides a platform for light-induced ET. The transient absorption apparatus and procedure for this experiment is described in **Section 4.4.1**. **Figure 5.8-B** shows the time course of the ZnPPIX Soret bleach recovery for AM1 with ZnPPIX alone and with both ZnPPIX and heme. **Figure 5.8-A** compares a similar experiment with a 3-histidine BT6 mutant also binding ZnPPIX and heme. Assuming a typical reorganization energy of 0.7 eV for intraprotein ET and a ΔG of -0.74 eV (ET

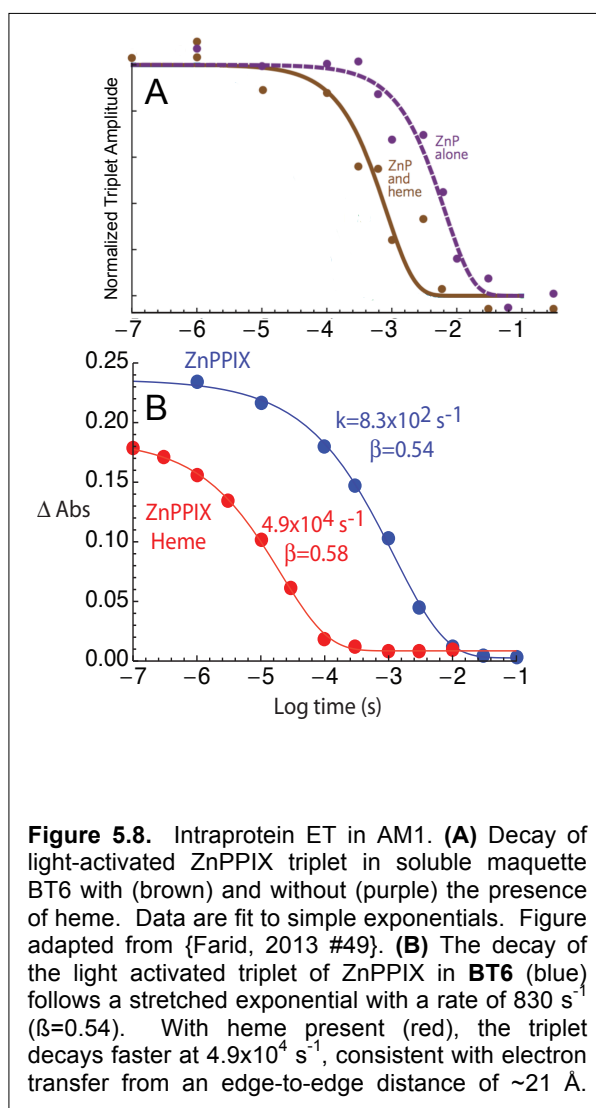


Figure 5.8. Intraprotein ET in AM1. **(A)** Decay of light-activated ZnPPIX triplet in soluble maquette BT6 with (brown) and without (purple) the presence of heme. Data are fit to simple exponentials. Figure adapted from {Farid, 2013 #49}. **(B)** The decay of the light activated triplet of ZnPPIX in **BT6** (blue) follows a stretched exponential with a rate of 830 s^{-1} ($\beta=0.54$). With heme present (red), the triplet decays faster at $4.9 \times 10^4 \text{ s}^{-1}$, consistent with electron transfer from an edge-to-edge distance of $\sim 21 \text{ \AA}$.

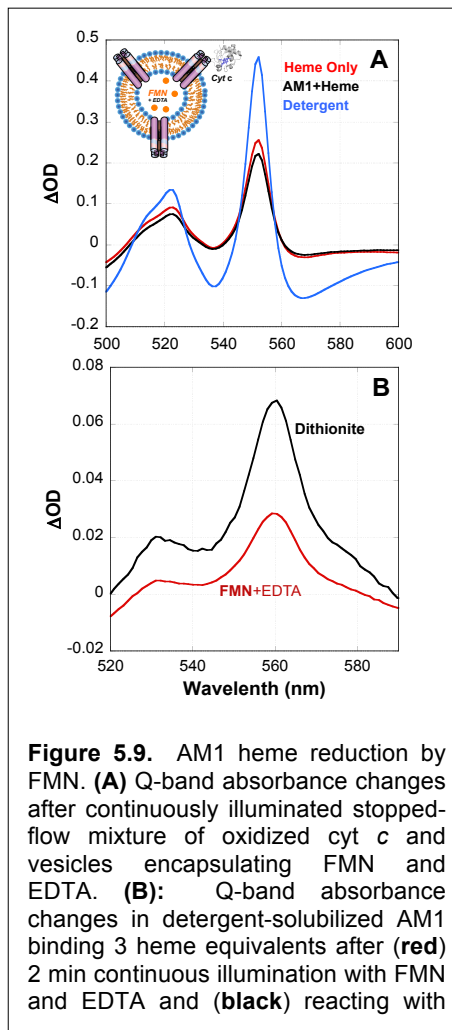
from -800 mV zinc porphyrin to heme with $E_m = +60 \text{ mV}$), an ET rate of $4.9 \times 10^4 \text{ s}^{-1}$ implies a cofactor edge-to-edge distance of 17.5 \AA . A similar computation for ZnPPIX in BT6 (frame A) implies an edge-to-edge distance of 19.5 \AA . This distinction is interesting, as the cofactor-binding histidines are located at the same relative sequence positions in both proteins. However, the cofactor locations are not uniquely defined in the 6-His AM1 protein. Also, the lipophilic domain in AM1 may yield a topology with cofactor distances differing from those in the water-soluble maquette. Future experiments will repeat this experiment using unambiguously defined bis-his and mono-his binding site for the heme and zinc porphyrin, respectively.

The transient absorption spectra of AM1 with ZnPPiX and heme does not show an accumulation of reduced heme (data not shown), in contrast to the clearly visible *cyt c* reduction described in the previous chapter (**Figure 4.11**). This suggests that, in AM1, the back-ET from reduced heme to the oxidizing ZnPPiX⁺ cation is faster than the initial light-induced ET from the triplet state. Similarly, an earlier ZnP + heme BT6 experiment summarized in **Figure 5.8-A** [25], and the Zn + Fe GL maquette without *cyt c* (**Figure 4.15**) did not present accumulation of reduced heme.

5.3.6 Transmembrane ET with AM1

Initially, transmembrane ET experiments with AM1 were performed using the ITS / K₃Fe(CN)₆ system introduced in **Section 4.2.2**. AM1 proteoliposomes were produced through the detergent depletion procedure described in Appendix **A1.7.3**; the only change to this procedure was the addition of 30 mM K₃Fe(CN)₆. One stoichiometric equivalent of heme was added to SDS-solubilized AM1 prior to detergent removal. The proteoliposomes were sonicated, extruded, and passed through a PD-10 column equilibrated to an isotonic Tris / KCl buffer solution to remove non-encapsulated K₃Fe(CN)₆. Finally, an additional three equivalents of heme were added prior to deoxygenation and stop-flow mixing with reduced ITS. Unfortunately the measured rate of ITS oxidation in this system did not consistently increase between holo-AM1 and heme alone (similar to AP6 experiments in **Figure 5.6**, data not shown).

It is possible that the failure to observe robust transmembrane ET arose not from inherent “ET-incompetence” in AP6 or AM1, but instead was a feature of other components in the experimental system. Perhaps ITS or ferricyanide do not couple well for ET with the maquette hemes. To test this notion, the AM1 vesicle experiment was repeated, replacing the ITS and



$\text{K}_3\text{Fe}(\text{CN})_6$ with other soluble redox reagents. A mixture of 8.5 mM free flavin mononucleotide (FMN) and 28 mM EDTA replaced the $\text{K}_3\text{Fe}(\text{CN})_6$ inside the vesicles. 35 μM cyt *c* replaced the ITS in the surrounding solution (See small cartoon, **Figure 5.9-A**). Note that bound flavin cofactors, in conjunction with EDTA in solution, have been used as photoreductants in previous maquette designs[32], [25]. The system described here replaces a maquette-bound flavin with soluble, unbound FMN.

There are several significant experimental differences between these two systems. First, FMN is a photoactive species, requiring illumination in the stopped flow to drive ET. Upon excitation, the flavin becomes strongly *oxidizing*, with an E_m on the order of +2.0 V. Excess EDTA serves as an irreversible “sacrificial” electron donor to quench the excited flavin, producing a singly-reduced radical semiquinone state. This process may be repeated to yield a doubly-reduced FMN. At pH 8.0 the E_m for the first electron in the doubly-reduced FMN is about -260 mV at pH 8.0[33]; this is a sufficiently reducing to drive the initial maquette heme reduction. Second, electrons are directed inward to encapsulated oxidant in the ITS / $\text{K}_3\text{Fe}(\text{CN})_6$ system, while they move outward in the FMN / cyt *c* system. A third difference in this arrangement is that the spectroscopically active species (cyt *c*) lies at the end of the redox chain, so cyt *c* redox change should only be observed upon complete transmembrane ET. In contrast, the ITS donor in the previous system lies at the beginning of the redox chain and thus could report oxidation even if ET failed to reach all maquette-bound hemes or the terminal acceptor.

The continuous light source employed to drive ET from the FMN largely ‘blinded’ the PMTs in the stopped-flow spectrometer, so it was not practical to track the spectral changes continuously after mixing. Instead, the light was periodically turned off to acquire “snapshots” over the course of the reaction. **Figure 5.9-A** shows a typical result after 120 sec illumination. The presence of heme, both with and without AM1, shows similar reduction of cyt *c* as indicated by the development of the reduced heme C α -band at 550 nm. AM1 is not helping to mediate cyt *c* reduction here. All the cyt *c* was quickly reduced upon lysing the liposomes with octyl-POE detergent, allowing direct contact between FMN and cyt *c*.

As a final control, I tested the ability of the photoexcited FMN, with excess EDTA as a sacrificial electron donor, to reduce heme in detergent-solubilized AM1; no lipid vesicles or cyt *c* were present in this experiment. 10 μM AM1 with three heme equivalents in 2 mM DDM was combined with 300 μM FMN and 5.4 mM EDTA and illuminated for 2 min. Excess dithionite was added to reduce any remaining oxidized heme. **Figure 5.9-B** shows the results of this

experiment; the peak at 560 nm is the reduced B-heme α -band. As expected, all heme was reduced by dithionite. FMN reduced only about half the heme in this system. This is a surprising result, suggesting that the potential of the activated FMN is insufficient to reduce all the hemes in AM1. Potentiometric measurements of obligate single-heme AM1 variants could help to address this possibility. Alternately, perhaps the small dithionite ion ($S_2O_4^{2-}$) is able to access all AM1 hemes whereas the larger flavin is sterically occluded from some population.

Replacing AP6 with AM1 still did not produce a robust maquette-mediated transmembrane ET system. The next chapter discusses possible explanations in the context of Moser-Dutton Ruler calculations.

5.4 Discussion: Modeling Electron transfer with AP6 and AM1

In principle, one would expect significant protein-mediated electron transfer across a membrane using either AP6 or AM1. This section introduces elementary Moser-Dutton Ruler computations to predict electron transfers between transmembrane redox centers, and discusses possible reasons why these rates have not been observed experimentally. The Moser-Dutton Ruler, introduced in **Section 1.2.2**, is an empirical relation derived from measured intra- and inter-protein electron transfer rates in a variety of natural and modified proteins:

$$\log_{10} k_{ET} = 13.0 - 0.6(R - 3.6) - 3.1 \frac{(\Delta G + \lambda)^2}{\lambda} \quad \text{Eqn. 1.5}$$

where k_{ET} is electron transfer rate in s^{-1} , R is the edge-to-edge cofactor distance in \AA , and ΔG and λ are the free energy change and reorganization energy in eV. In the following analysis we extend the Moser-Dutton Ruler to also include electron transfers between AP6/AM1 terminal hemes and soluble redox species (ITS, $K_3Fe(CN)_6$, FMN, or cyt *c*) on opposite sides of the membrane. Inter-heme distances were estimated by assuming straight helices and measuring edge-to-edge distances between cofactors placed in Pymol models. ET distances involving soluble molecules were estimated by adding 3 \AA to the closest solvent approaching the appropriate cofactor. The set of electron transfer rates between all cofactors yields a system of ordinary differential equations amenable to numerical solution. A Python program computed ET

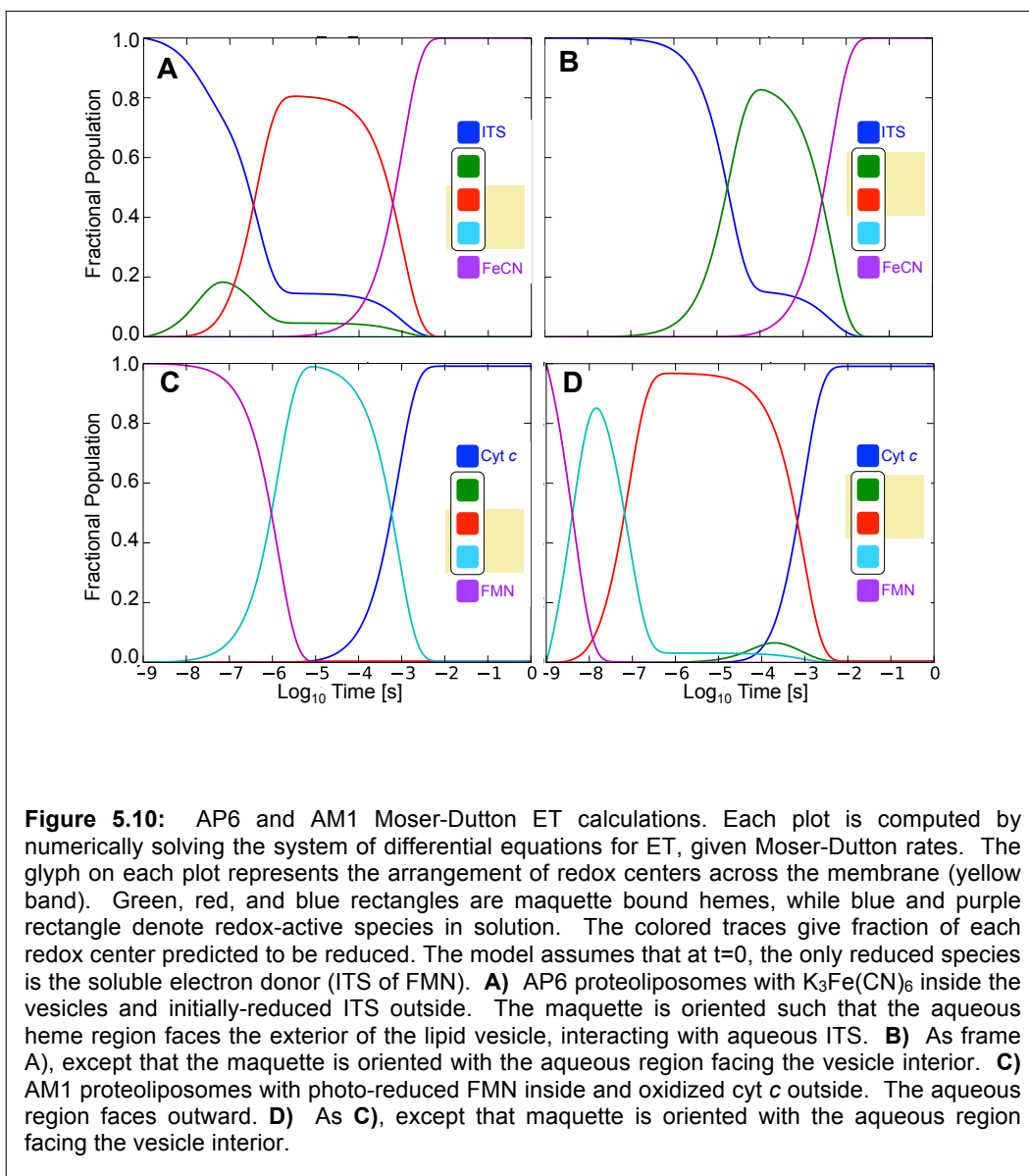
rates and solved the ODEs for AP6 and AM1. Importantly, there are two possible vectorial orientations for the amphiphilic maquettes with respect to the membrane; the aqueous region of the protein can extend either into the interior or exterior of the vesicle. In certain specific cases, the selection of lipid composition can control vectorial orientation of reconstituted membrane protein, but typically the orientation is random and should be assumed to be a combination of the two possibilities [34]. Since these two vectorial arrangements differ in their predicted ET rates, the system was solved for both orientations in AP6 and AM1. These models assume that maquette hemes in the membrane and aqueous regions use the higher and lower measured E_m values at pH 8.0. E_m values for soluble ITS, $K_3Fe(CN)_6$, FMN, and cyt *c* are, respectively, taken as -90 mV, 420 mV, -260 mV[33], and 250 mV. **Figure 5.10** shows these results.

Maquette	Protein Orientation w/r/t vesicle	$t_{1/2}$ (s)
AP6	Aqueous region out	7.2×10^{-4}
AP6	Aqueous region in	3.1×10^{-3}
AM1	Aqueous region out	6.0×10^{-4}
AM1	Aqueous region in	7.3×10^{-4}

Table 5.5 Computed half-times for transmembrane ET.

The calculations do not account for collisions with the soluble species. Instead, they make the major simplification that the soluble donor and acceptor are stationary. However, the models may reasonably be used to make qualitative comparisons between the systems, particularly in the time needed for an electron to traverse the membrane and reduce the soluble acceptor species. **Table 5.5** shows the computed terminal reduction half-times.

Interestingly, the first, third, and fourth rows show very similar times. Only the “aqueous-in” orientation of AP6 is predicted to be significantly slower.



AP6 offers six heme-binding sites, and these are located at three distinct positions along the length of the tetrahelical bundle (i.e. ligated at one of three histidines on the single-helix monomer). AP6 binds 4 hemes with at least $1 \mu\text{M}$ affinity (Table 4.2), although there is minimal binding on the remaining sites. If the four hemes are bound such that one position lacks any hemes, the system would lack a complete ET chain and transmembrane ET would be suppressed. AM1, with only three heme sites, has a liposome K_d of $4 \mu\text{M}$ at its third site. Although not sufficient to ensure complete occupation for $3.5 \text{ AM1 } \mu\text{M}$ concentrations employed in these

experiments, there should be enough fully-heme-equipped maquettes to exhibit significant ET if the system is in fact capable of heme-mediated ET across the bilayer.

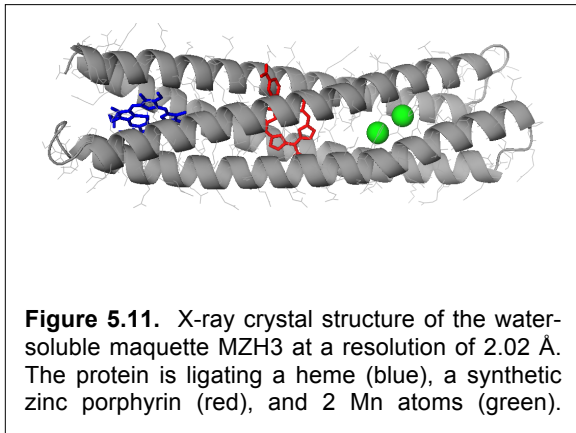
The absence of a 560 nm peak in **Figure 5.9-A** shows that even after 2 minutes of illumination in flavin-encapsulating proteoliposomes, there is no persistent reduction of maquette-bound hemes in AM1. This suggests the failure may lie in the initial ET from soluble donor to the maquette. However, there *is* partial heme reduction when the same protein is solubilized in detergent (**Figure 5.9-B**). Most of this reduction is probably in the aqueous-region heme, as this cofactor would have closer access to the FMN donor. The lack of any discernable B-heme reduction in **Figure 5.9-A** thus suggests that #1) AM1 in vesicles is oriented predominantly with aqueous region facing outwards such that the aqueous region is on the opposite side of the membrane from FMN and #2) the initial electron transfer from FMN to the first membrane-bound heme is very slow or non-existent. Repeating the AM1 experiment with the FMN/EDTA donor system *outside* the vesicles could strengthen this conclusion.

5.5 Design of Next-Generation Amphiphilic Maquettes

This section describes a final amphiphilic maquette, AM2. The goal of this design is to continue the effort to demonstrate robust maquette-mediated transmembrane ET. Hopefully the new design exhibits at least moderate binding at all heme sites, as is the case with AM1. Furthermore, in an ideal design the midpoint potentials for the hemes would provide an energetically downhill path for all electron transfers across the membrane. This need not be a strict requirement, however, as some endergonic steps are present in effective natural ET pathways[10].

The Discher group has procured the AM2 plasmid and expressed the fusion protein in inclusion bodies using the same procedures employed for AM1. At the time of writing this dissertation AM2 has not yet been purified or characterized, so no experimental data is presented here. Instead, this is purely a description and rationale for the AM2 design. The AM2 design takes less of a “fully first-principles” approach than does AM1. Unlike “pure” maquettes like AM1 and BT6, AM2 does draw sequence information from *cyt b* where the purpose for specific residues can be discerned.

The homotetrameric AP6, introduced in **Section 4.2**, draws the lipophilic portion of its sequence only from “helix D”, the straightest of the four transmembrane helices of bovine *cyt b*. Thus, it contains only a fraction of the sequence information in the natural model system. Although the Moser-Dutton ET approach would suggest otherwise, it is possible that structural



features provided by the other helices are needed for effective ET. Furthermore, the lipophilic region of AP6 houses four heme-binding sites (as opposed to two in *cyt b*). The AP6 design ligates heme between adjacent helices rather than diagonally across the bundle as in *cyt b*. (**Figures 5.1-B** and **5.2** contrast these heme-binding topologies). Despite these substantial differences between

AP6 and natural *cyt b*, AP6 does bind four hemes with $K_d \leq 1\mu\text{M}$, and at least two of these hemes are present in the lipophilic region. This suggests that the single-helix *cyt b* sequence offers value in this application, but is not sufficient in itself to produce an ET-competent maquette.

Another protein offering insight into amphiphilic bundle design is the Dutton lab maquette MZH3. This protein, designed by Nate Ennist, has yielded the first crystal structure of a *de novo* protein with bound porphyrins. **Figure 5.11** shows this structure. MZH3 is a water-soluble protein that forms a well-defined coiled-coil. A heme cofactor, shown in blue in **Figure 5.11**, is ligated between histidines in helices 1 and 3. The E_m for this heme has been measured at -150 mV (pH 7.4), as compared to -290 mV for the two hemes in BT6.

5.5.1 Design of AM2 Lipophilic Region

Cyt *b* clearly demonstrates the functional aim of the AM-series maquettes. We employed a bioinformatic approach to interrogate all the cytochrome *b* entries in the Entrez database in an effort to find conserved residues impacting ET function. An initial query for cyt *b* sequences in Entrez yielded a FASTA file with 335544 sequence entries. A Python script using the Biopython[35] sequence analysis module filtered these entries, removing unreadable, incomplete, or redundant entries. **Figure 5.12-A** lists the results of these initial filtering steps.

The cyt *b* chain in the *bc1* complex comprises more than just the four transmembrane helices. Bovine cyt *b*, for example, contains 379 residues, only about 100 of which lie in the region of interest in the heme-binding helices. Fortunately, simple sequence features may be used to identify these helices in the Entrez cyt *b* records. Two pairs of heme-binding histidines are nearly always 14 residues apart on helices 2 and 4. Likewise, helices 1 and 3 each contain

a pair of glycines, also 14 residues apart. These glycines are structurally important in minimizing steric clash with the hemes. The Python program located these residue pairs for each of the 6442 non-redundant sequences. The sequence was discarded if these pairs either could not be found or if the glycine and histidine pairs appeared in the incorrect order. 4815 sequences remained after this step from a range of plants, animals, protists, and prokaryotes. Next, the sequences for the four helices were extracted and aligned based on the locations of the aforementioned histidine and

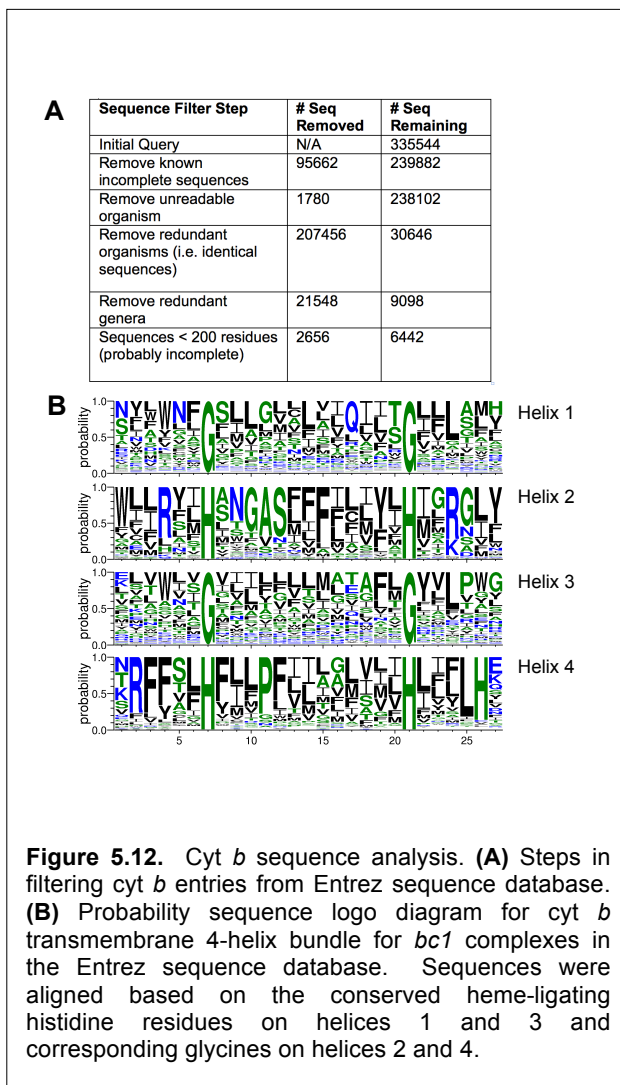


Figure 5.12. Cyt *b* sequence analysis. **(A)** Steps in filtering cyt *b* entries from Entrez sequence database. **(B)** Probability sequence logo diagram for cyt *b* transmembrane 4-helix bundle for *bc1* complexes in the Entrez sequence database. Sequences were aligned based on the conserved heme-ligating histidine residues on helices 1 and 3 and corresponding glycines on helices 2 and 4.

glycine pairs. Any sequences for a given helix with more than 40% redundancy were discarded. This left data sets for each individual helix ranging in size from 64 to 163 sequences. Sequence probability diagrams were prepared for each helix using WebLogo[36], shown in **Figure 5.12-B**.

Figure 5.13 summarizes the amino acid selection for the lipophilic region of AM2. The first step in this selection, shown in **5.13-A**, was to choose specific AM2 residues informed by the *cyt b* sequence alignment. These residues, chosen based on *cyt b* sequence consensus and functional information, are as follows:

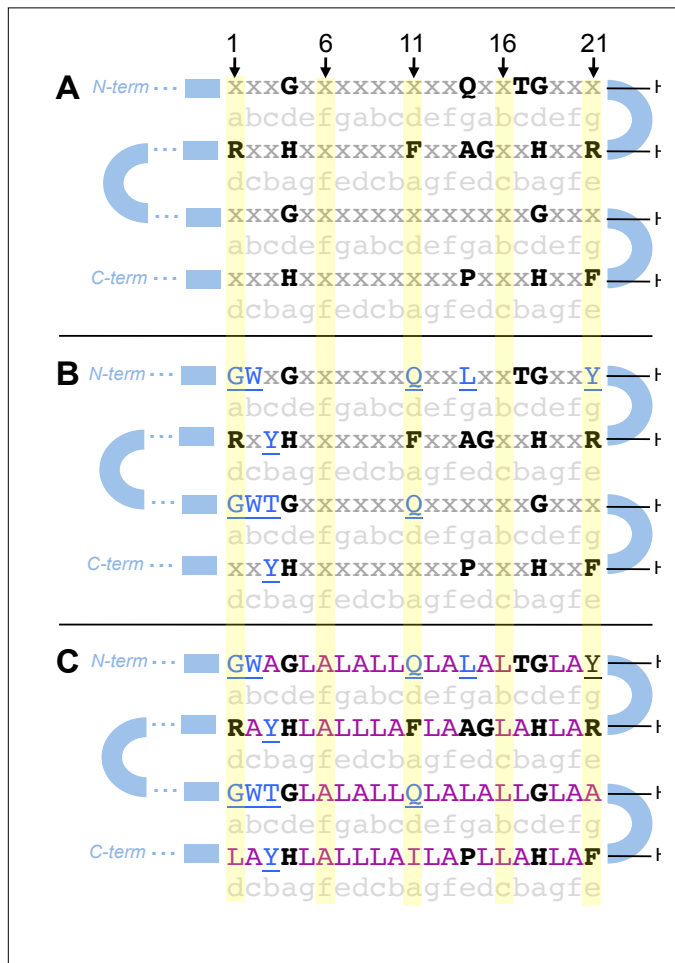


Figure 5.13. AM2 lipophilic sequence selection. Position numbers “1..21” at top of the figure are provided to aid referencing figure from text. The “a...g” designate positions on a helical wheel for an idealized coiled-coil with 3.5 residues per helical turn. “H.1 .. H.4” Blue curves and blocks denote loops and aqueous loop regions.

(A) Bold residues, including hemegating histidines, selected from *cyt b* transmembrane consensus shown in Figure 4.18. Note that because of the pseudo-structural representation shown here, the helix 2 and helix 4 residues are in “reverse order” when compared to the sequence logo in Figure 4.18.

(B) Additional residues, shown in underlined blue, selected for specific design goals as described in text. These residues are not informed by the *cyt b* consensus.

- **Histidine at P4 / P18 of Helices 2, 4.** These residues are required for heme ligation.
- **Glycines at P4 / P18 of Helices 1, 3.** These strongly-conserved, inward-facing glycines (also ubiquitous in *cyt b6* of the photosynthetic *b6f* complex) minimize steric clash with the heme. The MHZ3 heme site includes a similar pair of glycines. Likewise, glycines

are used in the non-ligating helices of the porphyrin sites of soluble [37],[38] and lipophilic[14] 4-helix bundles from the DeGrado group.

- **Arginines at P1 and P21 of Helix 2.** The basic sidechains of these residues form salt bridges with the heme propionates in *cyt b* [2] as well as in *cyt b6* [39]. Similarly, an arginine stabilizes a heme propionate in the MZH3 maquette.
- **Phenylalanine at P11, Helix 2.** This Phe is highly conserved in *cyt b*. The inward-facing location of this residue is consistent with the principle, used successfully in other Dutton lab designs, to employ bulky aromatic residues to “pack” the maquette core between heme sites [40].
- **Proline at P14, Helix 4.** It is surprising to see a potentially helix-breaking residue at such a central location in a transmembrane helix. Yet this proline is strongly conserved in Helix D of *cyt b* (and is present in AP6). A similar conserved proline is also present in the fourth transmembrane helix of *cyt b6*. A specific proline has been shown necessary for heme binding in a *cyt P450* enzyme[41]. Interestingly, however, changing this residue to leucine in *R. Sphaeroides* produced only subtle turnover rate changes and did not impact heme binding [42]. I kept this residue in AM2 based on its strong conservation.
- **Phenylalanine at P21, Helix 4.** This amino acid was incorporated, as it is a conserved, inward-facing aromatic residue likely to add stability in the interfacial region of the membrane.

Next, a few specific amino acids were assigned based on specific observations from the literature or maquette design experience, but they do not follow directly from the sequence alignment. These are illustrated in **Figure 5.13-B** and explained below:

- **Leucine at P14, Helix 1.** Most *cyt b* sequences have a glutamine at this position, as shown in **Figure 5.12-B**. Mutating the residue to a leucine has been shown to reduce the E_m of heme b_L from -90 to -120 mV [42]. Reducing the potential of b_L will, all else being equal, improve the driving force for ET from b_L to b_H and should result in better yield for transmembrane ET.
- **Tryptophan at P2, Helices 1 and 3.** Adding tryptophan residues aids in the spectroscopic quantitation of the apo-protein. The membrane interfacial region is an energetically favorable location for aromatics [43]. *Cyt b* exhibits a moderately

conserved tryptophan at P1 on these helices. Removing this tryptophan reduces the potential of the heme b_H by 40 mV to about 0 mV [44]. For the AM2 design this is a desirable change, as it reduces the magnitude of the uphill ET step from B_H to the -150 mV heme in the aqueous region; thus I moved the tryptophan from P1 (cyt *b*) to P2 (AM2).

- **Glycines at P1, Helices 1 and 3.** Glycines were added at the points where the cyt *b*-derived sequence is merged with aqueous MHZ3 region. These potentially helix-breaking residues are included to allow some rotational flexibility to compensate for possible mismatch in register in this “merger.” A similar scheme was employed by Discher in the design of earlier amphiphilic maquette AP1 [8].
- **Tyrosines at P21, Helix 1 and P3, Helices 2 and 4.** Aromatic tyrosines were added in these positions to improve the energetics of membrane insertion [43].
- **Threonine at P3, Helix 3.** This residue was added as a potential hydrogen-binding partner for heme-ligating histidine. The consensus shows a moderate propensity for a serine or histidine at this position. A similarly positioned serine or threonine has been incorporated in 4-helix bundle designs from the DeGrado lab and has been shown to improve porphyrin binding [37], [38], [14].

Finally the remaining positions were then filled with leucine and alanine residues in a proportion similar to that employed in AM1, as shown in **5.13-C**.

5.5.2 Design of AM2 Aqueous Region and Loops

The sequence of the aqueous portion of AM2 is quite similar to that of MHZ3. However, one important change was introduced due to a topological difference between MZH3 and cyt *b*. **Figure 5.14** illustrates this distinction. Viewed from the N-terminal end of the first helix, the sequence order the helices of MZH3 proceed anti-clockwise (**Figure 5.14-A** and **Figure 5.14-B**). However, the bundle is arranged in clockwise order in cyt *b* (**Figure 5.14-C**). This mismatch suggests that either the aqueous domain or the cyt *b*-derived lipophilic region of AM2 would be forced into an unfavorable topology if the heme-binding portion of MHZ3 were simply “grafted” onto the AM2 membrane region.

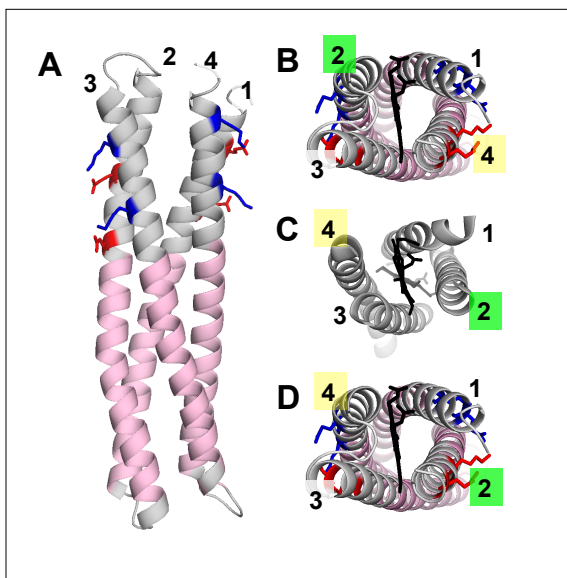
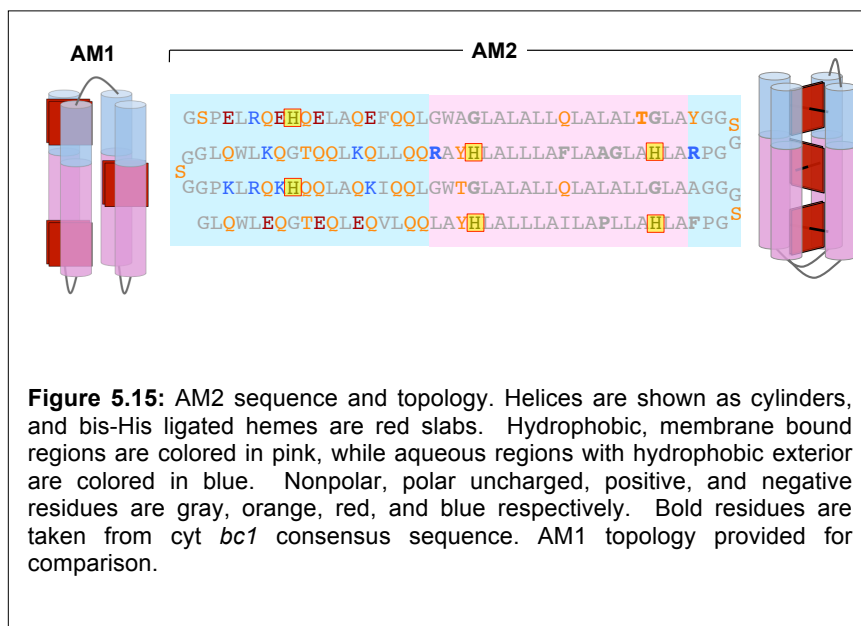


Figure 5.14. AM2 hydrophilic design and “salt-swap” concept. **(A)** X-ray crystal structure of maquette MZH3, used as a structural guide for design of AM2. The pink residues will correspond to the transmembrane domain in AM2. Numbers denote sequence order of the helices. Blue and red residues are Glu and Lys designed to promote interhelical salt bridges in MZH3. **(B)** Same structure in **A**, viewed from “top” of the bundle. **(C)** Cyt *b* transmembrane helices of bovine *bc1* complex, viewed from equivalent position. Note that the positions of helices 2 and 4 are opposite those in **B**, despite the similar coiled-coil structure. **(D)** Intended structure for AM2, with helix topology matching that of the cyt *b* TM helices. The external Glu and Lys of MZH3 are “swapped” between helices 2 and 4 to rearrange the interhelical salt bridges, promoting the desired topology.

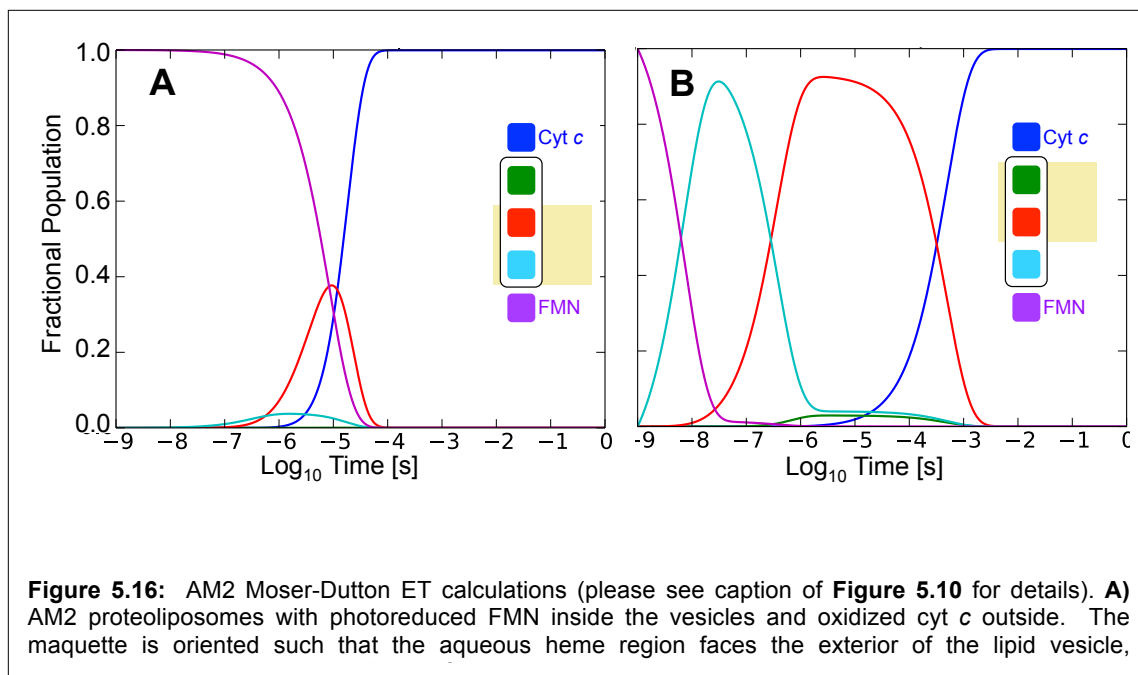
However, MZH3 possesses an explicit design feature that could allow for an easy change in the helix order. Nate Ennist designed MZH3 to include several lysines and glutamates to form interhelical salt bridges that specifically favor the anti-clockwise topology. Helices 1 and 2 contain lysines, while 3 and 4 have glutamates. Assuming no other structural changes, swapping the charges on helices 2 and 4 should destabilize the anti-clockwise orientation of MZH3 and instead favor a clockwise arrangement. This “salt swap” can be visualized by comparing the helical order in Figures 5.14-B (MZH3 crystal structure) and 5.14-D (swapped). The salt swap aims to promote a topological consistency between the two domains of AM2 and stabilize the overall structure.

Figure 5.15 shows the final sequence and intended topology for AM2, and compares this with the topology of AM1. Note that the hemes in AM2 are bound diagonally across the bundle between non-adjacent helices, while AM1 binds hemes between adjacent helices.



5.5.3 Moser-Dutton Simulation for Transmembrane ET in AM2

Figure 5.16 shows the results of a Moser-Dutton Ruler computation for AM2 transmembrane ET, assuming the same FMN / cyt *c* system employed with AM1. The predicted half-times for terminal reduction of cyt *c* for the aqueous-out and aqueous-in orientations are 1.6×10^{-5} s and 3.4×10^{-4} s; the aqueous-out rate is more than an order of magnitude faster than the predictions for AM1 and AP6. The faster rate results largely from closer cofactor spacing; the 11.5 Å spacing between the aqueous and “middle” hemes were taken from MHZ3 crystal structure. This is several Å closer than the predicted heme separation of BT6-style maquettes, helping to overcome the bottleneck in this endergonic ET step.



5.6 Conclusion

Transmembrane electron transfer is a fundamental feature of energetic metabolism, as exemplified by bacterial and mitochondrial *cyt b* in *bcl* complex as well as the other respiratory and photosynthetic complexes. Recapitulating this function has been a major goal in adapting soluble *de novo* designs to the membrane environment. The design and characterization of two heme-binding amphiphilic maquettes are described here. Each of these proteins represents a step forward in the relatively young field of manmade membrane protein design. The first, AP6, combines lipophilic sequence from *cyt b* with the completely *de novo* sequence of a previously designed soluble maquette. The second, AM1, is the first published monomeric membrane-bound *de novo* helical protein. AM1 contains no reference to natural sequence, and the highly “generic” sequence of its membrane portion offers a blank slate for potential mutations to improve function. The successful inclusion body expression and purification of the KSI-AM1

fusion (largely the work of Geetha Goparaju) is a major practical advance in amphiphilic maquette development. Both AP6 and AM1 bind heme with moderate affinity in membranes, but to date have failed to conclusively show ET between soluble redox species separated by a lipid bilayer. Moser-Dutton simulations (albeit with the important simplification of neglecting intermolecular collisions) suggest that transmembrane ET should occur on a ~ 1 ms timescale. The absence of visible bound heme reduction in AM1 proteoliposomes encapsulating photo-reducing FMN suggests that the bottleneck may be in the initial electron transfer from the soluble donor to the first heme in the chain.

In the ongoing effort to produce maquette-mediated transmembrane ET, I have designed AM2, a new amphiphilic maquette. By ligating hemes diagonally across the helices rather than between adjacent helices as in AP6 and AM1, AM2 aims to more closely adhere to the structure and topology of cyt *b*. Moreover, AM2 selects specific conserved residues from cyt *b* while maintaining a generic Leu- and Ala- rich sequence in other positions. AM2 draws its aqueous sequence from a MZH3, a new well-structured and highly adaptable water-soluble maquette. One additional design change that could offer improvement in future designs (not incorporated in AM2) would be to move the first and third hemes closer to the end of the helical bundle, particularly on the lipophilic end. Such a change might alleviate any bottleneck in the initial donor-to-heme ET step, as suggested in the results of the FMN / AM1 transmembrane ET experiments. Finally, crystallization of current or future AM designs would prove extremely valuable in assessing cofactor positioning. MZH3 offers the first crystal structure of a porphyrin-bound *de novo* protein, and perhaps this advancement could be carried on to amphiphilic maquettes.

5.6 References

- [1] G. Goparaju, B.A. Fry, S.E. Chobot, G. Wiedman, C.C. Moser, P.L. Dutton, B.M. Discher, First principles design of a core bioenergetic transmembrane electron-transfer protein, *Biochimica Et Biophysica Acta-Bioenergetics*, 1857 (2016) 503-512.
- [2] S. Iwata, J.W. Lee, K. Okada, J.K. Lee, M. Iwata, B. Rasmussen, T.A. Link, S. Ramaswamy, B.K. Jap, Complete structure of the 11-subunit bovine mitochondrial cytochrome bc(1) complex, *Science*, 281 (1998) 64-71.
- [3] J.D. Lear, Z.R. Wasserman, W.F. DeGrado, Synthetic amphiphilic peptide models for protein ion channels, *Science*, 240 (1988) 1177-1181.
- [4] T.A. Farid, G. Kodali, L.A. Solomon, B.R. Lichtenstein, M.M. Sheehan, B.A. Fry, C. Bialas, N.M. Ennist, J.A. Siedlecki, Z. Zhao, M.A. Stetz, K.G. Valentine, J.L.R. Anderson, A.J. Wand,

- B.M. Discher, C.C. Moser, P.L. Dutton, Elementary tetrahelical protein design for diverse oxidoreductase functions, *Nature Chemical Biology*, 9 (2013) 826-+.
- [5] S.S. Huang, R.L. Koder, M. Lewis, A.J. Wand, P.L. Dutton, The HP-1 maquette: From an apoprotein structure to a structured hemoprotein designed to promote redox-coupled proton exchange, *Proceedings of the National Academy of Sciences of the United States of America*, 101 (2004) 5536-5541.
- [6] P. Mitchell, The protonmotive Q cycle: a general formulation, *FEBS Letters*, 59 (1975) 137-139.
- [7] M. Shin, D.I. Arnon, Enzymic Mechanisms Of Pyridine Nucleotide Reduction In Chloroplasts, *Journal of Biological Chemistry*, 240 (1965) 1405-&.
- [8] Hultquis.De, R.T. Dean, R.H. Douglas, Homogeneous Cytochrome-B5 From Human Erythrocytes, *Biochem. Biophys. Res. Commun.*, 60 (1974) 28-34.
- [9] B.M. Discher, D. Noy, J. Strzalka, S. Ye, C.C. Moser, J.D. Lear, J.K. Blasie, P.L. Dutton, Design of amphiphilic protein maquettes: controlling assembly, membrane insertion, and cofactor interactions, *Biochemistry*, 44 (2005) 12329-12343.
- [10] A. Fago, A.J. Mathews, L. Moens, S. Dewilde, T. Brittain, The reaction of neuroglobin with potential redox protein partners cytochrome b(5) and cytochrome c, *Febs Letters*, 580 (2006) 4884-4888.
- [11] C.C. Page, C.C. Moser, P.L. Dutton, Mechanism for electron transfer within and between proteins, *Curr. Opin. Chem. Biol.*, 7 (2003) 551-556.
- [12] J.M. Tomich, A. Grove, T. Iwamoto, S. Marrer, M.S. Montal, M. Montal, Design Principles And Chemical Synthesis Of Oligomeric Channel Proteins, in: M. Blank, I. Vodyanoy (Eds.) *Biomembrane Electrochemistry*, Place Published, 1994, pp. 329-354.
- [13] J.M. Cordova, P.L. Noack, S.A. Hilcove, J.D. Lear, G. Ghirlanda, Design of a Functional Membrane Protein by Engineering a Heme-Binding Site in Glycophorin A, *Journal of the American Chemical Society*, 129 (2006) 512-518.
- [14] S. Shinde, J.M. Cordova, B.W. Woodrum, G. Ghirlanda, Modulation of function in a minimalist heme-binding membrane protein, *Journal of Biological Inorganic Chemistry*, 17 (2012) 557-564.
- [15] I.V. Korendovych, A. Senes, Y.H. Kim, J.D. Lear, H.C. Fry, M.J. Therien, J.K. Blasie, F.A. Walker, W.F. DeGrado, De Novo Design and Molecular Assembly of a Transmembrane Diporphyrin-Binding Protein Complex, *Journal of the American Chemical Society*, 132 (2010) 15516-15518.
- [16] R.L. Koder, J.L. Anderson, L.A. Solomon, K.S. Reddy, C.C. Moser, P.L. Dutton, Design and engineering of an O(2) transport protein, *Nature*, 458 (2009) 305-309.
- [17] C.C. Moser, J.M. Keske, K. Warncke, R.S. Farid, P.L. Dutton, Nature Of Biological Electron-Transfer, *Nature*, 355 (1992) 796-802.
- [18] S.E. Chobot, Deconvoluting the engineering and assembly instructions for Complex III activity, Publicly accessible Penn Dissertations, (2010).
- [19] P.L. Dutton, Redox potentiometry: determination of midpoint potentials of oxidation-reduction components of biological electron-transfer systems, *Methods in enzymology*, 54 (1978) 411-435.
- [20] S.C. Hokanson, Deconvoluting the engineering and assembly instructions for complex III activity (PhD Thesis Univ. of Pennsylvania), 2010.
- [21] J.A. Runquist, P.A. Loach, Catalysis Of Electron-Transfer Across Phospholipid-Bilayers By Iron-Porphyrin Complexes, *Biochimica et biophysica acta*, 637 (1981) 231-244.

- [22] T. Spratt, B. Bondurant, D.F. O'Brien, Rapid release of liposomal contents upon photoinitiated destabilization with UV exposure, *Biochimica Et Biophysica Acta-Biomembranes*, 1611 (2003) 35-43.
- [23] J. Henriksen, A.C. Rowat, E. Brief, Y.W. Hsueh, J.L. Thewalt, M.J. Zuckermann, J.H. Ipsen, Universal behavior of membranes with sterols, *Biophysical Journal*, 90 (2006) 1639-1649.
- [24] D.A. Kendall, R.C. Macdonald, A Fluorescence Assay To Monitor Vesicle Fusion And Lysis, *Journal of Biological Chemistry*, 257 (1982) 3892-3895.
- [25] B.L. Welch, On The Comparison Of Several Mean Values - An Alternative Approach, *Biometrika*, 38 (1951) 330-336.
- [26] T.A. Farid, G. Kodali, L.A. Solomon, B.R. Lichtenstein, M.M. Sheehan, B.A. Fry, C. Bialas, N.M. Ennist, J.A. Siedlecki, Z. Zhao, M.A. Stetz, K.G. Valentine, J.L.R. Anderson, A.J. Wand, B.M. Discher, C.C. Moser, P.L. Dutton, Elementary tetrahelical protein design for diverse oxidoreductase functions, *Nature Chemical Biology*, 9 (2013) 826-833.
- [27] W.C. Wimley, T.P. Creamer, S.H. White, Solvation energies of amino acid side chains and backbone in a family of host-guest pentapeptides, *Biochemistry*, 35 (1996) 5109-5124.
- [28] E. Rodríguez-Carmona, O. Cano-Garrido, J. Seras-Franzoso, A. Villaverde, E. García-Fruitós, Isolation of cell-free bacterial inclusion bodies, *Microbial Cell Factories*, 9 (2010) 1-9.
- [29] H. Polet, J. Steinhardt, Binding-induced alterations in ultraviolet absorption of native serum albumin, *Biochemistry*, 7 (1968) 1348-1356.
- [30] B.R. Gibney, S.S. Huang, J.J. Skalicky, E.J. Fuentes, A.J. Wand, P.L. Dutton, Hydrophobic modulation of heme properties in heme protein maquettes, *Biochemistry*, 40 (2001) 10550-10561.
- [31] H. Zhang, S.E. Chobot, A. Osyczka, C.A. Wraight, P.L. Dutton, C.C. Moser, Quinone and non-quinone redox couples in Complex III, *Journal of bioenergetics and biomembranes*, 40 (2008) 493-499.
- [32] T.A. Farid, Engineering an artificial, multifunctional oxidoreductase protein maquette [Thesis, University of Pennsylvania], (2012).
- [33] R.E. Sharp, C.C. Moser, F. Rabanal, P.L. Dutton, Design, synthesis, and characterization of a photoactivatable flavocytochrome molecular maquette, *Proceedings of the National Academy of Sciences*, 95 (1998) 10465-10470.
- [34] S.G. Mayhew, The effects of pH and semiquinone formation on the oxidation-reduction potentials of flavin mononucleotide - A reappraisal, *European Journal of Biochemistry*, 265 (1999) 698-702.
- [35] R. Tunuguntla, M. Bangar, K. Kim, P. Stroeve, C.M. Ajo-Franklin, A. Noy, Lipid Bilayer Composition Can Influence the Orientation of Proteorhodopsin in Artificial Membranes, *Biophysical Journal*, 105 (2013) 1388-1396.
- [36] P.J.A. Cock, T. Antao, J.T. Chang, B.A. Chapman, C.J. Cox, A. Dalke, I. Friedberg, T. Hamelryck, F. Kauff, B. Wilczynski, M.J.L. de Hoon, Biopython: freely available Python tools for computational molecular biology and bioinformatics, *Bioinformatics*, 25 (2009) 1422-1423.
- [37] G.E. Crooks, G. Hon, J.M. Chandonia, S.E. Brenner, WebLogo: A sequence logo generator, *Genome Research*, 14 (2004) 1188-1190.
- [38] H.C. Fry, A. Lehmann, J.G. Saven, W.F. DeGrado, M.J. Therien, Computational Design and Elaboration of a de Novo Heterotetrameric alpha-Helical Protein That Selectively Binds an Emissive Abiological (Porphinato)zinc Chromophore, *Journal of the American Chemical Society*, 132 (2010) 3997-4005.
- [39] G.M. Bender, A. Lehmann, H. Zou, H. Cheng, H.C. Fry, D. Engel, M.J. Therien, J.K. Blasie, H. Roder, J.G. Saven, W.F. DeGrado, De novo design of a single-chain diphenylporphyrin metalloprotein, *Journal of the American Chemical Society*, 129 (2007) 10732-10740.

- [40] D. Stroebel, Y. Choquet, J.L. Popot, D. Picot, An atypical haem in the cytochrome b(6)f complex, *Nature*, 426 (2003) 413-418.
- [41] S.S. Huang, B.R. Gibney, S.E. Stayrook, P.L. Dutton, M. Lewis, X-ray structure of a Maquette scaffold, *Journal of Molecular Biology*, 326 (2003) 1219-1225.
- [42] Y.M. Zheng, M.B. Fisher, N. Yokotani, Y. Fujii-Kuriyama, A.E. Rettie, Identification of a meander region proline residue critical for heme binding to cytochrome P450: Implications for the catalytic function of human CYP4B1, *Biochemistry*, 37 (1998) 12847-12851.
- [43] C.H. Yun, Z.G. Wang, A.R. Crofts, R.B. Gennis, Examination Of The Functional Roles Of 5 Highly Conserved Residues In The Cytochrome-B Subunit Of The Bc1 Complex Of *Rhodobacter-Sphaeroides*, *Journal of Biological Chemistry*, 267 (1992) 5901-5909.
- [44] W.C. Wimley, S.H. White, Experimentally determined hydrophobicity scale for proteins at membrane interfaces, *Nature Structural Biology*, 3 (1996) 842-848.
- [45] F.A.J. Rotsaert, R. Covian, B.L. Trumpower, Mutations in cytochrome b that affect kinetics of the electron transfer reactions at center N in the yeast cytochrome bc(1) complex, *Biochimica Et Biophysica Acta-Bioenergetics*, 1777 (2008) 239-249.
- [46] R. Aurora, G.D. Rose, Helix capping, *Protein Science*, 7 (1998) 21-38.

Chapter 6 Conclusions

Protein-mediated electron transfer (ET) is fundamental in biology, and all organisms require the function of a wide range of oxidoreductases. The maquette design approach has offered an insightful, effective, and often surprisingly simple approach to study ET processes. To date, maquette ET work has focused primarily on electron transfers between cofactors residing in a single water-soluble protein. Such ET functions are biologically necessary but not sufficient; all organisms also require ET in membrane-bound proteins as well as interprotein ET between diffusing redox partners. The ultimate goal of the maquette project is to engineer artificial oxidoreductases for high-value applications such as solar-driven fuel production or nitrogen fixation. Just as biology requires more from its oxidoreductases than the transit of electrons within one protein, these technologies are quite likely to involve multi-protein electron transport chains, whether they are ultimately implemented *in vivo* or *in vitro*. The work in this dissertation represents substantial progress in maquette development for interprotein and membrane-bound electron transfer.

Chapter 2 shows that BT6, a negatively charged B-heme binding maquette [1], reduces bovine cyt *c* at 1.9 to $3.4 \times 10^7 \text{ M}^{-1}\text{-s}^{-1}$ at a 250 mM ionic strength. The ionic strength dependence of this interaction agrees fairly well with a Debye-Huckel description of monopole-driven interactions. However, the Debye-Huckel treatment is derived from a charge of radius significantly smaller than the Debye length. This assumption is not valid for the upper range of ionic strengths employed in here, where a Debye length of $\sim 6 \text{ \AA}$ is less than the dimensions of the proteins. This chapter also introduces a photolysis-induced ET method (detailed in **Chapter 3**) that provides improved temporal resolution for viewing the interprotein maquette ET process. The rates of this ET process compare favorably with second-order rate constants in natural redox proteins. These results demonstrate that a completely artificial protein can interact strongly with a natural redox partner, and that this interaction can be rationally modulated through protein electrostatic changes. Finally, varying the concentration of the cyt *c* electron acceptor at low ionic strength shows biphasic ET behavior, with the amplitude of the fast phase increasing with the molar ratio of cyt *c*. This result suggests that ET is proceeding from a combination of bound

and diffusing partners, with a K_d in the low μM range. Hoffman et. al. observed similar biphasic behavior in ET from Zn-myoglobin to cyt *b5* at low ionic strength. [2].

Chapter 4 introduces photoactivatable maquettes binding a synthetic zinc porphyrin (ZnP) cofactor. With the likely exception of one design incorporating a strongly unfavorable dipole moment, these maquettes reduce cyt *c* upon photoactivation. (In the unfavorable DPM maquette, the presence of cyt *c* still quenches the ZnP triplet, but without spectroscopic evidence of cyt *c* reduction). All of the maquettes were designed with some dipole character, and the results suggest that intentionally dipolar designs should orient this dipole moment parallel to the maquette axis for best effect. GL-H96, the fastest of these proteins, reduces cyt *c* with second order behavior even at 4 mM ionic strength, implying a rough second order rate constant of $3.4 \times 10^8 \text{ M}^{-1}\text{s}^{-1}$ from the reaction half-time measurements. It is not obvious that the proteins would maintain diffusional kinetics at this very low salt concentration. The quenching half-time for this protein increases by about a factor 10 upon transition to physiologically reasonable 110 mM ionic strength, implying a still quite fast ET rate on the order of $3 \times 10^7 \text{ M}^{-1}\text{s}^{-1}$. GL-H96 has a modestly unfavorably dipole and a net negative charge of -6. This is much smaller than the -19 charge of BT6, which also exhibits similar rates of cyt *c* reduction. The greater exergonicity on the ZnP photoreduction ($\sim 1 \text{ eV}$) may compensate for H96's weaker monopole interaction with cyt *c*; future experiments using a range of driving forces would serve to decouple these effects. Finally, the mutation of the GL-H66 protein to accommodate a heme cofactor in addition to ZnP yields a maquette capable of cyt *c* photo-oxidation (in lieu of photoreduction).

Chapter 5 discusses the Discher group's progress in amphiphilic maquette development. We introduce AM1, the first report of a completely artificial cofactor-binding monomeric membrane protein [3]. Largely due to Geetha Goparaju's patient efforts, the lab has developed a unique protocol to express AM1 in high-yielding inclusion bodies. The protein binds heme and ZnPPiX cofactors in detergent and proteoliposomes. A major goal in the design of AM1 and its tetrameric predecessor AP6 was to develop maquette-mediated electron transfer across a bilayer, and the chapter discusses my efforts to this end. To date we have not conclusively shown transmembrane ET. However, several results discussed here should prove helpful in this continuing effort, including the development of a multi-lipid mixture that minimizes the leakage from maquette proteoliposomes. I also present a new maquette design, AM2, combining features from an existing soluble maquette design with specific residues informed by natural cyt *b* of the *bcl* complex.

The results in the first three chapters clearly show that several maquettes engage in productive ET with natural cyt *c*, and that these reactions often proceed at physiological useful rates. All of the cyt *c* reductions are quite exergonic, and cyt *c* is known to exhibit promiscuity in its redox interactions [4]. Still, it is not a trivial conclusion that the ET reactions should occur at physiological rates given that no effort was made to design a specific redox partner beyond incorporating intuitive surface charge distributions. This is a testament to the generous tolerances governing interprotein ET, in contrast to more specific protein-protein interactions.

The triplet state of each photoactivatable maquette design presented in **Chapter 4** is quenched in the presence of oxidized cyt *c*, although the quenching mechanisms have not been fully described. Three of the four ZnP maquettes clearly demonstrate ET to cyt *c*, as shown by the development of the 550 nm feature of reduced C-heme. Despite robust ZnP quenching, however, the strongly dipolar DPM maquette does not produce the 550 nm feature. This suggests that an energy transfer mechanism may instead be responsible. Furthermore, the experiments performed here do not rule out the possibility that energy transfer may play some role even in quenching those maquettes that are shown spectroscopically to reduce cyt *c*. Indeed, ET-incompetent pre-reduced cyt *c* also shows modest quenching of the ^3Zn state. Interestingly, these observations contrast with experiments of Vanderkooi and coworkers showing that the triplet state of Zn-substituted cyt *c* is not quenched, either through electron or energy transfer, by an excess of oxidized Fe-cyt *c* [5]. **Figure 4.16** shows the observed quenching ionic strength dependence with that predicted by the theory of van Leeuwen[6]. All of the observations show a weaker ionic strength than predicted by the model, and interestingly the DPM maquette shows negligible dependence on ionic strength. This suggests a long-range quenching mechanism on length scales exceeding the Debye distance, supporting a Forster mechanism rather than a shorter-range Dexter quenching. Measuring the maquette ZnP emission spectra would allow calculation of the Forster length to address this hypothesis.

Additionally, there exists a possibility that a fraction of the excited ZnP maquettes may actually *photooxidize* already-reduced cyt *c* rather than photoreduce cyt *c* as intended. Zinc porphyrin triplets, both ligated to protein and diffusing freely in solution, have been shown to exhibit ET quenching through an oxidative mechanism to yield a Zn anion radical [7]. Typically the formation of the cation is more energetically favorable than the anion by several hundred mV, although my results do not preclude some anion population. The Zn porphyrin anion exhibits a modest absorbance peak around 700 nm [7], a region excluded from my transient absorption

measurements. Future experiments should probe this spectral range to rule out the presence of an anion population. Most publications examining the photo-induced ET of Zn-substituted proteins, including those of Hoffman and coworkers, do not address the possibility of anion production. However, Chang et. al. have shown that excited Zn-Mb forms an anion in the presence of a large excess of a sacrificial electron donor [8].

The camera-based transient absorption apparatus employed for the experiments in **Chapter 4** provides excellent spectral resolution at discrete timepoints. The results unambiguously show the presence of the ^3ZnP , ZnP^+ , and $\text{cyt } c_{\text{red}}$ spectral features. However, the temporal resolution is, at best, limited to ~ 20 logarithmically spaced timepoints. Instead, published experiments examining fast ET multi-phasic kinetics typically acquire many closely-spaced timepoints ($\leq 1 \mu\text{S}$) at a limited number of wavelengths. Given that the camera-based experiments presented here have shown which wavelengths best describe specific reacting species, future maquette interprotein ET studies should perhaps focus on acquiring more complete trajectories at a few selected wavelengths. This would provide a more complete description of the reaction kinetics, particularly in terms of varying ionic strength.

Maquette development is moving toward increasingly complex function, including the interprotein and transmembrane ET progress discussed here. As these new functions stipulate increasing precise structures, the first-principles scheme may benefit from combination with other approaches to protein design. For instance, Dutton lab member Josh Mancini has improved bilin binding in maquettes through the use of error-prone PCR on specific designs, guided by fluorescence binding assays. The AM2 design discussed in **Chapter 5** essentially takes a “watered-down” maquette approach, using a maquette-designed “background” sequence while importing specific natural sequence elements from a cytochrome *b* consensus. It is notable that a purely computational design for a porphyrin-binding amphiphilic bundle also failed to show transmembrane ET despite good cofactor binding [9]; this supports the hypothesis that there are indeed necessary sequence features in cytochrome *b* that extend beyond a straightforward structural role. There is increasing interest in the maquette community to incorporate computational tools for structural prediction and design. As maquettes move toward *in vivo* function and other applications where more interaction specificity is needed, it seems increasingly likely that the fruitful first-principles approach may act as a starting point for a wider palette of protein engineering techniques.

6.1 References

- [1] T.A. Farid, G. Kodali, L.A. Solomon, B.R. Lichtenstein, M.M. Sheehan, B.A. Fry, C. Bialas, N.M. Ennist, J.A. Siedlecki, Z. Zhao, M.A. Stetz, K.G. Valentine, J.L.R. Anderson, A.J. Wand, B.M. Discher, C.C. Moser, P.L. Dutton, Elementary tetrahelical protein design for diverse oxidoreductase functions, *Nature Chemical Biology*, 9 (2013) 826-+.
- [2] P. Xiong, J.M. Nocek, A.K.K. Griffin, J. Wang, B.M. Hoffman, Electrostatic Redesign of the Myoglobin, Cytochrome b(5) Interface To Create a Well-Defined Docked Complex with Rapid Interprotein Electron Transfer, *Journal of the American Chemical Society*, 131 (2009) 6938-+.
- [3] G. Goparaju, B.A. Fry, S.E. Chobot, G. Wiedman, C.C. Moser, P.L. Dutton, B.M. Discher, First principles design of a core bioenergetic transmembrane electron-transfer protein, *Biochimica Et Biophysica Acta-Bioenergetics*, 1857 (2016) 503-512.
- [4] A.N. Volkov, N.A.J. van Nuland, Electron Transfer Interactome of Cytochrome c, *Plos Computational Biology*, 8 (2012).
- [5] S.N. Dixit, A.J. Waring, J.M. Vanderkooi, Triplet Absorption And Phosphorescence Emission In Zinc Cytochrome-C, *Febs Letters*, 125 (1981) 86-88.
- [6] J.W. van Leeuwen, The Ionic-Strength Dependence Of The Rate Of A Reaction Between 2 Large Proteins With A Dipole-Moment, *Biochimica et biophysica acta*, 743 (1983) 408-421.
- [7] C.Y. Shen, N.M. Kostic, Reductive quenching of the triplet state of zinc cytochrome c by the hexacyanoferrate(II) anion and by conjugate bases of ethylenediaminetetraacetic acid, *Inorganic Chemistry*, 35 (1996) 2780-2784.
- [8] C.H. Chang, Y.T. Hu, C.F. Lo, L. Luo, H.M. Lin, C.H. Chang, C.Y. Lin, E.W.G. Diau, T.K. Wu, Photoactivation Studies of Zinc Porphyrin-Myoglobin System and Its Application for Light-Chemical Energy Conversion, *International Journal of Biological Sciences*, 7 (2011) 1203-1213.
- [9] I.V. Korendovych, A. Senes, Y.H. Kim, J.D. Lear, H.C. Fry, M.J. Therien, J.K. Blasie, F.A. Walker, W.F. DeGrado, De Novo Design and Molecular Assembly of a Transmembrane Diporphyrin-Binding Protein Complex, *Journal of the American Chemical Society*, 132 (2010) 15516-15518.

Appendix A1 Supplementary Experimental Methods

A1.1 O₂ Removal in Stopped-Flow Apparatus

Chapters 2 and 5 report results from anaerobic stopped-flow ET experiments in the OLIS RSM-1000 stopped-flow spectrophotometer. Initial results indicated oxidation of reduced species even in the absence of an oxidant species, suggesting that atmospheric oxygen was penetrating the stopped flow. One potential complication is the PTFE (Teflon) seals on the stopped-flow syringes; PTFE is fairly permeable to O₂, and any atmospheric O₂ adsorbed into the syringe seals before loading the instrument would eventually diffuse into the sample [2]. I tested two approaches to reduce the oxygen levels in the system. The first was to purge the instrument by incubating the syringes with deoxygenated buffer for one hour prior to experiments. The second was to add the an enzymatic O₂ scrubbing system comprising 80 nM glucose oxidase, 12 nM catalase, and 1 mM glucose [4]. **Figure A1.1** shows how purging and scrubbing impact the oxidation rate of reduced indigotrisulfonate (ITS). Both pre-purging and scrubbing cumulatively reduce the background oxidation rate. Thus, I employed both techniques for all subsequent stopped-flow ET experiments.

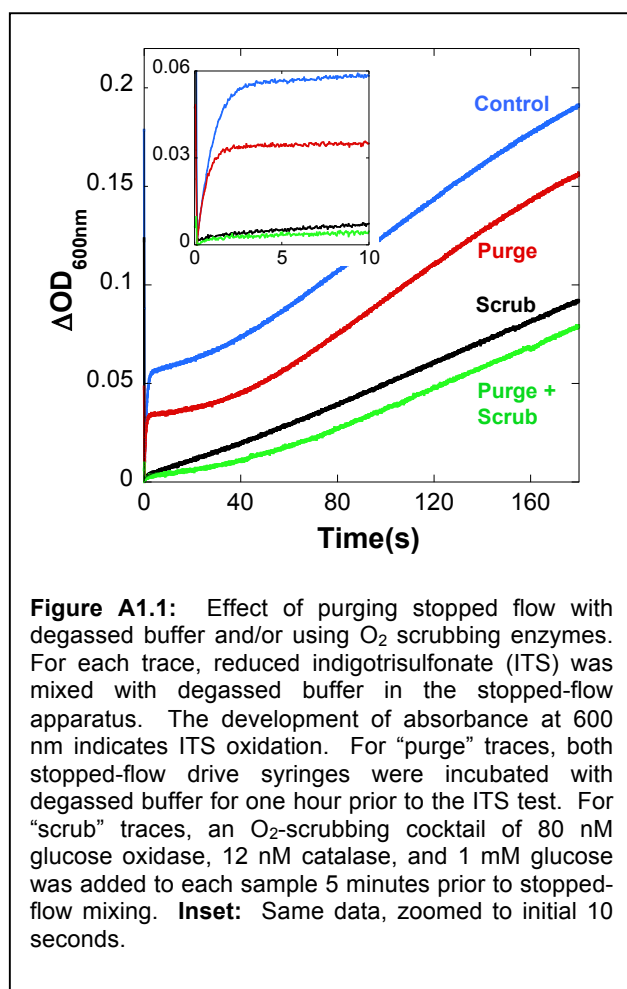


Figure A1.1: Effect of purging stopped flow with degassed buffer and/or using O₂ scrubbing enzymes. For each trace, reduced indigotrisulfonate (ITS) was mixed with degassed buffer in the stopped-flow apparatus. The development of absorbance at 600 nm indicates ITS oxidation. For “purge” traces, both stopped-flow drive syringes were incubated with degassed buffer for one hour prior to the ITS test. For “scrub” traces, an O₂-scrubbing cocktail of 80 nM glucose oxidase, 12 nM catalase, and 1 mM glucose was added to each sample 5 minutes prior to stopped-flow mixing. **Inset:** Same data, zoomed to initial 10 seconds.

A1.2 Circular Dichroism Spectroscopy

An AVIV-410 circular dichroism spectrometer measured CD spectra. All data were obtained at 20 °C. In each experiment three spectra averaged from 250 nm to 190 nm at 1 nm increments. Water-soluble maquettes from **Chapter 4** were measured at the low ionic strength condition employed for ET experiments: 3 mM NaCl, 2 mM Tris, pH 8.0. All “GL” maquettes were solubilized to 30 μM, while the DPM maquette was measured at 8 μM due to lower solubility in the low-salt buffer. The amphiphilic homotetramer AP6 was measured at 20 μM concentration in 2 mM DPC detergent with 100 mM NaCl, 50 mM, Na₂HPO₄, pH 7.9. The amphiphilic monomer AM1 was measured at 20 μM concentration in 2 mM DDM and 3 mM SDS detergents with 100 mM NaCl, 50 mM, Na₂HPO₄, pH 7.9. In each case the CDNN program [5] computed helical fraction from the measured CD spectra.

A1.3 Porphyrin Binding Titrations

A1.3.1 Binding titrations for soluble maquettes

Heme stock concentration was verified using the hemochrome assay[6]. The concentration of ZnP stocks was verified by titrating 1 μM aliquots into 20% pyridine and taking the best-fit for the absorbance at each point, given an extinction coefficient of the 417 nm Soret peak of 360000 M⁻¹cm⁻¹ [Zhenyu Zhao, personal communication]. Maquettes were dissolved in 3 mM Tris, 2 mM NaCl at pH 8.0. ZnP or heme was dissolved in DMSO to ~ 300 μM. A Varian Cary UV-Vis spectrophotometer measured all spectra. Titrations were performed by adding 1 μM aliquots of the porphyrin stock to a 1 mL sample containing a few μM of maquette (concentrations for each experiment given in **Table 4.1**). After each porphyrin stock addition, the sample was mixed and equilibrated for at least 5 minutes before saving the spectrum.

The data were analyzed by fitting the set of measured Soret absorbances to the absorbances predicted by a concentrations of total and unbound cofactor [C] and [C_{free}] as follows:

$$Abs = \epsilon_{bound} ([C] - [C_{free}]) + \epsilon_{free} [C_{free}] \quad \text{Eqn. A1.1}$$

where

$$[C_{free}] = \frac{[Maq] + [C] + K_d - \sqrt{([Maq] + [C] + K_d)^2 - (4 * [Maq] * [C])}}{2} \quad \text{Eqn. A1.2}$$

A Python script solved for best-fit values for K_d , ϵ_{bound} , and ϵ_{free} by minimizing the sum-squared errors between the observed Soret peaks and those predicted by **Eqn. A1.1**.

A1.3.2 Binding titrations for amphiphilic maquettes

Heme binding titrations were performed for AP6 solubilized 2 mM DPC and in phospholipid vesicles (80% POPC, 20% POPS). We employed fresh heme stock solutions in DMSO for DPC-solubilized AP6 and heme in 50 mM KOH for proteoliposomes titrations. Barry's hemochrome assay[6] verified heme stock concentrations. The binding titrations were performed in 50 NaH₂PO₄ and 100mM NaCl at pH 8.0. The data were fit to an analytical expression describing independent binding sites using a custom Mathematica program (Wolfram Research).

A1.4 Redox Potentiometry

Redox titrations were performed in a 1 mL cuvette equipped with stirrer and Ag/AgCl and platinum redox electrodes (MI-800/411, Microelectrodes Inc.). The electrodes were standardized with quinhydrone. All potentials reported are referenced to a standard hydrogen electrode (SHE). Solution redox potentials were adjusted by small aliquots (~ μ L) of freshly prepared solutions of sodium dithionite or potassium ferricyanide. Electrode-solution-heme redox mediation was facilitated by redox mediators as follows: 25 μ M 2,3,5,6-tetramethyl-p-phenylenediamine (DAD), 25 μ M 1,2-naphthaquinone (NQ), 25 μ M 2-hydroxy-1,4-naphthoquinone (HNQ), 20 μ M phenazine methosulfate (PMS), 20 μ M phenazine ethosulfate (PES), 20 μ M phenazine (PHE), 20 μ M anthraquinone-2-sulfonate (AQS), 20 μ M benzyl

viologen (BV), 20 μM methyl viologen (MV), 50 μM duroquinone (DQ); 6 μM indigotrisulfonate (ITS), and 10 μM pyocyanine (PC). Stock solutions of all the mediators except BV, MV and PC were made in DMSO. BV, MV and PC were prepared in water. After equilibration at each potential, the heme optical spectrum was recorded and the course of the reduction of heme was followed by the increase in the sharp α -band absorption at 559 nm relative to a 575 nm reference wavelength. The data were analyzed with the Nernst equation with n -values of 1.0 for both hemes:

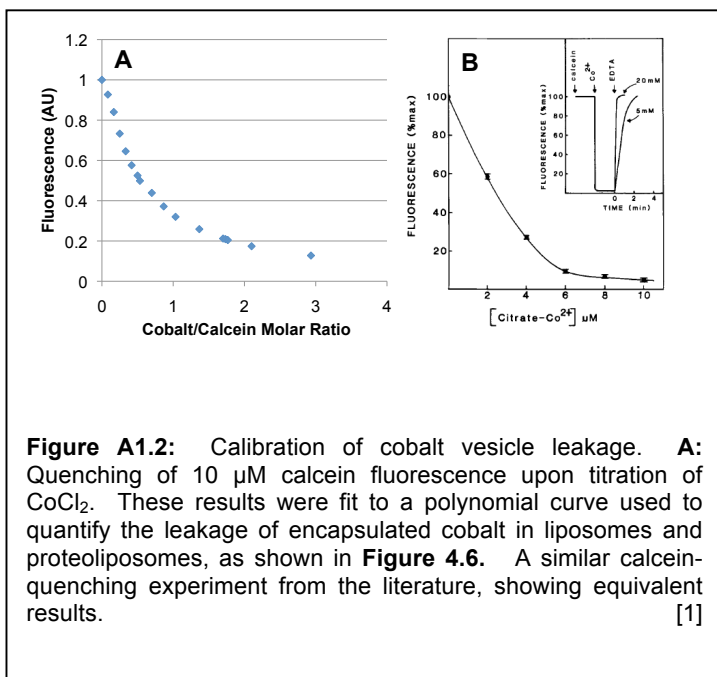
$$R = \frac{f}{10^{(E_h - E_{m1})/(RT/nF)}} + \frac{(1-f)}{10^{(E_h - E_{m2})/(RT/nF)}} \quad \text{Eqn. A1.3}$$

where R is the fraction of reduced heme, f is the fraction of heme in each site (when both hemes were fully bound, f was fixed at 0.5), E_h is the solution redox potential vs. SHE, $n=1$ is the number of electrons participating in the redox reaction, and E_{mi} is the redox midpoint potential.

A1.5 Preparing oxidized or reduced cyt *c*

Typically, dry bovine cyt *c* is mainly in the oxidized ferric redox state, but some fraction may be reduced. The procedure described here was employed to guarantee either complete oxidation or reduction of the cyt *c* stock prior to stopped-flow or transient absorption ET experiments. Bovine heart cyt *c* (97%+ purity, Sigma) was used in each case. 300 μM oxidized cyt *c* stocks were produced by dissolving dry cyt *c* in 2 mM Tris, 3 mM NaCl, pH 8.0. 3 stoichiometric equivalents of 200 mM K_3FeCN_6 were added and incubated for 10 min. PD-10 buffer exchange then removed K_3FeCN_6 . Reduced cyt *c* stocks were produced in the same manner, but the K_3FeCN_6 was replaced with sodium ascorbate. The reduced stocks were transferred to in septum-topped glass vials and degassed with argon. All cyt *c* stocks were flash frozen and stored at -20 C° until use.

A1.6 Calibrating Co^{2+} Quenching of Calcein Fluorescence



Section 4.2.2 describes an assay using calcein fluorescence quenching by vesicle-encapsulated Co^{2+} to compare the leakiness of several liposome formulations. This assay was calibrated by titrating known concentrations of CoCl_2 against calcein, recording the resulting decrease in fluorescence.

Figure A1.2 shows that this calibration agrees well with a similar experiment from the literature.

A1.7 Transmembrane ET Experiments with AP6 Proteoliposomes

POPC (Avanti Polar Lipids) in chloroform was placed in small glass vials. For samples incorporating protein, 60 μM AP6 in methanol was added. Quantities were selected to yield 2.5 mM lipid and 2.5 μM protein in a final sample volume of 2 mL. The solvent was gently evaporated under a stream of argon, leaving a visible lipid film on the glass. Residual solvent was removed under vacuum for 4 hours or overnight. 1 mL 30 mM $\text{K}_3\text{Fe}(\text{CN})_6$ in 150 mM KCl, 20 mM Tris, pH 8.0 was added to the sample, followed by 1 min vortex mixing. The sample was then subjected to 10 min microtip sonication on ice (QSonica Q700) at 30% power with a 50% duty cycle. The liposome mixture was passed through a 100 nm track-etch membrane (Whatman) 11 times using a hand-held vesicle extruder press (Avanti Polar Lipids). This process aims to yield uniform and monolamellar vesicles. $\text{K}_3\text{Fe}(\text{CN})_6$ is present inside the vesicles as well as in the surrounding buffer. The sample was then passed through a PD-10 size exchange / desalting gravity column (GE Life Sciences) equilibrated to an isotonic Tris / KCl buffer lacking

$\text{K}_3\text{Fe}(\text{CN})_6$. The For samples requiring heme, ~ 5 mM freshly prepared heme in 50 mM KOH was added to yield 5 molar equivalents of heme (heme stock concentration verified via hemochrome assay[6]). Additional buffer was added to the sample to bring the total volume to 2 mL.

40 μM ITS in the same buffer conditions was prepared separately. Both the liposome and ITS solutions were degassed under scrubbed argon with stirring for 1 hour. Meanwhile, a fresh solution of 5 mM sodium dithionite was prepared using deoxygenated 50 KOH. The samples were loaded onto the stopped flow via anaerobic canula transfer and held under degassed argon for the duration of experiment. The dithionite was carefully titrated in the ITS solution until it was ~ 90% reduced; the dramatic blue-to-yellow color change of ITS upon reduction makes this procedure reasonably repeatable. The reduced ITS was then mixed with the $\text{K}_3\text{Fe}(\text{CN})_6$ -encapsulating liposomes in the stopped flow, tracking the spectral range from 480 nm to 700 nm over 3 minutes. At the end of the experiment the Triton x-100 detergent was added to lyse the liposomes, releasing $\text{K}_3\text{Fe}(\text{CN})_6$ into bulk solution.

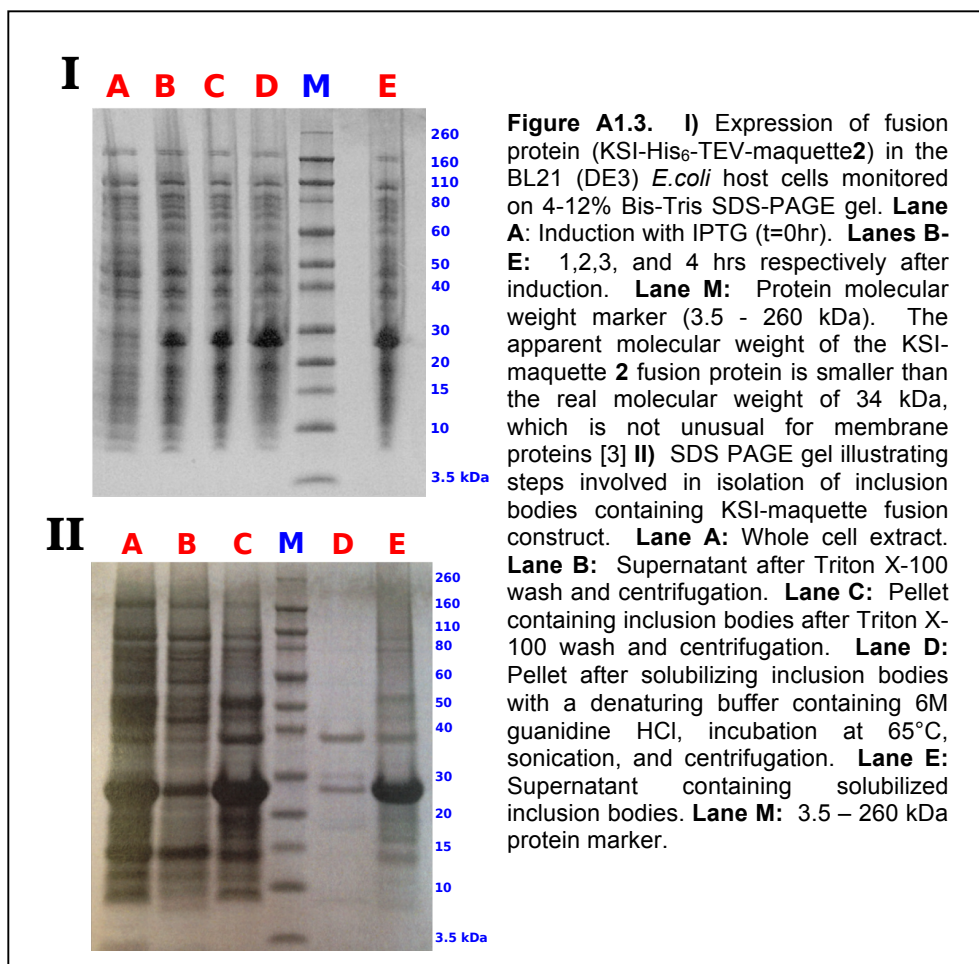
Initial experiments showed surprisingly fast ITS oxidation even in the absence of heme and protein, leading to two changes that were later added to this procedure (see **Section 5.2.3**). First, the fill syringes and drive syringes of the spinning-disk stopped-flow spectrometer (OLIS, Inc.) were soaked for one hour with degassed buffer prior to the experiment 5 minutes before transferring the liposome and ITS samples to the stopped-flow instrument. Secondly, the enzymatic O_2 scrubbing cocktail of 80 mM glucose oxidase, 12 mM catalase, and 1 mM glucose was added to both solutions five minutes before loading them onto the stop flow. [4] (see **Section A1.1**). Finally, the POPC lipid was replaced with a 70::15::15 molar mixture of POPC / POPS / cholesterol (Avanti Polar Lipids).

A1.8 Expression and Purification of AM1

A1.8.1 AM1 Expression

DNA 2.0 provided a gene incorporating the AM1 sequence with a KpnI restriction enzyme site, His-tag, and tobacco etch virus (TEV) protease cleavage site. Base-pairs encoding a GGDG protein loop was added between the His-tag and TEV protease cleavage sites to enhance TEV cleavage efficiency. The gene was cloned into a pET31b(+) vector (Novagen), fusing a Δ^5 -3-ketosteroidisomerase (KSI) with AM1 to promote the formation of inclusion bodies during protein overexpression [7]. We made two modifications to the pET31b(+) vector prior to inserting the gene for the AM1 construct. First, a cysteine residue originally present in the pET31b(+) vector between KSI and our cloning site was mutated to glycine to eliminate unwanted disulfide dimers. Second, an AAT codon for asparagine was inserted to the cloning site to adjust the melting temperature of the primers. An enzyme-free cloning method[8] enabled the cloning and mutagenesis steps. The modified pET31b(+) vector was transformed into DH5 α cells using standard transformation protocol. The presence of the intended KSI-AM1 sequence into the pET31b(+) vector was confirmed by DNA sequencing using KSI, T7 terminator and T7 promoter primers.

A 125 mL starter culture with 75 mg/L ampicillin was shaken at 37 °C for 12-16 hours, transferred to 2 L Terrific Broth containing 75 mg/L ampicillin, and finally shaken overnight at 37 °C. 2 mM IPTG was added to induce protein expression when the 600 nm absorbance reached 0.8 OD. At 5 hours post-induction the cells were pelleted and stored at -20 °C. An SDS-PAGE gel, shown in **Figure A1.3-A**, tracked the AM1 expression.



A1.8.2 AM1 Inclusion Body Isolation and Ni-NTA Purification

The cell pellets were thawed and resuspended in buffer (50 mM Tris, 300 mM NaCl, 20 mM MgSO₄, 20 mM CaCl₂, 50 mg/L PMSF, 500 mg/L lysozyme, pH 8.0). Triton X-100 was added to a final concentration of 1% and the suspension was stirred at 4 °C for 30 min. DNase I was added to a final concentration of 0.2 g/L and the suspension was stirred at 4 °C for an additional 30 min. The suspension was then subjected to 3 freeze-thaw cycles. 20 min centrifugation at 10,000 g pelleted the inclusion bodies. The detergent resuspension, stirring, and centrifugation steps were repeated an additional two times. The final pellets containing the inclusion bodies were stored at -80 °C for future use [7]. The SDS-PAGE gel in **Figure 1.3-B** the inclusion body purification steps.

Inclusion bodies were solubilized in denaturing buffer (6 M guanidine-HCl, 100 mM NaH₂PO₄, 10 mM Tris, 2% Tween-20, pH 8.0) in a bath sonicator at 65 °C. The solubilized fusion protein was separated from insoluble debris by centrifugation at 15,000 g for 20min. An ACTA FPLC (GE Healthcare) ran the sample through a 5 mL His-Trap Ni-NTA column (GE Healthcare) at 1 mL/min. The column was washed with 40 mL of denaturing wash buffer (6 M Urea, 100 mM NaH₂PO₄, 10 mM Tris, 2% Tween-20, pH 6.3) followed by 65 mL of urea-free wash buffer (50 mM NaH₂PO₄, 300 mM NaCl, 10 mM imidazole, 2% Tween-20, pH 8.0). A step-function change to high-imidazole buffer (50 mM NaH₂PO₄, 300 mM NaCl, 250 mM imidazole, 2% Tween-20, pH 8.0) quickly eluted the fusion protein from the His-Trap Ni-NTA column. SDS-PAGE confirmed the presence of the fusion protein in the Ni-NTA elution. The apparent molecular weight of the construct is about 27 kDa, consistent with the solubilized inclusion body protein seen in the previous gel in **Figure A1.3-A**.

To cleave the AM1 maquette from the His-tag and KSI under non-aggregating conditions, the TEV cleavage reaction must be performed in the presence of detergent(s) and/or denaturant(s). However, such conditions risk disabling of the TEV protease. To address this concern, we tested TEV cleavage activity on His-tagged BT6 [9] in the presence of various surfactants and denaturants. These tests showed that the TEV protease remains active in a solution with both 2% Tween-20 and 2 M urea. We solubilized the lyophilized fusion protein in 8% Tween-20 with sonication at 37 °C. Urea and buffer were then added to yield a solution containing 2% Tween-20, 2 M urea, 50 mM Tris-HCl (pH 8.0), 0.5 mM EDTA, 1 mM DTT. TEV protease was added to this mixture, and the cleavage reaction proceeded overnight at 4 °C. Efficiency of TEV cleavage of the maquette from KSI was confirmed by SDS-PAGE, as shown in **Figure A1.3-B**. Cleaved samples were precipitated by 7% trichloroacetic acid. The precipitate was solubilized in 100% hexafluoroacetone (HFA) and purified by reversed-phase HPLC (Waters) on a C4 column (Vydac) with the following solvents: 50:50 water (0.1% TFA): acetonitrile (0.1% TFA) for 20min followed by 100% acetonitrile (0.1% TFA) for 10min and 100% methanol with 50mM HFA.

A1.8.3 AM1 SDS Solubilization, DDM Exchange, and Liposome Incorporation

We tested the solubility of AM1 in various detergents including n-dodecylphosphocholine (DPC), dodecylmaltoside (DDM), sodium cholate, Zwittergent 3-18, β -octylglucoside, octyl-POE, and SDS near or above their critical micellar concentration (CMC). AM1 solubilizes most readily in SDS. 7 mM SDS stock was prepared in 50 mM NaH_2PO_4 , 100 mM NaCl, pH 8.0. With mild sonication at 37 °C, AM1 readily dissolves to about 30 μM under these conditions. The dissolved protein was diluted in buffer to keep the SDS concentration at 3 mM (safely above its CMC of 1.8 mM) for circular dichroism and cofactor binding characterization.

Since SDS is a strong ionic detergent not ideal for maintaining native structure, we developed a detergent exchange protocol to transfer the maquette to nonionic DDM. AM1 is first dissolved in 7 mM SDS and 0.34 mM DDM in 50 mM NaH_2PO_4 , pH 8.0. Addition of a few μL of 3.5 M KCl followed by incubation at room temperature for 5 min results in the precipitation of insoluble potassium dodecyl sulfate. The sample was centrifuged at 14,000 g for 5 min to collect the supernatant containing protein stabilized in DDM [10, 11]. We confirmed spectroscopically that the concentration of the maquette before and after SDS precipitation did not change.

AM1 may also be solubilized for MALDI-TOF by adding acetonitrile to the lyophilized protein, followed by sonication and dilution with an equal volume of methanol.

We employed a detergent depletion procedure to incorporate SDS-solubilized AM1 into lipid vesicles. 80::20 POPC/POPS in chloroform (Avanti Polar Lipids) was dried under argon to form a thin film on a glass vial, and residual solvent was removed by applying vacuum overnight. The dry lipid mixture was dissolved in a detergent buffer containing 0.6% (w/v) octyl-POE, 50mM NaH_2PO_4 and 100mM NaCl, pH 8.0. The solubilized lipids were kept at room temperature for 5-10 min before adding the AM1 solubilized in 7mM SDS. The protein-lipid mixture was incubated at room temperature 15 min. The detergent was removed with Bio-Beads SM-2 (BioRad). 1 g of Bio-Beads was added per 14 mg SDS and 40 mg of octyl-POE, providing depletion capacity in excess of the reported removal for these detergents [12, 13]. The detergent/protein/lipid mixture was added to the Bio-Beads and the mixture was incubated at room temperature for 60 min. The resulting proteoliposomes were retrieved by centrifugation at 3000 g for 15 min.

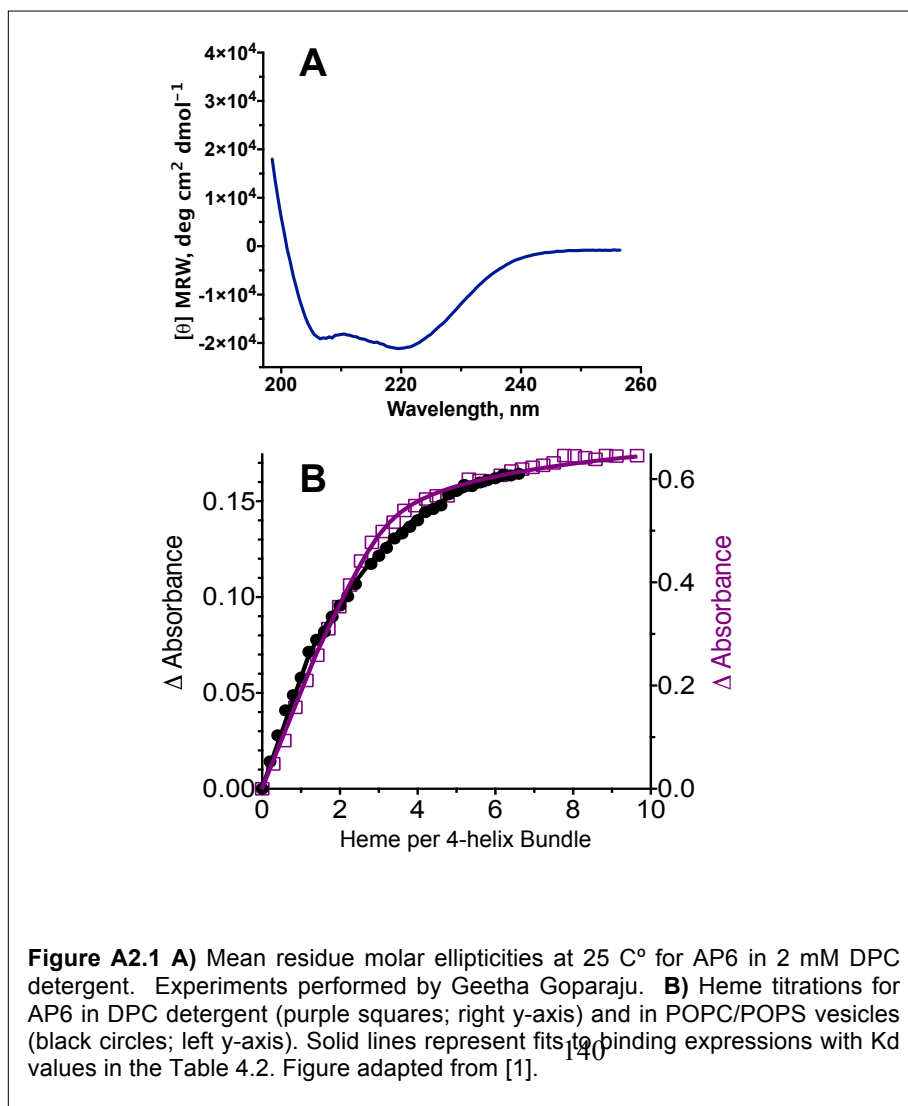
We observed that total heme binding in vesicle-incorporated AM1 improved by adding one stoichiometric unit of heme to the SDS-solubilized protein prior to detergent depletion. The detergent depletion procedure resulted in negligible loss of the heme, and additional heme units were added after vesicle incorporation.

A1.8 References

- [1] D.A. Kendall, R.C. Macdonald, A Fluorescence Assay To Monitor Vesicle Fusion And Lysis, *Journal of Biological Chemistry*, 257 (1982) 3892-3895.
- [2] Pasterna.Ra, Christen.Mv, J. Heller, Diffusion And Permeation Of Oxygen, Nitrogen, Carbon Dioxide, And Nitrogen Dioxide Through Polytetrafluoroethylene, *Macromolecules*, 3 (1970) 366-&.
- [3] A. Rath, M. Glibowicka, V.G. Nadeau, G. Chen, C.M. Deber, Detergent binding explains anomalous SDS-PAGE migration of membrane proteins, *Proceedings of the National Academy of Sciences of the United States of America*, 106 (2009) 1760-1765.
- [4] L. Risinger, X.R. Yang, G. Johansson, Deoxygenation Of Supporting Electrolytes In Stripping Voltammetry By Glucose And Co-Immobilized Glucose-Oxidase And Catalase In A Flow System, *Analytica Chimica Acta*, 200 (1987) 313-318.
- [5] G. Bohm, R. Muhr, R. Jaenicke, Quantitative-Analysis Of Protein Far Uv Circular-Dichroism Spectra By Neural Networks, *Protein Engineering*, 5 (1992) 191-195.
- [6] E.A. Berry, B.L. Trumpower, Simultaneous determination of hemes a, b, and c from pyridine hemochrome spectra, *Anal Biochem*, 161 (1987) 1-15.
- [7] E. Rodríguez-Carmona, O. Cano-Garrido, J. Seras-Franzoso, A. Villaverde, E. García-Fruitós, Isolation of cell-free bacterial inclusion bodies, *Microbial Cell Factories*, 9 (2010) 1-9.
- [8] D. Tillett, B.A. Neilan, Enzyme-free cloning: a rapid method to clone PCR products independent of vector restriction enzyme sites, *Nucleic acids research*, 27 (1999) e26-e28.
- [9] T.A. Farid, G. Kodali, L.A. Solomon, B.R. Lichtenstein, M.M. Sheehan, B.A. Fry, C. Bialas, N.M. Ennist, J.A. Siedlecki, Z. Zhao, M.A. Stetz, K.G. Valentine, J.L.R. Anderson, A.J. Wand, B.M. Discher, C.C. Moser, P.L. Dutton, Elementary tetrahelical protein design for diverse oxidoreductase functions, *Nature Chemical Biology*, 9 (2013) 826-+.
- [10] C. Dreher, A. Prodoehl, M. Weber, D. Schneider, Heme binding properties of heterologously expressed spinach cytochrome b(6): Implications for transmembrane b-type cytochrome formation, *Febs Letters*, 581 (2007) 2647-2651.
- [11] J.-Y. Zhou, G.P. Dann, T. Shi, L. Wang, X. Gao, D. Su, C.D. Nicora, A.K. Shukla, R.J. Moore, T. Liu, D.G. Camp, II, R.D. Smith, W.-J. Qian, Simple Sodium Dodecyl Sulfate-Assisted Sample Preparation Method for LC-MS-Based Proteomics Applications, *Analytical Chemistry*, 84 (2012) 2862-2867.
- [12] J.L. Rigaud, G. Mosser, J.J. Lacapere, A. Olofsson, D. Levy, J.L. Ranck, Bio-beads: An efficient strategy for two-dimensional crystallization of membrane proteins, *Journal of Structural Biology*, 118 (1997) 226-235.
- [13] J.J. Lacapere, F. Delavoie, H. Li, G. Peranzi, J. Maccario, V. Papadopoulos, B. Vidic, Structural and functional study of reconstituted peripheral benzodiazepine receptor, *Biochem. Biophys. Res. Commun.*, 284 (2001) 536-541.

Appendix A2 Biophysical Characterization of Amphiphilic Maquettes

This appendix gives the data for the biophysical characterization of the amphiphilic maquettes AP6 and AM1 introduced in **Chapter 5**. The CD, binding, and potentiometry experiments were performed by Discher group post-doc Geetha Goparaju. The MALDI experiment was performed by Bryan Fry. Results are published in Reference [1].



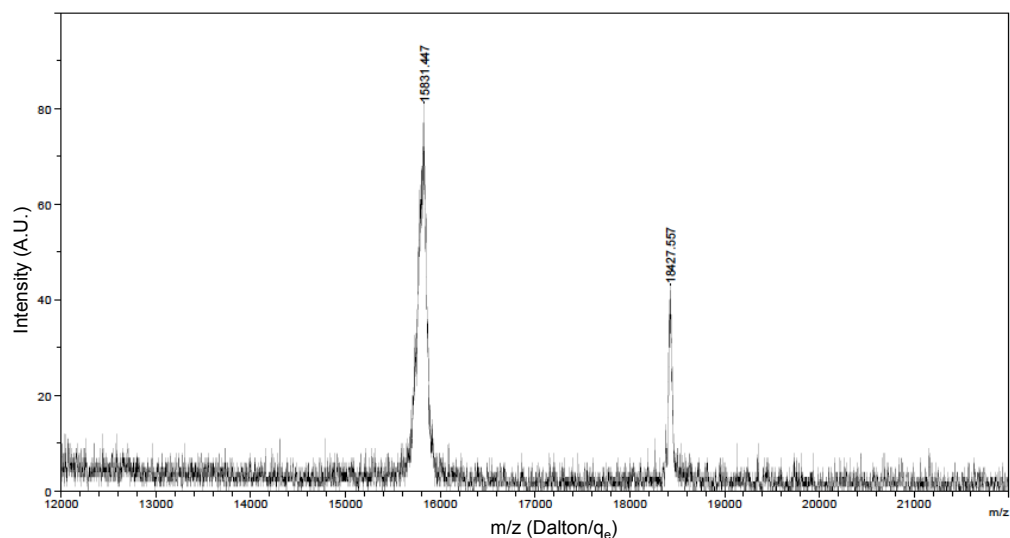


Figure A2.2. MALDI-TOF spectrum of TEV-cleaved AM1. The lower-mass peak is the cleavage fragment consisting of the TEV site, His-tag, and ketosteroid isomerase. The higher-mass peak, measured at 18427 dalton, close to the predicted mass of 18419 dalton.

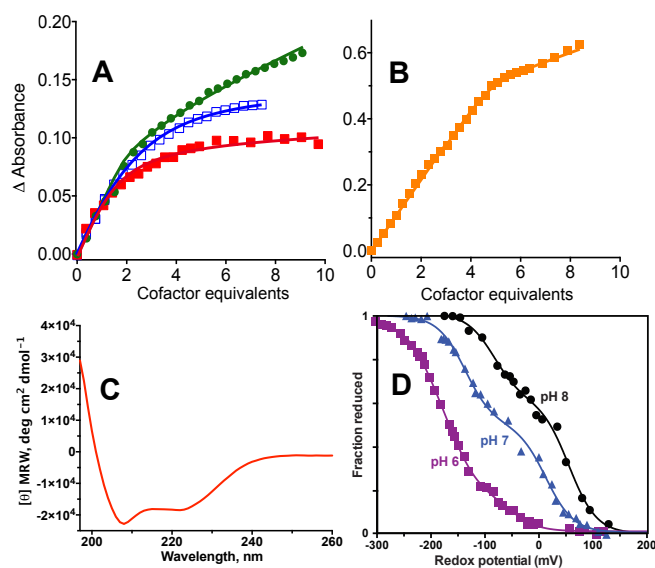
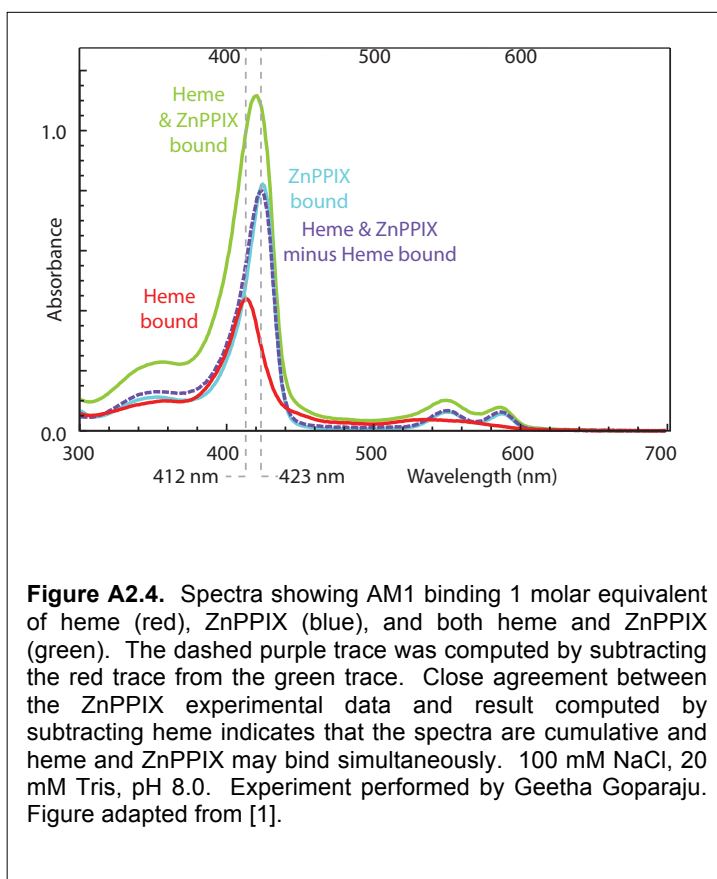


Figure A2.3. Biophysical characterization of the AM1 maquette. **(A)** Heme titrations for AM1 in SDS (filled red squares) and DDM (open blue squares) detergents and in POCP/POPS vesicles (green circles). **(B)** ZnPIX titrations for AM1 in SDS detergent. Solid lines represent fits to binding expressions with K_d values in the Table 4.3. **(C)** Mean residue molar ellipticities at 25 °C for AM1 in 3 mM SDS. **(D)** Redox titrations of 2 stoichiometric equivalents of heme in **AM1**. At pH 6, protonation of ligating His becomes more likely and less of the higher potential heme appears to be bound. Experiments performed by Geetha Goparaju.



A2.1 References

[1] G. Goparaju, B.A. Fry, S.E. Chobot, G. Wiedman, C.C. Moser, P.L. Dutton, B.M. Discher, First principles design of a core bioenergetic transmembrane electron-transfer protein, *Biochimica Et Biophysica Acta-Bioenergetics*, 1857 (2016) 503-512.